Author:
Zhang, Lizhong

Title:
Spatiotemporal Seismic Hazard and Risk Assessment of Global M9.0 Megathrust Earthquake Sequences

Spatiotemporal Seismic Hazard and Risk Assessment of Global M9.0 Megathrust Earthquake Sequences

Lizhong Zhang

Department of Civil Engineering

University of Bristol

A dissertation submitted to the University of Bristol in accordance with the requirements for award of the degree of Doctor of Philosophy in the Faculty of Engineering

2019

Word Count: 58,862

Abstract

Megathrust earthquake sequences can impact multiple buildings and infrastructure in a city/municipality due to not only the mainshock but also the triggered aftershocks along the subduction interface and in the overriding crust. The time between the mainshocks and aftershocks usually is too short to retrofit the structures; therefore, aftershocks can cause additional damage. To have a better understanding of the impact of aftershocks on city-wide seismic risk assessment, this thesis develops a new simulation framework of spatiotemporal seismic hazard and risk assessment of future M9.0 sequences. Different components under the new simulation framework including the seismicity model and the fragility model are developed.

The epidemic type aftershock sequence (ETAS) model, a spatiotemporal seismicity model, is modified to characterise aftershocks of large and anisotropic finite M9.0 mainshock sources. To give realistic ranges of aftershock simulations in regions with limited data after a future giant shock, the variability of the ETAS model parameters is assessed in global subduction zones that have experienced M≥7.5 earthquakes. Considering known biases of the parameters (due to model formulation, the isotropic spatial distribution, and finite-size effects of catalogues), the variability of the ETAS parameters from robust estimates is not significant. A set of ETAS parameters of future M9.0 sequences is proposed for hazard assessment.

Cascadia subduction zone is considered as a case study to demonstrate how the new simulation framework can be applied to a subduction-zone region with limited observed data. To account for damage accumulation of wood-frame houses due to aftershocks in Canada, a new approach that adopts cloud analysis using real mainshock-aftershock sequences with moderate scaling factors is proposed to develop state-dependent fragility curves. By implementing the updated components of the spatiotemporal seismicity model and the state-dependent fragility model, the simulation framework can be used for quasi real-time aftershock hazard and risk assessments and post-event risk management.

Keywords: Spatiotemporal seismic hazard and risk assessment of megathrust sequences; Spatiotemporal ETAS model; M9.0 megathrust events triggering crustal and subduction aftershocks; Global subduction zones; State-dependent aftershock fragility curves of wood-frame houses; Damage state estimation of spatially distributed wood-frame houses.

Acknowledgements

I would like to thank my supervisor Dr Katsuichiro Goda for offering me a PhD opportunity with the best research topic and for his continuous support during my PhD. I enjoyed my PhD life because of his kind guidance, and his high quality and high impact research. Thank you, Katsu, for your quick reply every time and constructive comments.

It was an honour to work with Dr Maximilian Werner as my supervisor, so I have multidisciplinary experiences also from statistical seismology. Thanks for his patience, for his valuable feedback, for training me as an independent researcher, and for guiding me to develop critical thinking on research.

I would like to thank my supervisor, Dr Flavia De Luca for her advice to improve the quality of my work, for her encouragement, and for her available time to meet and discuss various issues. Many thanks to Dr Nick Alexander and Dr Nicolas Luco for agreeing to be my examiners of my PhD viva.

Thank you, Dr Raffaele De Risi, for your help and suggestions during my PhD, your sense of humour, and your amazing magic shows. I would also like to acknowledge the contributions from Dr Solomon Tesfamariam for his constructive comments about my work and for sharing the building dataset in Victoria, Canada. I am grateful to Dr Ario Muhammad for his help and many interesting discussions during my PhD. Many thanks to all my officemates in 0.91 from Department of Engineering at University of Bristol, Mr Ahmer Ali, you will be the next one.

I would like to thank Dr Myrto Papaspiliou and Dr Rosa Sobradelo for offering me an internship at Willis Tower Watson London during my PhD, which gave me a tremendous opportunity to widen my views on different applications of my works. I also would like to acknowledge all my colleagues at Willis Tower Watson for their kind helps and for making my stay there a great pleasure. I thank London Mathematical Laboratory for their supports when I stayed in London.

Thank you, Yanyan for your understanding and support. Most importantly, I would like to thank my parents and all my family members for their supports.

Author’s Declaration

I declare that the work in this dissertation was carried out in accordance with the regulations of the University of Bristol. The work is original except where indicated by special reference in the text and no part of the dissertation has been submitted for any other degree.

Any views expressed in the dissertation are those of the author and in no way represent those of the University of Bristol.

The dissertation has not been presented to any other universities for examination either in the United Kingdom or overseas.

Signed: ……

Date: ……

List of Publications

Zhang, L., M.J. Werner, and K. Goda (2018) Spatiotemporal seismic hazard and risk assessment of aftershocks of M 9 megathrust earthquakes, *Bull. Seismol. Soc. Am.* **108**, 3313–3335.

Zhang, L. and K. Goda (2019) Spatiotemporal Seismic Risk Assessment of Wood-frame Houses in Victoria, Canada under M9 Megathrust Subduction Sequences, In: *13th International Conference on Applications of Statistics and Probability in Civil Engineering(ICASP13)*, Seoul, South Korea, May 26-30, 2019.

Zhang, L., M.J. Werner, and K. Goda (2020) Variability of ETAS parameters in global subduction zones and applications to mainshock-aftershock hazard assessment, Bull. Seismol. Soc. Am. **110**, 191–212.

Zhang, L., K. Goda, F. De Luca, and R. De Risi (2020) Mainshock-aftershock state-dependent fragility curves: the case of wood-frame houses in British Columbia, Canada, *Earthq. Eng. Struct. Dyn* (accepted).

Zhang, L., K. Goda, M.J. Werner, and S. Tesfamariam (2020) Spatiotemporal seismic hazard and risk assessment of M9.0 megathrust earthquake sequences of wood-frame houses in Victoria, British Columbia, Canada, *Earthq. Eng. Struct. Dyn.* (under review).

Contents

Abstract i

Acknowledgements ii

Author's Declaration iv

List of Publications v

Contents vi

List of Figures xii

List of Tables xxv

List of Abbreviations and Symbols xxvii

Abbreviations xxvii

Symbols xxix

Chapter 1 Introduction 1

1.1 Background and motivation 1

1.2 Aims and objectives 7

1.3 Thesis outline 8

Chapter 2 Spatiotemporal Seismic Hazard and Risk Assessment of Aftershocks of M9.0 Megathrust Earthquakes 11

2.1 Introduction 11

2.2 Data 15

2.3 Overview of framework 16

2.4 Spatiotemporal ETAS model 18

2.4.1 ETAS model 18
2.4.1.1 ETAS parameter estimation and stochastic declustering 19
2.4.1.2 ETAS simulation 20
2.4.1.3 Earthquake rupture model 23
2.5 Seismicity analysis of M9-triggered aftershock sequences in Tohoku 25
2.5.1 ETAS parameter estimation in Tohoku 25
2.5.2 ETAS simulation in the Tohoku region 29
2.6 Seismic hazard analysis of M9-triggered aftershock sequences in Tohoku 32
2.6.1 Comparison of daily observed PGVs with simulated PGVs 35
2.6.2 Spatiotemporal aftershock hazard assessment 36
2.6.3 Comparison of spatiotemporal aftershock hazard rates with conventional long-term hazard rates 43
2.7 Seismic risk analysis of M9-triggered aftershock sequences in Tohoku 46
2.8 Conclusions 49
Chapter 3 Variability of ETAS Parameters in Global Subduction Zones and Applications to Mainshock-aftershock Hazard Assessment 52
3.1 Introduction 52
3.2 ETAS model 56
3.2.1 ETAS parameter estimation 56
3.2.2 ETAS residual analysis 58
3.3 Data 59
3.3.1 Earthquake catalogues of global M$\geqslant$7.5 subduction earthquakes 59

3.4 Comparison of ETAS parameters by region and magnitude....63
3.4.1 Case 1 - Long time period catalogues....64
3.4.1.1 Regional dependence of ETAS parameters in Case 1....64
3.4.1.2 Magnitude dependence of ETAS parameters in Case 1....68
3.4.2 Case 2 - Long time period Catalogues with fixed α....70
3.4.2.1 Residual analysis of Cases 1 and 2....71
3.4.2.2 ETAS parameter results of Case 2....72
3.4.3 Case 3 - Individual sequences....75
3.4.4 ETAS parameter estimation of multiple subduction earthquakes....79
3.5 Global ETAS parameters for M9-class events and its simulation....81
3.5.1 Global ETAS parameters for M9-class events....81
3.5.2 ETAS simulations of M9-class events....82
3.6 Conclusions....86
Chapter 4 Development of State-dependent Aftershock Fragility Curves of Wood-frame Houses in British Columbia, Canada....88
4.1 Introduction....88
4.2 Cumulative damage due to mainshock-aftershock sequences....92
4.2.1 UBC-SAWS model....93
4.2.2 Mainshock-aftershock ground motion records....95
4.2.3 EDPs....99
4.2.4 IMs....103
4.2.4.1 Evaluation of IMs....104

4.2.5 Methods to develop seismic fragility curves 105
4.2.5.1 Cumulative lognormal distribution 105
4.2.5.2 Multinomial distribution 106
4.2.6 Aftershock fragility curves 106
4.3 Evaluation of EDPs and IMs using real ground motion records 108
4.3.1 Pre-EDP 109
4.3.2 Ground motion records 110
4.3.3 Mainshock EDP-IM 113
4.3.4 Evaluation of EDPs 115
4.3.5 Evaluation of IMs 117
4.4 State-dependent fragility modelling 120
4.4.1 Pre- and post-DS definitions 120
4.4.2 Procedures to develop the aftershock fragility curves 125
4.4.3 Comparison of aftershock fragility curves with Sa(T=0.3s), Sa(T=0.5s), and PGV 127
4.4.4 Comparison of aftershock fragility curves with DS definitions based on Cases 1 and 2 132
4.4.5 Comparison of aftershock fragility curves using approaches 1-3 136
4.4.6 Aftershock fragility curves of Houses 1-4 with PGV 139
4.5 Conclusions 144
Chapter 5 Spatiotemporal Risk Assessment of Wood-frame Houses under M9.0 Earthquake Sequences in Victoria, British Columbia, Canada 147

5.1 Introduction 147
5.2 Spatiotemporal seismic hazard and risk assessment in Victoria 151
5.2.1 Seismicity model 153
5.2.1.1 Analysis of ANSS and SHEEF catalogues in the CSZ 153
5.2.1.2 ETAS parameters in global subduction zones and Queen Charlotte Island 156
5.2.1.3 ETAS simulation 158
5.2.2 Ground motion model 162
5.2.3 Seismic risk model 165
5.3 Results and discussion 168
5.3.1 Impact of mainshocks on DS and loss estimations 169
5.3.2 Impact of aftershocks on DS and loss estimations 174
5.3.3 Extreme case with a triggered crustal aftershock near Victoria 182
5.4 Conclusions 185
Chapter 6 Conclusions and Outlook 188
6.1 Conclusions 188
6.2 Future research 192
Appendix A 195
A.1 2D Gaussian distribution 195
A.2 Anisotropic power law distribution 197
Appendix B 198
B.1 Daily hazard rate from JSHIS 198

B.2 Daily mainshock-aftershock hazard rate from the ETAS model 198

B.3 Daily conditional and unconditional aftershock hazard rates 199

Appendix C 200

C.1 Comparison of the mainshock rupture model and the scaling law 200

Appendix D 202

D.1 ETAS residual results of Cases 1 and 2 202

D.2 Log-likelihood values and Akaike information criterion values 212

Appendix E 213

E.1 Standard errors of ETAS parameters for each geographical region from boxplots 213

Boxplots of the ETAS parameters for Case 1 214

ETAS parameters classified by the largest magnitude in each sub-catalogue for Case 1 . 215

ETAS parameters classified by region for Case 2 216

Boxplots of the ETAS parameters for Case 2 217

Appendix F 219

F.1 Sufficiency and efficiency of IMs for Houses 1-3. 219

References 222

List of Figures

Figure 1-1. Spatiotemporal seismic hazard and risk framework. 6

Figure 2-1. Framework for spatiotemporal seismic hazard and risk assessment. 17

Figure 2-2. An example of the spatial probability density function of the first generation of aftershocks outside a simulated rupture area (500 km×300 km). We employ 1D and 2D kernel power-laws for aftershocks outside the rupture area, respectively. 22

Figure 2-3. (a) Target (dotted line) and data (dashed line) windows for ETAS parameter estimation. Stars denote the three locations chosen to illustrate the hazard and risk calculations: Sendai (141.03ºE, 38.31ºN), Fukushima II NPP (141.01ºE, 37.32ºN), and Tokyo (139.77ºE, 35.72ºN). (b) Magnitude of completeness (M_c) of the JMA catalogue from 1970 to 2015 using a sliding time window of 200 events in the target window. (c) Observed magnitude-frequency distributions and fitted Gutenberg-Richter laws with maximum likelihood estimates of the *b*-values and 5^{th}-95^{th} percentiles. (d) Observed 2D aftershock histogram with M⩾5.5 during the 100 days after the 2011 Tohoku mainshock. 26

Figure 2-4. Comparison of observed and simulated aftershocks with M⩾5.5 after the 2011 Tohoku earthquake: (a) Magnitude frequency histogram in the first 100 days and 95% uncertainty range from the simulations in square root scale. (b) Daily number of events in the first 30 days with 95% uncertainty range. 30

Figure 2-5. Two ETAS simulations in comparison with the 2011 Tohoku events with M⩾5.5. (a, c) Simulated 2D aftershock histograms during the first 100 days. (b, d) Comparison of daily numbers of observed and simulated aftershocks. The mainshock source parameters (epicentre, slip angle, strike angle, rupture length, and rupture width) are randomly generated from the empirical distributions. 31

Figure 2-6. (a) Median values of PGV with V_{s30} = 300 m/s for subduction earthquakes from M6.0-M9.0 using the GMPE by Morikawa and Fujiwara (2013). (b) Median values of PGV with V_{s30} = 300 m/s for crustal earthquakes from M5.0-M8.0 using the GMPE by Morikawa and Fujiwara (2013). (c) Fragility curves (the exceeding probability of damage states against PGV) of wood-frame houses for Japan with slight damage, moderate damage, and heavy damage. 34

Figure 2-7. Comparison of mean simulated and observed rate of PGV > 1 cm/s per day during the first 7 days after the 2011 Tohoku mainshock in (a) Sendai, (b) Fukushima II NPP and (c) Tokyo. Vertical bars denote 10^{th} to 90^{th} percentile range of simulated ground motions. 36

Figure 2-8. Rates of exceeding aftershock PGVs on left y-axis (diamond) on Day 1 in Sendai in comparison with PGV rates of simulated mainshock on right y-axis (upward-pointing triangle). 37

Figure 2-9. (a) Rates of exceeding aftershock PGVs (diamond) on Day 1 in Sendai in comparison with Fukushima II NPP (square), and Tokyo (star). (b) Three soil conditions with V_{s30} = 200 m/s (circle with dashed line), 300 m/s (diamond), and 400 m/s (circle with dotted line). (c) time periods with T = 1 day (diamond), 1week (circle), 1 month (right-pointing triangle), and 1 year (star). (d) Day 1 (diamond), Day 2 (upward-pointing triangle), Day 3 (pentagram), Day 4 (downward-pointing triangle), and Day 5(square). 38

Figure 2-10. Daily rates of exceeding PGV for crustal and subduction aftershocks (circles with solid line), crustal (upward-pointing triangles with dashed line) and subduction (squares with dotted line) aftershocks in the first 7 days in (a) Sendai, (b) Fukushima II NPP, and (c) Tokyo. 40

Figure 2-11. Daily rates of exceeding PGV for crustal and subduction aftershocks in the first 7 days 20km, 40km, and 60km away from Fukushima II NPP. 41

Figure 2-12. Daily hazard rates of PGV > 60 cm/s due to crustal and subduction aftershocks in comparison with simulated mainshock (stars) in (a) Sendai and (b) Fukushima II NPP. ...42

Figure 2-13. Left panels: comparison between daily time-dependent hazard rate (squares) and the 2017 JSHIS long-term hazard rate corresponding to 2% in 50 years (dash-dotted line) with return periods 300, 600, and 1000 years in (a) Sendai, (c) Fukushima II NPP, and (e) Tokyo. Right panels: comparison with the 2010 JSHIS rate. 44

Figure 2-14. (a) Decay of conditional aftershock hazard rates in Sendai immediately after the Tohoku-like mainshock in one year. (b) Decay of unconditional aftershock hazard rates considering a 600-year return period of the Tohoku-like mainshock. 46

Figure 2-15. Comparison of mean daily DS rates of simulated mainshock and aftershocks in (a) Sendai and (b) Fukushima II NPP. 47

Figure 2-16. Mean daily damage state rates of crustal and subduction aftershocks for DS_1, DS_2 and DS_3 in (a) Sendai and (b) Fukushima II NPP. 49

Figure 3-1. Map of earthquake locations with M$\geqslant$7.5. Earthquakes are grouped by regions, which are Japan (JPN), Eastern Indonesia (EI), Papua New Guinea (PNG), Western Indonesia (WI), New Zealand (NZ), North America (NA), Central America (CA), and South America (SA). The numbers in parentheses correspond to the indices in **Table 3-2**.....62

Figure 3-2. ETAS parameter estimates classified by region for Case 1 based on long-time catalogues with free α (SA: South America, NA: North America, JPN: Japan, PNG: Papua New Guinea, EI: Eastern Indonesia, WI: Western Indonesia, and NZ: New Zealand). 65

Figure 3-3. Anti-correlation between estimated K_0 and α parameters, colour-coded by the ratios of rupture length to width of the largest earthquakes within the sub-catalogues.....67

Figure 3-4. ETAS parameter results of Case 2 with fixed α classified by the largest magnitudes in sub-catalogues (ETAS parameter results of Case 1 are plotted without numbering for comparison).....73

Figure 3-5. ETAS parameter results classified by mainshock magnitudes for Case 3 based on individual sequences. 77

Figure 3-6. Parameter results from the sub-catalogues with multiple subduction earthquakes in Indonesia, Chile, and Japan. 80

Figure 3-7. Comparison of observed and simulated M5.5+ aftershocks of the 2004 Aceh-Andaman earthquake: (a) magnitude frequency distribution in square root scale during the first three months, (b) daily number of events during the first 30 days, (c) observed 2D aftershock histograms during the first three months, (d) a simulated 2D aftershock histogram over the same period. 83

Figure 3-8. Comparison of observed and simulated M5.5+ aftershocks after the 2010 Maule earthquake: (a) magnitude frequency distribution during the first three months, (b) daily number of events during the first 30 days, (c) observed 2D aftershock histogram during the first three months, (d) a simulated 2D aftershock histogram over the same period. 84

Figure 3-9. Comparison of observed and simulated M5.5+ aftershocks after the 2011 Tohoku earthquake: (a) magnitude frequency distribution in square root scale during the first three months, (b) daily number of events during the first 30 days, (c) observed 2D aftershock histogram during the first three months, (d) a simulated 2D aftershock histogram during the first three months. 85

Figure 4-1. Illustration of damage accumulation due to aftershocks. 92

Figure 4-2. Illustration of the UBC-SAWS model: (a) generic model of wood-frame houses, (b) ground and first floor plans of wood-frame houses, and (c) pushover analysis of Houses 1-4.....94

Figure 4-3. (a) An example of the 2011 Tohoku mainshock-aftershock sequence with (b) the displacement response time-history of House 4 of the maximum displacement (Max disp), the

residual displacement (Res disp) and the incremental maximum displacement (Δ Max disp), and (c) hysteretic response plot.....102

Figure 4-4. (a) An example of the 2011 Tohoku mainshock-aftershock sequence with (b) the displacement response time-history of House 4 of the maximum displacement (Max disp), the residual displacement (Res disp) and the incremental maximum displacement (Δ Max disp). 110

Figure 4-5. Magnitude-distance plot of the mainshocks (with filled colours) and aftershocks (with unfilled colours) including (a) crustal-NGA, (b) crustal-KKiKSK, (c) interface, and (d) inslab events. Rupture distance is the closest distance from the earthquake rupture plate to the site. 111

Figure 4-6. Response spectra (a) of mainshocks and aftershocks with 16^{th}, 50^{th}, and 84^{th} percentiles, and design spectrum with site class C in Victoria (b) of different earthquake types from both mainshocks and aftershocks with 16^{th}, 50^{th}, and 84^{th} percentiles. 113

Figure 4-7. IM-EDP plots of mainshocks of this study and Goda and Salami (2014). 114

Figure 4-8. Plots of 9 Cases of post-EDPs against pre-EDPs colour-coded based on $\log_{10}(Sa(T=0.3s))$ for House 4 (a) pre-MaxISDR and post-MaxISDR, (b) pre-MaxIISDR and post-MaxISDR, (c) pre-ResISDR and post-MaxISDR, (d) pre-MaxISDR and post-MaxIISDR, (e) pre-MaxIISDR and post- MaxIISDR, (f) pre-ResISDR and post-MaxIISDR, (g) pre-MaxISDR and post-ResISDR, (h) pre-MaxIISDR and post-ResISDR, (i) pre-ResISDR and post- ResISDR. 116

Figure 4-9. Plot of (a) efficiency (β_{IM}), sufficiency (p_{IM}) for (b) rupture distance and (c) magnitude, and (d) relative sufficiency of each IM given the non-collapse EDP with unscaled records for House 4. 119

Figure 4-10. Plot of post-MaxISDR against pre-ResISDR with Sa(T=0.3s) for House 4 using unscaled records. 124

Figure 4-11. (a) Plot of post-MaxISDR against Sa(T=0.3s) of House 4 for mainshocks only (596 records × 2 horizontal components × 5 scaling factors=5960 points). (b) Plot of post-MaxISDR against pre-ResISDR for aftershocks (1685 records × 2 horizontal components × 5 scaling factors=16850 points). 125

Figure 4-12. Plot of post-MaxISDRs against IM(T=0.3s) for House 4 with scaling factors 1-5 given pre-ResISDR (a) 0.01%-0.3%, (b) 0.3%-0.75%, (c) 0.75%-1.5%, and (d) 1.5%-3% from **Table 4-4**. 127

Figure 4-13. Plots of (a) the mainshock fragility curves, and the plots of aftershock fragility curves for (b) post-DS_1, (c) post-DS_2, (d) post-DS_3, (e) post-DS_4 based on pre-ResISDR, post-MaxISDR, and Sa(T=0.3s) for House 4 considering the DS definition based on Case 1 and fitting Approach 1. 129

Figure 4-14. Plots of (a) the mainshock fragility curves, and the plots of aftershock fragility curves for (b) post-DS_1, (c) post-DS_2, (d) post-DS_3, (e) post-DS_4 based on pre-ResISDR, post-MaxISDR, and Sa(T=0.5s) for House 4 considering the DS definition based on Case 1 and fitting Approach 1. 130

Figure 4-15. Plots of (a) the mainshock fragility curves, and the plots of aftershock fragility curves for (b) post-DS_1, (c) post-DS_2, (d) post-DS_3, (e) post-DS_4 based on pre-ResISDR, post-MaxISDR, and PGV for House 4 considering the DS definition based on Case 1 and fitting Approach 1. 131

Figure 4-16. Plots of (a) the mainshock fragility curves, and the plots of aftershock fragility curves for (b) post-DS_1, (c) post-DS_2, (d) post-DS_3 based on pre-ResISDR, post-MaxISDR, and Sa(T=0.3s) for House 4 considering the DS definition based on Case 2 and fitting Approach 1 133

Figure 4-17. Plots of (a) the mainshock fragility curves, and the plots of aftershock fragility curves for (b) post-DS_1, (c) post-DS_2, (d) post-DS_3 based on pre-ResISDR, post-MaxISDR,

and Sa(T=0.5s) for House 4 considering the DS definition based on Case 2 and fitting Approach 1.....134

Figure 4-18. Plots of (a) the mainshock fragility curves, and the plots of aftershock fragility curves for (b) post-DS_1, (c) post-DS_2, (d) post-DS_3 based on pre-ResISDR, post-MaxISDR, and PGV for House 4 considering the DS definition based on Case 2 and fitting Approach 1. 135

Figure 4-19. Plots of (a) the mainshock fragility curves, and the plots of aftershock fragility curves for (b) post-DS_1, (c) post-DS_2, (d) post-DS_3, (e) post-DS_4 based on pre-ResISDR, post-MaxISDR, and Sa(T=0.3s) for House 4 considering the DS definition based on Case 1 and fitting Approach 2. 137

Figure 4-20. Plots of (a) the mainshock fragility curves, and the plots of aftershock fragility curves for (b) post-DS_1, (c) post-DS_2, (d) post-DS_3, (e) post-DS_4 based on pre-ResISDR, post-MaxISDR, and Sa(T=0.3s) for House 4 considering the DS definition based on Case 1 and fitting Approach 3. 138

Figure 4-21. Plots of (a) the mainshock fragility curves, and the plots of aftershock fragility curves for (b) post-DS_1, (c) post-DS_2, (d) post-DS_3 based on pre-ResISDR, post-MaxISDR, and PGV for House 1 considering the DS definition based on Case 2 and fitting Approach 3. 140

Figure 4-22. Plots of (a) the mainshock fragility curves, and the plots of aftershock fragility curves for (b) post-DS_1, (c) post-DS_2, (d) post-DS_3 based on pre-ResISDR, post-MaxISDR, and PGV for House 2 considering the DS definition based on Case 2 and fitting Approach 3. 141

Figure 4-23. Plots of (a) the mainshock fragility curves, and the plots of aftershock fragility curves for (b) post-DS_1, (c) post-DS_2, (d) post-DS_3 based on pre-ResISDR, post-MaxISDR,

and PGV for House 3 considering the DS definition based on Case 2 and fitting Approach 3. 142

Figure 4-24. Plots of (a) the mainshock fragility curves, and the plots of aftershock fragility curves for (b) post-DS_1, (c) post-DS_2, (d) post-DS_3 based on pre-ResISDR, post-MaxISDR, and PGV for House 4 considering the DS definition based on Case 2 and fitting Approach 3. 143

Figure 5-1. Simulation framework of spatiotemporal seismic hazard and risk assessments (the same figure as **Figure 1-1**). 152

Figure 5-2. Seismicity of the Cascadia Subduction Zone in target window (dashed red polygon) listed in the ANSS catalogue (top) and the SHEEF catalogue (bottom) during 1981-2017: (a, c) epicentral locations and (b, d) latitudinal distribution. 154

Figure 5-3. Observed magnitude–frequency distributions (MFD) and fitted Gutenberg–Richter laws with the maximum-likelihood estimates of the *b*-values and 5^{th}–95^{th} percentiles from (a) the ANSS and (b) the SHEFF catalogues. 155

Figure 5-4. (a) Epicentres, and (b) latitudinal distribution of earthquakes during 1981-2017 near Queen Charlotte Island. The spatial window is based on the rupture plane of the 2012 M7.8 Haida Gwaii event. 157

Figure 5-5. Observed magnitude–frequency distribution and fitted Gutenberg–Richter law with a maximum-likelihood *b*-value and 5^{th}–95^{th} percentiles of the seismicity in **Figure 5-4**. 158

Figure 5-6. An example of the spatial probability density function of the first generation of aftershocks outside a simulated rupture area (rupture length × rupture width = 1100 km × 130 km). 160

Figure 5-7. Histogram of depths from past events with M$\geqslant$2. 161

Figure 5-8. (a) Simulated magnitude frequency distributions of aftershocks. (b) The daily number of simulated events over a month after the mainshock.....162

Figure 5-9. (a) Median values of peak ground velocity (PGV) with V_{S30} = 300 m/s for subduction earthquakes from M 7.0–9.0, using the ground-motion prediction equation (GMPE) by Ghofrani and Atkinson (2014) (b) Median values of PGV with V_{S30} = 300 m/s for crustal earthquakes from M 5.0–7.0, using the GMPE by Boore *et al.* (2014).....164

Figure 5-10. V_{s30} map of the City of Victoria from Wald and Allen (2007).....165

Figure 5-11. (a) mainshock fragility curves, and aftershock fragility curves for (b) post-DS_1, (c) post-DS_2, and (d) post-DS_3 for House 4.....166

Figure 5-12. Spatial distribution of wood-frame houses in Victoria (6,711 in total with House 1 #387, House 2 #197, House 3 #257, and House 4 #5,869).....168

Figure 5-13. (a) Damage probability of Houses 1-4 after mainshocks based on 6,711 houses in Victoria. (b) Loss exceedance curves of mainshocks. 10^{th}, 50^{th}, and 90^{th} percentiles of aggregated losses by mainshocks are 14, 66, and 194million Canadian dollars (m CAD$), respectively. 170

Figure 5-14. Plots of single simulations of mainshock shaking maps corresponding to (a) 10^{th}, (b) 50^{th}, and (c) 90^{th} percentiles of total losses. 171

Figure 5-15. Plots of a single simulation of DS distributions of wood-frame houses for (a) 10^{th}, (c) 50^{th}, and (e) 90^{th} percentiles of total losses (m $CAD) by mainshocks. The block map of seismic loss distribution of wood-frame houses in the City of Victoria for (b) 10^{th}, (d) 50^{th}, and (f) 90^{th} percentile scenarios.....173

Figure 5-16. (a) Damage probability of Houses 1-4 and (b) loss exceedance curves of mainshock-aftershock sequences at durations of 1 day, 1 week, 1 month, and 1 year based on 6,711 houses in Victoria. 10^{th}, 50^{th}, and 90^{th} percentiles of aggregated losses by mainshock-

aftershocks within 1 week are 20, 77, and 224 million Canadian dollars (m CAD$), respectively. 175

Figure 5-17. Plots of three single simulations of aftershock epicentres and latitudinal distribution of aftershocks with time on day 7 after the mainshock in the western Canada corresponding to (a, b) 10^{th} percentiles, (c, d) 50^{th} percentiles, and (e, f) 90^{th} percentiles of total losses. 177

Figure 5-18. Plots of three single simulations of mainshock PGV map, and maximum aftershock PGV hazard map by day 7 for the city of Victoria, Canada corresponding to (a, b) 10^{th} percentiles, (c, d) 50^{th} percentiles, and (e, f) 90^{th} percentiles of total losses. 178

Figure 5-19. Three single simulations of DS distributions of wood-frame houses due to the mainshock (left panels) and additional damage to the aftershock sequence within 1 week (right panels) corresponding to (a, b) 10^{th} percentiles, (c, d) 50^{th} percentiles, and (e, f) 90^{th} percentiles of total losses.....180

Figure 5-20. Three single simulations of seismic loss distribution (m $CAD) of wood-frame houses due to the mainshock (left panels) and additional damage to the aftershock sequence within 1 week (right panels) corresponding to (a, b) 10^{th} percentiles, (c, d) 50^{th} percentiles, and (e, f) 90^{th} percentiles of total losses. 181

Figure 5-21. Single simulation corresponding to the 90^{th} percentile of total losses: (a) aftershock epicentres, (b) latitudinal distribution of aftershocks with time to day 30 after the mainshock, (c) mainshock hazard map, and (d) the maximum aftershock hazard map within 30 days after the mainshock for the City of Victoria, Canada.....183

Figure 5-22. Plots of a single simulation of DS distribution of wood-frame houses for 90^{th} percentiles of total losses by (a) mainshock and (b) mainshock-aftershock sequences on day 30. The block map of seismic loss distribution (m CAD$) of wood-frame houses in the City of Victoria by (c) mainshock and (d) mainshock-aftershock sequence on day 30. 184

Figure A-1. An example of the spatial PDF of the first generation of aftershocks with a simulated rupture area (500 km×300 km).....196

Figure A-2. Simulated 2D aftershock histogram with M≥5.5 during the 100 days after the mainshock. 196

Figure A-3. An example of the spatial PDF of the first generation of aftershocks with a simulated rupture area (500 km×300 km).....197

Figure C-1. Comparisons between empirical scaling laws (Thingbaijam *et al.*, 2017)and effective rupture models of megathrust M≥7.5 earthquakes: (a) rupture length, (b) rupture width, and (c) rupture area. 201

Figure D-1. Residual analysis of Cases 1 (dashed line) and 2 (dash-dotted line) for Event 1 with Poisson unit rate (solid line) and 99% error bonds (dotted line) on left y axis (filled square is the start time of the mainshock and filled pentagon is the start time of the target window). Background probability of Case 1 (unfilled-square) and Case 2 (unfilled-circle) on right y axis. 202

Figure D-2. Residual analysis of Cases 1 (dashed line) and 2 (dash-dotted line) for Event 2. 203

Figure D-3. Residual analysis of Cases 1 (dashed line) and 2 (dash-dotted line) for Event 5. 203

Figure D-4. Residual analysis of Cases 1 (dashed line) and 2 (dash-dotted line) for Event 8. 204

Figure D-5. Residual analysis of Cases 1 (dashed line) and 2 (dash-dotted line) for Event 9. 204

Figure D-6. Residual analysis of Cases 1 (dashed line) and 2 (dash-dotted line) for Event 10. 205

Figure D-7. Residual analysis of Cases 1 (dashed line) and 2 (dash-dotted line) for Event 15. 205

Figure D-8. Residual analysis of Cases 1 (dashed line) and 2 (dash-dotted line) for Event 16. 206

Figure D-9. Residual analysis of Cases 1 (dashed line) and 2 (dash-dotted line) for Event 118. 206

Figure D-10. Residual analysis of Cases 1 (dashed line) and 2 (dash-dotted line) for Event 19. 207

Figure D-11. Residual analysis of Cases 1 (dashed line) and 2 (dash-dotted line) for Event 20. 207

Figure D-12. Residual analysis of Cases 1 (dashed line) and 2 (dash-dotted line) for Event 21. 208

Figure D-13. Residual analysis of Cases 1 (dashed line) and 2 (dash-dotted line) for Event 25. 208

Figure D-14. Residual analysis of Cases 1 (dashed line) and 2 (dash-dotted line) for Event 29. 209

Figure D-15. Residual analysis of Cases 1 (dashed line) and 2 (dash-dotted line) for Event 31. 209

Figure D-16. Residual analysis of Cases 1 (dashed line) and 2 (dash-dotted line) for Event 32. 210

Figure D-17. Residual analysis of Cases 1 (dashed line) and 2 (dash-dotted line) for Event 33. 210

Figure D-18. Residual analysis of Cases 1 (dashed line) and 2 (dash-dotted line) for Event 34. 211

Figure E-1. Boxplots of the ETAS parameter estimates classified by region in South America (SA), North America (NA), Japan (JPN), Papua New Guinea (PNG), Eastern Indonesia (EI), Western Indonesia (WI), and New Zealand (NZ) for Case 1. 214

Figure E-2. ETAS parameter results classified by the largest magnitude for Case 1 based on long time period catalogues with all ETAS parameters free. 215

Figure E-3. ETAS parameter results classified by region in South America (SA), North America (NA), Japan (JPN), Papua New Guinea (PNG), Eastern Indonesia (EI), western Indonesia (WI), and New Zealand (NZ) for Case 2 based on long time period catalogues with fixed α. 216

Figure E-4. Boxplots of the ETAS parameter estimates classified by region in South America (SA), North America (NA), Japan (JPN), Papua New Guinea (PNG), Eastern Indonesia (EI), western Indonesia (WI), and New Zealand (NZ) for Case 2 based on long time period catalogs with fixed α. Individual samples are plotted in circles with error bars. 217

Figure F-1. Plot of (a) efficiency (β_{IM}), sufficiency (p_{IM}) for (b) rupture distance and (c) magnitude, and (d) relative sufficiency of each IM given the non-collapse EDP with unscaled records for House 1. 219

Figure F-2. Plot of (a) efficiency (β_{IM}), sufficiency (p_{IM}) for (b) rupture distance and (c) magnitude, and (d) relative sufficiency of each IM given the non-collapse EDP with unscaled records for House 2. 220

Figure F-3. Plot of (a) efficiency (β_{IM}), sufficiency (p_{IM}) for (b) rupture distance and (c) magnitude, and (d) relative sufficiency of each IM given the non-collapse EDP with unscaled records for House 3. 221

List of Tables

Table 2-1. Selected record stations for PGV comparisons.....15

Table 2-2. Temporal windows and M_{cut} for ETAS parameter estimation.....28

Table 2-3. ETAS parameter estimation results (standard errors are shown in parentheses)...28

Table 3-1. Summary of three cases of temporal auxiliary and target windows. 58

Table 3-2. Summary of the selected large subduction earthquakes. 60

Table 3-3. Summary of the p_{lm} values of ETAS parameters for Case 1 (bold indicates statistically significant dependency and the "+" sign of the p_{lm} values indicates the correlation between the ETAS parameters and the earthquake characteristics). 69

Table 3-4. Summary of the p_{lm} values of ETAS parameters for Case 2 (Boldface indicates significant co-dependence). 75

Table 3-5. Summary of the estimated ETAS parameters of multiple subduction earthquakes with time windows 1981-2017.....79

Table 3-6. Suggested ETAS parameters for future **M**9.0 events. 82

Table 3-7. Summary of the mainshock source parameters of the ETAS simulations.....82

Table 4-1. Summary of ground motion record information in the literature 97

Table 4-2. Summary of IMs in this study.....103

Table 4-3. Collapse state limits of Houses 1-4.....123

Table 4-4. Summary of DSs for Cases 1 and 2 associated with the lower limits of ResISDR and MaxISDR (CS=collapse state). 123

Table 4-5. Median values (θ_{IM}) of mainshock-aftershock fragility curves (standard deviations (β_{IM}) are shown in the parentheses) from the cumulative lognormal distribution with damage state definition Case 1 and fitting Approach 1.....132

Table 4-6. Median values (θ_{IM}) of mainshock-aftershock fragility curves (standard deviations (β_{IM}) are shown in the parentheses) from the cumulative lognormal distribution with damage state definition Case 2 and fitting Approach 1.....136

Table 4-7. Estimated parameters of mainshock-aftershock fragility curves of House 4 from Approach 2 (cumulative lognormal distribution) and Approach 3 (multinomial distributions). 139

Table 4-8. Parameters θ_1 and θ_2 from the multinomial distribution using the DS definition based on Case 2 and fitting approach 3 for Houses 1-4.....144

Table 5-1. ETAS parameter estimates from global subduction zones and the Haida Gwaii event (standard errors are shown in parentheses).....158

Table D-1. Log-likelihood values and Akaike information criterion (AIC) values for Cases 1 and 2.....212

Table E-1. Summary of the p_{lm} values of ETAS parameters for Case 3 (Boldface indicates significant co-dependence). 218

List of Abbreviations and Symbols

Abbreviations

AI	Arias Intensity
AIC	Akaike Information Criterion
ANSS	Advanced National Seismic System
CA	Central America
CAD$	Canadian dollars
CASHEW	Cyclic Analysis of SHEar Walls
CAV	Cumulative Absolute Velocity
CMS	Conditional Mean Spectra
CSZ	Cascadia Subduction Zone
DM	Damage Measure
DS	Damage State
DV	Decision Variable
ECDFs	Empirical Cumulative Distribution Functions
EDP	Engineering Demand Parameter
EI	Eastern Indonesia
ETAS	Epidemic Type Aftershock Sequence
gCMT	global Centroid Moment Tensor
GMPE	Ground Motion Prediction Equation
GWB	Gypsum Wallboard
IDA	Incremental Dynamic Analysis
IM	Intensity Measure
ISC	International Seismological Centre

JMA	Japan Meteorological Agency
JPN	Japan
JSHIS	Japan Seismic Hazard Information Station
MaxISDR	Maximum Inter-story Drift Ratio
MaxIISDR	Maximum Incremental Inter-story Drift Ratio
MaxRDR	Maximum Roof Drift Ratio
MLE	Maximum Likelihood Estimation
MMI	Modified Mercalli intensity
NA	North America
NEHRP	National Earthquake Hazard Reduction Program
NEIC	National Earthquake Information Centre
NGA	Next Generation Attenuation
NMSZ	New Madrid Seismic Zone
NPP	Nuclear Power Plant
OSB	Oriented Strand Board
PBEE	Performance-Based Earthquake Engineering
PDF	Probability Density Function
PGA	Peak Ground Velocity
PNG	Papua New Guinea
PSHA	Probability Seismic Hazard Analysis
ResISDR	Residual Inter-story Drift Ratio
ResRDR	Residual Roof Drift Ratio
SA	South America
SAWS	Seismic Analysis of Wood-frame Structure
SDOF	Single-degree-of-freedom System

SHEEF	Seismic Hazard Earthquake Epicentre File
SI	Spectral Intensity
SMGAs	Strong-motion Generation Areas
WI	Western Indonesia

Symbols

α	ETAS productivity parameter
a_{IM}	Coefficient of the linear regression between $\log_{10}(EDP)$ and $\log_{10}(IM)$
b	b-value in the Gutenberg-Richter law
Beta	Beta function
β_{IM}	Efficiency of IM
b_{IM}	Coefficient of the linear regression between $\log_{10}(EDP)$ and $\log_{10}(IM)$
c	ETAS temporal parameter
C_{bc}	Cost to prevent L_{bc} by taking action in the benefit-cost approach
c_{IM}	Coefficient of the regression between Res_{IM} and rupture distance/magnitude
d	ETAS spatial parameter
d_{IM}	Coefficient of the regression between Res_{IM} and rupture distance/magnitude
g	Triggering rate in the ETAS model
γ	ETAS spatial parameter
h	Kernel bandwidth
H_t	Historical seismicity up to time t
I	Relative sufficiency
I_{JMA}	JMA intensity
K_0	ETAS productivity parameter
k_{1d}	1D kernel power law

k_{2d}	2D kernel power law
λ	Total seismicity rate in the ETAS model
λ_{PBEE}	Probabilistic description of the PBEE framework
L_{bc}	Loss without taking actions in the benefit-cost approach
L/W	Length-to-width
M	Moment magnitude
M_{c}	Magnitude completeness
M_{cut}	Magnitude cut-off
M_{j}	JMA magnitude
nDS	Total number of DS
μ	Background rate in the ETAS model
p	ETAS temporal parameter
P_{bc}	Probability that structures could reach higher building tags
p_{lm}	Slope coefficient of the linear regression
q	ETAS spatial parameter
R_{bc}	Benefit-cost ratio
Res_{IM}	Residual between IM and EDP
Sa	Spectral acceleration
τ	Transformed time in the residual analysis of the ETAS model
φ	Probability of background event in the ETAS model
Φ	Standard normal distribution
θ_{IM}	Median value of fragility curves
θ	Regression parameters of multinomial distribution
V_{s30}	Shear-wave velocities in the upper 30 m

Chapter 1 Introduction

1.1 Background and motivation

Recently destructive moment magnitude (M) 9.0 earthquakes in subduction zones have triggered numerous large aftershocks in Indonesia, Chile, and Japan. According to the National Earthquake Information Centre (NEIC) and Japan Meteorological Agency (JMA) catalogues, more than eighty M≥5.5 aftershocks were triggered within two months of the 2004 M9.1 Aceh-Andaman earthquake, while the 2011 M9.0 Tohoku mainshock triggered circa 200 JMA magnitude (M_j) ≥ 5.5 aftershocks within two months. Seismicity rates were increased by several orders of magnitude, not just along with the ruptured plate interface, but also near population centres in the overriding continental crust. The triggered aftershocks could cause additional damage to buildings and infrastructure given the short time between the mainshock to aftershocks. In particular, triggered shallow aftershocks near population centres and critical infrastructures can be dangerous. For example, a month after the Tohoku mainshock, a large M6.6 aftershock struck near the Fukushima Nuclear Power Plant, 300 km from the epicentre of the Tohoku mainshock (Fukushima *et al.*, 2013; Toda and Tsutsumi, 2013). The socioeconomic impact of the M9.0 earthquake sequence with its secondary effects (e.g., tsunami and geohazards) was also significant. The insured losses of the 2004 M9.1 Aceh-Andaman earthquake, the 2010 M8.8 Maule earthquake, and the 2011 M9.0 Tohoku earthquake were approximately $3.21, $9.79, and $27.5 billion US dollars, respectively, which were all ranked in the top 10 highest insured losses (Daniell *et al.*, 2011). For effective earthquake risk management, it is vital to assess the spatiotemporal seismic hazard and risk of megathrust sequences in urban areas for decision-making in post-earthquake risk management right after the mainshock, including humanitarian relief, building tagging, inspection

prioritisation, retrofitting, informing the population of residual risks, and rapid seismic loss estimation (Jordan *et al.*, 2011).

Similar M9.0-class sequences could take place in other subduction zones in the future, for example, the Mentawai subduction zone in Indonesia (Natawidjaja *et al.*, 2006) and the Cascadia subduction zone (CSZ) in North America (Wang and Tréhu, 2016). These subduction zone regions have not been active recently, but M9.0-class events did occur hundreds of years ago, which are beyond the time window of the instrumental catalogue. Therefore, only a few (e.g., M8.0-class events) or no sequences were recorded in these subduction-zone regions (Sieh *et al.*, 2008; Goldfinger *et al.*, 2012). Also, because of the short instrumental catalogue, seismic hazard and risk assessments of M9.0-class earthquake sequences based on the regional catalogue alone are not feasible.

Despite the apparent aftershock hazard and risk to people and infrastructure, current long-term national seismic hazard maps (e.g., Petersen *et al.*, 2014) mostly ignore the influence of time-dependent aftershock triggering and secondary earthquake clustering. This is because conventional probability seismic hazard analysis (PSHA) (Cornell, 1968) does not include aftershock hazard and models the seismicity as a Poisson process with a constant rate in space and time based on declustered catalogues. This might be reasonable because PSHA is typically related to long-term seismic risk mitigation purposes (e.g., seismic design code provision and policy-writing for natural hazard insurance/reinsurance). In other words, PSHA does not fulfil the requirement of short-term spatiotemporal seismic hazard and risk assessment. On the other hand, seismic hazard and risk assessment (Deierlein *et al.*, 2003; McGuire, 2004) is valuable to assess the impact of seismicity rates and ground motion intensities in terms of structural responses and possible economic consequences. Once a seismic intensity measure (IM) at a target site is evaluated using ground motion prediction equation (GMPEs), seismic performance of structures can be evaluated with seismic fragility curves. The convolution of

hazard and vulnerability allows computing risk considering all uncertainty from hazard up to risk components. In order to develop a new simulation framework for spatiotemporal hazard and risk assessment, a new seismicity model describing the seismicity rate in space and time and a new fragility model considering the cumulative damage due to aftershocks need to be developed to replace the Poisson process and mainshock fragility curves, respectively.

An example of such spatiotemporal seismicity models is the Epidemic Type Aftershock Sequence (ETAS) model (Ogata, 1998). The ETAS model is a statistical model that describes the seismicity rate in space and time; it combines different empirical scaling laws of productivity, temporal, and spatial distributions of aftershocks including the Gutenberg-Richter law, Omori-Utsu law, and Utsu-Seki law (Gutenberg and Richter, 1944; Utsu *et al.*, 1995; Ogata, 1998). The ETAS parameters are estimated based on observed seismicity data using the maximum likelihood estimation (MLE), which requires a complete and homogeneous observed catalogue. In other words, a robust ETAS parameter estimation (e.g., with limited uncertainties) requires a well-recorded instrumental catalogue as input to calibrate the productivity, temporal and spatial parameters and allows a stable performance of the ETAS simulations. The ETAS model has been extensively studied for the shallow crustal seismicity for earthquake forecasting purposes (Lombardi and Marzocchi, 2010; Werner *et al.*, 2011; Zhuang, 2011; Field *et al.*, 2017a). Iervolino *et al.* (2015) and Field *et al.* (2017b) further implemented the spatiotemporal ETAS model to build operational earthquake loss forecasting for Italy and California, respectively. It is important to point out that applying the standard ETAS model for crustal seismicity to subduction seismicity data can lead to a significant bias of isotropic spatial distribution, i.e. Utsu-Seki law (Seif *et al.*, 2017; Zhang *et al.*, 2018). Considering a typical M9.0 event (e.g., the 2011 Tohoku sequence with a 500 km × 300 km rupture plane), the rupture length can be significantly larger than the rupture width (Thingbaijam *et al.*, 2017). Therefore, the conventional ETAS model is unable to capture observed anisotropy of aftershocks triggered

by M9.0-class events realistically. A modified ETAS model considering the anisotropic spatial distributions of aftershocks is necessary to conduct the spatiotemporal seismic hazard and risk assessment for future M9.0 events in any subduction-zone regions.

In subduction-zone regions like the Mentawai subduction zone and CSZ, there is a critical shortage of earthquake catalogue data to calibrate the ETAS parameters using local earthquake catalogues alone. To forecast aftershock activities for seismic risk management purposes in different tectonic regions, sequence-based temporal productivity of mainshock (e.g., Omori-Utsu law from Utsu and Ogata (1995)) has been investigated globally (Page *et al.*, 2016). This approach would allow conducting hazard assessments for the subduction-zone region without observations by assessing the characteristics of aftershocks globally. A set of 'representative' parameters can be suggested from global earthquake catalogues due to the unavailable observed catalogues. However, two aspects need to be further investigated.

First, the spatial component of aftershock occurrence should be included, because the impact of M9.0 sequences varies not only in time but also in space. Specifically, the triggered crustal seismicity near an urban area would have a significant socioeconomic impact (e.g. fatalities and economic losses). Second, rather than individual megathrust sequences, the entire instrumental earthquake catalogues in the subduction zones should also be included to investigate the characteristics of earthquake clustering across subduction-zone regions. In other words, how the seismicity rate varies in space and time across different subduction zones is important to provide useful suggestions for future M9.0-class sequences in any region by assessing the variability of the ETAS parameters in global subduction zones.

In addition to the seismicity model, the fragility model for the spatiotemporal seismic hazard and risk framework needs to be modified. The conventional fragility curves facilitate seismic risk analysis (McGuire, 2004), enabling the estimation of the probability of exceeding a damage state (DS) of a structure for a mainshock only (Porter, 2015). This is appropriate to

assess the long-term performance of the structure based on PSHA. However, considering that the time to repair structures between the M9.0 mainshock and aftershocks is too short, a fragility model that can estimate the DS of the structure after each subsequent event during a M9.0 earthquake sequence is necessary. Luco *et al.* (2004) proposed a procedure to develop the state-dependent fragility curves. To link the pre-DS to post-DS, a structural model was subjected to scaled mainshock records to attain pre-DSs. Subsequently, mainshock records are repeatedly used as aftershock records and applied to the mainshock-damaged building using incremental dynamic analysis (IDA) (Luco *et al.*, 2004; Jalayer and Ebrahimian, 2017). However, it might be unrealistic to represent the characteristics of real mainshock-aftershock sequences using mainshock records only, because ground motion characteristics of mainshock and aftershock records are different and cannot be matched solely by the peak amplitude of the ground motions (Ruiz-Garcia, 2012). Real sequences of records might be necessary to obtain the structural response after each event and consider damage accumulations during an earthquake sequence. In addition, the computational cost of Luco *et al*'s approach is high (Raghunandan *et al.*, 2015a). A new approach to develop state-dependent fragility curves showing the characteristics of real mainshock-aftershock sequences with a low computational cost is desirable.

The new spatiotemporal seismicity model (ETAS model) and the fragility model (state-dependent-fragility curves) are the key updates of the new seismic hazard and risk framework. **Figure 1-1** presents an illustration of the new framework. In terms of the seismicity and hazard components, the ETAS model can be applied as the seismicity model. The output of the ETAS simulation can be combined with applicable GMPEs for subduction and crustal earthquakes to obtain seismic estimates over a short period. Subsequently, the daily hazard rate at different target sites can be applied to the state-dependent fragility model. This allows conducting a

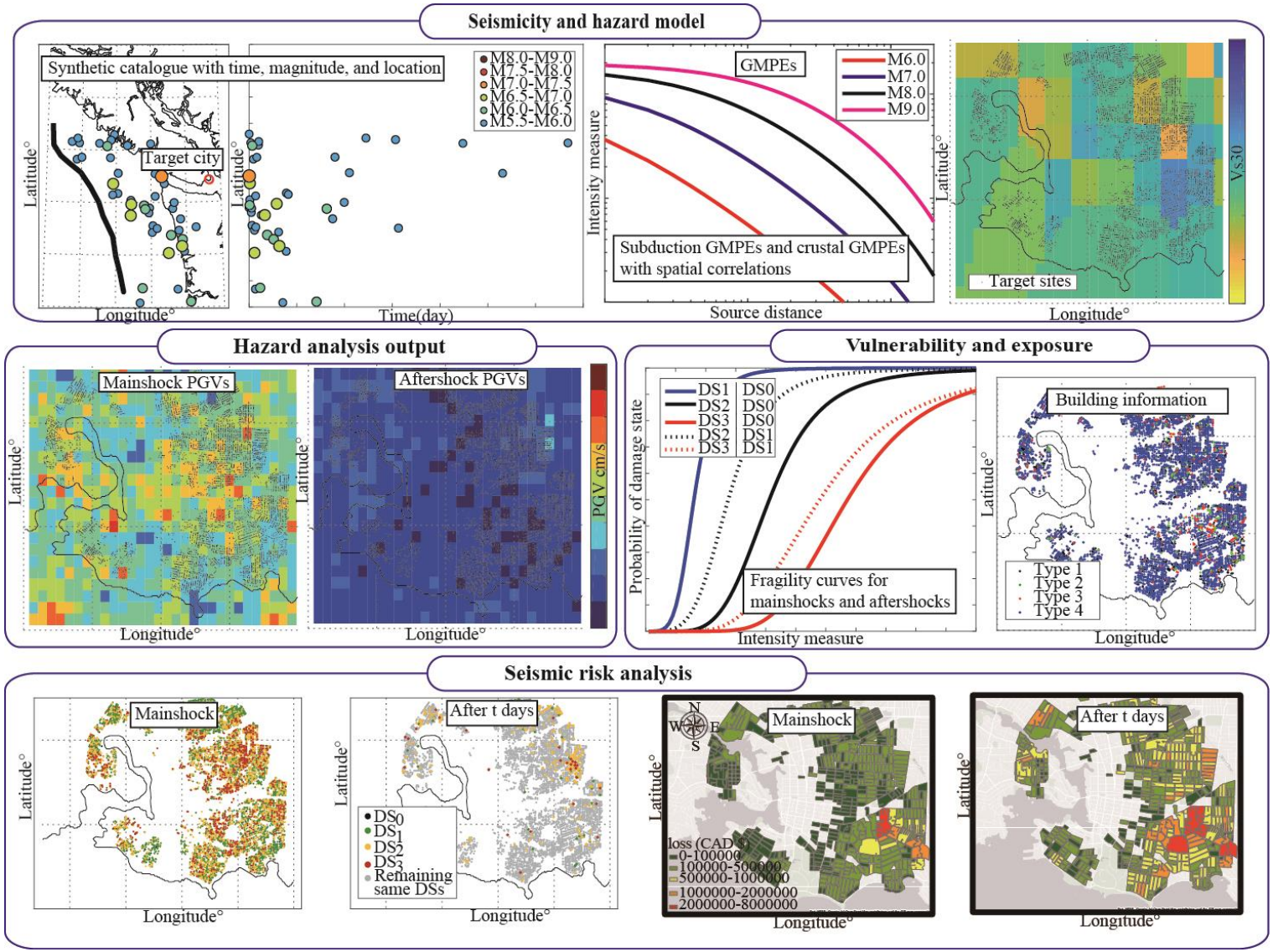

Figure 1-1. Spatiotemporal seismic hazard and risk framework.

regional spatiotemporal seismic hazard and risk assessment of future M9.0 earthquake sequences. The new simulation framework can forecast the time-dependent DS of structures and further estimate the potential loss for any building portfolios that are threatened by future M9.0 megathrust sequences. The output of the simulation framework can quantify the impact of aftershocks triggered by M9.0-class events on seismic risk assessment for a building portfolio and help to make decisions effectively for post-earthquake risk assessment.

1.2 Aims and objectives

This study develops a new simulation framework for spatiotemporal seismic hazard and risk assessment of global M9.0 subduction-zone sequences. The developed spatiotemporal simulation framework is innovative, and its main novelty is attributed to the integration of two compatible elements: namely (1) the ETAS seismicity model with a new spatially anisotropic aftershock kernel for the global M9.0 sequences and calibrated from the global subduction-zone earthquake catalogues, and (2) a new approach to develop the state-dependent fragility model using non-linear dynamic analyses with real mainshock-aftershock records. The new simulation framework can be applied to any subduction-zone subjected to future M9.0 events. The output of the framework can provide aftershock forecasting given the occurrence of a M9.0 event, estimation of the DS of the structure due to the cumulative damage effect of aftershocks, and rapid seismic loss estimation of a building portfolio due to the M9.0 sequence at different time intervals. Most importantly, the rich output from the new risk assessment tool facilitates various decisions related to post-earthquake risk management. The three main objectives of this study are:

- To develop a new simulation framework for conducting a spatiotemporal seismic hazard assessment of global M9.0 megathrust subduction earthquakes triggering both subduction and crustal aftershocks. This is achieved through the validation of the new

simulation framework by conducting a case study of the 2011 Tohoku sequence (**Chapter 2**), assessing the characteristics of global subduction zone regions that experienced M≥7.5 earthquakes, and suggesting global ETAS parameters for future M9.0 sequences (**Chapter 3**).

- To propose a new approach that adopts cloud analysis using real mainshock-aftershock sequences with moderate scaling factors for the development of the state-dependent fragility curves of wood-frame houses for Victoria, British Columbia, Canada (**Chapter 4**).
- To demonstrate how the new simulation framework can be applied to different subduction-zone regions by conducting the spatiotemporal seismic hazard and risk assessment of M9.0 sequences in the City of Victoria, British Columbia, Canada, and integrating the global ETAS simulation framework and the state-dependent fragility curves of wood-frame houses (**Chapter 5**).

1.3 Thesis outline

This thesis includes six chapters. The subsequent five chapters are summarised in the following.

Chapter 2 expands the conventional ETAS simulation with an isotropic spatial distribution to an anisotropic aftershock kernel for M9.0 earthquake sequences. The anisotropic aftershock kernel is constrained by the empirical scaling law of rupture dimensions, and the aftershocks outside the mainshock rupture zone are modelled by a power-law decay. The case study of the 2011 Tohoku sequence is set up to validate the modified ETAS simulation framework. The results show that the simulated seismicity rate and hazard rate from synthetic catalogues agree well with the 2011 Tohoku sequences. Upon the availability of a mainshock source model (e.g., strike and dip angles, and rupture length and widths) immediately after the

mainshock, the new simulation framework can be used for quasi-real-time aftershock hazard and risk assessment.

Chapter 3 investigates whether the ETAS parameters of global subduction-zone regions/sequences with M≥7.5 from 1999 to 2018 are region-dependent, magnitude-dependent, or stable within the subduction-zone setting. The estimated ETAS parameters provide a direct comparison with different mainshocks across different subduction-zone regions in productivity, time and space. The results show that the variability of the ETAS parameters is not significant neither across different subduction-zone regions nor as a function of maximum observed magnitudes. Preferred ETAS parameters are suggested based on the global subduction-zone ETAS parameters. Synthetic catalogues generated with the suggested ETAS parameters agree well with the 2004 M9.1 Aceh-Andaman earthquake, the 2010 M8.8 Maule earthquake, and the 2011 M9.0 Tohoku earthquake sequences.

Chapter 4 proposes a new approach for the development of the state-dependent fragility curves to assess the cumulative damage of wood-frame houses due to aftershocks. Structural responses before and after each event of mainshock-aftershock sequences are used to obtain statistical relationships among an engineering demand parameter prior to the seismic event (pre-EDP), the IM of the seismic event, and the engineering demand parameter after the seismic event (post-EDP). Different EDPs and IMs are also discussed to define the most suitable combination of IM- pre-EDP-post-EDP for the wood-frame houses. The results show that peak ground velocity (PGV), pre-residual inter-story drift ratio (ResISDR), and post-maximum inter-story drift ratio (MaxISDR) are the most preferred IM-pre-EDP-post-EDP combination.

Chapter 5 implements the new simulation framework of the spatiotemporal seismic hazard and risk assessment of M9.0 sequences for Victoria, British Columbia, Canada. CSZ is considered as a case study to show how the new ETAS simulation framework can be used for

the region without direct observations to constrain M9.0 seismicity. By integrating the modified anisotropic aftershock kernel for M9.0 earthquake sequences from **Chapter 2**, the suggested ETAS parameters of global M9.0 megathrust earthquake sequences from **Chapter 3**, and the state-dependent fragility curves of the wood-frame houses from **Chapter 4**, a comprehensive risk assessment tool is developed and applied to the real building dataset in the City of Victoria, British Columbia, Canada. The results of synthetic catalogues, mainshock-aftershock hazard maps, and spatial distribution of DS and loss maps corresponding to 10^{th}, 50^{th}, and 90^{th} percentiles of total losses with different durations (e.g., one week and one month) after mainshocks are provided to show the potential impact of M9.0 sequence scenarios that could occur and cause different seismic losses in Victoria. The potential applications of combining aftershock forecasting with the state-dependent fragility curves are also discussed for short-term post-earthquake risk assessments (e.g., real-time DS forecasting of an individual house).

Chapter 6 summarises the key findings of this study and the future plan in the next stage.

Chapter 2 Spatiotemporal Seismic Hazard and Risk Assessment of Aftershocks of M9.0 Megathrust Earthquakes*

2.1 Introduction

Recent great earthquakes along subduction zones have triggered numerous aftershocks over many years and regions of hundreds of kilometres. Seismicity rates are increased by orders of magnitude not just along the ruptured plate interface, but also at population centres in the overriding continental crust. Despite the obvious seismic hazard and risk to people and infrastructure, current seismic hazard models largely neglect the influence of time-dependent aftershock triggering and secondary earthquake clustering. This influence is important, however, for decision-making in post-earthquake risk management, including humanitarian relief, building tagging, inspection prioritisation, retrofitting, and informing the population of residual risks (e.g., Jordan and Jones, 2010; Jordan *et al.*, 2011).

The 2011 Tohoku earthquake sequence exemplifies this secondary hazard and risk in the onshore crust. The sequence started on March 9, 2011, with the M7.3 foreshock, followed on March 11 by the M9.0 mainshock, which ruptured a 530 km × 200 km fault plane (Yagi and Fukahata, 2011b) between the Pacific and North American Plates in the northeast offshore region of Japan. In total, more than 200 aftershocks with depths less than 100 km and Japan Meteorological Agency (JMA) magnitude M_j greater than 5.5 occurred within 100 days of the

* This chapter is published at Bulletin of the Seismological Society of America:

Zhang, L., M.J. Werner, and K. Goda (2018) Spatiotemporal seismic hazard and risk assessment of aftershocks of M 9 megathrust earthquakes, *Bull. Seismol. Soc. Am.* **108**, 3313–3335.

mainshock. Amongst the five $M_j \geq 7$ aftershocks, three occurred along the plate interface, one in the subducting slab, and one in the shallow continental crust on April 11. The latter ruptured the Yunodake and Itozawa faults in Fukushima Prefecture at a distance of 300 km from the epicentre of the mainshock (Fukushima *et al.*, 2013; Toda and Tsutsumi, 2013), and the aftershock triggered its own cascade of secondary aftershocks.

While stochastic models of seismicity cascades certainly exist, their current formulations are not well suited to accurately assess the seismic hazard and risk of quakes triggered by a great megathrust earthquake in a subduction zone setting. First, most models of clustered seismicity are two-dimensional, which is problematic for accurate hazard calculations for subduction zones having complex 3D geometry. Second, many models employ spatial distributions of aftershocks that are isotropic around the mainshock epicentre, constituting a poor representation of the aftershock zones of great subduction earthquakes. Third, models typically neglect available scaling laws of the rupture areas of great earthquakes, even though they constrain the aftershock zone strongly. For instance, the Epidemic Type Aftershock Sequences (ETAS) model is widely used to forecast the spatiotemporal seismicity rate for crustal seismicity (Kagan and Knopoff, 1987; Ogata, 1988, 1998; Lombardi and Marzocchi, 2010; Werner *et al.*, 2011; Zhuang, 2011; Gerstenberger *et al.*, 2014; Marzocchi *et al.*, 2014; Field *et al.*, 2017a). Conventionally, an isotropic power law is used in the ETAS model. Ogata (1998) and Zhuang *et al.* (2004) used a 2D Gaussian distribution to model the anisotropy of the aftershocks. However, the spatial distribution of aftershocks may be better represented by a power law, which decays more gradually than the Gaussian distribution in the far field (Felzer and Brodsky, 2006). This is related to the agreement of the static stress triggering and aftershock spatial distribution with power-law decay (Toda *et al.*, 2011; Hainzl *et al.*, 2014). In this study, we develop a new spatially anisotropic aftershock kernel that combines a simulated 2D mainshock rupture area (from scaling laws) with a power-law beyond the rupture.

This new formulation is important because seismic hazard and risk due to triggered crustal events are sensitive to the spatial distribution of aftershocks near the rupture boundary in the continental crust, where buildings and other infrastructure are nearby.

The importance of aftershocks in seismic hazard has been highlighted previously. For instance, Marzocchi and Taroni (2014) concluded that aftershocks should be included in probabilistic seismic hazard analysis (PSHA) because only using the PSHA result from the declustered catalogue underestimates hazard rates. Approaches for including aftershocks can be distinguished by the time period of interest (exposure time): (1) long-term (years to centuries), time-independent approaches that integrate aftershock hazard on unconditional mainshock occurrences; and (2) short-term (days to years) approaches that estimate aftershock hazard conditional on specified mainshock sources.

Several studies have implemented the former approach. For example, Toro and Silva (2001) first incorporated earthquake clustering into PSHA. They assumed an earthquake sequence could be modelled by the probabilities of unions of events exceeding a specific ground motion level and each event was assumed to be independent in time for the New Madrid Seismic Zone (NMSZ) in the U.S. This approach was further applied by Boyd (2012) to gridded hazard curves in San Jose, California. Boyd (2012) showed that the hazard curves (peak ground acceleration and spectral acceleration (T=1s)) from the U.S. 2008 national seismic hazard maps were increased by 10%-20% when aftershocks were included.

The second approach requires detailed mainshock source models but is more effective for short-term decision-making. This approach has been applied globally for crustal seismicity. For example, Yeo and Cornell (2009) developed a time-dependent aftershock probabilistic seismic hazard analysis using the modified Omori law combined with an empirical scaling relation for rupture area (e.g., Wells and Coppersmith, 1994). Yaghmaei-Sabegh *et al.* (2017) conducted PSHA using a temporal ETAS model. The uniform aftershock spatial distribution

was considered given linear faults of M7-level earthquakes for the NMSZ. The temporal ETAS model from Yaghmaei-Sabegh *et al.* (2017) considered multiple generations of aftershocks. Iervolino *et al.* (2015) and Field *et al.* (2017b) developed operational earthquake loss forecasting in Italy and California, respectively, based on spatiotemporal ETAS earthquake clustering models of (shallow) clustered seismicity (Marzocchi *et al.*, 2014; Field *et al.*, 2017a). None of these studies, however, assessed the seismic effects of great megathrust earthquakes. It should be noted that the second approach is also useful for aftershock scenarios of megathrust events for different subduction regions (e.g., Chile, Indonesia, and Japan). The source modelling is general because it is only constrained by empirical scaling laws and subduction-zone geometrical constraints.

This chapter develops a new framework to conduct spatiotemporal seismic hazard and risk assessments focusing on a M9.0 megathrust event triggering moderate-to-large aftershocks ($M \geq 5.5$) along the plate interface and in the continental crust. We investigate the importance of the aftershock sequence in terms of ground motion intensity and seismic fragility. Our target region is northeast Japan to demonstrate how the new framework can be applied in a subduction zone. The novelties of this study are twofold. First, we employ the ETAS model (Ogata and Zhuang, 2006; Zhuang, 2011; Seif *et al.*, 2017) to model aftershock cascades of a M9.0 megathrust earthquake. Second, we model the spatial distribution of major aftershocks with an appropriate anisotropic power-law kernel, a mainshock rupture zone constrained by empirical length-width scaling laws, and the empirical depth profile. The three objectives of this chapter are: 1) to develop a tool by convolving an ETAS model, ground motion prediction equations (GMPE), and a seismic fragility model to enable more risk-informed decision-making in post-earthquake situations of megathrust events, 2) to show that the new framework can capture the observed M9.0 Tohoku megathrust earthquake sequence, and 3) to conduct seismic hazard and risk analyses at different onshore sites for Japan using the new simulation framework. The

limitation of the new simulation framework is that to reduce the uncertainty of the synthetic aftershock catalogue, well-constrained estimates of the mainshock source parameters are necessary. Therefore, the new simulation framework is applicable for quasi-real time hazard assessment immediately after the mainshock source model is available. Otherwise, different mainshock rupture scenarios should be considered for a region without such data.

2.2 Data

Since northeast Japan is the target region, specific catalogues are selected for different purposes. (1) To estimate the parameters of the ETAS model, we use the JMA catalogue. (2) To consider the uncertainty of the source parameters of the 2011 Tohoku mainshock, we use the locations from the ANSS (Advanced National Seismic System), global Centroid Moment Tensor (gCMT), International Seismological Centre (ISC), and JMA catalogues. (3) To model the 3D rupture areas of the large aftershocks, we use depths of past events from the JMA catalogue, the slab model of the Japan Trench from Hayes *et al.* (2012), and focal mechanisms from the gCMT catalogue. (4) To show the comparison between simulated peak ground velocity (PGV) and observed PGV, the ground motion data are taken from Goda *et al.* (2015). The selected strong-motion stations with near-surface ground information, the distances to the target sites, and the available number of records are summarised in **Table 2-1**.

Table 2-1. Selected record stations for PGV comparisons.

Location	Record station name	Number of records	Distance to the target site (km)	V_{s30} (m/s)
Sendai	MYG012	305	1.4	436
Fukushima II NPP	FKS010	555	10.0	430
Tokyo	EKO.ERI	85	0.9	266

2.3 Overview of framework

The framework for spatiotemporal seismic hazard and risk assessment due to a megathrust subduction earthquake sequence consists of a seismicity model, seismic hazard analysis, and seismic risk analysis, and is illustrated in **Figure 2-1**. Although the target region is northeast Japan in this study, the framework is applicable to other subduction zones (e.g., Indonesia and Chile). We adopt the spatiotemporal ETAS model as the seismicity source model; this constitutes the key technical element in the framework. The parameters of the ETAS model are estimated from earthquake catalogues. The calibrated ETAS model generates realistic synthetic mainshock-aftershock sequences that capture observed aftershock rates in space and time. Additional features including rupture dimensions, depths, earthquake types, and focal mechanisms are assigned in the synthetic catalogues.

In addition, earthquakes with the same magnitude can have different ground motion characteristics in terms of duration and frequency content. Building damage assessments are sensitive to these characteristics. For this reason, we use the GMPEs developed for subduction earthquakes and crustal earthquakes to calculate their specific ranges of seismic intensities. In our study, ‘crustal earthquakes’ refer to the onshore-crustal events with depths less than 30 km in the continental crust, and ‘subduction earthquakes’ refer to the subduction-zone events that take place on (near) the subduction plate interface. Next, we integrate the space-time aftershock rate of the ETAS model with the GMPE to assess the time-dependent seismic hazard at multiple sites in terms of daily rates of seismic intensity exceeding a certain threshold.

Different comparisons of the observed and synthetic catalogues can be carried out. For example, we compare the daily exceedance rates of observed and simulated ground motions, and we assess the relative importance of crustal and subduction earthquakes in terms of ground motions. In addition, we compare the time-dependent hazard rates with the long-term hazard rates in the target region to assess the importance of the triggered aftershocks.

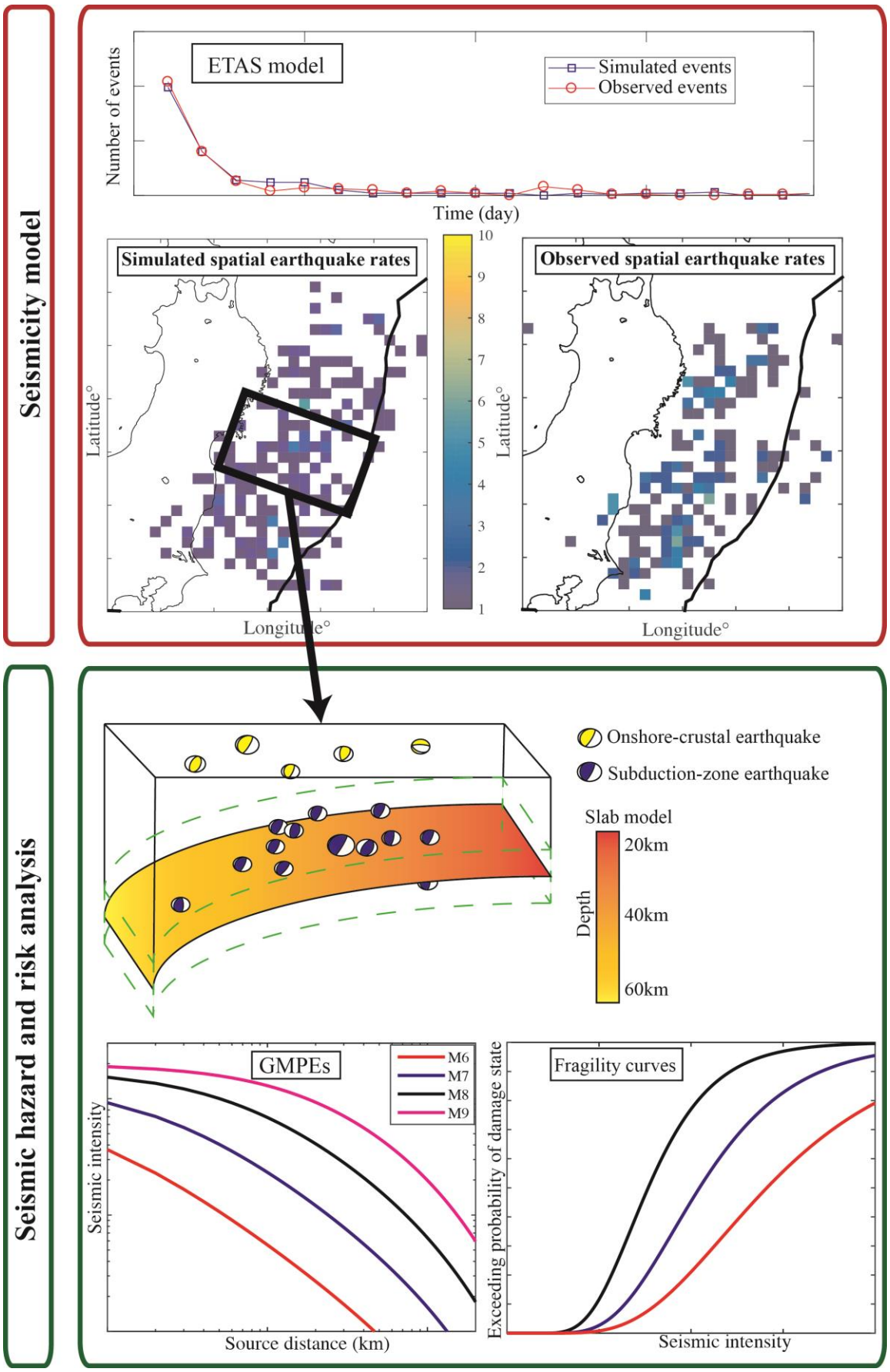

Figure 2-1. Framework for spatiotemporal seismic hazard and risk assessment.

Seismic risk analysis evaluates the probabilities of occurrence of consequences in building damage and loss given a major event or sequence (McGuire, 2004). Seismic risk analysis is useful for decision-making in the short- and long-term periods. A viable approach to assessing seismic risk from seismic hazard is using fragility curves, which we employ here to show how the spatiotemporal hazard can be accommodated in the seismic risk analysis.

In the following, we first describe the new generic framework including parameter estimation and catalogue simulations of the ETAS model in **Section 2.4**. Then we consider northeast Japan as the target region and present the procedures and results of the seismicity model, hazard analysis, and risk analysis for M9.0 earthquake sequences offshore Japan.

2.4 Spatiotemporal ETAS model

2.4.1 ETAS model

The total seismic rate $\lambda(t,x,y|H_t)$ of the spatiotemporal ETAS model consists of a background rate $\mu(x,y)$ and a triggering rate $g(t-t_j, x-x_j, y-y_j; M_j)$ at time t and location (x,y) (Zhuang, 2011; Seif *et al*., 2017), and can be expressed as follows:

$$\lambda(t,x,y|H_t) = \mu(x,y) + \sum_{j:t_j<t} g(t-t_j, x-x_j, y-y_j; M_j) \quad (2\text{-}1)$$

where H_t represents the historical seismicity up to time t ($H_t = \{x_j, y_j, t_j, M_j\}; t_j<t$). The triggering function $g(t,x,y;M)$ includes the productivity ($K_0\, e^{\alpha(M-M_{cut})}$), the normalized modified Omori law $v(t)$, and an isotropic spatial distribution $f(x,y|M)$ of seismic events:

$$g(t,x,y;M) = K_0\, e^{\alpha(M-M_{cut})} \cdot v(t) \cdot f(x,y|M) \quad (2\text{-}2)$$

where M_{cut} is the cut-off magnitude to select earthquakes larger than M_{cut}. K_0 (events/day) and α (magnitude^{-1}) are the productivity parameters. α determines how the triggering productivity of an earthquake increases with magnitude, whereas K_0 measures the intensity of aftershock generation, defining the number of triggered events above M_{cut}.

The temporal distribution is the normalised modified Omori law:

$$v(t) = c^{p-1}(t + c)^{-p}(p - 1) \quad (2\text{-}3)$$

where c (days) and p are parameters. c is applied to eliminate a singularity at $t = 0$ and affected by the number of events in the catalogue during the early phase of the aftershock process (Seif *et al.*, 2017). The p-value is associated with the decay rate of aftershocks in time; the decay rate increases with the p-value.

The isotropic spatial distribution of triggered events is defined by:

$$f(x, y|M) = \frac{(q-1)}{\pi\left(x^2+y^2+d\ e^{\gamma(M-M_{cut})}\right)}\left(1 + \frac{x^2+y^2}{d\ e^{\gamma(M-M_{cut})}}\right)^{-q} \quad (2\text{-}4)$$

where d (km^2), q, and γ (magnitude^{-1}) are parameters. $d\ e^{\gamma(M-M_{cut})}$ is a measure of the source dimension and scales the spatial aftershock footprint, whereas q describes the spatial decay of aftershocks.

2.4.1.1 *ETAS parameter estimation and stochastic declustering*

We use the ETAS model with the isotropic spatial distribution for the ETAS parameter estimation and in Section 2.4.1.2 we develop a new ETAS simulation framework with an anisotropic distribution. The ETAS parameters are estimated by using the maximum likelihood estimation (MLE) method (Zhuang, 2011; Seif *et al.*, 2017). To estimate the parameters of the ETAS model reliably, the input earthquake catalogue needs to be complete and homogeneous over an appropriate target window. The target window is a specific range of space, time, and magnitude to filter seismic events. However, some events outside the target window may trigger seismic events in the target window. Therefore, an auxiliary window is often introduced to reduce the bias, which is larger than the target window, and the combination of the auxiliary and target windows is referred to as data window (Wang *et al.*, 2010).

The log-likelihood function can be expressed as:

$$logL = \sum_{i:t_i \in [0,T],(x_i,y_i)\in S)} \log(\lambda\,(t_i, x_i, y_i)) - \int_0^T \int\int_S \lambda(t,x,y)dx\,dy\,dt \quad (2\text{-}5)$$

where *n* is the number of events in the target window, λ is the total seismic rate from **Equation (2-1)**, and *S* and *T* are the spatial and temporal ranges of the target window. Since the ETAS model (**Equation (2-1)**) divides the input seismicity into background and triggered events, we used the same algorithm as Zhuang *et al.* (2002), who developed stochastic declustering for the ETAS parameter estimation. Therefore, rather than declustering the catalogue before the parameter estimation, the spatial background rate is estimated jointly, and the probability of background event (φ_i) is calculated by:

$$\varphi_i = \frac{\mu(x_i,y_i)}{\lambda(x_i y_i t_i)} \quad (2\text{-}6)$$

where φ_i is the probability that the event$_i$ is a background event. $\mu(x_i, y_i)$ and $\lambda(x_i y_i t_i | H_{t_i})$ are the background rate and the total seismicity rate, respectively, in **Equation (2-1)**. The background rate is estimated with adaptive Gaussian kernels (Zhuang *et al.*, 2002).

2.4.1.2 *ETAS simulation*

The conventional ETAS model distributes aftershocks isotropically around a mainshock epicentre, which is more applicable to M7.0-class earthquake sequences and less to M8.0-9.0 megathrust subduction events. For example, according to Ogata and Zhuang (2006), the performances of the isotropic and anisotropic spatial distributions are similar for the offshore Tohoku region from 1926 to 1995 with a maximum M_j = 7.9 in the historical catalogue. In addition, recent empirical scaling laws by Thingbaijam *et al.* (2017) indicate that differences between fault width and fault length of subduction-interface events are indistinguishable when M < 7.5. When the magnitude exceeds M8.0, however, the fault length is generally greater than the fault width.

We modify the ETAS simulation approach of Seif *et al.* (2017) to capture the spatial distribution of aftershocks of a M9.0 Tohoku-like subduction earthquake. We divide the first generation of aftershocks into two groups: the first group occurs in the mainshock rupture area, while the second group obeys a power-law decay with distance beyond the rupture area. Subsequent generations of triggered events follow the isotropic power law in **Equation (2-4)** to mimic isotropic secondary clustering. The proportions of the aftershocks inside and outside of the rupture area are determined based on the observed spatial distribution of aftershocks (e.g., the 2010 Maule earthquake sequence and the 2011 Tohoku earthquake sequence). We simulate variations in the mainshock rupture area and geometry to account for their uncertainty in future megathrust earthquakes. The 2D mainshock rupture area is obtained from sampled rupture lengths and widths constrained by empirical relationships. Strike and dip angles are based on different focal mechanism solutions (e.g., from gCMT and the U.S Geological Survey) of the same historical M9.0 event in the target region.

The first-generation aftershocks inside and outside the rupture area are distributed using a 2D uniform distribution and power law kernels (Vere-Jones, 1992; Woo, 1996), respectively. The 2D uniform distribution implies that any location inside the rupture area is equally ready for an aftershock. After several attempts of approximating Tohoku's anisotropic spatial distribution with a single kernel (e.g. anisotropic Gaussians with various variance scaling functions), we found that this combination can capture the observed characteristics much better. Other attempts, i.e. 2D Gaussian and anisotropic kernel distributions, are described in **Appendix A**. Several authors (Das and Henry, 2003; Asano *et al.*, 2011; Rietbrock *et al.*, 2012) inferred relations between slip and aftershocks, but they are not yet ready for implementation because (i) a slip model forecast is required, (ii) the relations are currently qualitative and occasionally debatable, and (iii) the relations do not usually apply to off-fault aftershocks. Although aftershocks within the rupture area of megathrust earthquakes are not usually

distributed uniformly, the observed clustering appears well approximated by secondary aftershocks that cluster around the first generation of uniformly distributed aftershocks.

To be consistent with the empirically-supported power-law decay in the far field (Felzer and Brodsky, 2006; Toda *et al.*, 2011; Hainzl *et al.*, 2014), we developed a power-law component with distance from the rupture area. To this end, we modelled seismicity decay perpendicularly to the four edges of the rectangle using the 1D power law, and seismicity decay in the four corners of the rectangle as quarter circles of a 2D power law (**Figure 2-2**).

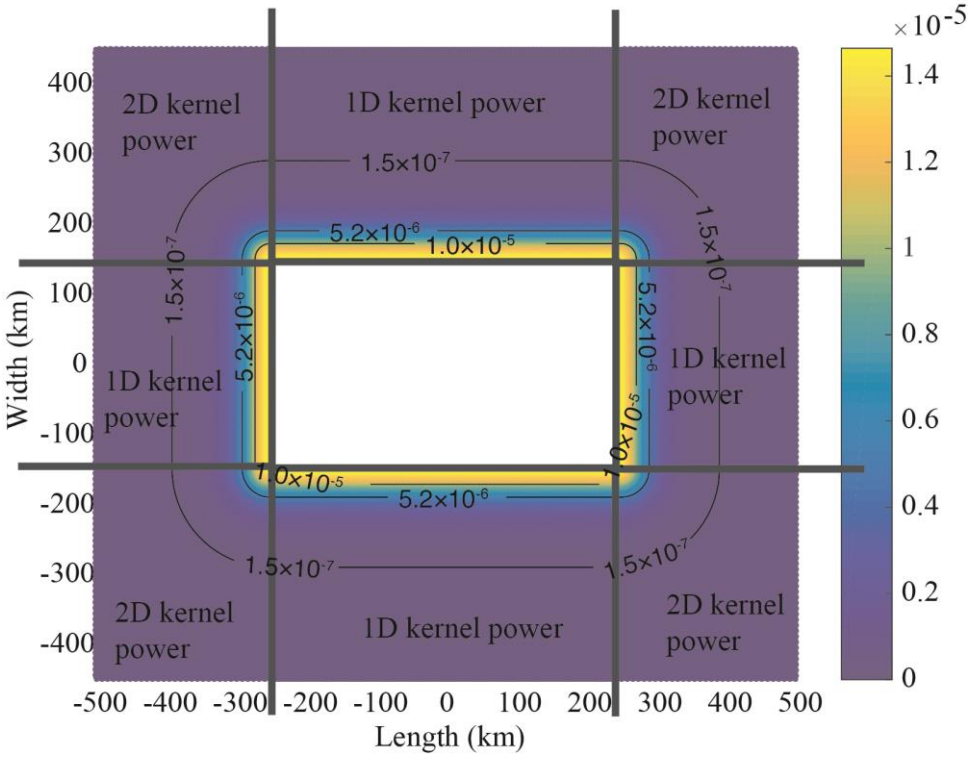

Figure 2-2. An example of the spatial probability density function of the first generation of aftershocks outside a simulated rupture area (500 km×300 km). We employ 1D and 2D kernel power-laws for aftershocks outside the rupture area, respectively.

The 1D power law is given by:

$$k_{1d}(x_{1d}, y_{1d}) = Beta(q - 0.5, 0.5)^{-1} h^{-1} (1 + \frac{x_{1d}^2 + y_{1d}^2}{h^2})^{-q} \quad (2\text{-}7)$$

while the 2D power law is described by:

$$k_{2d}(x_{2d}, y_{2d}) = \frac{q-1}{\pi h^{-2}}\left(1 + \frac{x_{2d}^2+y_{2d}^2}{h^2}\right)^{-q} \quad (2\text{-}8)$$

where q is the power-law exponent, h (km) is the kernel bandwidth, and *Beta*(•) is the beta function. An example of the resulting spatial probability density function (PDF) of (first-generation) aftershocks of a mainshock rupture with 500 km length and 300 km width is displayed in **Figure 2-2**. x_{1d}, y_{1d}, x_{2d}, and y_{2d} are the spatial coordinates of aftershocks outside the rupture area with $\pm\frac{500km}{2}$ in x (rupture length) and $\pm\frac{300km}{2}$ in y (rupture width). We assign the exponent q of the power laws the same value as the exponent of the isotropic decay in **Equation (2-4)**. Therefore, the decay rates of the anisotropic and isotropic spatial aftershock distributions are identical in the far field.

2.4.1.3 *Earthquake rupture model*

The outputs of the ETAS simulations are the synthetic catalogues including occurred times, locations of epicentres, and magnitudes of the events. As indicated in **Section 2.3**, we assign additional features including the depth, earthquake type, and focal mechanism to each simulated earthquake. This is described in detail next.

Depths for earthquakes with M<8.0 are sampled from empirical cumulative distribution functions (ECDFs) of depth that are obtained based on an instrumental catalogue. We divide the target window into sub-regions with 10 km width from the trench line to the continental crust to estimate the ECDFs of depth in each sub-region. Past earthquakes M≥5.0 are used. The events with depths less than 5 km are eliminated because the majority of these events are remote events and their depths are poorly estimated with depths of 0 km (Power *et al.*, 1994). The zero-depth estimate indicates that the depth is poorly constrained, so including zero-depth locations would likely overestimate the hazard estimate. Bins with a small number of events (< 20) are combined with the closest bin to avoid insufficient events for defining the ECDFs

of depth. In addition, all simulated earthquakes with M≥8.0 are treated as subduction-interface earthquakes and the depths are assigned directly from a slab model. This is because the largest historical crustal earthquake in different regions is less than M8.0. For example, Kanaori *et al.* (1991) listed destructive earthquakes from 715 to 1984 with M≥6.4 for Japan. The largest magnitude for inland Japan is the M8.0 Nobi earthquake. In addition, historical large crustal earthquakes in Mexico are in the range of 7.5≤M≤7.8 (Suárez *et al.*, 1994). For crustal seismicity in California, Field *et al.* (2017a) also consider a maximum magnitude of 8.0.

Earthquake types (continental-crust, subduction plate-boundary, or subduction intra-plate) are defined by the sampled depths and the slab model: earthquakes more than 20 km above the plate interface are defined as crustal earthquakes, the layer within ±20km of the plate interface is assumed to contain subduction-interface earthquakes (allowing for depth uncertainty), and remaining earthquakes are treated as intra-slab earthquakes.

To obtain the range of strike and dip angles for crustal and subduction earthquakes, we use M5.5+ earthquakes in the gCMT catalogue in the target window. Due to the plate motion of the subduction zone, the crustal and subduction earthquakes have similar strike directions as the subduction plane. Following that, we assume the strike and dip angles of the subduction aftershock are similar to the strike and dip angles of the subduction plane. The strike and dip angles of nodal planes 1 and 2 that are closer to the strike and dip angles of the subduction plane are selected. For crustal aftershocks, in the target region of northeast Japan, the strike angle of historical shallow crustal earthquakes and active faults with depths less than 15 km is in good agreement with the strike angle of the subduction plane, for example, the 1998 M6.3 Iwate earthquake (strike angle=216º), the 2003 M6.1 northern Miyagi earthquake (strike angle=203º), and the 2008 M6.9 Iwate-Miyagi Nairiku earthquake (strike angle=209º) (Nakahara *et al.*, 2002; Miura *et al.*, 2004; Asano and Iwata, 2011). In addition, according to the Japan Seismic Hazard Information Station (JSHIS), the strike angles of the Nagamachi-

Rifu-sen fault, the Fukushima-bonchi-seien fault, and the Nagai-bonchi-seien fault are 231.9º, 212.6º, and 186.7º, respectively. Therefore, we select the strike angle which is closer to the strike angle of the subduction plane from the two nodal planes of the crustal event. The ECDFs of strike and dip angles for crustal and subduction earthquakes are evaluated, and the simulated angles are assigned to the large aftershocks with M≥6.5.

To simulate ground motions, we require the shortest distance between a source and a site. The source models depend on magnitude and location. We do not simulate the finite rupture planes of M<6.5 earthquakes, and so calculate the distance to the hypocentre. Simulated M≥8 earthquakes are constrained to the plate interface, and we calculate distances to the nearest point on the simulated (finite) rupture plane. Source models for M≥6.5 crustal and subduction-interface aftershocks are generated from empirical scaling laws and the empirical distributions of strike and dip angles. The slab model provides the boundary of the projected 2D rupture area of interface earthquakes, while the finite rupture planes of crustal aftershocks are simulated based on the source model.

In the following, we show the specific results associated with the target region of Tohoku, Japan from seismicity analysis to hazard and risk analysis.

2.5 Seismicity analysis of M9-triggered aftershock sequences in Tohoku

2.5.1 ETAS parameter estimation in Tohoku

The ETAS parameter estimation requires a homogeneous catalogue, therefore the JMA catalogue is used as it has a unified magnitude scale M_j and a low magnitude of completeness in Japan. The spatial target and data windows of the ETAS parameter estimation are shown in **Figure 2-3**(a). The target window encompasses the rupture area of the 2011 Tohoku mainshock, its aftershock field, and onshore regions to include events in the continental crust. The data window is larger than the target window by a 2º extension along all sides of the target

window. Because we focus on future megathrust subduction events triggering subduction aftershocks and crustal aftershocks in the subducting plate and overriding crust, respectively, the selected events in the target window include not only the 2011 Tohoku sequences but also other large subduction and crustal earthquakes before 2011. More specifically, we select events between January 1, 1970, and December 31, 2015 and with depths less than 100 km without setting a magnitude threshold. This leads to over 83,000 events in total.

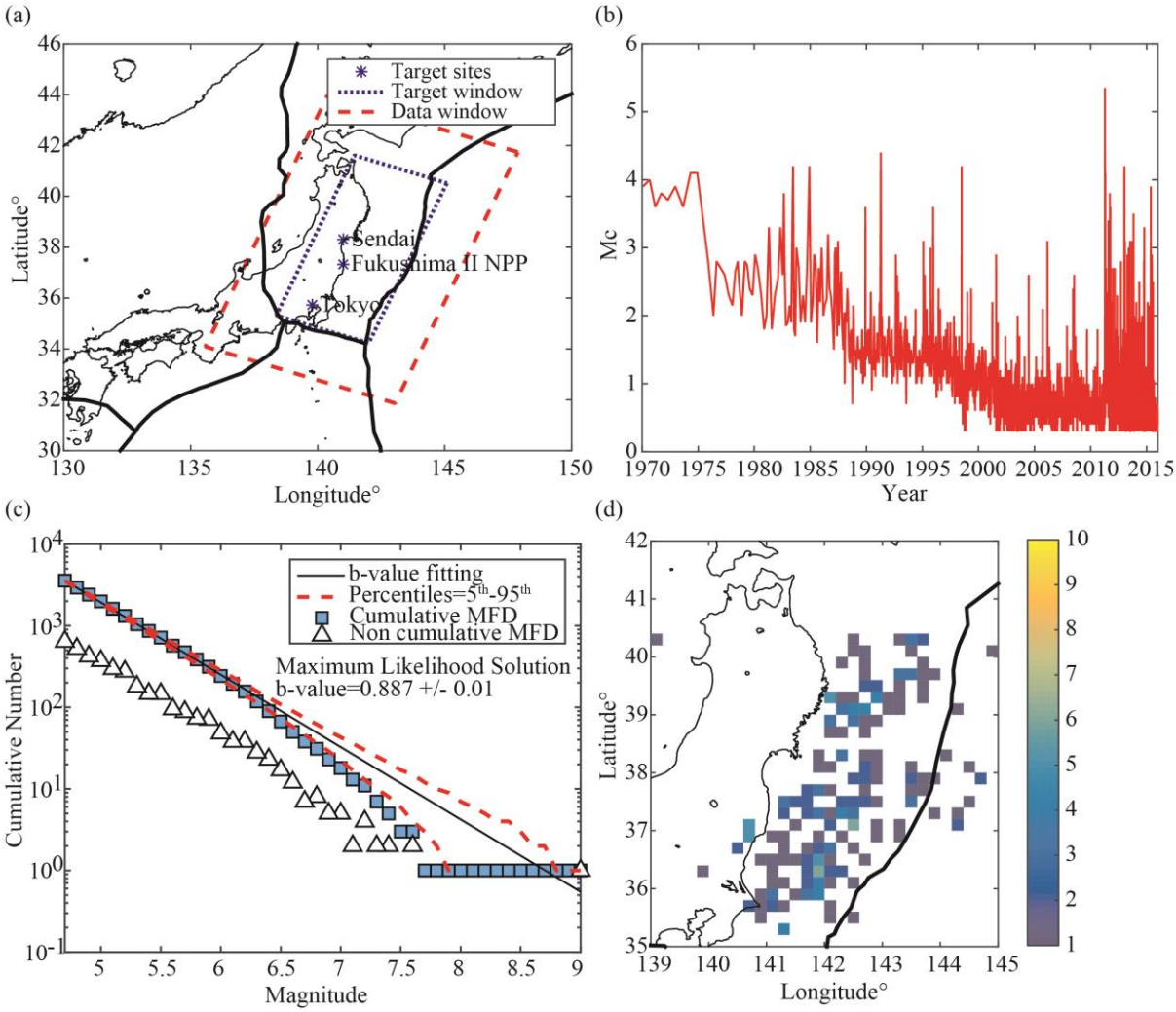

Figure 2-3. (a) Target (dotted line) and data (dashed line) windows for ETAS parameter estimation. Stars denote the three locations chosen to illustrate the hazard and risk calculations: Sendai (141.03ºE, 38.31ºN), Fukushima II NPP (141.01ºE, 37.32ºN), and Tokyo (139.77ºE, 35.72ºN). (b) Magnitude of completeness (M_c) of the JMA catalogue from 1970 to 2015 using

a sliding time window of 200 events in the target window. (c) Observed magnitude-frequency distributions and fitted Gutenberg-Richter laws with maximum likelihood estimates of the *b*-values and 5^{th}-95^{th} percentiles. (d) Observed 2D aftershock histogram with M≥5.5 during the 100 days after the 2011 Tohoku mainshock.

The temporal completeness M_c is estimated in a sliding time window of 200 events using the method suggested by Amorèse (2007) and Seif *et al.* (2017) from 1970 to 2015 (**Figure 2-3**b). Due to missing aftershocks immediately after the Tohoku mainshock, M_c briefly increases to M_j 5.3. In this study, M_{cut} is set to 4.7 for seismic hazard analysis, because a large offshore region is selected in the target and data windows which leads to a high magnitude of completeness during the 2011 Tohoku sequence. In addition, M_{cut} is kept constant to reduce the bias in the ETAS simulation (Harte, 2015). This also allows the direct application of the GMPE by Morikawa and Fujiwara (2013) in subsequent seismic hazard analyses, which is applicable to events with M≥5.5 in Japan. Selecting a lower magnitude cut-off with 4.7 rather than the GMPE threshold of 5.5 in the ETAS simulation is beneficial to assess the potential of M4.7 earthquakes for triggering M≥5.5 aftershocks. The *b*-value estimation with 5^{th}-95^{th} percentiles (Aki, 1965; Shi and Bolt, 1982) of the selected events from 1970 to 2015 with M_{cut}=4.7 is displayed in **Figure 2-3**(c). The 2D histogram of observed events in the 100 days after the 2011 Tohoku mainshock with M≥5.5 is shown in **Figure 2-3**(d).

Because the empirical laws of triggered seismicity are thought to be reliable (e.g., the Gutenberg-Richter law and the modified Omori law), ETAS parameters are expected to be robust given a complete and sufficiently large catalogue. We investigate the sensitivity of the ETAS parameters by considering two time periods: Case 1 covers 1970-2015 (3568 events), while Case 2 (1725 events) comprises the 2011 Tohoku sequence only (see **Table 2-2**).

Table 2-2. Temporal windows and M_{cut} for ETAS parameter estimation.

Cases	Auxiliary window	Target window	M_{cut}	Fixed parameters
1	1970.01.01-1980.01.01	1980.01.01-2015.12.31	4.7	NA
2	2008.03.11-2011.03.10	2011.03.11-2015.03.11	4.7	NA
3	1970.01.01-1980.01.01	1980.01.01-2015.12.31	4.7	α

The mean estimates of the parameters together with their standard errors for Cases 1 and 2 are shown in **Table 2-3**. The productivity parameters α and K_0 change slightly between Cases 1 and 2. When data that exhibit an anisotropic aftershock distribution after a large mainshock are fitted with the isotropic distribution of the ETAS model, K_0 and α tend to be overestimated and underestimated, respectively, as in Cases 1 and 2 (Hainzl *et al.*, 2013).

Table 2-3. ETAS parameter estimation results (standard errors are shown in parentheses).

Cases	K_0 (event/day)	α (magnitude^{-1})	c (day)	p	d (km^2)	γ (magnitude^{-1})	q
1	0.18 (0.01)	1.78 (0.03)	0.02 (0.003)	1.16 (0.01)	13.37 (2.26)	1.69 (0.04)	2.12 (0.13)
2	0.18 (0.02)	1.72 (0.05)	0.05 (0.010)	1.28 (0.03)	13.32 (3.83)	1.68 (0.06)	1.96 (0.21)
3	0.06 (0.0021)	2.30 (fixed) (0)	0.03 (0.004)	1.18 (0.01)	6.89 (1.40)	2.04 (0.04)	2.13 (0.14)
4	0.06 (0.0021)	2.30 (fixed) (0)	0.0215 (0.0030)	1.16 (0.01)	13.37 (2.26)	1.69 (0.04)	2.12 (0.13)

Due to the bias of the productivity parameters, we conduct a third parameter estimation (Case 3). The same earthquake catalogue as in Case 1 is used, and the temporal and auxiliary windows of Case 3 are summarised in **Table 2-2**. As suggested by Helmstetter *et al.* (2005), Hainzl *et al.* (2013), and Seif *et al.* (2017), K_0 is estimated with fixed α = 2.3 to ensure the productivity of the simulated catalogues is similar to that of the catalogue.

The temporal parameters c and p differ significantly between Cases 1 and 2. It seems likely that the short window of Case 2 and missing early aftershocks lead to biased c and p-values. We also compare the values with those estimated by Ogata and Zhuang (2006). Ogata and Zhuang (2006) obtained c and p-values of 0.0243 and 1.050, respectively, with M_c = 4.5 for the offshore Tohoku region (see Table 2 in Ogata and Zhuang (2006)). Their c value is

essentially identical to ours, but their *p*-value is much smaller. We presume that their temporal window extends too far back to be complete offshore (Nanjo *et al.*, 2010), and thus the aftershock decay may be less well captured.

The final parameter set that is used to simulate catalogues is summarised as Case 4 in **Table 2-3**. The ETAS parameters in Case 4 are chosen from Cases 1 and 3. The parameters that are relatively independent of magnitude in space and time (i.e. *c*, *p*, *d*, and *q*) are taken from Case 1. The spatial parameter γ is also from Case 1, as the spatial distribution of aftershocks triggered by the mainshock is used to simulate the subsequent generation of aftershocks. The value of K_0 is selected from Case 3 estimated with a fixed $\alpha = 2.3$ since α is underestimated in the parameter estimation of Cases 1 and 2.

2.5.2 ETAS simulation in the Tohoku region

We generate synthetic catalogues as described in **Section 2.4** and validate the simulations by comparing daily average numbers of simulated events with the actual 2011 Tohoku sequence. We constrain the simulations to mimic the Tohoku sequence as follows. First, a M9.0 earthquake initiates the aftershock sequences. We account for the uncertainty of the mainshock source in terms of magnitude, epicentre, strike, and dip. (1) The magnitude of the mainshock is sampled from a uniform distribution between M8.95 and M9.05. (2) The epicentre is simulated randomly from a 2D Gaussian distribution that is fit to the four location estimates of the 2011 Tohoku mainshock by the ANSS (142.37°E,38.30°N), gCMT (142.37°E, 38.32°N), ISC (142.50°E, 38.30°N), and JMA (142.86°E, 38.10°N) catalogues. To ensure that the rupture area of the mainshock is on the subduction interface and does not extend beyond the trench, the simulated epicentre of the mainshock is constrained to lie farther than 150 km from the trench. The threshold distance of 150 km corresponds to a half of the maximum rupture width of 300 km of a bilateral rupture. (3) The dip and strike angles are sampled from uniform

distributions between 10º-13º and 195º-203º, respectively, selected from available rupture models of the Tohoku earthquake (Koketsu *et al.*, 2011; Shao *et al.*, 2011; Suzuki *et al.*, 2011; Yagi and Fukahata, 2011b). (4) The rupture lengths and widths are sampled from the empirical scaling laws of Thingbaijam *et al.* (2017) with a covariance between rupture length and width from Goda *et al.* (2016). From the sampled epicentre, and strike and slip angles, the location and orientation of the rupture area are calculated by assuming a bilateral rupture. We divide the first-generation aftershocks into those triggered within the (2D) rupture plane and those triggered outside the rupture plane according to the observed partitioning during the Tohoku sequence: about 90% of aftershocks are projected onto the rupture area, while 10% occur outside. Finally, we capture the uncertainty of the ETAS parameters by sampling parameters from normal distributions with means and standard errors from Case 4 in **Table 2-3**. Following the simulation procedures that are described above, 100,000 synthetic M4.7+ catalogues are simulated over a one-year period in this study.

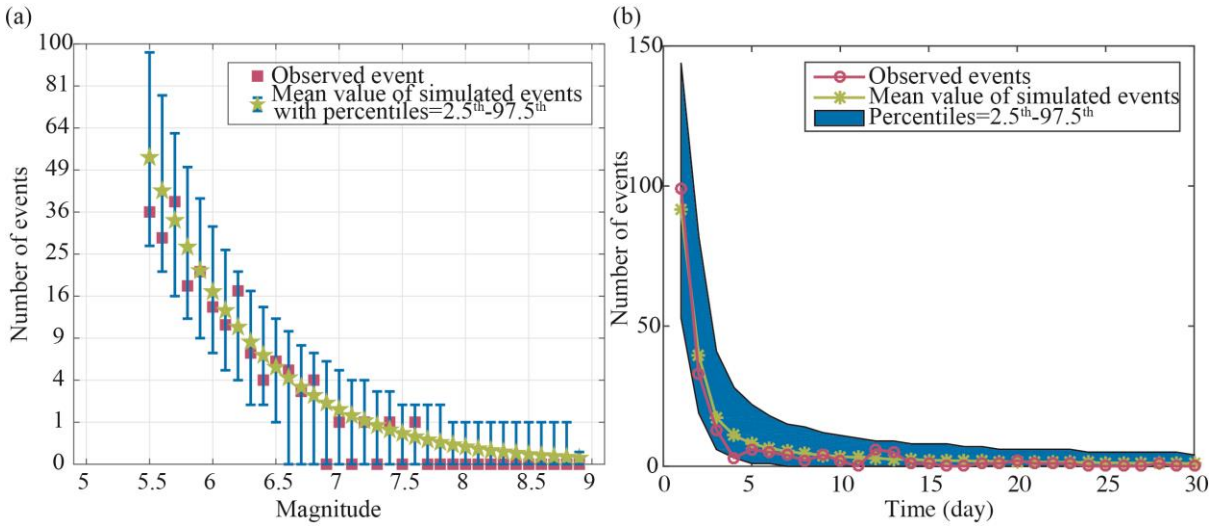

Figure 2-4. Comparison of observed and simulated aftershocks with M≥5.5 after the 2011 Tohoku earthquake: (a) Magnitude frequency histogram in the first 100 days and 95% uncertainty range from the simulations in square root scale. (b) Daily number of events in the first 30 days with 95% uncertainty range.

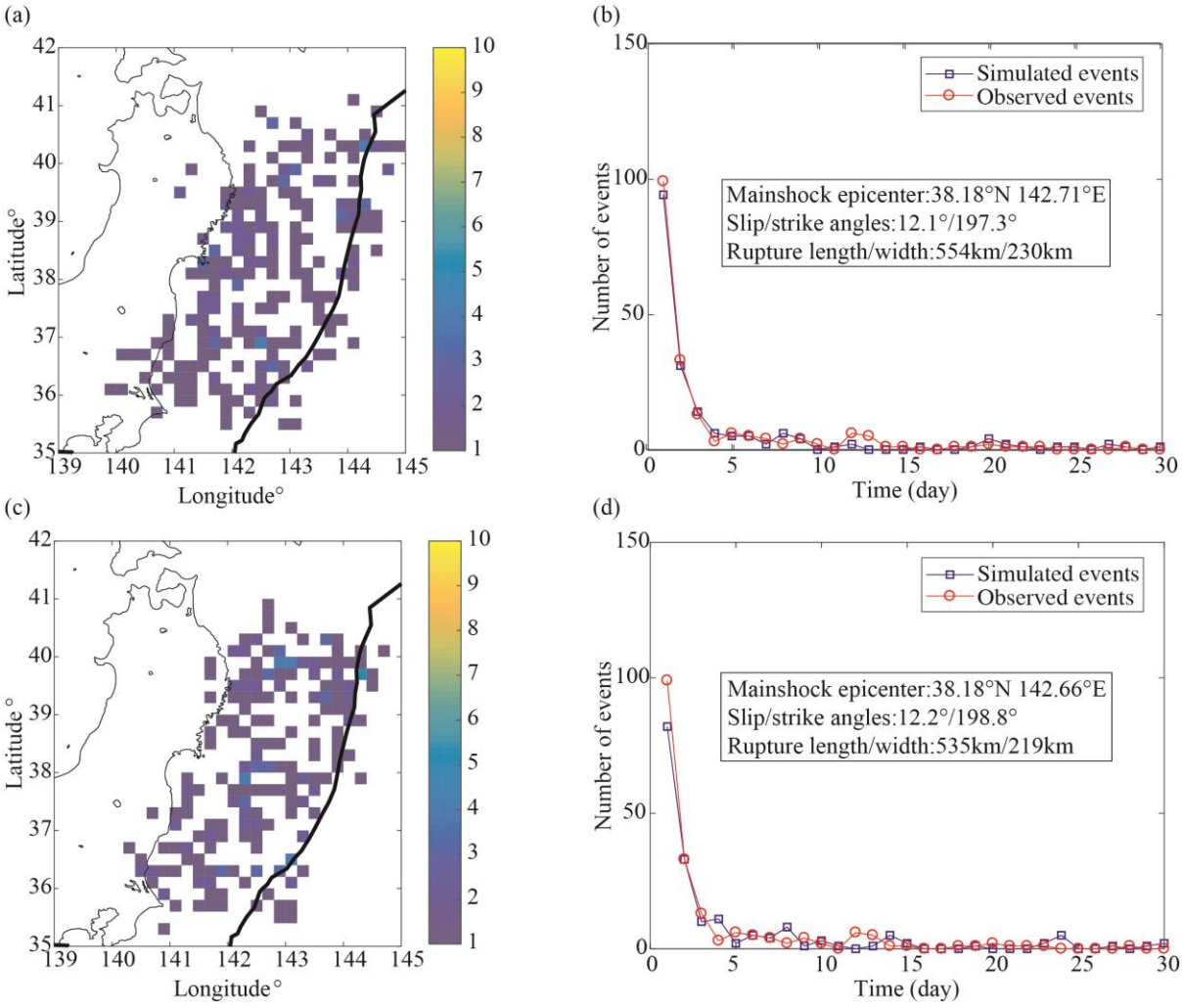

Figure 2-5. Two ETAS simulations in comparison with the 2011 Tohoku events with M≥5.5. (a, c) Simulated 2D aftershock histograms during the first 100 days. (b, d) Comparison of daily numbers of observed and simulated aftershocks. The mainshock source parameters (epicentre, slip angle, strike angle, rupture length, and rupture width) are randomly generated from the empirical distributions.

To illustrate the ETAS model's ability to mimic the 2011 Tohoku sequence, we compare simulations with observations. First, we compare observed and simulated magnitude-frequency histograms above M5.5 in the first 100 days in **Figure 2-4**(a). The observed magnitude-frequency histogram falls into the range of simulated magnitude-frequency histograms. Second, we compare the daily numbers of observed and simulated events over 30

days in **Figure 2-4**(b), again finding good agreement between the observations and the range of simulations. Third, to inspect spatial agreement, we show two examples of simulations with mainshock rupture areas similar to the 2011 Tohoku earthquake. In **Figure 2-5**(a) and (c), we show the spatial aftershock rates of two single simulations over 100 days with M≥5.5 (to be compared with **Figure 2-3**d); the spatial distributions show qualitative agreement. In **Figure 2-5**(b) and (d), the daily number of events of the two simulations is compared with the observed daily number of events, exhibiting good agreement. In the figure panels, the sampled mainshock epicentre, strike and slip angles, and rupture area for each simulation are also included.

2.6 Seismic hazard analysis of M9-triggered aftershock sequences in Tohoku

In this study, three sites are considered for seismic hazard and risk calculations, due to the potential high seismic risk, and the subsequent social and economic impact in the region: Sendai City (141.03ºE, 38.31ºN) in Miyagi Prefecture, Fukushima Daini Nuclear Power Plant (Fukushima II NPP) site (141.01ºE, 37.32ºN) in Fukushima Prefecture, and Tokyo (139.77ºE, 35.72ºN) in Tokyo Metropolis (see **Figure 2-3**a). Sendai is the capital of Miyagi Prefecture and has a high population density near the 2011 Tohoku mainshock. The Fukushima II NPP site is located at 2 km northeast of the Fukushima Daini NPP and 10 km south of the Fukushima Daiichi NPP, where the nuclear disaster occurred due to the 2011 Tohoku earthquake and tsunami. Although Tokyo, the capital of Japan with the highest population density in the country, is approximately 400 km away from the epicentre of the 2011 Tohoku mainshock, major subduction and crustal aftershocks could potentially be triggered which would lead to casualties, building and infrastructure damage, and large economic losses.

We select a GMPE and seismic fragility model appropriate for Japan. We use a GMPE developed by Morikawa and Fujiwara (2013). Compared with other GMPEs (Zhao *et al.*, 2006;

Abrahamson *et al.*, 2014, 2016) that calibrate parameters from global ground motion records, the GMPE from Morikawa and Fujiwara (2013) is only calibrated on Japanese ground motion records, including the 2011 Tohoku sequence. In addition, the latest GMPE for subduction earthquakes (Abrahamson *et al.*, 2016) does not provide PGV, which is the potential required input for Japanese fragility curves. The general required input for Japanese fragility curves is JMA intensity (I_{JMA}), PGA, or peak ground velocity (PGV) (Yamaguchi and Yamazaki, 2001; Midorikawa *et al.*, 2011). However, the standard deviation of PGA is higher than I_{JMA} and PGV (Yamaguchi and Yamazaki, 2001; Wu *et al.*, 2016), and I_{JMA} as an intensity measure is only widely used in Japan. Therefore, we use PGV in this study.

The median values of PGV for subduction and crustal earthquakes from Morikawa and Fujiwara (2013) with V_{s30} = 300 m/s are shown in **Figure 2-6**(a) and (b), respectively. An existing seismic fragility model of wood-frame houses for Japan by Yamaguchi and Yamazaki (2001) is used to evaluate the probabilities of exceeding different damage states. The slight, moderate, and heavy damage are referred to as damage state 1 (DS_1), damage state 2 (DS_2), and damage state 3 (DS_3), respectively. The fragility curves in terms of PGV are shown in **Figure 2-6**(c). This chapter does not estimate the cumulative damage due to triggered aftershocks because the fragility curve of aftershocks is not available in Japan.

The required inputs for the GMPE from Morikawa and Fujiwara (2013) are magnitude, source distance, type of event, and time-averaged shear-wave velocity in the uppermost 30 m (V_{s30}) of the site. The magnitude is from the synthetic catalogues, and the earthquake type and the source distance are estimated using available local catalogues (see **Section 2.4.1.3**). M_j is converted to M using empirical equations by Scordilis (2005) because the magnitude type input to the GMPE is moment magnitude. V_{s30} = 200 m/s, 300 m/s, and 400 m/s are used to investigate the effects of different soil conditions. To consider the uncertainty of the GMPE, the PGV is sampled given the inter-event sigma and intra-event sigma from the lognormal

distribution (Goda *et al.*, 2011; Morikawa and Fujiwara, 2013). The ratio of inter-event sigma and intra-event sigma is taken from Zhao *et al.* (2006). Inter-event sigma is the variability for different events, and intra-event sigma is the variability for different record stations of the same event (Youngs *et al.*, 1995). Therefore, in the simulation the same inter-event variability is used for the same event at different sites. We do not include spatial correlation model in this chapter, because the intensity measure is highly correlated with a distance less than 50 km and the three sites (Sendai, Fukushima II NPP, and Tokyo) are far away from each other.

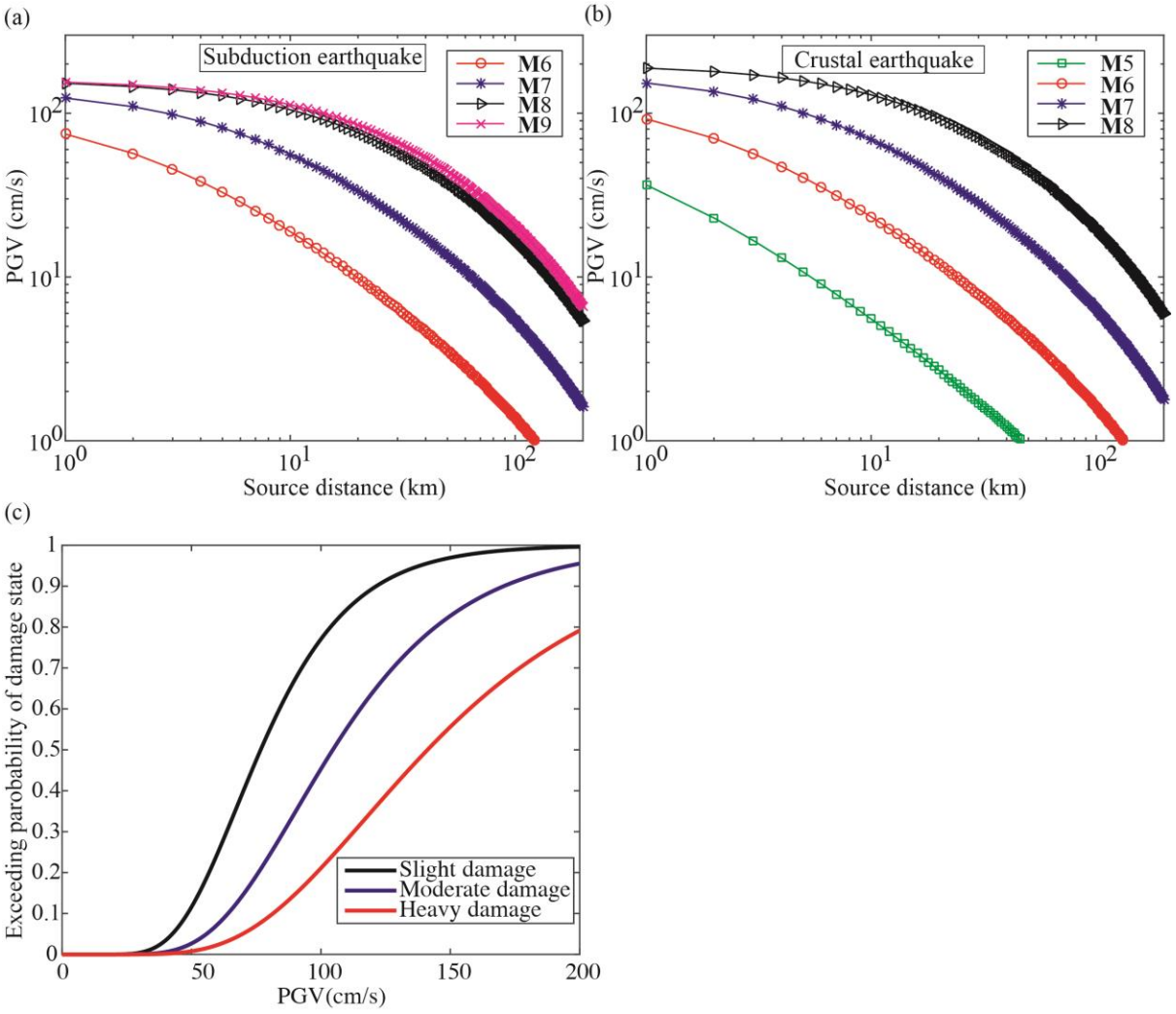

Figure 2-6. (a) Median values of PGV with V_{s30} = 300 m/s for subduction earthquakes from M6.0-M9.0 using the GMPE by Morikawa and Fujiwara (2013). (b) Median values of PGV with V_{s30} = 300 m/s for crustal earthquakes from M5.0-M8.0 using the GMPE by Morikawa

and Fujiwara (2013). (c) Fragility curves (the exceeding probability of damage states against PGV) of wood-frame houses for Japan with slight damage, moderate damage, and heavy damage.

2.6.1 Comparison of daily observed PGVs with simulated PGVs

To show that the new framework can anticipate the observed time-varying daily hazard rates in Sendai, Fukushima II NPP, and Tokyo, the observed daily PGV rate ≥ 1 cm/s during the first 7 days is shown in **Figure 2-7**. One-week time window is considered because the seismicity rate is high in the first week of mainshocks (see **Figure 2-4**b). The closest stations to the target sites are selected and summarised in **Table 2-1**. The hazard results with V_{s30} = 400 m/s, 400 m/s, and 200 m/s are selected in Sendai, Fukushima II NPP, and Tokyo, respectively, to match the V_{s30} values at the recording stations. From **Figure 2-7**, the observed PGV ≥ 1 cm/s is in the range between 10^{th} and 90^{th} percentiles of the simulated PGV. However, only the observed PGV on Day 1 in Fukushima II NPP is outside of the percentile range of the simulated PGV in **Figure 2-7**(b). One reason could be the complex earthquake rupture process of the Tohoku mainshock in space, which our model does not reproduce. Inversion analysis results by Kurahashi and Irikura (2013) indicated that five strong-motion generation areas (SMGAs) of the Tohoku mainshock are not close to the Fukushima II NPP location and thus observed ground motions are not as intense as predicted using the GMPE which is simply as a function of the shortest distance (rupture distance) to the fault plane. Therefore, the simulated PGV is higher than the observed PGVs at Fukushima II NPP on Day 1.

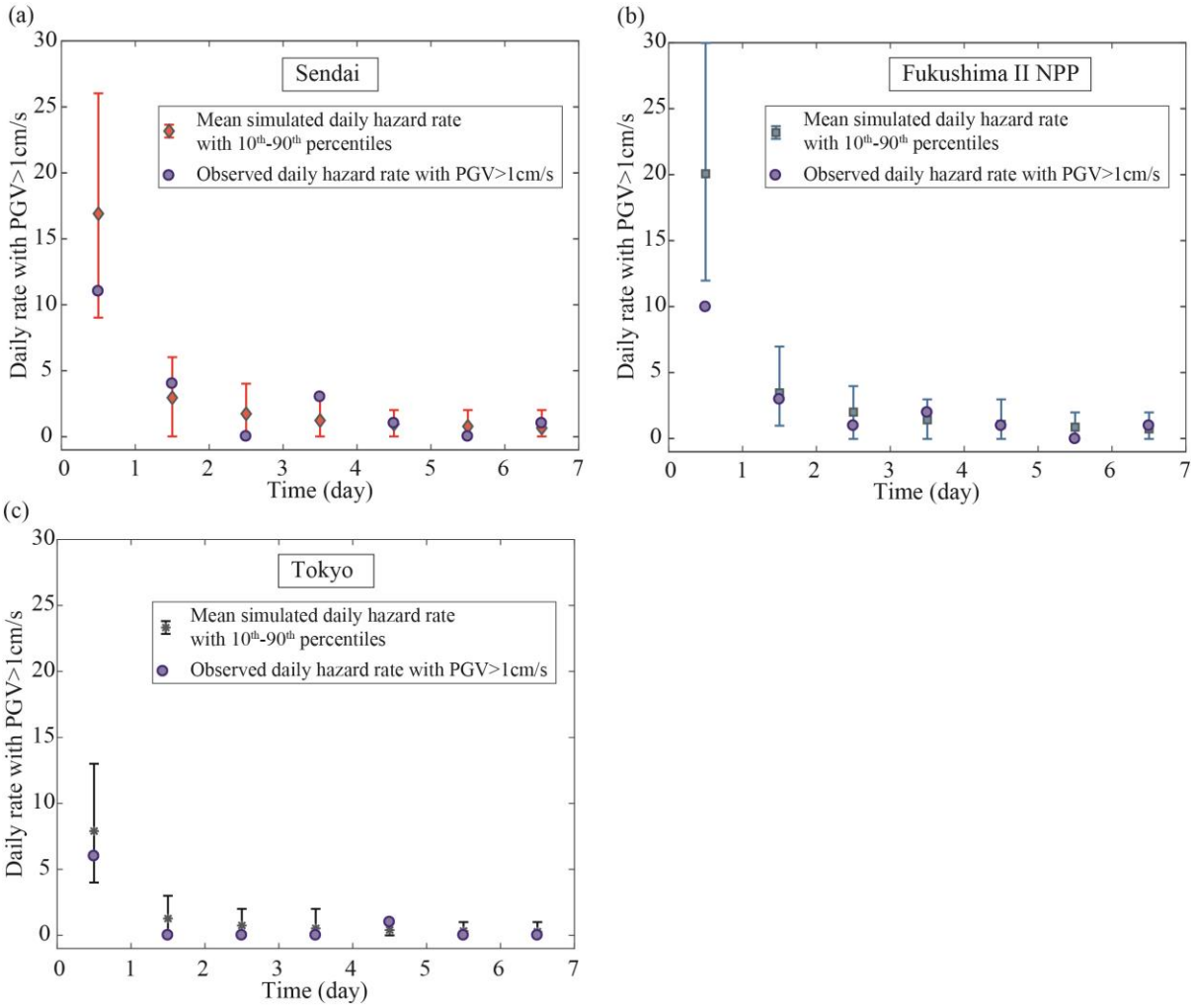

Figure 2-7. Comparison of mean simulated and observed rate of PGV > 1 cm/s per day during the first 7 days after the 2011 Tohoku mainshock in (a) Sendai, (b) Fukushima II NPP and (c) Tokyo. Vertical bars denote 10th to 90th percentile range of simulated ground motions.

2.6.2 Spatiotemporal aftershock hazard assessment

From the simulations, aftershocks have greater impact on high PGV values (150 cm/s) than the mainshock. The rates of exceeding PGV from 20 cm/s to 200 cm/s due to the simulated mainshock and from aftershocks on Day 1 with V_{s30} = 300 m/s in Sendai are shown in **Figure 2-8** to assess the relative importance of simulated mainshock and aftershock hazards. To relate PGV values to damage potential, three Modified Mercalli intensity scales (MMI) are introduced to link with PGV values in **Figure 2-8** with PGV > 31 cm/s (MMI VII), 60 cm/s

(MMI VIII), and 116 cm/s (MMI IX). The simulated mainshock dominates the lower hazard levels, but the aftershock rate is larger than the simulated mainshock beyond a PGV of 150 cm/s (MMI IX). This is because the simulated mainshock always strikes the subduction plate interface, at some distance (typically 40-50km in Sendai) to each site. However, crustal aftershocks are occasionally closer and can thus lead to large PGV values.

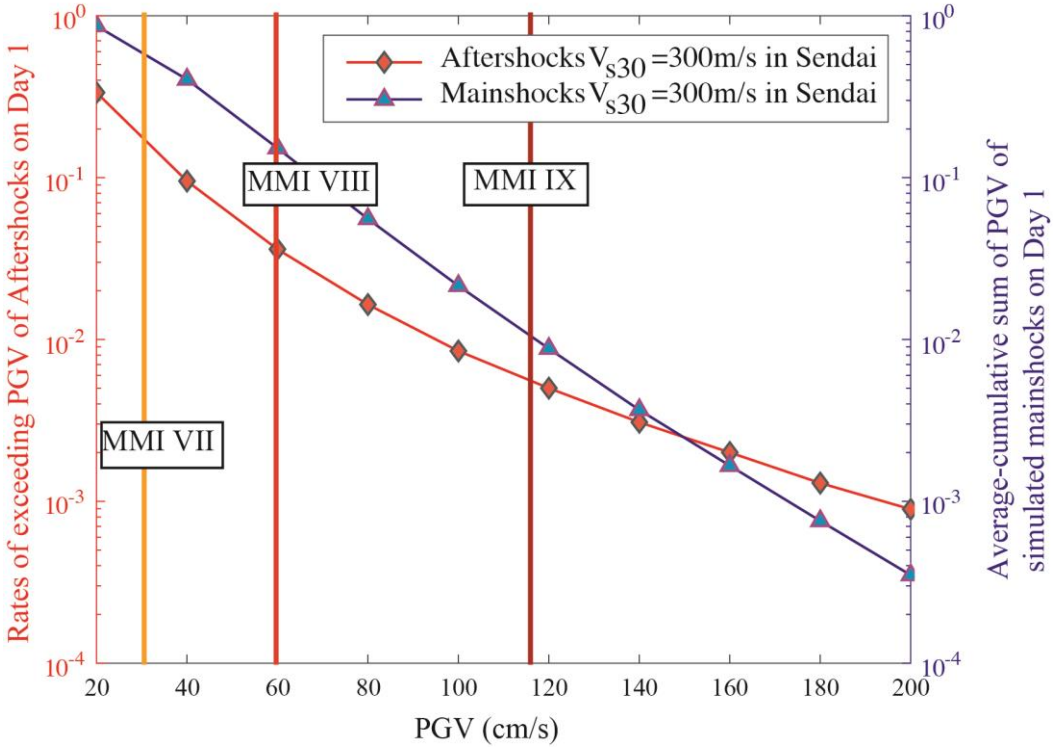

Figure 2-8. Rates of exceeding aftershock PGVs on left y-axis (diamond) on Day 1 in Sendai in comparison with PGV rates of simulated mainshock on right y-axis (upward-pointing triangle).

The aftershock hazard rate in Fukushima II NPP is higher than in Sendai, as shown in **Figure 2-9**(a). Fukushima II NPP is closer to the mainshock rupture area than Sendai, thus more aftershocks are likely to occur nearby. The hazard rate in Tokyo on Day 1 is relatively low because Tokyo is far from the mainshock rupture. This contrasts with the observation that

the seismicity in the Kanto region intensified after the 2011 Tohoku mainshock (Nanjo *et al.*, 2013). However, Nanjo *et al.* (2013) considered a lower magnitude threshold with M≥1.0 and no event with M≥6.0 is observed in the Kanto region during the one year period after the 2011 Tohoku mainshock. Considering uncertainty in the estimation, the increased probability of large events of the 2011 Tohoku sequences is insignificant. Moreover, the three largest historical events (1703 M8.2 Genroku earthquake, 1854 M8.4 Tonankai-Tokai earthquake, and 1923 M7.9 Kanto earthquake) are thought to dominate the seismic hazard in Tokyo (Stein *et al.*, 2006).

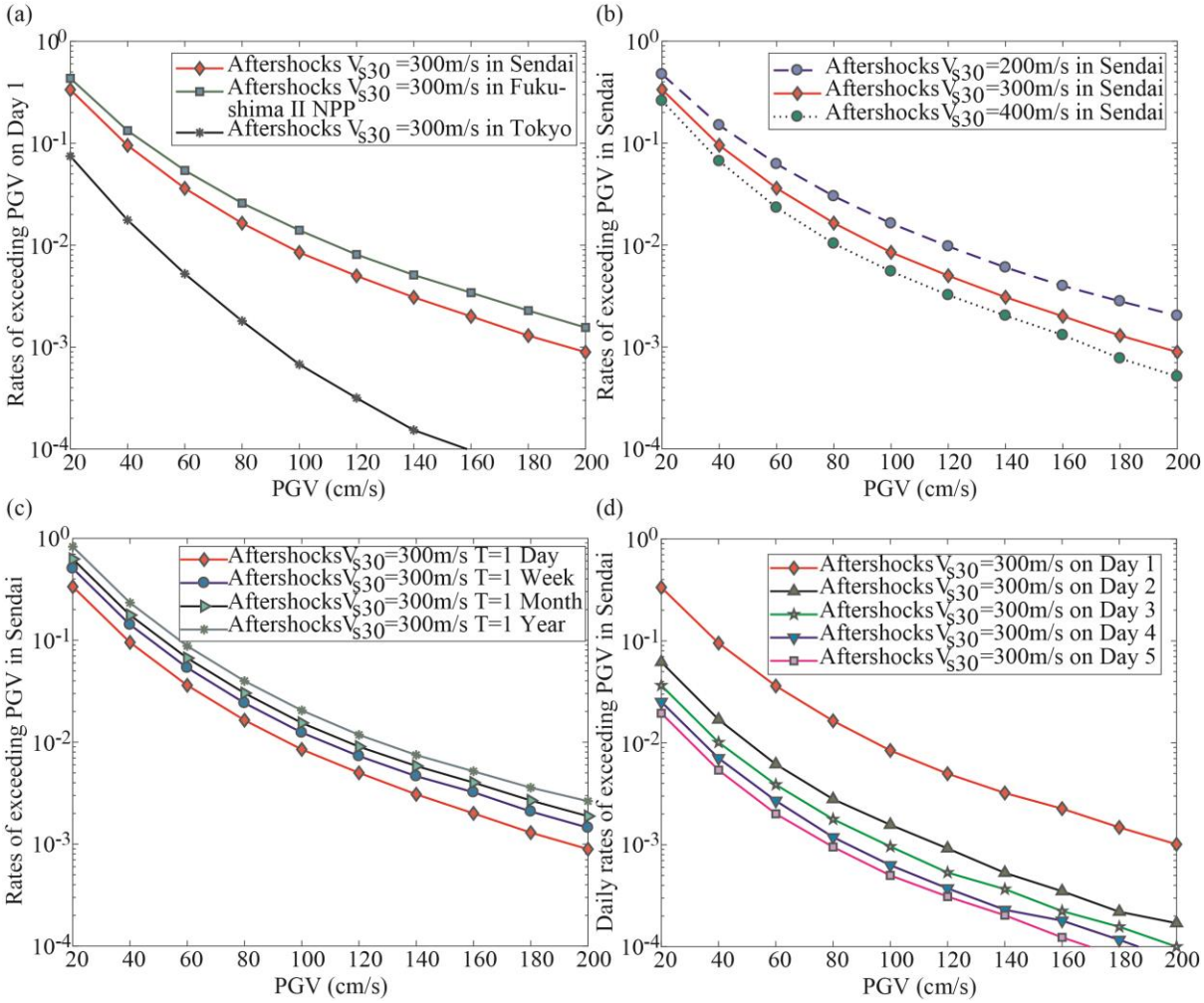

Figure 2-9. (a) Rates of exceeding aftershock PGVs (diamond) on Day 1 in Sendai in comparison with Fukushima II NPP (square), and Tokyo (star). (b) Three soil conditions with

V_{s30} = 200 m/s (circle with dashed line), 300 m/s (diamond), and 400 m/s (circle with dotted line). (c) time periods with T = 1 day (diamond), 1week (circle), 1 month (right-pointing triangle), and 1 year (star). (d) Day 1 (diamond), Day 2 (upward-pointing triangle), Day 3 (pentagram), Day 4 (downward-pointing triangle), and Day 5(square).

The differences of the aftershock hazard rates for V_{s30} =200 m/s, 300 m/s, and 400m/s from **Figure 2-9**(b) illustrate the effect of the site amplification parameter with a reference V_{s30} value (350 m/s) from the GMPE (Morikawa and Fujiwara, 2013). To contrast the rates of exceeding PGV from 20 cm/s to 200 cm/s over different periods, the rates within 1 day, 1 week, 1 month, and 1 year in Sendai are shown in **Figure 2-9**(c), whilst the daily rates of exceeding PGV from Day 1 to Day 5 are shown in **Figure 2-9**(d). Depending on the situation, the aftershock hazard rate may be critical for seismic hazard analysis within one week after the mainshock occurred. This is consistent with the results shown in **Figure 2-4** for the daily seismicity rate, where the seismicity rate for M≥5.5 drops significantly in the first 3 days and then decays slowly.

Subduction aftershocks contribute more to the total hazard below PGV = 60 cm/s, while crustal aftershock hazard is greater above 60 cm/s in Sendai and Fukushima II NPP. The daily rates of exceeding PGV from 20 cm/s to 200 cm/s in the first 7 days due to crustal and subduction earthquakes are shown in **Figure 2-10** to investigate the proportions of aftershock hazard rates that are contributed by crustal and subduction earthquakes in Sendai, Fukushima II NPP, and Tokyo. Subduction aftershocks are more numerous than crustal aftershocks, but they are farther from the considered sites. As a result, subduction aftershocks dominate the hazard below 60 cm/s. In Tokyo, the hazard rate from crustal aftershocks is low, and the aftershock hazard rates are dominated by subduction aftershocks that occur in offshore areas.

In addition, MMI VII (PGV > 31 cm/s), MMI VIII (PGV > 60 cm/s), and MMI IX (PGV > 116 cm/s) are indicated in **Figure 2-10** to illustrate the hazard contributions by continental crustal and subduction earthquakes. In Sendai and Fukushima II NPP, subduction aftershocks dominate the MMI VII rate as shown in **Figure 2-10**(a) and (b). Subduction and crustal aftershocks contribute equally to the MMI VIII exceedances during the first week (**Figure 2-10**a and b), whereas crustal aftershocks generate higher rates of MMI IX.

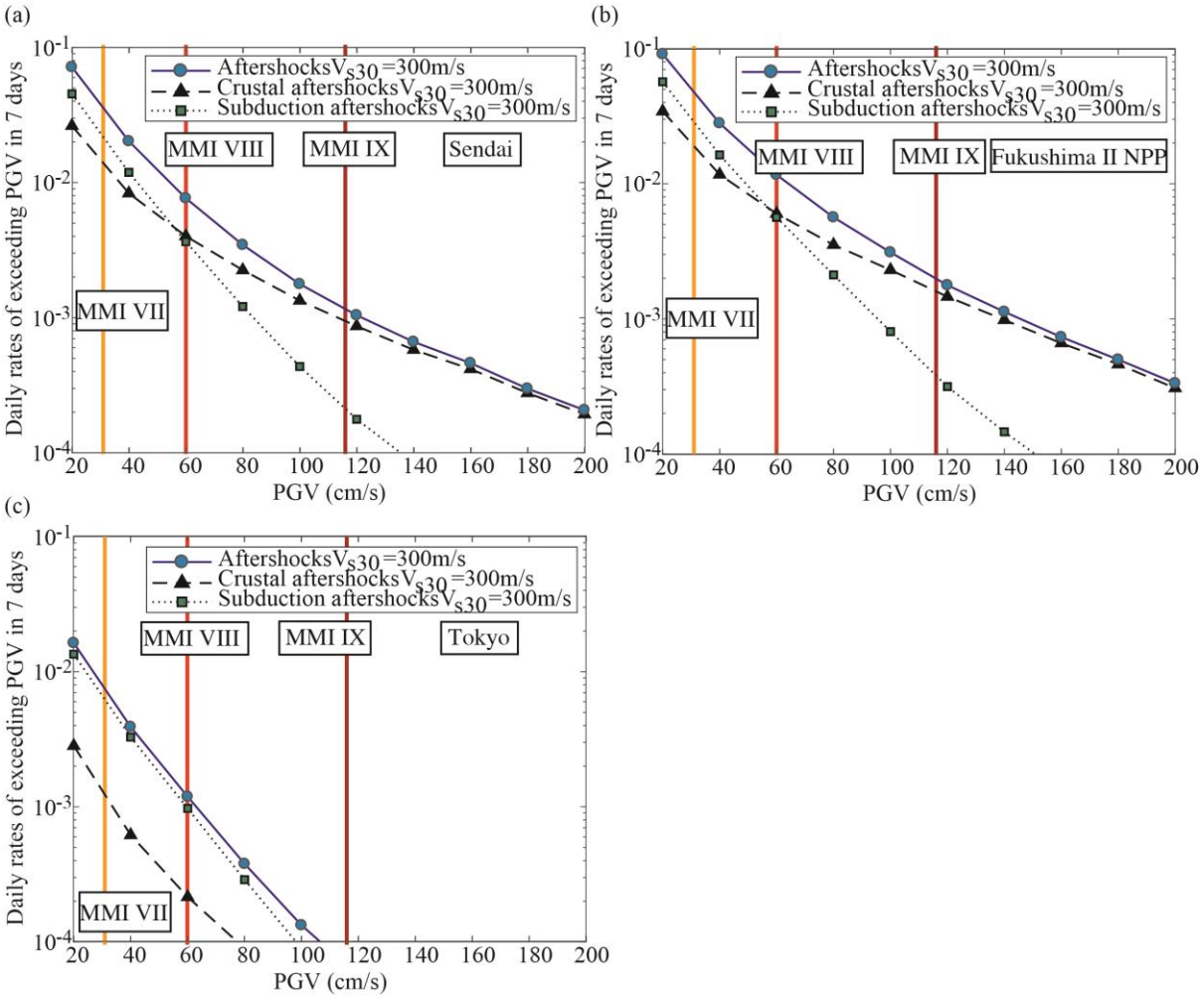

Figure 2-10. Daily rates of exceeding PGV for crustal and subduction aftershocks (circles with solid line), crustal (upward-pointing triangles with dashed line) and subduction (squares with dotted line) aftershocks in the first 7 days in (a) Sendai, (b) Fukushima II NPP, and (c) Tokyo.

To investigate how the hazard varies with increasing distance from the source model, we consider three additional sites which increase in distance from Fukushima II NPP by successive 20 km intervals. In **Figure 2-11** the daily rates of exceeding PGV in the first 7 days both for crustal and subduction aftershocks gradually decay with distance. The crustal aftershock hazard is higher than subduction aftershock hazard for PGV>40cm/s. This shows that in comparison with the Fukushima II NPP site, the effect of subduction aftershocks on the hazard rate is decreased at the three inland sites, because the inland sites are farther from the subduction zone.

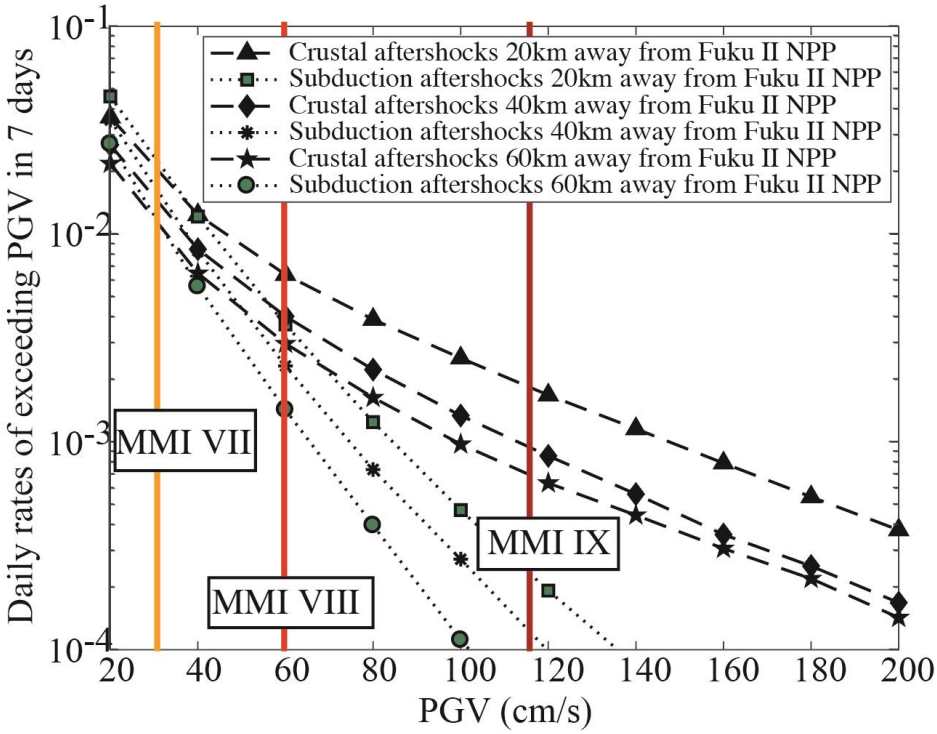

Figure 2-11. Daily rates of exceeding PGV for crustal and subduction aftershocks in the first 7 days 20km, 40km, and 60km away from Fukushima II NPP.

To compare the simulated mainshock hazard and the time-dependent aftershock hazard rate from Days 1 to 7, **Figure 2-12**(a) and (b) show the chances of exceeding PGV > 60 cm/s at Sendai and Fukushima II NPP, respectively, due to the simulated mainshocks and

aftershocks (assuming V_{s30} = 300 m/s). **Figure 2-12**(a) shows that the probability of PGV > 60 cm/s in Sendai due to the mainshock is 0.152, whereas the chance is 0.036 due to aftershocks on Day 1. This means that the aftershock hazard on Day 1 adds about 23% to the (conditional) hazard from the mainshock in Sendai on that day. We expect this contribution to varying only by a small amount along the Japanese shoreline close to the rupture area. The result for Fukushima II NPP (**Figure 2-12**b) shows a similar proportion on Day 1 with the mainshock and aftershock contributions of 0.222 and 0.055, respectively.

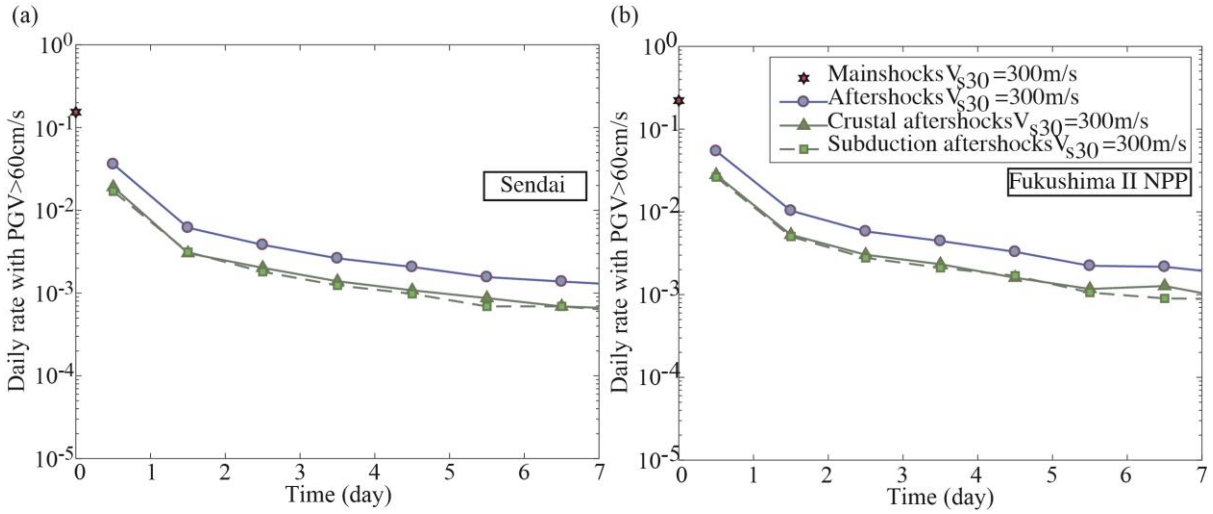

Figure 2-12. Daily hazard rates of PGV > 60 cm/s due to crustal and subduction aftershocks in comparison with simulated mainshock (stars) in (a) Sendai and (b) Fukushima II NPP.

To investigate the relative contributions from crustal and subduction aftershocks over several days after the mainshock, **Figure 2-12**(a) and (b) also show the daily hazard rates of crustal and subduction earthquakes. The hazard rates with MMI VIII of subduction and crustal aftershocks in Sendai and Fukushima II NPP are indistinguishable. This is because PGV = 60 cm/s corresponds to the point where the two contributions are about equal (see also **Figure 2-10**).

2.6.3 Comparison of spatiotemporal aftershock hazard rates with conventional long-term hazard rates

A comparison between the long-term hazard rates from JSHIS and the unconditional time-dependent hazard rates from the mainshock-aftershock sequence with V_{s30} = 300 m/s is displayed in **Figure 2-13** for Sendai, Fukushima II NPP, and Tokyo. The hazard rates in JSHIS consider all types of earthquakes including continental-crust, subduction plate-boundary, and subduction intra-plate. To make the JSHIS hazard rate and the time-dependent aftershock hazard rate comparable, we contrast the unconditional time-dependent daily hazard rates by assuming return periods of 300, 600, and 1000 years for the M9.0 Tohoku-type subduction earthquake with the daily hazard rates based on the long-term hazard map from JSHIS. The return periods of 300, 600, and 1000 are based on the literature. Kagan and Jackson (2013) suggested return periods of 300-400 years for the Tohoku-like event based on the seismic moment-frequency relation. According to the historical tsunami records, JSHIS considered return periods of 400-800 years for the Tohoku-like event. On the other hand, Simons *et al.* (2011) suggested return periods in the range of 500-1000 years based on the slip accumulation.

The long-term hazard rate follows a Poisson distribution with 2% probability in 50 years. Detailed calculations of the JSHIS hazard rate and the unconditional time-dependent aftershock hazard rate are provided in **Appendix B**. We show comparisons with the 2010 version (before the 2011 Tohoku event) and the latest 2017 version, each at the PGV exceeded with 2% probability in 50 years. The JSHIS values are computed from all possible earthquakes, including subduction and crustal earthquakes in land and sea areas. The PGV values of the 2017 map corresponding to the 2% probability of exceedance in 50 years are 71 cm/s, 94 cm/s, and 134 cm/s, with V_{s30} = 351 m/s, 351 m/s, and 403 m/s for Sendai, Fukushima II NPP, as Tokyo, respectively, and indicated in **Figure 2-13** (a), (c), and (e). The values from the 2010 map are displayed in **Figure 2-13** (b), (d), and (f).

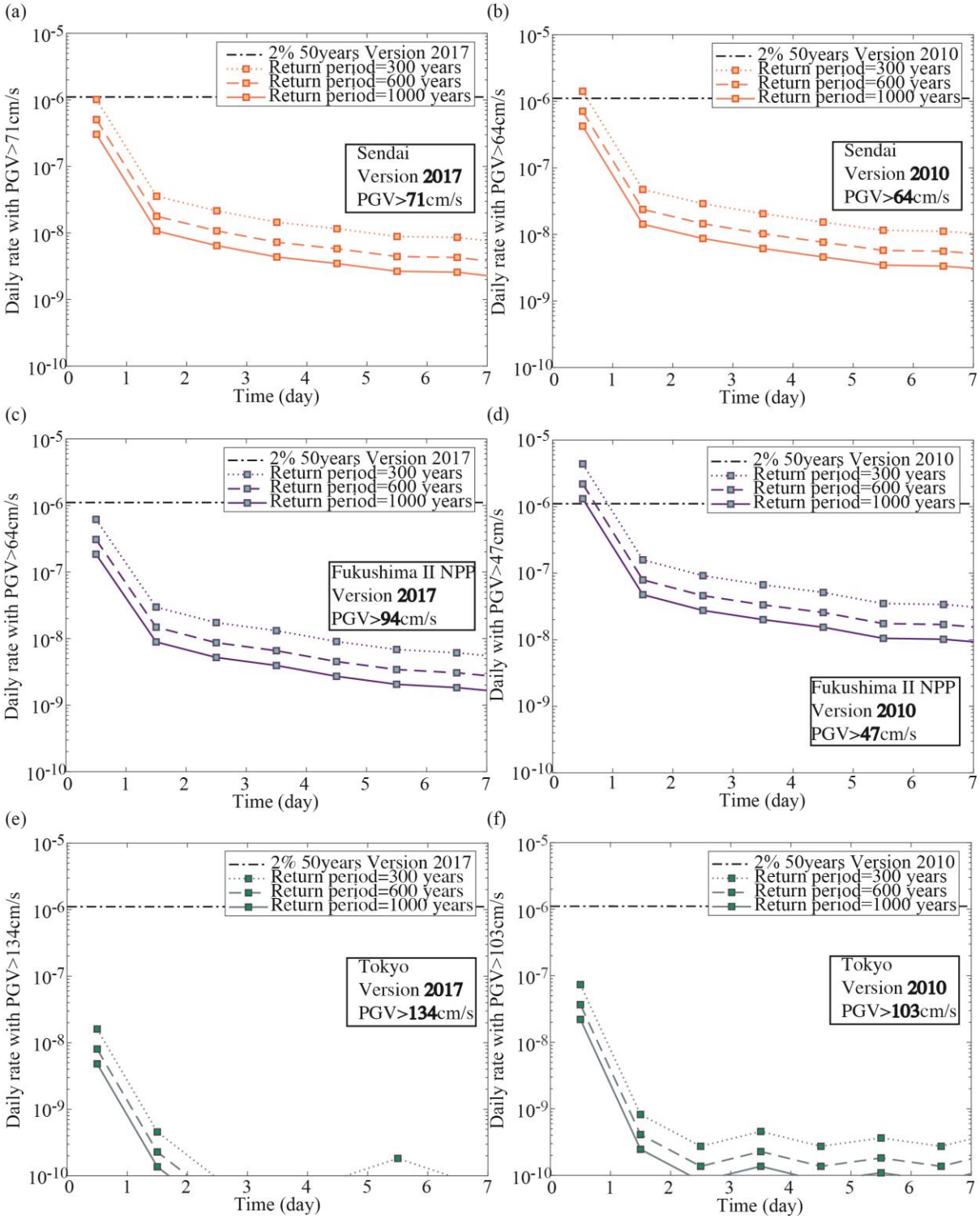

Figure 2-13. Left panels: comparison between daily time-dependent hazard rate (squares) and the 2017 JSHIS long-term hazard rate corresponding to 2% in 50 years (dash-dotted line) with

return periods 300, 600, and 1000 years in (a) Sendai, (c) Fukushima II NPP, and (e) Tokyo. Right panels: comparison with the 2010 JSHIS rate.

After the 2011 Tohoku event, the long-term hazard map was updated significantly. The 2017 JSHIS map is higher than the time-dependent rate at all sites assuming V_{s30} = 300 m/s, as shown in **Figure 2-13** (a), (c), (e). In contrast, the aftershock hazards on Day 1 in Sendai and Fukushima II NPP are greater than the 2010 JSHIS hazard level (**Figure 2-13**b and d). As shown in **Figure 2-13**(f), Tokyo has the lowest aftershock hazard rate among the three sites.

Conducting the spatial and temporal hazard assessment using the new framework for the region where a potential M9.0 event can occur in future is important. Before the 2011 Tohoku event, the PGV of the 2010 JSHIS hazard map was lower in Fukushima II NPP (47 cm/s) than in Sendai (64 cm/s). However, after the 2011 Tohoku event, the PGV in Fukushima II NPP was increased significantly (94 cm/s) relative to the PGV in Sendai (71 cm/s). It indicates that for some regions where M9.0 megathrust subduction sequences have never been recorded (e.g., Cascadia subduction zone), conducting spatiotemporal seismic hazard and risk assessments is necessary to investigate the difference in comparison with the conventional probabilistic seismic hazard analysis results.

Because of the updated long-term hazard rate for 2% in 50 years based on the 2011 Tohoku sequence, the effects from a M9.0 earthquake (including its aftershock sequence) to buildings that are newly built after 2017 are limited. However, for buildings that were built before the Tohoku sequence, the damage that may be caused by such sequences could be significant. Therefore, time-dependent rates shown in **Figure 2-12** and **Figure 2-13** may be useful for decision-making.

To investigate the change of daily aftershock hazard rates before and after the M9.0 Tohoku-type subduction earthquake, the conditional daily hazard rates from triggered aftershocks right after the Tohoku-like mainshock and the unconditional daily hazard rate from

triggered aftershocks are shown in **Figure 2-14**(a) and (b), respectively. The detailed calculations of the conditional and unconditional daily hazard rates are provided in **Appendix B**. According to **Figure 2-14**(a), the forecasted daily aftershock hazard rate immediately following the Tohoku-like mainshock is significantly higher than the 2017 version long-term hazard rate in Sendai and gradually decays over time. The conditional daily aftershock hazard rates could take more than 5 years to trend back to the long-term hazard map from JSHIS given V_{s30} = 300 m/s. The daily unconditional daily hazard rate of aftershocks considering the Tohoku-like mainshock with a 600-years return period is increased by 3% of the long-term hazard rate with V_{s30} = 200 m/s on Day 1 in **Figure 2-14**(b).

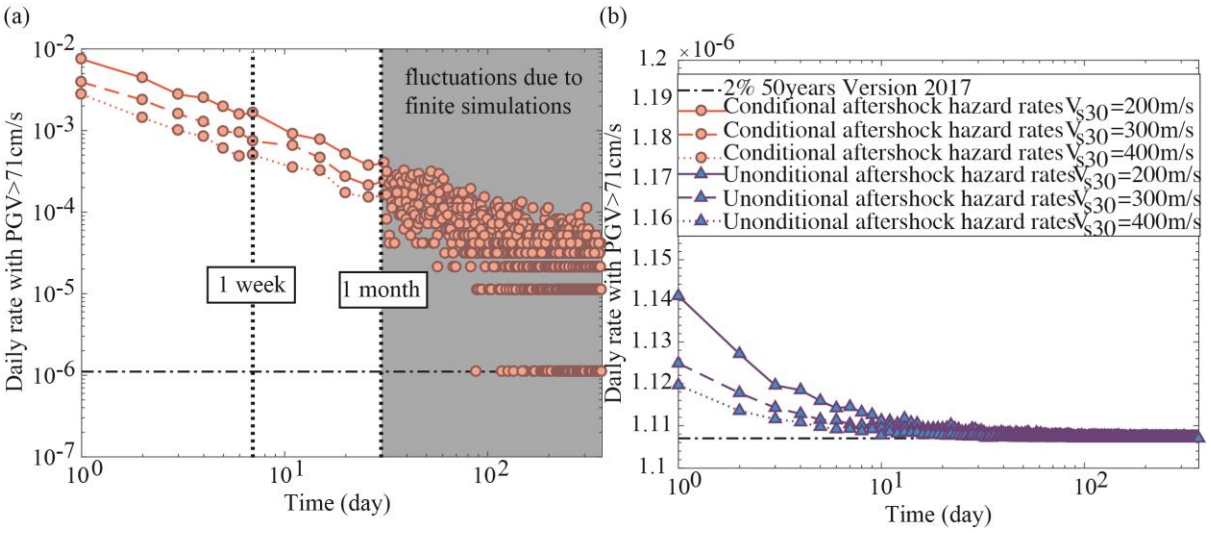

Figure 2-14. (a) Decay of conditional aftershock hazard rates in Sendai immediately after the Tohoku-like mainshock in one year. (b) Decay of unconditional aftershock hazard rates considering a 600-year return period of the Tohoku-like mainshock.

2.7 Seismic risk analysis of M9-triggered aftershock sequences in Tohoku

The fragility curves of wood-frame houses from Yamaguchi and Yamazaki (2001) are used (1) to conduct the seismic risk analysis of mainshocks and aftershocks, and (2) to investigate the effects of earthquake types on the wood-frame houses in Japan.

The probability of the damage reaching DS_1 due to the simulated mainshock and aftershocks on Day 1 is 11% and 3%, respectively, in Sendai. Aftershocks thus contribute about one-fifth of the mainshock's damage probability to DS_1 for wood-frame houses on Day 1 (ignoring the damage accumulation effects). The temporal changes of the rates of the three damage states in Sendai and Fukushima II NPP are highlighted in **Figure 2-15**. The daily damage state rates decay rapidly over the first few days, but also display the slow (heavy-tailed) decay characteristics of the ETAS seismicity model (also seen in the daily hazard rates of **Figure 2-12**).

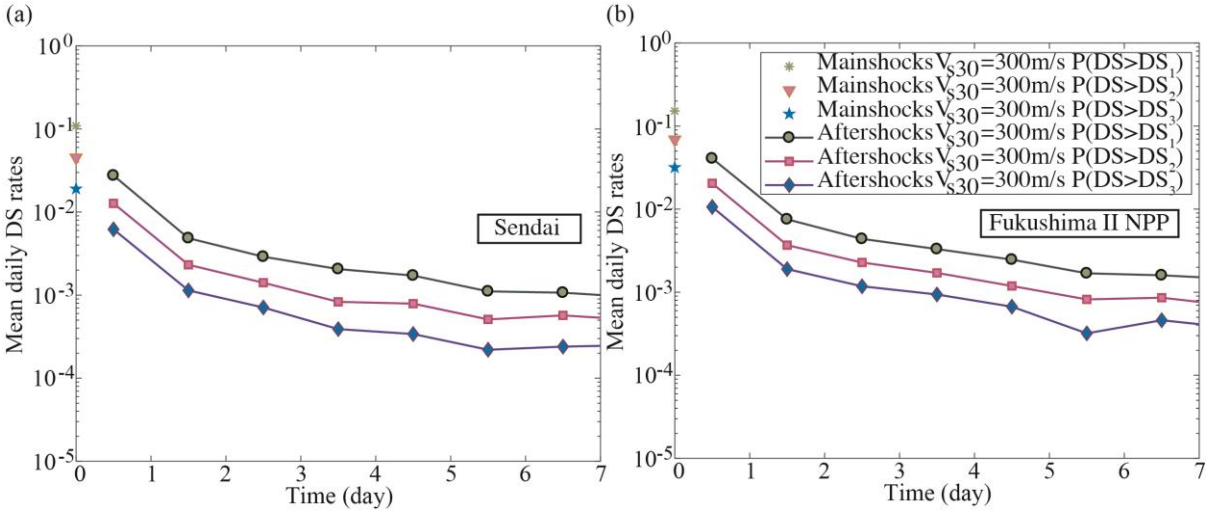

Figure 2-15. Comparison of mean daily DS rates of simulated mainshock and aftershocks in (a) Sendai and (b) Fukushima II NPP.

The seismic risk information in **Figure 2-15** can be useful for decision-making about post-earthquake building-tagging and inspection prioritisation. The number of days after the mainshock occurred should be taken into consideration as a key factor of the short-term seismic risk assessment. From **Figure 2-15**(a) and (b), the average damage state rates in Sendai and Fukushima II NPP are decreased after Day 5. This suggests that the building may be exposed to significant risk due to mainshock-aftershock sequences in the first 5 days. Different

strategies can be used for post-earthquake building inspection, depending on the number of available inspectors and emergency workers. Houses can be inspected immediately after the mainshock, but the inspectors should be informed in advance about the increased hazard. Therefore, the inspectors can take the potential aftershock hazard into account in the following days. If larger aftershocks are triggered, houses that are tagged with DS_1 and DS_2 need to be assessed once more. Alternatively, the inspection of the houses can take place after Day 5 to make sure the damage potential due to the more likely aftershocks is included.

The damage state rates of wood-frame houses that are caused by crustal and subduction aftershock hazards are shown in **Figure 2-16**. Crustal and subduction earthquakes induce about the same DS_1 rates. The DS_2 and DS_3 rates, however, are dominated by crustal earthquakes in Sendai and Fukushima II NPP. The median values of the fragility curves for DS_1, DS_2, and DS_3 are 77 cm/s, 105 cm/s, and 141 cm/s, respectively. Experiencing a PGV = 60 cm/s, which corresponds to the value of intersection between the subduction aftershock and crustal aftershock in **Figure 2-10**, could result in DS_1 for the wood-frame houses, whereas DS_2 and DS_3 require a PGV higher than 60 cm/s, which are mainly contributed from large crustal earthquakes. This suggests that crustal aftershocks could cause more significant damage than the subduction aftershocks for wood-frame houses in Japan. The decision-making for wood-frame houses in post-earthquake risk assessments described above is an example of how the time-dependent hazard rate can be implemented for risk analyses. In general, the daily hazard rates in **Figure 2-12** can be widely applied for different types of buildings and infrastructure.

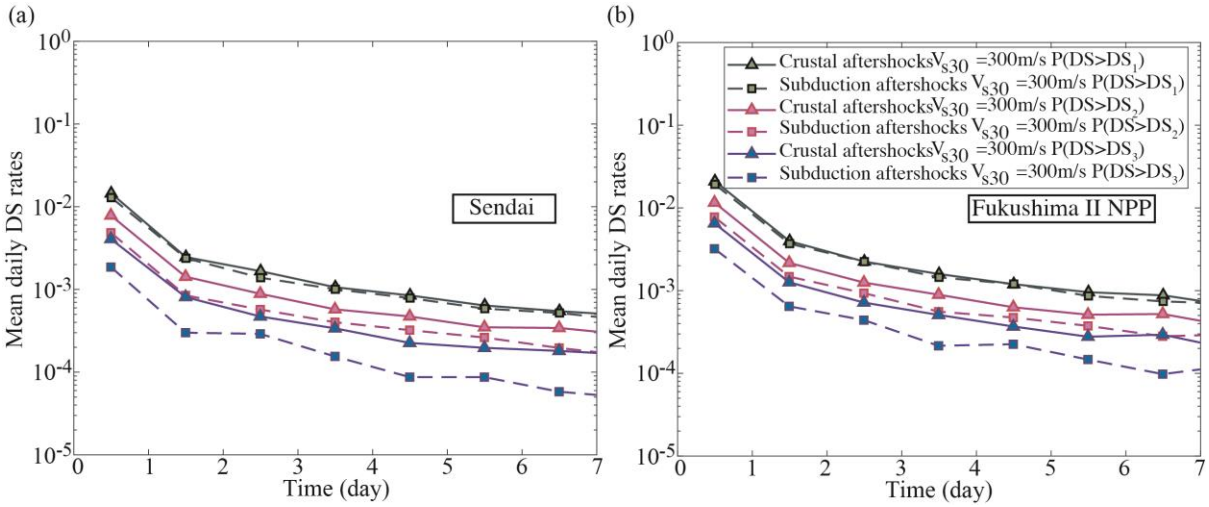

Figure 2-16. Mean daily damage state rates of crustal and subduction aftershocks for DS_1, DS_2 and DS_3 in (a) Sendai and (b) Fukushima II NPP.

2.8 Conclusions

This chapter investigated the importance of subduction and crustal aftershocks triggered by a M9.0 megathrust subduction event in spatiotemporal seismic hazard and risk assessments. The developed framework includes a seismicity model, hazard analysis, and risk analysis. Specifically, we convolved the ETAS model with a GMPE and fragility model to conduct the hazard and risk analyses. To model the M9.0 megathrust subduction sequences in space, we proposed a new spatial distribution of the first-generation aftershocks by combining the latest scaling law of rupture area with a power law decay beyond the main rupture area. By using this new spatial distribution, good agreement is achieved between the observed 2011 Tohoku sequence and the simulated daily seismicity rates with M≥5.5 and PGV rates ≥ 1 cm/s. We estimated how much simulated aftershock hazards add to simulated mainshock hazards considering uncertainties of the seismicity model, GMPEs, and fragility curves.

The results showed that:

- Aftershocks on Day 1 at the onshore sites that are close to the mainshock rupture area (e.g., Sendai and Fukushima II NPP in this study) could have a higher impact on high

PGV values > 150 cm/s than the simulated mainshock, due to occasional crustal aftershocks.

- The aftershock hazard rate in Fukushima II NPP is higher than in Sendai, because Fukushima II NPP is closer to the mainshock rupture plane than Sendai.
- According to our model, a M9.0 2011 Tohoku-like earthquake sequence does not have a significant impact on JSHIS's estimate for Tokyo, which is dominated by presumed recurrences of the 1703 M8.2 Genroku earthquake, the 1854 M8.4 Tonankai-Tokai earthquake, and the 1923 M7.9 Kanto earthquake.
- Triggered subduction earthquakes are more numerous than crustal counterparts with M5.5, but the crustal aftershocks contribute greater hazard above PGV = 60 cm/s (MMI VIII) and V_{s30} = 300 m/s than the subduction aftershocks. Therefore, the subduction aftershocks have a significant impact on MMI VII, whereas the crustal earthquakes contribute more to MMI IX and beyond.
- The aftershock hazard rate contributes about 23% of the PGV rate on Day 1 in Sendai. Fukushima II NPP shows a similar proportion on Day 1, but the mainshock and aftershock rates are higher than Sendai by a factor of 1.5.
- The daily hazard rate from aftershocks alone exceeds the 2010 long-term (total) hazard level from the JSHIS (which considers all earthquakes) on Day 1 in Sendai and Fukushima II NPP. The daily aftershock hazard rate immediately after the mainshock is significantly high and could take more than 5 years to trend back to the 2017 JSHIS long-term hazard map in Sendai.
- Assuming V_{s30} = 300 m/s, the simulated mainshock and aftershocks contribute approximately 80% and 20% to the total DS_1 rate at Sendai and Fukushima II NPP on Day 1, and the mean damage state rate gradually decreases from Day 2 to 5. This may

be useful for prioritising building inspection. Wood-frame houses in Sendai and Fukushima II NPP can be inspected by a structural engineer after Day 5.

- Crustal aftershocks have a higher probability to damage the wood-frame houses than the subduction earthquakes in Sendai and Fukushima II NPP.

The developed procedure to assess the spatiotemporal seismic hazard analysis with the ETAS model and GMPEs is generic and can be applied to other regions with M8.5+ subduction earthquakes. However, the mainshock source parameters (e.g., epicentre, rupture length and width, and strike and dip angles) are necessary as input for the ETAS simulation. If we ignore the observed M9.0 sequence (e.g., the 2011 Tohoku event), the uncertainty of the hazard rates would be increased. Therefore, if the mainshock source parameters are available immediately after the mainshock, quasi-real time aftershock hazard can be assessed. The output of the short-term hazard and risk results may be particularly beneficial for short-term decision-making within the first 7 days after the mainshock. For the regions without observed M9.0-class events, different mainshock rupture scenarios should be considered in the new simulation framework.

Local conditions (e.g., stress fields or volcanic zones) of the inland area may provide additional constraints on remote triggering in a refined model version. Several studies have shown that static and dynamic stress changes (Ishibe *et al.*, 2011; Toda *et al.*, 2011; Kato *et al.*, 2013) should be considered as physical mechanisms of distant aftershocks. These mechanisms do not solely depend on distance as the only factor that controls aftershock rates in the far field. Local stress fields could be examined before the megathrust event for susceptibility to remote aftershock triggering (Imanishi *et al.*, 2012). In addition, Hirose *et al.* (2011) concluded that the seismicity rate tends to increase in volcanic regions after the rupture of major active fault.

Chapter 3 Variability of ETAS Parameters in Global Subduction Zones and Applications to Mainshock-aftershock Hazard Assessment†

3.1 Introduction

Megathrust subduction earthquakes trigger numerous aftershocks over a prolonged period of time and a range of distances. The seismicity rate increases significantly and then decays in time, sometimes punctuated by secondary aftershock sequences. Large aftershocks have been triggered at distances of more than 100 km and may occur months later (Toda *et al.*, 2011). Over eighty M≥5.5 aftershocks were triggered within two months of the 2004 M9.1 Aceh-Andaman earthquake, while the 2011 M9.0 Tohoku earthquake triggered circa 200 M_j≥5.5 aftershocks within two months, according to the National Earthquake Information Centre (NEIC) and Japan Meteorological Agency (JMA) catalogues, respectively. The aftershocks are triggered not only near the subduction interface but also in the upper crust of onshore regions. Shallow aftershocks near population centres and critical infrastructures can be particularly dangerous. For instance, the Maule, Chile earthquake on 27 February 2010 triggered shallow onshore M6.9 and M7.0 earthquakes on 11 March about 200 km from the mainshock near Pichilemu. These two triggered events occurred within 15 minutes and 11 km of each other (Farías *et al.*, 2011; Ryder *et al.*, 2012). A month after the Tohoku mainshock, the Yunodake

† This chapter is published at Bulletin of the Seismological Society of America:

Zhang, L., M.J. Werner, and K. Goda (2020) Variability of ETAS parameters in global subduction zones and applications to mainshock-aftershock hazard assessment, *Bull. Seismol. Soc. Am*. **110**, 191–212.

and Itozawa faults ruptured, and a large aftershock of M6.6 struck near the Fukushima Nuclear Power Plant 240 km from the epicentre of the Tohoku mainshock (Fukushima *et al.*, 2013; Toda and Tsutsumi, 2013). For effective earthquake risk management, the increased aftershock rates in space and time along the subduction plate interface and in the shallow onshore crust should be considered (Ebrahimian *et al.*, 2014; Iervolino *et al.*, 2015; Field *et al.*, 2017b; Zhang *et al.*, 2018).

To assess the effect of aftershocks triggered by megathrust subduction earthquakes on seismic hazard and risk analysis, Zhang *et al.* (2018) developed a new simulation framework for spatiotemporal seismic hazard and risk assessment of M9.0 earthquake sequences. They built a new spatially anisotropic aftershock kernel and combined a simulated 2D mainshock rupture plane from a rupture scaling law (e.g., Thingbaijam *et al.* (2017)) with a power law beyond the rupture in the Epidemic Type Aftershock Sequence (ETAS) simulation. A case study of the 2011 Tohoku sequence showed that synthetic catalogues compared well with observations. To provide seismic hazard and risk information in other subduction zones, however, we need to assess the variability of ETAS model parameters in different subduction zones. This is particularly important for the regions where major earthquakes are anticipated in the future but few or none have been observed, such as in the Mentawai subduction zone in Indonesia (Natawidjaja *et al.*, 2006) and the Cascadia subduction zone in North America (Wang and Tréhu, 2016).

Given a sufficiently complete and long earthquake catalogue, one might expect the variability of ETAS parameters is insignificant across different subduction-zone regions. The ETAS model synthesises different empirical ‘laws’ of seismicity, including the Gutenberg-Richter law, the Omori-Utsu law, and the Utsu-Seki law, which are universally observed and appear robust. A single set of the ETAS parameters might be sufficient for forecasting spatiotemporal earthquake sequences in subduction zones globally for hazard purposes.

Prior research has mostly focused on ETAS parameter variations in different tectonic settings. Chu *et al.* (2011) found that the ETAS parameters vary across different tectonic settings, but interpreted these differences as a result solely of different absolute seismicity rates rather than necessary differences in clustering properties across zones. Similarly, Page *et al.* (2016) investigated the spatial variation of the aftershock productivity in different tectonic regions and concluded that the variability of aftershock productivity in the same tectonic region is less than the variability across different tectonic regions. Utsu *et al.* (1995) reviewed *p*-value variations with tectonic conditions, including stress, heat flow, temperature, etc. Heat flow appears broadly stable across different subduction zones (Zaliapin and Ben-Zion, 2016), so the *p*-values might also be stable. Narteau *et al.* (2009) found that the *c*-value in Omori's law depends on fault type and possibly differential stress, indicating that thrust events have smaller *c*-values than normal and strike-slip events. On the other hand, some studies that focused on individual sequences suggested a regional dependence of the Gutenberg-Richter law and the Omori-Utsu law (Utsu *et al.*, 1995; Shcherbakov *et al.*, 2013; Wetzler *et al.*, 2016). Substantial variations of the ETAS parameters have been reported in different regions from sequence to sequence (e.g., Kumazawa *et al.*, 2014; Nicolis *et al.*, 2015; Zakharova *et al.*, 2017). Currently, whether ETAS parameters vary significantly in time or space in subduction zones remains unclear.

Past studies used different versions of the ETAS models calibrated to different catalogues (e.g., global (Chu *et al.*, 2011; Bansal and Ogata, 2013) or local (Nicolis *et al.*, 2015)) to characterise the occurrence and triggering of earthquakes in subduction zones. Because of differences of the catalogues' quality and spatiotemporal data windows, the magnitude completeness (M_c) significantly differs across regions. Sornette and Werner (2005a) argued that ETAS parameters change with completeness magnitude, implying that parameter comparisons should be made at the same completeness magnitude. In addition, different

formulations of ETAS models can lead to different ETAS parameters. Therefore, it is difficult to compare ETAS parameters from the literature. For example, Chu *et al.* (2011) estimated ETAS parameters from the NEIC catalogue with cut-off magnitude (M_{cut}) =5.0 in different tectonic zones. Bansal and Ogata (2013) applied the ETAS model using the NEIC catalogue with M_{cut}=4.7 to assess the change of seismicity rates before the 2004 Aceh-Andaman earthquake. Nicolis *et al.* (2015) investigated the change of seismicity rates in Chile from 2007 to 2014 using the local Chilean catalogue with M_{cut}=3.0, during which two major subduction earthquake sequences occurred (i.e., the 2010 Maule and 2014 Iquique earthquakes). To have a fair comparison and investigate the change of the ETAS parameters in different subduction-zone regions, the sub-catalogue for the parameter estimation should be processed in a consistent way across different regions.

This chapter assesses patterns of the ETAS parameters by focusing on zones that experienced subduction-zone M≥7.5 earthquakes. We investigate whether ETAS parameters depend on the magnitudes and/or locations of the largest earthquakes. In addition, some megathrust events occurred nearby within the same subduction zone (e.g., the 2010 Maule and 2015 Illapel earthquakes), providing an opportunity to investigate the effect of multiple megathrust subduction earthquakes in the same subduction zone on the ETAS parameters. After examining the variability of the ETAS parameters, we propose a representative set of global M9.0 subduction-zone ETAS parameters for the purpose of mainshock-aftershock sequence hazard and risk assessments. The parameter choices take into account known parameter biases resulting from the assumption of isotropic distributions of aftershocks in the ETAS parameter estimation.

The objectives of this study are three-fold:

(1) To assess the variability of earthquake clustering statistics across subduction zones, characterised in terms of productivity, temporal, and spatial parameters of the ETAS model.

(2) To evaluate the effect of multiple subduction earthquake sequences on the variability of the ETAS parameters by focusing on regions where multiple large (M≥8.3) events occurred recently (e.g., Western Indonesia, Chile, and Eastern Japan).

(3) To develop a global M9.0-class ETAS simulation framework. We demonstrate its applicability by comparing observed and synthetic aftershocks of the 2004 Aceh-Andaman earthquake, the 2010 Maule earthquake, and the 2011 Tohoku earthquake.

3.2 ETAS model

3.2.1 ETAS parameter estimation

The ETAS parameters are obtained via the maximum likelihood estimation (see **Section 2.4**). To estimate the parameters of the ETAS model reliably for global subduction zones, the input earthquake catalogue needs to be complete and homogeneous over an appropriate target window. The target window specifies a range of space, time, and magnitude to filter seismic events. However, some events outside the target window may trigger seismic events in the target window. Therefore, an auxiliary window is often introduced to reduce the bias (Wang *et al.*, 2010). To process the data consistently, the following procedure is implemented to identify the spatial auxiliary and target windows:

1. The spatial target window is considered as the rupture area of the subduction mainshock with a 50% extension on each side, i.e. the spatial target window is twice as large as the rupture length and width, as suggested by Kagan (2004).
2. The spatial auxiliary window is 30% larger than the spatial target window on each side.

3. Events with depths less than 100 km are considered to include crustal and subduction earthquakes and exclude major intra-slab earthquakes.

The relatively large spatial windows that are twice as large as the rupture length suggested by Kagan (2002, 2004), partially as a result of the large location errors in global catalogues (Kagan, 2004). The spatial selection approach by Kagan (2002) was also tested and used by others (Shcherbakov *et al.*, 2004; Nanjo *et al.*, 2007). Since the rupture models of recent megathrust events are available (Mai and Thingbaijam, 2014), the rupture dimensions are taken from the rupture models rather than the scaling law of Kagan (2002).

Table 3-1 summarises three cases of temporal windows to investigate the triggering characteristics in subduction zones of a variety of sequences of different magnitudes estimated over (1) long time periods and (2) short time periods (individual sequences):

- Case 1: To investigate whether ETAS parameters vary systematically across regions or with maximum magnitudes in a region, we use a long temporal window between 1981 and 2017, of which the first five years are considered as the auxiliary window.
- Case 2: Because the poor assumption of an isotropic spatial aftershock distribution in **Equation (2-4)** is known to bias K_0 and α (Hainzl *et al.*, 2013), we fix α=2.3 in Case 2 and re-estimate parameters, following Seif *et al.* (2017). The same sub-catalogues are used as in Case 1.
- Case 3: To assess whether ETAS parameters vary among individual sequences, we estimate parameters over shorter time periods that increase with the magnitude of the largest earthquake. For mainshocks with $7.5 \leq M < 8.0$, the temporal auxiliary and target windows are set to 0.5 and 1 year, respectively. For $8.1 \leq M < 8.7$, the temporal auxiliary and target windows are 1 and 2 years, respectively, whereas for $M \geq 8.7$ the temporal auxiliary and target windows are 2 and 4 years, respectively. These target windows of 1, 2, and 4 years cover 91%, 93%, and 94% of the total rate for a single generation of

triggered events, respectively, assuming a typical Omori law with p = 1.28 and c = 0.05 (Zhang *et al.*, 2018).

Table 3-1. Summary of three cases of temporal auxiliary and target windows.

Cases 1 and 2		Case 3 (individual sequences of triggered events are analysed)					
		7.5≤M<8		8.1≤M<8.7		M≥8.7	
Auxiliary window	Target window	Auxiliary window	Target window	Auxiliary window	Target window	Auxiliary window	Target window
5 years	31 years	0.5 year	1 year	1 year	2 years	2 years	4 years

3.2.2 ETAS residual analysis

Residual analysis (Ogata, 1988; Werner, 2007; Harte, 2012; Kumazawa *et al.*, 2014; Lombardi, 2017a) is a useful tool for checking the goodness-of-fit of the ETAS model to an earthquake catalogue. A transformed time sequence τ_i is calculated as:

$$\tau_i = \int\int_S \int_0^{t_i} \lambda(t,x,y)dt\,dx\,dy \quad (3\text{-}1)$$

which is the integral of the conditional intensity function (λ) from 0 to t_i (time of the ith event in **Equation (2-5)**) in the region S. The transformed time follows a stationary Poisson process with unit rate if the ETAS model fits the catalogue well (Ogata, 1988). The goodness-of-fit assessment is based on the expectation that a well-calibrated conditional intensity function should integrate to the observed number of events, i.e. the integral of λ to the ith event should equal i (within fluctuations of a Poisson process). Significant deviations from the unit rate beyond the expected randomness of a unit-rate Poisson process indicate that either too few or too many events are occurring with respect to the model's anticipated rate. We use residual analysis as a visual quality check to gauge the model fit, noting however that our purpose is the stochastic simulation of aftershocks and its application to hazard, rather than strict hypothesis testing.

3.3 Data

3.3.1 Earthquake catalogues of global M≥7.5 subduction earthquakes

To compare the ETAS parameters from different regions in a consistent way, the NEIC catalogue is used for all parameter estimations. The NEIC has been used in several global studies of aftershock statistics (e.g. Kagan, 2004; Shcherbakov *et al.*, 2013; Page *et al.*, 2016). In response to improved detection capability, the IASPEI Seismic Format was introduced to the NEIC catalogue in January 1999 (Storchak *et al.*, 2003) and we therefore select global megathrust subduction earthquakes from 1999 to 2017 to obtain reasonably complete sub-catalogues of aftershocks. These are summarised in **Table 3-2** together with source information from Hayes *et al.* (2017). The majority of events listed in **Table 3-2** are thrust subduction events with dip angles of less than 30º. The global subduction catalogues also include oblique reverse events with considerable components of thrust that occurred on plate boundaries (Events 23, 26, and 28 in Western Indonesia, Philippines, and North America, respectively) (Ye *et al.*, 2012; Kao *et al.*, 2015). In particular, we included Event 28 (the 2012 M7.8 Haida Gwaii event) in Western Canada, which Hyndman (2015) concluded to be a megathrust event and is the largest thrust event ever recorded near the North Cascadia subduction zone (Bird and Lamontagne, 2015). The index number of each event is shown in the first column of **Table 3-2**. Mainshock rupture models are adopted from the SRCMOD database (Mai and Thingbaijam, 2014). Because rupture models of some M7.5-8.0 earthquakes are not available in SRCMOD, these are collected from the U.S. Geological Survey (USGS). The difference of the M7.5-8.0-class mainshock rupture models from the SRCMOD database and the USGS is insignificant. Therefore, we use the mainshock rupture models from different sources depending on the availability. **Table 3-2** also lists the effective length and width of each slip model which we calculated using autocorrelation widths following Thingbaijam and Mai (2016). **Figure 3-1** shows the locations of the megathrust events classified by regions.

Table 3-2. Summary of the selected large subduction earthquakes.

Earthquake catalogue								Mainshock rupture model			Long time windows- Cases 1 and 2 from Table 3-1.			Subduction sequences - Case 3 from Table 3-1.		
Index	Date/Time (UTC)	**M**	Region	Faulting style	Latitude º	Longitude º	Depth (km)	Reference	Effective length (km)	Effective Width (km)	M_c	*b*-value	Number of events M⩾ 4.5	M_c	*b*-value	Number of events **M**⩾4.5
1	11/16/2000 07:42	7.8	Papua New Guinea	Reverse (thrust)	-5.23	153.1	30	USGS	108	100	4.5	0.95±0.016	3105	4.6	0.96±0.043	567
2	11/17/2000 21:01	7.8	Papua New Guinea	Reverse (thrust)	-5.5	151.78	33	USGS	132	87.6	4.5	0.95±0.015	3465	4.6	0.93±0.042	543
3	06/23/2001 20:33	8.4	Peru	Reverse (thrust)	-16.27	-73.64	33	USGS	252	208	4.9	1.10±0.050	1215	4.6	0.96±0.058	299
4	07/07/2001 09:38	7.6	Peru	Reverse (thrust)	-17.54	-72.08	33	USGS	140	91.8	4.9	1.21±0.083	479	4.7	1.15±0.101	182
5	03/05/2002 21:16	7.5	Philippines	Reverse (thrust)	6.03	124.25	31	USGS	105	98	4.4	0.99±0.047	322	4.3	1.04±0.121	58
6	01/22/2003 02:06	7.6	Mexico	Reverse (thrust)	18.77	–104.10	24	Yagi *et al.*, 2004	70	85	3.9	0.88±0.047	94	4	1.20±0.281	8
7	09/25/2003 19:50	8.3	Japan	Reverse (thrust)	41.82	143.91	27	Koketsu *et al.*, 2004	120	100	4.6	1.00±0.028	1391	4.4	0.80±0.043	269
8	11/17/2003 06:43	7.8	Alaska	Reverse (thrust)	51.15	178.65	33	USGS	132	140.4	4.5	0.90±0.025	1212	4.1	0.91±0.056	116
9	11/11/2004 21:26	7.5	Indonesia	Reverse (thrust)	–8.15	124.87	10	USGS	84	72.8	4.4	0.95±0.047	329	4.3	0.97±0.074	111
10	12/26/2004 0:58	9.0	Indonesia	Reverse (thrust)	3.3	95.98	30	Rhie *et al.*, 2007	970	200	4.5	1.11±0.015	5526	4.5	1.12±0.019	3298
11	03/28/2005 16:09	8.6	Indonesia	Reverse (thrust)	2.09	97.11	30	CALTECH‡	380	192	4.5	1.11±0.017	4275	4.5	1.21±0.027	2077
12	7/17/2006 8:19	7.7	Indonesia	Reverse (thrust)	–9.28	107.42	20	Yagi and Fukahata, 2011	220	140	4.7	1.18±0.041	1089	4.8	1.38±0.103	348
13	11/15/2006 11:14	8.3	Kuril Islands	Reverse (thrust)	46.59	153.27	10	Lay *et al.*, 2009	240	100	4.6	1.14±0.021	3279	4.5	1.21±0.036	1077
14	1/21/2007 11:27	7.5	Indonesia	Reverse (thrust)	1.07	126.28	22	USGS	165	56.32	4.6	1.03±0.018	3119	4.6	1.08±0.061	345
15	04/01/2007 20:39	8.1	Solomon Islands	Reverse (thrust)	–8.47	157.04	24	CALTECH	285	80	4.5	0.92±0.015	3408	4.6	1.02±0.045	593
16	8/15/2007 23:40	8	Peru	Reverse (thrust)	–13.39	–76.60	39	CALTECH	168	160	4.4	0.89±0.034	509	4.2	0.75±0.051	112
17	09/12/2007 11:10	8.5	Indonesia	Reverse (thrust)	–4.44	101.37	34	CALTECH	342	208	4.7	1.05±0.022	3149	4.4	0.82±0.027	634
18	11/14/2007 15:40	7.7	Chile	Reverse (thrust)	–22.25	–69.89	40	Béjar-Pizarro *et al.*, 2010	210	98	4.2	0.76±0.016	1145	5.2	0.75±0.132	115

‡California Institute of Technology

19	01/03/2009 19:43	7.7	Indonesia	Reverse (thrust)	–0.41	132.89	17	USGS	96	78	4.5	0.99±0.052	329	4.6	1.10±0.100	173
20	07/15/2009 9:22	7.8	New Zealand	Reverse (thrust)	–45.76	166.56	12	USGS	88	72	4.2	0.93±0.042	269	4.5	1.16±0.114	118
21	02/27/2010 6:34	8.8	Chile	Reverse (thrust)	–36.12	–72.90	23	Luttrell *et al.*, 2011	520	177.3	4.3	0.97±0.012	4285	4.6	1.10±0.029	1737
22	04/06/2010 22:15	7.8	Indonesia	Reverse (thrust)	2.38	97.05	31	USGS	144	156	5.3	0.88±0.069	2008	4.1	0.78±0.057	85
23	06/12/2010 19:26	7.5	Indonesia	Oblique Reverse	7.88	91.94	35	USGS	78	58	4.2	0.87±0.049	157	4.5	1.05±0.201	40
24	10/25/2010 14:42	7.8	Indonesia	Reverse (thrust)	–3.49	100.08	20	USGS	195	140	4.6	0.99±0.028	1579	4.5	1.12±0.088	175
25	03/11/2011 05:46	9	Japan	Reverse (thrust)	38.3	142.37	29	Wei *et al.*, 2012	450	200	4.5	1.08±0.010	10519	5	1.05±0.032	5022
26	8/31/2012 12:47	7.6	Philippines	Oblique Reverse	10.81	126.64	28	USGS	72	66	4.7	1.40±0.057	897	4.4	1.12±0.066	236
27	09/05/2012 14:42	7.6	Costa Rica	Reverse (thrust)	10.09	–85.32	35	USGS	110	88	4.8	0.80±0.060	379	4.3	1.17±0.220	32
28	10/28/2012 3:04	7.8	BC, Canada	Oblique Reverse	52.79	–132.10	14	Lay *et al.*, 2013	144	54	4	0.76±0.036	171	4	0.87±0.060	80
29	02/06/2013 01:12	8	Solomon Islands	Reverse (thrust)	–10.80	165.11	24	USGS	221	143	4.5	0.87±0.014	3155	4.6	1.02±0.039	723
30	04/01/2014 23:46	8.2	Chile	Reverse (thrust)	–19.61	–70.77	25	CALTECH	240	160	4.8	1.03±0.038	1313	4.4	0.95±0.043	409
31	4/19/2014 13:28	7.5	Papua New Guinea	Reverse (thrust)	–6.75	155.02	44	USGS	56	68	4.5	0.95±0.025	1267	4.4	1.06±0.050	356
32	3/29/2015 23:48	7.5	Papua New Guinea	Reverse (thrust)	–4.73	152.56	41	USGS	132	102	4.5	0.95±0.016	3441	4.3	0.98±0.041	343
33	05/05/2015 01:44	7.5	Papua New Guinea	Reverse (thrust)	–5.46	151.88	55	USGS	110	110	4.5	0.95±0.015	3375	4.6	1.07±0.070	316
34	9/16/2015 22:54	8.3	Chile	Reverse (thrust)	–31.57	–71.67	22	USGS	216	140.8	4.2	0.97±0.014	2421	4.2	1.00±0.029	623
35	04/16/2016 23:58	7.8	Ecuador	Reverse (thrust)	0.38	-79.92	20	USGS	154	140	5.4	0.81±0.113	262	4.1	0.70±0.055	79
36	12/25/2016 14:22	7.6	Chile	Reverse (thrust)	-43.41	-73.94	38	USGS	96	56	4	0.76±0.102	24	4.1	0.99±0.273	11

To ensure that ETAS parameter variations do not simply reflect differences in the quality of a catalogue, the sub-catalogues need to be homogeneous. The results of M_c and *b*-value estimation (Shi and Bolt, 1982; Marzocchi and Sandri, 2003; Woessner and Wiemer, 2005), and the number of events M≥4.5 for Cases 1 and 2 (**Table 3-1**) are shown in **Table 3-2**. To ensure that parameter estimates are reliable and comparable, the sub-catalogues with higher bulk completeness threshold M_c>4.5 and those with less than 100 events above M4.5 are excluded. This leaves 21, 21, and 16 sub-catalogues for Cases 1, 2, and 3, respectively. Some space-time volumes in **Table 3-2** do not have a sufficient number of events, because their numbers vary with target window size (scaled by the largest earthquake size), aftershock productivity, background rate, missing early aftershocks, and possibly offshore completeness variations.

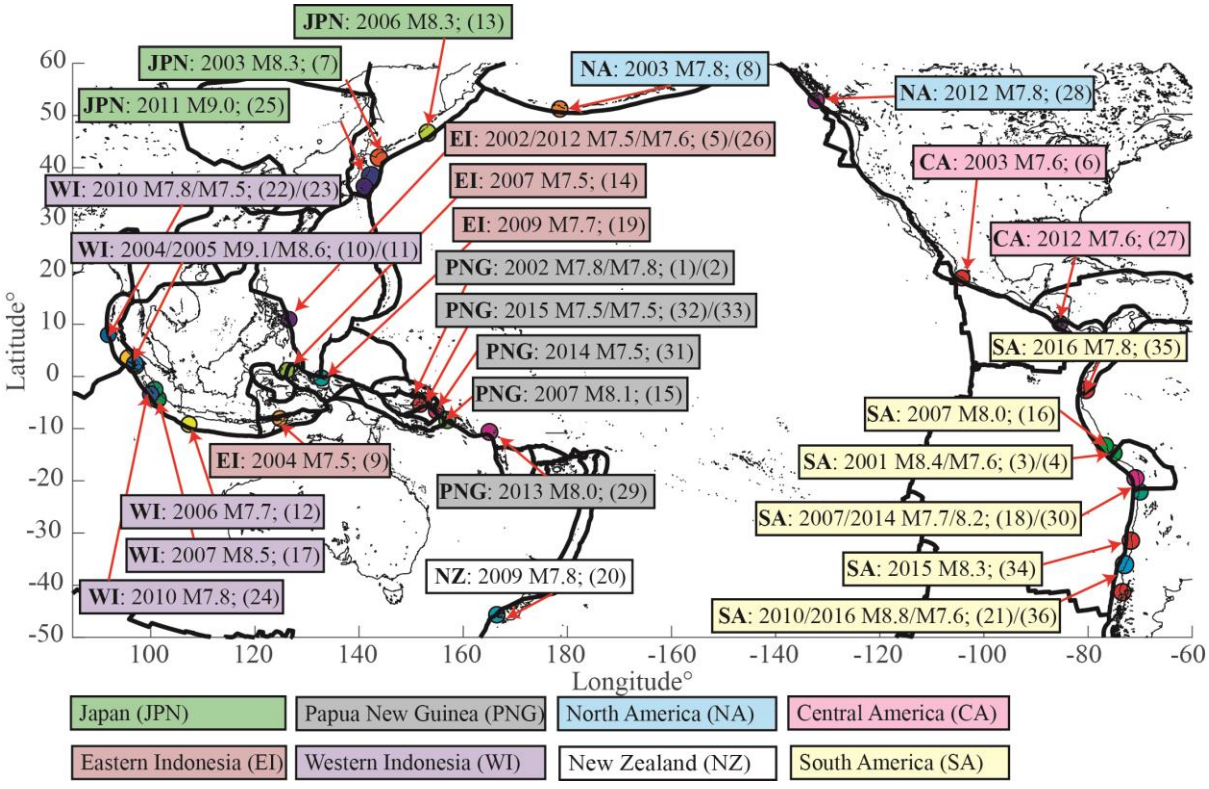

Figure 3-1. Map of earthquake locations with M≥7.5. Earthquakes are grouped by regions, which are Japan (JPN), Eastern Indonesia (EI), Papua New Guinea (PNG), Western Indonesia

(WI), New Zealand (NZ), North America (NA), Central America (CA), and South America (SA). The numbers in parentheses correspond to the indices in **Table 3-2**.

The effective rupture length and width of each event in **Table 3-2** are compared with the length-width scaling relationships by Thingbaijam *et al.* (2017) in **Appendix C**. We will use this scaling law (and its prescribed uncertainty) to simulate the variability of the anisotropic mainshock rupture dimension in **Section 3.5.2**. The observation from **Appendix C** suggests that the scaling law from Thingbaijam *et al.* (2017) can be used to simulate the mainshock rupture planes of M8.0-9.0 events in the ETAS simulation framework, and that predicted widths/lengths of M7.5-M7.9 earthquakes might need a slightly larger standard deviation to capture the observed variability.

3.4 Comparison of ETAS parameters by region and magnitude

This section discusses the productivity parameters (K_0 and α), temporal parameters (c and p), and spatial parameters (γ, d and q) of the ETAS model and their variability within global subduction regions. All ETAS parameters are classified according to regions and the largest magnitudes to investigate any systematic changes for Cases 1-3 shown in **Table 3-1** (Case 1: longer catalogues with free α, Case 2: longer catalogues with fixed α, and Case 3: individual sequences with free α). Regional classification is solely based on geographical proximity, which is shown in **Figure 3-1**. To show robust estimates from different cases, we only present the ETAS parameter results with $q < 4$ and $d < 500$ from Cases 1-3. Unusually large q and d values indicate insufficient data with distance to fit the spatial power law robustly (Seif *et al.*, 2017). This leads to 18, 18, and 10 parameter sets for Cases 1, 2, and 3, respectively.

In the following, we first present the ETAS parameter results of Case 1 based on long-time catalogues. To dismiss the bias of the isotropic spatial distribution to the productivity parameters, Case 2 re-estimates the ETAS parameters using the same catalogues as Case 1 with fixed α. The residual analysis of Cases 1 and 2 is also compared (Full results are available in

Appendix D). The ETAS parameters from Case 3 are estimated based on the temporal target windows of individual sequences as defined in **Table 3-1**.

In each case, we compare the estimated ETAS parameters with the literature and explain possible reasons for bias in the ETAS parameters. To compare the ETAS parameters quantitatively, we calculate the median ETAS parameters and their standard errors across different regions. We also quantify the dependence of the ETAS parameters on the largest magnitude and rupture dimensions using a test of correlation (e.g., Luco *et al.*, 2002). At the end of each subsection, we quantify the variability of the ETAS parameters of each case to infer the robustness of the estimate values.

3.4.1 Case 1 - Long time period catalogues

3.4.1.1 *Regional dependence of ETAS parameters in Case 1*

Figure 3-2 shows the ETAS parameter results of Case 1 classified by region. From previous studies, we expect K_0 and α values to lie in the range 0.006-0.8 and 1.1-2.3, respectively (Ogata and Zhuang, 2006; Seif *et al.*, 2017; Zhang *et al.*, 2018). Several lines of credible evidence advocate that α should equal 2.3, which corresponds to $\alpha = b \ln 10$ with b=1.0 (Helmstetter *et al.*, 2005, 2006; Hainzl *et al.*, 2008; Seif *et al.*, 2017). We observe, however, a broad range of K_0 and α values, which we ascribe to two known effects. First, these two productivity parameters are anti-correlated, because of the mathematical formulation of the model (Sornette and Werner, 2005b; Lombardi, 2017b). Second, since the modelled spatial aftershock distribution is isotropic, while observed aftershocks distribute anisotropically, α is underestimated and K_0 is overestimated (Hainzl *et al.*, 2008; Seif *et al.*, 2017). An example of this bias arises for Event 10 (the M9.1 2004 Aceh-Andaman earthquake), whose rupture length (970 km) is much larger than its rupture width (200 km) (see **Table 3-2** and **Figure C-1**(a) and (b)), while its α value is the smallest of all sub-catalogues and its K_0 is the second highest.

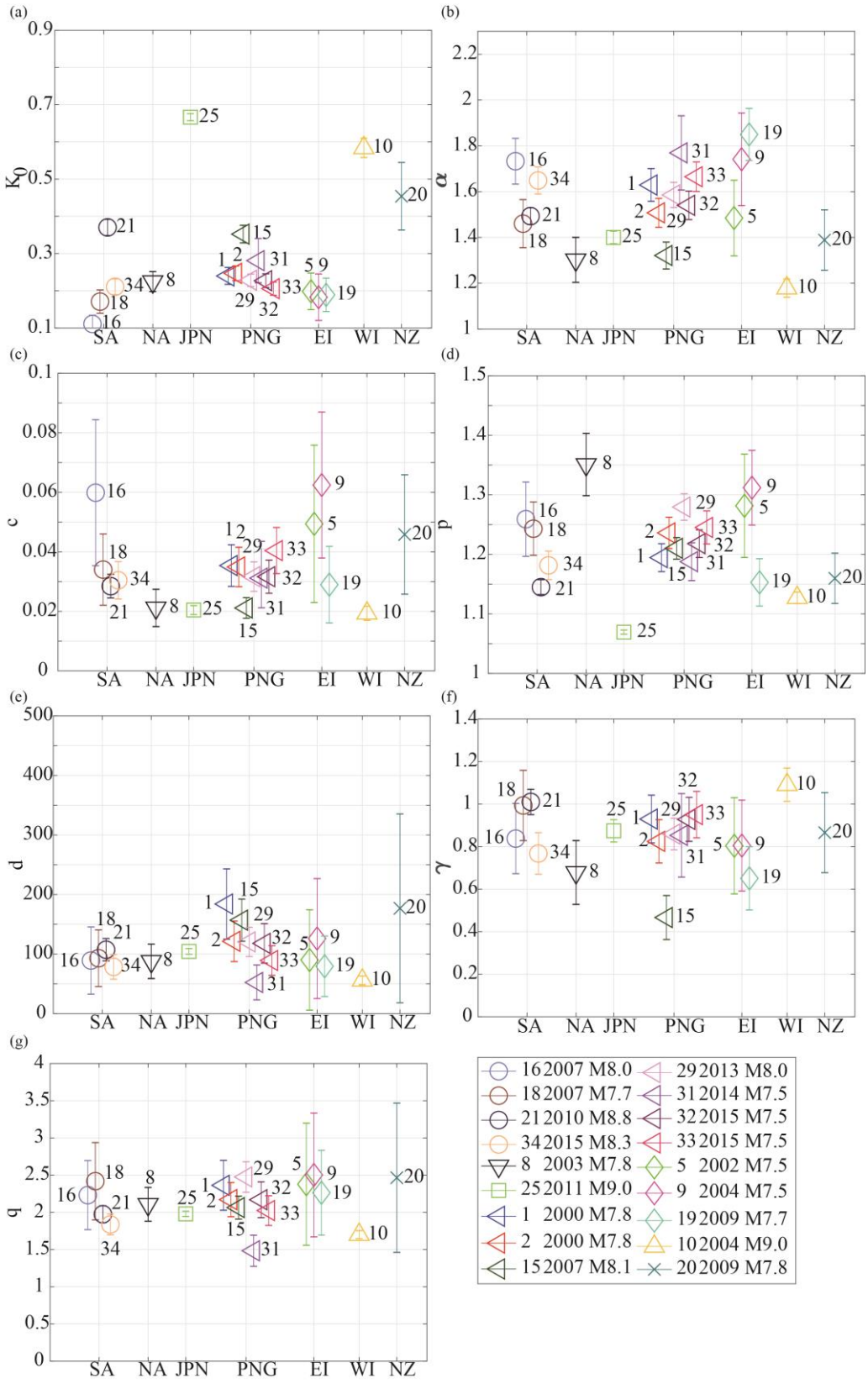

Figure 3-2. ETAS parameter estimates classified by region for Case 1 based on long-time catalogues with free α (SA: South America, NA: North America, JPN: Japan, PNG: Papua New Guinea, EI: Eastern Indonesia, WI: Western Indonesia, and NZ: New Zealand).

To further investigate the relationship between the productivity parameters and the anisotropy of large earthquake sequences, **Figure 3-3** shows a plot of α against K_0. An inverse relationship between α and K_0 can be observed in **Figure 3-3**, as expected from Sornette and Werner (2005b). The ratio of the effective rupture length and width of the mainshock is colour-coded for each sub-catalogue. A large length-to-width (L/W) ratio indicates the anisotropy of aftershock sequences, which could bias the productivity parameters (Hainzl *et al.*, 2008). For example, in **Figure 3-3** four out of five sub-catalogues have K_0 values larger than 0.3 and moderate to large L/W ratios (L/W ratios>2.5) including all M9.0 class events. Except for Event 20 (the 2009 New Zealand earthquake), all the events with L/W ratios<1.5 have K_0 values less than 0.3. We further looked at the sub-catalogue of Event 20 in New Zealand. Multiple M7.0 thrust events were recorded in the South Island of New Zealand including the 1993 M7.0 and 2003 M7.2 events, which might have an impact on the ETAS parameter estimation of Event 20. To reduce the bias due to the isotropic model, α will be fixed in Case 2 based on long-time catalogues and further discussion will be given in **Section 3.4.2**.

Typical ranges of *p* and *c*-values from the long-time catalogue for the Tohoku region are 1.05-1.16 and 0.0215-0.0245, respectively (Ogata and Zhuang, 2006; Zhang *et al.*, 2018). These temporal parameters are also known to be subject to potential bias due to a small sample size of early aftershocks in the sub-catalogue that leads to a large *c*-value (Hainzl, 2016; Seif *et al.*, 2017). The four largest *c*-values with greater uncertainties shown in **Figure 3-2**(c) correspond to Events 5, 9, 16 and 20 with relatively small numbers of events (322, 329, 509, and 269) in Philippines, Indonesia, Peru, and New Zealand, respectively. This highlights the difficulty to estimate *c* with a smaller number of events. In **Figure 3-2**(c) and (d), the *c*- and *p*-values of M9-class Events 10, 21, and 25 are robust and consistent with those found by Zhang *et al.* (2018). The small to moderate variations of the temporal parameters appear consistent

with under-sampling and missing early aftershocks in the sub-catalogues of the M7.5-8.5 events.

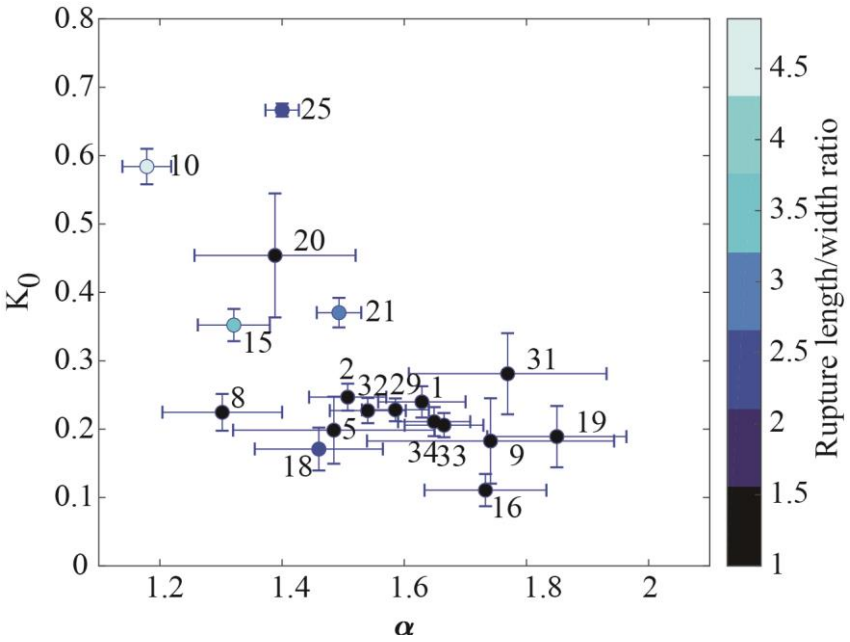

Figure 3-3. Anti-correlation between estimated K_0 and α parameters, colour-coded by the ratios of rupture length to width of the largest earthquakes within the sub-catalogues.

Typical ranges of spatial parameters from recent studies (e.g., Ogata and Zhuang, 2006; Seif *et al.*, 2017; Zhang *et al.*, 2018) are d = 7.89-29.92, γ = 1.32-1.69, and q = 1.59-2.13. γ and d define the scaling of spatial aftershock distributions with mainshock magnitude. A large γ value (e.g., $\gamma > 1.5$) reflects a better fit for the isotropic power law of the ETAS model. Assuming constant stress drop for different earthquakes, several studies argued γ should equal ln(10) = 2.3, such that ruptures scale according to $e^{0.5\log(10)\cdot M}$ (Helmstetter *et al.*, 2005; Seif *et al.*, 2017). Similarly to K_0 and α in the productivity term, γ and d values are also anti-correlated due to the mathematical formulation of the isotropic spatial distribution. q describes the aftershock decay in the far field. A large q indicates a fast decay due to the limited number of events outside the mainshock rupture plane (Seif *et al.*, 2017). In **Figure 3-2**(e), d-values are

larger than the observed ranges (7.89-29.92) from the literature. On the other hand, the γ values are systematically lower than expected in **Figure 3-2**(f), only Events 10, 18, and 21 in Indonesia and Chile have γ values greater than 1. This can be explained by a lack of early aftershocks, resulting in overestimated d and underestimated γ-values (Seif *et al.*, 2017). The q-values range between 1.6-2.4 in **Figure 3-2**(g). Considering the uncertainty this is consistent with results by Ogata and Zhuang (2006) and Zhang *et al.* (2018).

To quantify the change of the ETAS parameters across regions, boxplots of the ETAS parameters in each region and the detailed calculation of the total standard error of each parameter for the boxplots are provided in **Appendix E**. Due to a small number of sub-catalogues in North America, Japan, Eastern Indonesia, Western Indonesia, and New Zealand, the variability of the parameters in these regions might be affected by the number of events associated with the maximum magnitude. The differences between the maximum observed magnitudes ($7.5 \leq M \leq 9.0$) and M_{cut} lead to significantly different numbers of events in the target windows. We therefore focus on the boxplots of Papua New Guinea (8 sub-catalogues with M from 7.7 to 8.8) and South America (4 sub-catalogues with M from 7.5-8.1) given their larger number of sub-catalogues and wider magnitude ranges. Considering the medians and interquartile ranges, we see little evidence for systematic parameter differences between Papua New Guinea and South America. We interpret individual parameter variations as due to different largest magnitudes in the same region and the known biases due to the model formulation. In summary, we do not observe a clear dependence of ETAS parameters on regions in Case 1.

3.4.1.2 *Magnitude dependence of ETAS parameters in Case 1*

To assess the dependence of the ETAS parameters on the magnitudes of the largest earthquakes within the sub-catalogues, the estimated parameters of Case 1 are grouped by the largest

magnitudes in **Appendix E**. We observe that except for the productivity parameters which are biased by the model formulation and anisotropy of aftershocks, temporal and spatial parameters of M9.0 events are robust across different subduction zones with small standard errors. The parameters of sub-catalogues of M7.5-8.5 events vary more than those of M9.0 events with greater errors.

To quantify the dependence of the ETAS parameters on magnitude, rupture length, rupture width, and rupture area, we employ the p_{lm} value from a linear regression of the ETAS parameters with these mainshock characteristics. When the p_{lm} value of the slope coefficient of the linear regression is lower than a significance level of 0.01, the ETAS parameter is considered to be dependent on the variable in this study. In addition, given that multiple tests of each ETAS parameter are carried out, the p_{lm} value is adjusted by the Bonferroni correction. The sign of the significance level of p_{lm} values is also included to show the correlation between the ETAS parameters and these mainshock characteristics. The result of the p_{lm} values from 18 robust ETAS estimates is shown in **Table 3-3**. Considering that the scaling law of rupture dimensions (e.g., Thingbaijam *et al.* 2017) is a log-linear relationship between the logarithm of rupture dimensions and magnitude, we assess the p_{lm} values of α and γ with the logarithm of rupture dimensions, as shown in **Table 3-3**.

Table 3-3. Summary of the p_{lm} values of ETAS parameters for Case 1 (bold indicates statistically significant dependency and the "+" sign of the p_{lm} values indicates the correlation between the ETAS parameters and the earthquake characteristics).

	K_0	α	c	p	d	γ	q
Magnitude	**+0.0011**	0.1284	0.1127	0.0132	1.0000	1.0000	0.3666
Rupture length	**+0.0046**	0.0231	0.1380	0.1057	0.9865	0.8686	0.2500
Rupture width	0.1417	0.4251	0.6898	0.6041	0.8728	0.4162	0.9735
Rupture area	**+0.0035**	0.1761	0.2258	0.0936	0.7153	0.2788	0.2282

In **Table 3-3**, K_0 shows dependence on magnitude, rupture length, and rupture area of the largest earthquake in the sub-catalogues. K_0 grows with the magnitude, rupture length, and rupture area of the largest earthquake. The dependence of K_0 on magnitude and rupture dimensions might reflect the known bias from the isotropic spatial distribution, because the two largest K_0 are from two M9.0-class events with large rupture lengths and areas (Events 10 and 25 in Western Indonesia and Japan).

Overall, ETAS parameter results grouped by regions and magnitudes suggest: (1) the estimated values of K_0 and α are biased due to the anti-correlation of the productivity parameters and the isotropic spatial distribution in the ETAS parameter estimation; (2) sample size fluctuations due to varying target windows and high M_{cut} impact the *c*-value; (3) the median ETAS parameters of Papua New Guinea and South America are similar, which seems robust given the larger sample sizes and wider magnitude bins here than in other regions; (4) temporal parameters from Case 1 are consistent with observations from other studies. Although spatial parameters from Case 1 exhibit less variability, we believe γ- and *d*- values from Case 1 are biased as suggested by other researchers.

3.4.2 Case 2 - Long time period Catalogues with fixed α

To reduce the bias of the productivity parameters due to the isotropic spatial distribution, a viable solution is to re-estimate ETAS parameters with fixed α = 2.3 (Helmstetter *et al.*, 2006; Hainzl *et al.*, 2013). The fixed α corresponds to *b*-value = 1 assuming the magnitude frequency distribution is independent of the mainshock magnitude (Felzer *et al.*, 2004). Recent studies have investigated ETAS parameters after α is fixed at 2.3. K_0 and *d*-values decrease, whereas the other parameters increase (Seif *et al.*, 2017; Zhang *et al.*, 2018).

This subsection investigates (1) the difference of the ETAS parameters between Case 1 with free α and Case 2 with fixed α, and (2) the variation of the ETAS parameters with regions

and the largest magnitudes in Case 2. Since Case 2 uses the same sub-catalogues as Case 1, to evaluate the goodness-of-fit of the ETAS model to the catalogues and to interpret the changes of estimates after the α-value is fixed, we first present the residual analysis and Akaike Information Criterion (AIC) of Cases 1 and 2. Next, we discuss the results of the ETAS parameters of Case 2, in comparison with those for Case 1.

3.4.2.1 *Residual analysis of Cases 1 and 2*

To assess the goodness-of-fit of the calibrated models to the catalogues, we conduct a residual analysis for the ETAS model fitting. Detailed results of Cases 1 and 2 are provided in **Appendix D**. The 99% error bound of Kolmogorov-Smirnov statistics is also included as suggested by Ogata (1988). There are four main observations. First, 8 out of 18 fitted sub-catalogues are within the 99% confidence bounds in Cases 1 and 2. The residual analysis of the other 10 sub-catalogues shows potentially significant discrepancies between the calibrated ETAS model and seismicity data, which can be related to the large mainshock-aftershock sequences and temporal fluctuations of the background seismicity in the observed catalogues (Harte, 2012; Bansal and Ogata, 2013; Hainzl *et al.*, 2013). These should be investigated further to understand how the ETAS model (or its parameter estimation) can be improved. However, statistical forecasting after a megathrust earthquake involves much greater fluctuations than in retrospective fitting, i.e. the model can still be useful for the purpose of aftershock hazard and risk analysis with appropriate consideration of the anisotropy of the aftershocks and parameter selection (e.g., Zhang *et al.* 2018).

Second, all M9-class sub-catalogue analyses are outside the 99% confidence bounds during the mainshock-aftershock sequences for both Cases 1 and 2 and thus fail the formal residual analysis test. This might show that the spatial and temporal characteristics of the M9-class event sub-catalogues are different from the ETAS model with an isotropic spatial distribution. The model tends to underpredict the aftershock productivity of large earthquakes,

as expected in Case 1 when the α-value is biased towards small values because of anisotropic aftershock distributions. Similar observations were reported by Harte (2012) and Kumazawa *et al.* (2014).

Third, by fixing α in Case 2 improvements in fitting mainshock-aftershock sequences can only be observed for some sub-catalogues (Events 5, 16, and 34), while no significant changes are seen for other sub-catalogues. Events with better fitting are all M8-class events from South America and Eastern Indonesia. This suggests that effects other than the isotropic assumption might affect the residual fitting, e.g., the stochastic declustering.

Fourth, the number of background events of Case 1 is systematically smaller than in Case 2 with fixed α. In other words, a smaller number of events are defined as triggered events by the stochastic declustering in Case 2 than in Case 1. This might result from a combined effect of the isotropic spatial aftershock distribution and the stochastic declustering.

We also compare the log-likelihood values and AIC of Case 1 with Case 2 (see **Table D-1** in **Appendix D**). Case 1 with an additional free parameter α has a better performance than Case 2 in terms of AIC, which is consistent with the observation from Hainzl *et al.* (2013). We emphasise that fixing α improves the aftershock productivity forecast, which is important for hazard, at the cost of a lower likelihood of retrospective data.

3.4.2.2 *ETAS parameter results of Case 2*

Because of the known bias of α, the ETAS parameters are re-estimated with α = 2.3, as recommended by Seif *et al.* (2017) and others. Similarly to Case 1, we do not observe systematic ETAS parameter variations with region, and therefore provide parameter results classified by region and the boxplots of the ETAS parameters in **Appendix E**. **Figure 3-4** shows the parameter estimates of Case 2 with fixed α classified by the largest magnitudes in sub-catalogues. To have a clear comparison between Cases 1 and 2, the former results are plotted in grey without numbering.

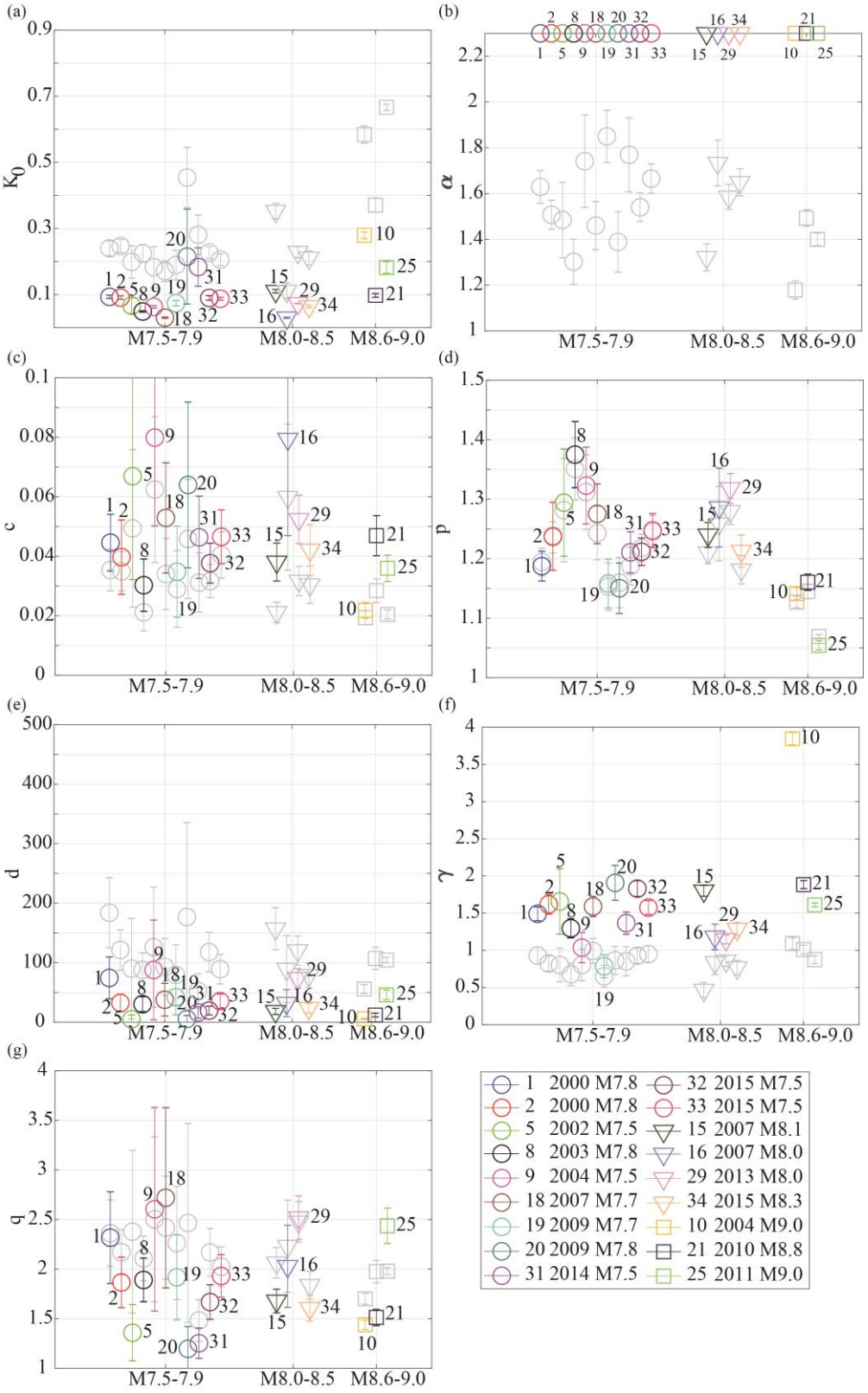

Figure 3-4. ETAS parameter results of Case 2 with fixed α classified by the largest magnitudes in sub-catalogues (ETAS parameter results of Case 1 are plotted without numbering for comparison).

In **Figure 3-4**(a), the K_0 values associated with M7.5-class sub-catalogues (Events 20 and 31 in New Zealand and Papua New Guinea) and M9-class sub-catalogues (Events 10 and 25 in Indonesia and Japan) are larger than 0.14 and 0.1, respectively, leading to supercritical processes for these sub-catalogues. The supercritical process means the average number of aftershocks per earthquake is larger than 1 (Seif *et al.*, 2017). Supercritical ETAS simulations can lead to aftershock number singularities in finite time (Helmstetter and Sornette, 2002). These K_0 estimates might be overestimated, because the cumulative number of observed events in the transformed time domain from Events 10, 20, 25, and 31 that is calculated based on the estimated ETAS parameters is larger than the theoretical number of events in the residual analysis. The rest of K_0 values are more robust than Case 1 with α free.

All *c*-values and 14 out of 18 *p*-values increase from Case 1 to Case 2, similar to results by Seif *et al.* (2017) and Zhang *et al.* (2018). This might be related to the increased background rates in Case 2. As indicated in **Section 3.4.2.1**, the total number of background events of Case 1 is systematically smaller than Case 2. Therefore, a smaller number of events are used to fit the temporal parameters in Case 2, which might lead to a quicker decay (large *p*-value) in time than Case 1. In addition, as concluded in **Section 3.4.1.1**, the *c* estimates may be biased by the sample size, therefore all *c*-values are increased in Case 2.

γ-values systematically increase in Case 2 leading to smaller *d*-values. The γ- and *d*-values from Case 2 are within the range of expected parameters from the literature (Seif *et al.*, 2017; Zhang *et al.*, 2018), reflecting a better fit with the conventional isotropic spatial distribution. An unusual γ = 3.7 of Event 10 is observed; this is larger than the maximum theoretical value γ = 2.3 discussed in **Section 3.4.1.1**. 14 out of 18 *q*-values are decreased, which is inconsistent with an increased *q*-value as reported in other studies (Seif *et al.*, 2017; Zhang *et al.*, 2018). This suggests other sources affect *q*, which could be the relatively large location errors of the global earthquake catalogues (Console *et al.*, 2003).

We evaluate the p_{lm}-value for the ETAS parameters of Case 2 from 18 estimates in **Table 3-4**. The previously observed co-dependencies on magnitude and rupture dimensions (**Table 3-3**) are not robust with the fixing α. The productivity and spatial parameters from Case 2 with fixed α are consistent with the observations from other studies and show more robust estimates than Case 1. The temporal parameters of Case 2 are also associated with relatively small variability; however, this might be due to biases by the sample size and stochastic declustering.

Table 3-4. Summary of the p_{lm} values of ETAS parameters for Case 2 (Boldface indicates significant co-dependence).

	K_0	α	c	p	d	γ	q
Magnitude	0.1724	0	0.3709	0.0429	1.0000	0.0833	1.0000
Rupture length	0.0424	0	0.2032	0.2327	0.9417	0.0124	1.0000
Rupture width	1.0000	0	1.0000	0.8790	1.0000	0.4805	1.0000
Rupture area	0.0288	0	0.2623	0.1835	1.0000	0.0414	1.0000

3.4.3 Case 3 - Individual sequences

Case 3 only has 10 robust estimations in total from individual sequences. Since the number of sub-catalogues with sufficient quality in each region is small, it is difficult to infer systematic regional variations of the ETAS parameter in Case 3. In **Figure 3-5**, we show the ETAS parameter results of Case 3 grouped by mainshock magnitudes. We further calculate the p_{lm}-values of the regressions of ETAS parameters of Case 3 with the 10 robust estimates on rupture dimensions and magnitude and show full results in **Appendix E**. We see no evidence that the ETAS parameters from individual sequences depend on magnitude or rupture dimensions (p_{lm}-values > 0.01).

According to **Figure 3-5** (a) and (b), K_0- and α-values of M7.5-7.9 earthquake sequences vary significantly (K_0 from 0.2 to 0.7 and α from 1.0 to 2.0), whereas the productivity

terms of M8.0-9.0 events are robust with smaller uncertainties. Because of the missing aftershocks immediately after large mainshocks (Seif *et al.*, 2017), *c*-values based on individual sequences from Case 3 are likely to be biased which leads to the overestimation in comparison with Case 1. Only Events 7, 11, 17, and 26 in Japan, Indonesia, and Philippines have *p*-values less than 1.25, the other aftershock sequences display faster temporal decay. A possible explanation is the high M_{cut} in comparison with other studies (e.g., M_{cut} = 2 from Seif *et al.* (2017)): The events below M_{cut} in the tail of the temporal distribution are excluded, leading to an apparently fast decay of some sequences.

In **Figure 3-5** (e) and (g), the *d* and *q* of Case 3 have larger standard errors for M7.5-8.5 events, suggesting that the far-field earthquakes are not within our space-magnitude target window given the proximity of the mainshock magnitudes to the completeness threshold. In comparison with γ from Case 1 with the longer catalogues (**Figure 3-2** (f)), the sequence-based γ from **Figure 3-5** (f) is larger and closer to expected values. For example, γ of Case 3 from the 2004 Aceh-Andaman earthquake increases from 1.09 to 1.53 in **Figure 3-5** (f). This might indicate that the ETAS model considers the 2004 Aceh-Andaman earthquake sequence as several individual sequences.

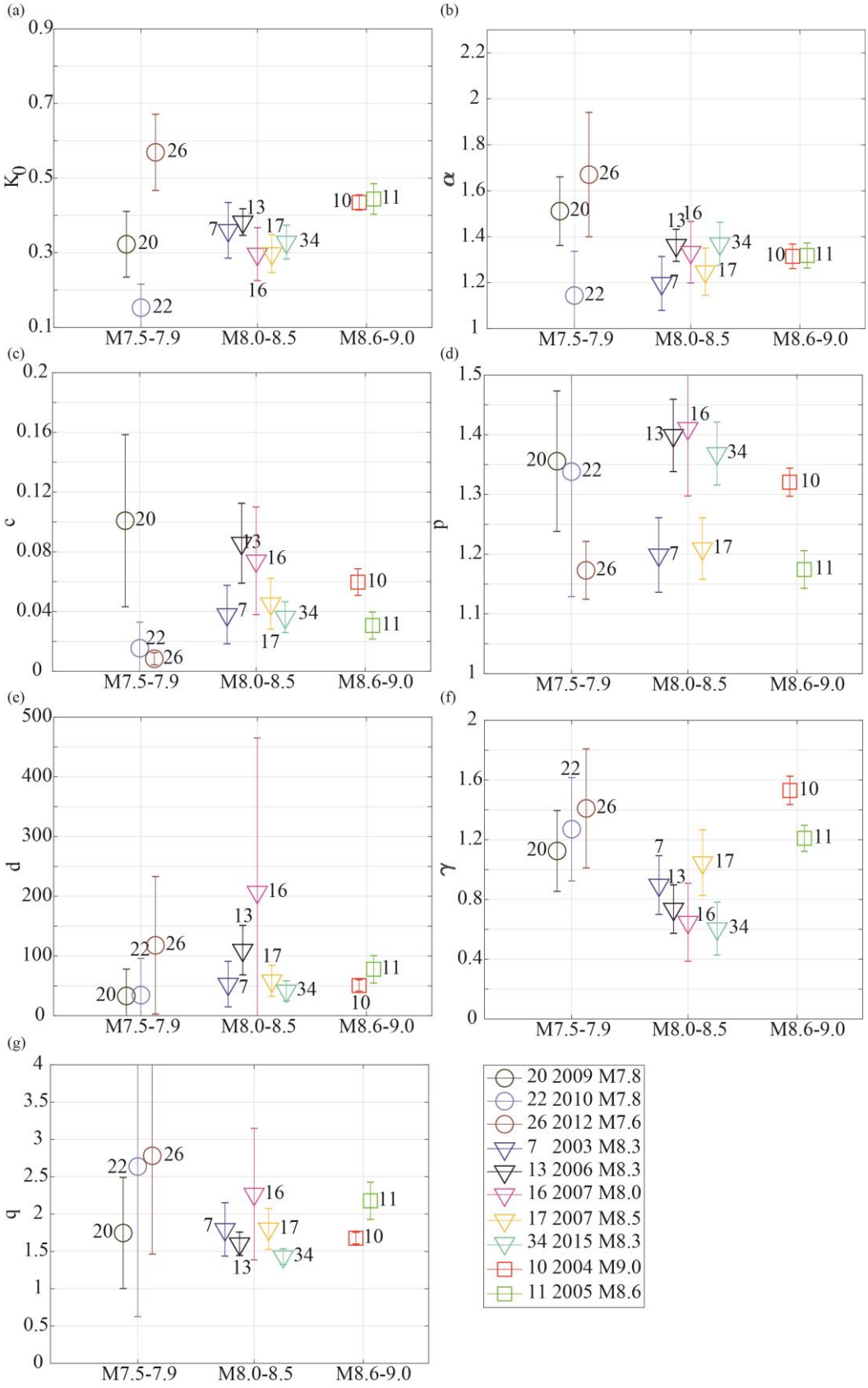

Figure 3-5. ETAS parameter results classified by mainshock magnitudes for Case 3 based on individual sequences.

Comparing the ETAS parameter estimates from Cases 1 to 3, four main observations are: (1) the parameter estimates from the longer catalogues (Cases 1 and 2) with smaller errors and less variability are more robust than those from individual sequences (Case 3). (2) From Case 1, K_0 appears to depend on magnitude and rupture dimensions, but this can be explained in terms of the known parameter correlations due to mathematical model formulation and the biases due to the effects of isotropic spatial aftershock distribution. (3) Given the range of variability of the estimated parameters, there is only weak evidence that ETAS parameters vary with the largest magnitude and region in Cases 1 and 2. (4) Although some moderate variability is observed (e.g. the productivity parameters in Case 1 with free α), the temporal parameters from Case 1 and the productivity and spatial parameters from Case 2 with fixed α show robust estimates consistent with prior studies (Ogata and Zhuang, 2006; Seif *et al.*, 2017; Zhang *et al.*, 2018).

It appears that a consistent comparison of ETAS parameters requires not only a uniform completeness threshold but also a similar maximum (observed) magnitude. This ensures similar sample sizes. The sub-catalogue range of this study in the maximum observed magnitude is from 7.5 to 9.0, while other studies that focus on regional or local seismicity often have wider ranges of magnitudes. For example, Seif *et al.* (2017) used Californian and Italian catalogues with maximum magnitudes near M7.0 and M_{cut}=2. This five-magnitude unit range resulted in robust ETAS parameters. On the other hand, this study focuses on global subduction events with mainshock magnitudes M7.5-9.0 and M_{cut}=4.5 due to the (relatively) sparse global monitoring system. Therefore, only regions with M8.0-9.0 events have a similar magnitude range and robust ETAS parameter estimates.

3.4.4 ETAS parameter estimation of multiple subduction earthquakes

To investigate the change of the ETAS parameters due to multiple large earthquakes occurring in the same region, parameters are re-estimated in enlarged spatial regions of offshore Indonesia, Japan, and Chile that included more than one large earthquake and their sequences. Estimates are summarised in **Table 3-5**.

Table 3-5. Summary of the estimated ETAS parameters of multiple subduction earthquakes with time windows 1981-2017.

	Indonesia A	Indonesia B	Indonesia C	Chile A	Chile B	Japan A	Japan B
Event index	10	37 (Events 10, 11, and 22)	38 (Events 10, 11, 17, 22, and 24)	21	39 (Events 21 and 34)	25	40 (Events 7 and 25)

Figure 3-6 shows nearly no changes in the ETAS parameters of M9-class events when additional large subduction earthquake sequences in broadly the same region are included. This indicates that the estimated ETAS parameters are not fluctuating abruptly over time within the same region. But the finding could also be a (less intriguing) result of the aftershock numbers being dominated by the largest M9.0 sequences. Subsequent, less productive sequences of smaller mainshocks might have different ETAS parameters but do not influence the overall estimates. Again, similar sample sizes and magnitude ranges are important for making such comparisons.

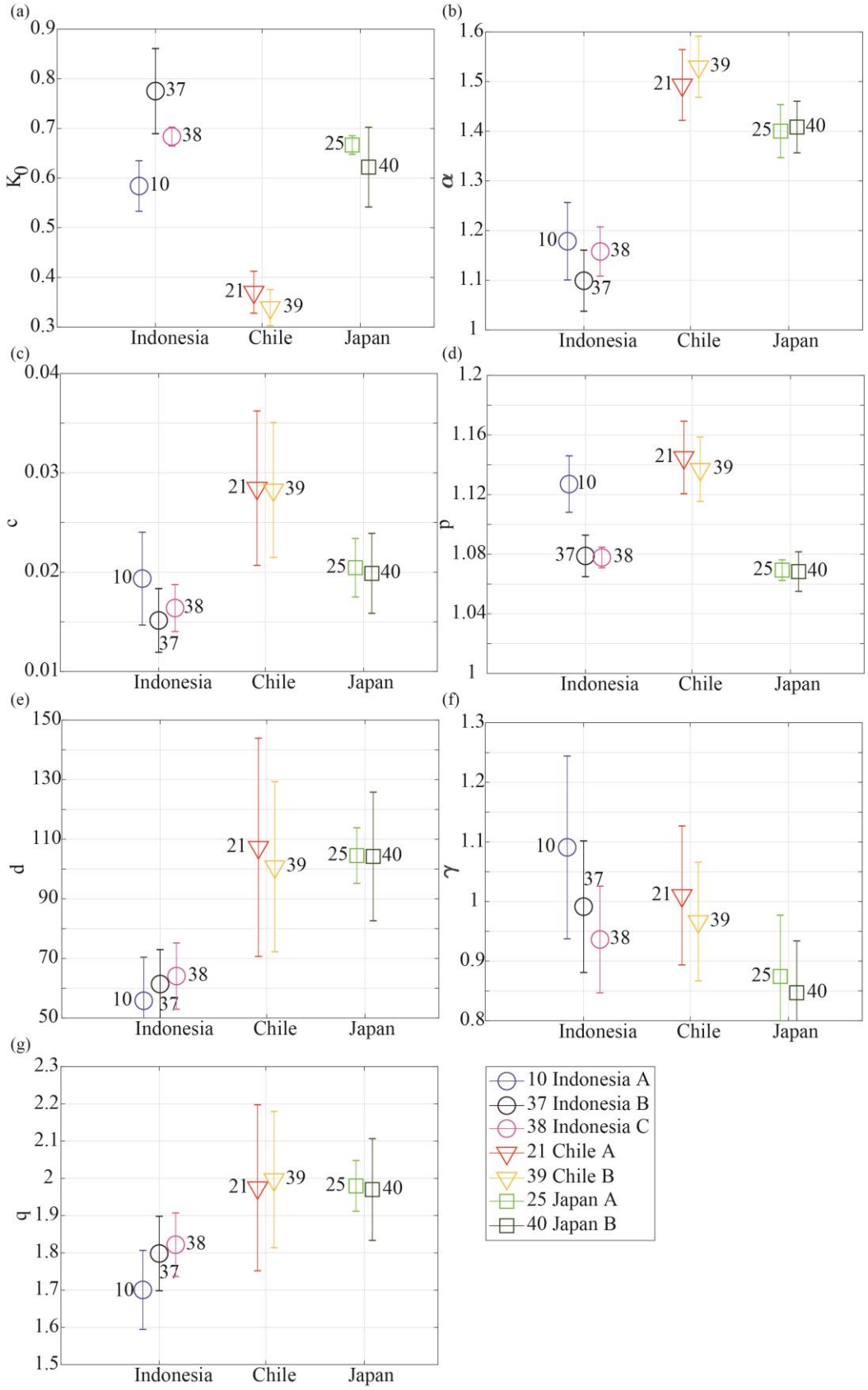

Figure 3-6. Parameter results from the sub-catalogues with multiple subduction earthquakes in Indonesia, Chile, and Japan.

3.5 Global ETAS parameters for M9-class events and its simulation

In this section, representative ETAS parameters are proposed for future M9.0-class events, and their performances are checked by comparing forward simulations with observed sequences of M9.0-class earthquakes. As pointed out in the Introduction (**Section 2.1**), the ETAS simulation framework includes an anisotropic distribution for the first generation of aftershocks of M9.0-class earthquakes to match observed aftershock patterns better (Zhang *et al.*, 2018).

3.5.1 Global ETAS parameters for M9-class events

To find a representative set of ETAS parameters for future generic M9.0 sequences, we use the robust estimates of temporal parameters from Case 1 and productivity and spatial parameters from Case 2 based on the findings from **Section 3.4**. Due to the known parameter biases from the model formulation, the isotropic spatial distribution, and the sample size, the criteria to find an acceptable set of ETAS parameters for generic future M9.0 sequences are:

- Productivity terms should not be supercritical to avoid explosive ETAS simulations.
- To ensure the total seismicity rate is in the range of the observed sequence, only parameter estimates that result in acceptable residual analysis results (within 99% error bounds) are included for K_0 selection.
- Unusual and suspicious parameter estimates are excluded. For example, parameter sets with $q > 3$, $d > 50$, and $\gamma > 2.3$ or $\gamma < 1$ are not considered, which is consistent with the observations from other studies (Ogata and Zhuang, 2006; Chu *et al.*, 2011; Seif *et al.*, 2017).

Different parameter sets are selected based on the criteria above. The final set of the parameters is calculated from the median value of the selected sub-catalogues and the standard error is calculated following the same procedure as for boxplots in **Appendix E**. The final set of parameters with median values and stand errors is summarised in **Table 3-6**.

Table 3-6. Suggested ETAS parameters for future **M**9.0 events.

	K_0 (event/day)	α (magnitude^{-1})	c (day)	p	d (km^2)	γ (magnitude^{-1})	q
Median values	0.04	2.30	0.03	1.21	23.48	1.61	1.68
Standard errors	0.02	0	0.01	0.08	18.17	0.29	0.55

3.5.2 ETAS simulations of M9-class events

To show that the proposed global M9.0 ETAS parameters from the **Section 3.5.1** are consistent with previously observed sequences, we simulate the 2004 Aceh-Andaman, the 2010 Maule, and the 2011 Tohoku earthquake sequences using the framework developed by Zhang *et al.* (2018). The synthetic catalogues of M9-class earthquake sequences are generated based on the ETAS parameters (K_0 = 0.04±0.02, α = 2.3, c = 0.03±0.01, p = 1.21±0.08, γ =1.61±0.29, d = 23.48±18.17, and q = 1.68±0.55). The ETAS parameters are randomly sampled from a normal distribution (Schoenberg *et al.*, 2010). Other simulation input information is summarised in **Table 3-7**. Rupture dimensions are sampled from the scaling law by Thingbaijam *et al.* (2017) and the uncertainty of the mainshock source parameters is also considered by assuming a bounded uniform distribution for strike and dip angles. 10,000 simulations are performed for each sequence.

Table 3-7. Summary of the mainshock source parameters of the ETAS simulations

	Rupture length (km)	Rupture width (km)	Length-width ratio	Strike angle	Dip angle	Mainshock epicentre	Mainshock magnitude
2004 Ache-Andaman event	1100-1300	200-300	4.5-5	344º-346º	15º-16º	93.5ºE, 8.2ºN	9.1
2010 Maule event	550-580	140-200	3-4	16º-18º	17º-18º	-72.7ºW, -35.7ºS	8.8
2011 Tohoku event	450-550	200-240	2-3	202º-210º	10º-12º	142.2ºE, 37.7ºN	9.0

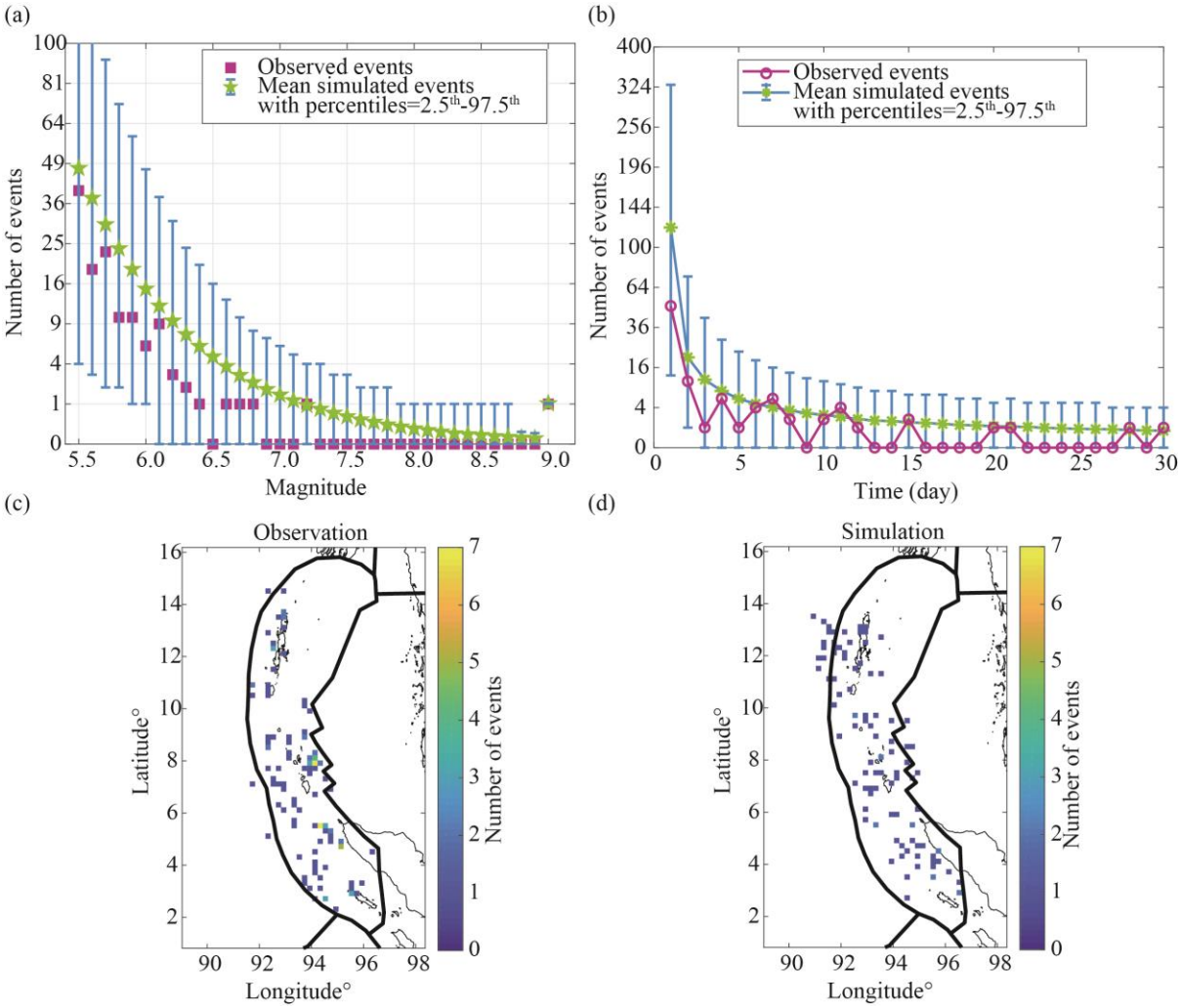

Figure 3-7. Comparison of observed and simulated M5.5+ aftershocks of the 2004 Aceh-Andaman earthquake: (a) magnitude frequency distribution in square root scale during the first three months, (b) daily number of events during the first 30 days, (c) observed 2D aftershock histograms during the first three months, (d) a simulated 2D aftershock histogram over the same period.

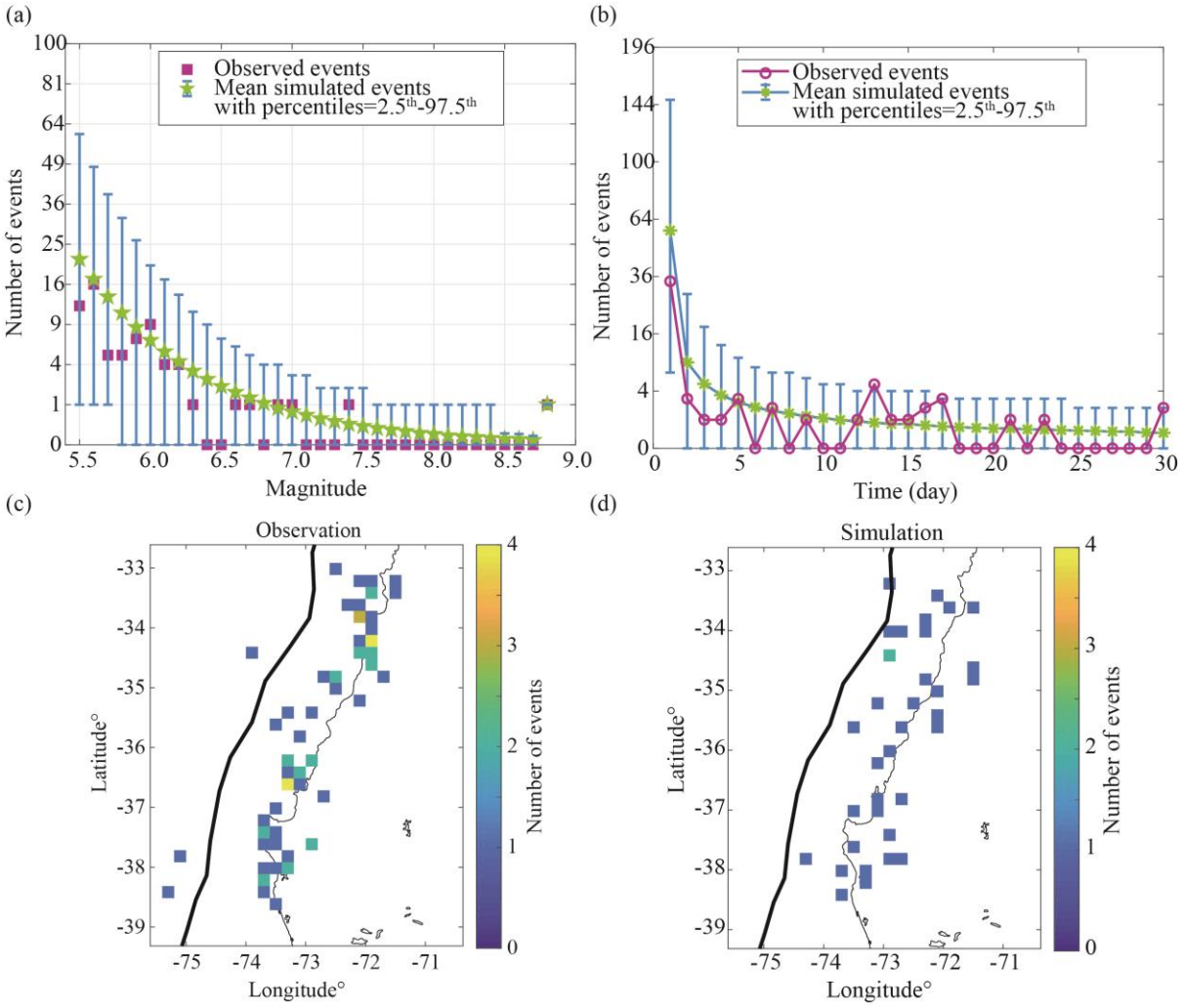

Figure 3-8. Comparison of observed and simulated M5.5+ aftershocks after the 2010 Maule earthquake: (a) magnitude frequency distribution during the first three months, (b) daily number of events during the first 30 days, (c) observed 2D aftershock histogram during the first three months, (d) a simulated 2D aftershock histogram over the same period.

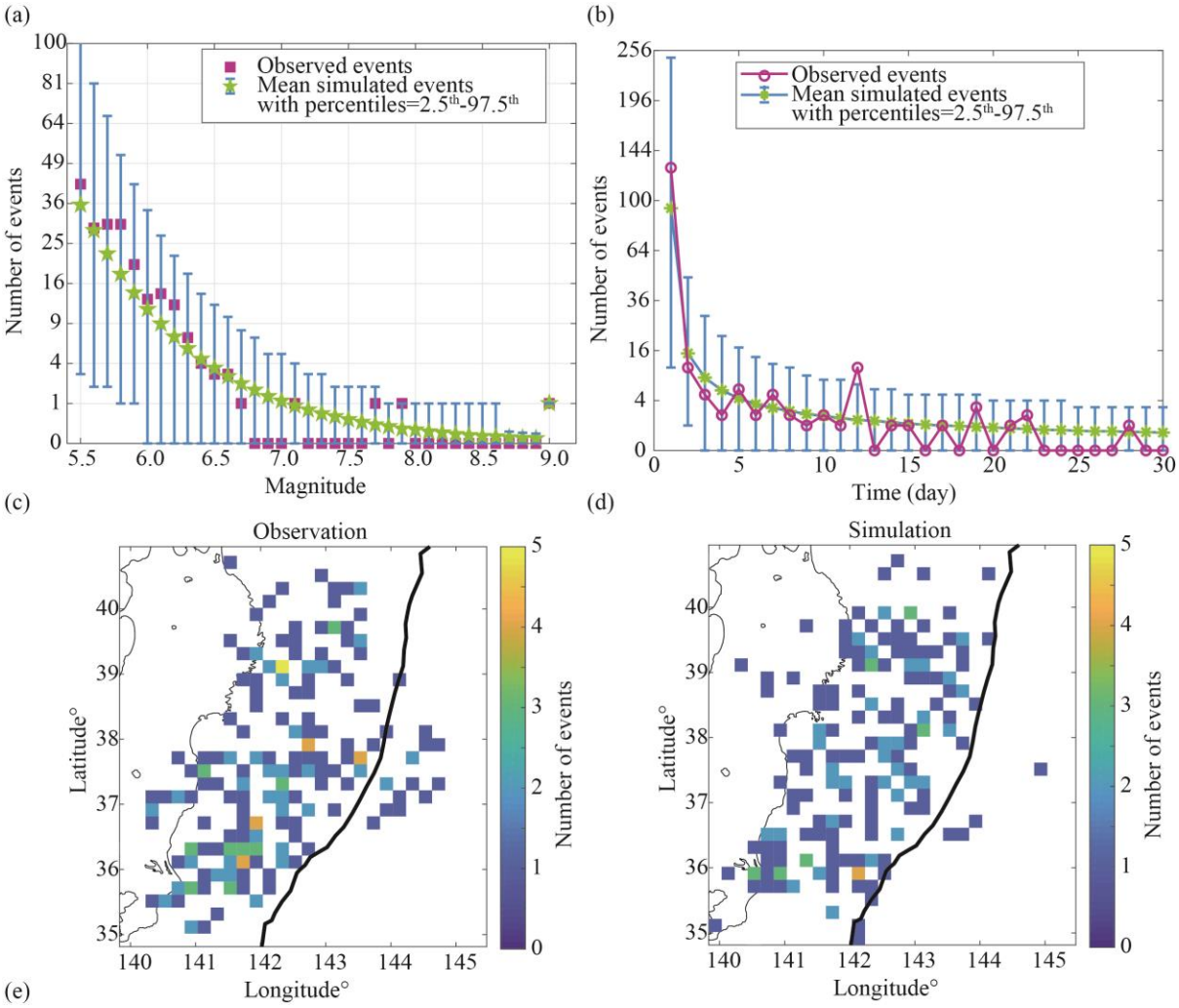

Figure 3-9. Comparison of observed and simulated M5.5+ aftershocks after the 2011 Tohoku earthquake: (a) magnitude frequency distribution in square root scale during the first three months, (b) daily number of events during the first 30 days, (c) observed 2D aftershock histogram during the first three months, (d) a simulated 2D aftershock histogram during the first three months.

From **Figure 3-7**, **Figure 3-8**, and **Figure 3-9**, the observations of the 2004 Aceh-Andaman and 2010 Maule earthquakes, especially within the first week of the mainshock, are in the ranges of the ETAS simulations. The spike on day 13 in **Figure 3-8** is the M6.9 Pichilemu earthquake followed by a M6.7 aftershock. The mean of the simulated daily numbers exceeds the aftershock numbers observed on day 1 after both the Aceh-Andaman and Maule

mainshocks (**Figure 3-7** and **Figure 3-8**). The aftershocks on day 1 after Tohoku, on the other hand, are more numerous than the mean forecast (**Figure 3-9**(b)). This is related to the K_0-value. The numbers of M≥5.5 aftershocks of the 2004 Aceh-Andaman earthquake and the 2010 Maule earthquake on day 1 are approximately 40 for both sequences, while for the Tohoku sequence, the number of M≥5.5 aftershocks on day 1 is more than 100, noting that Zhang *et al.* (2018) reported K_0 = 0.064 for the Tohoku sequence. The K_0 estimated in this study thus represents the averaged case across different subduction regions. Importantly, the range of forecasts captures the observed values.

3.6 Conclusions

This chapter investigated the global variability of the ETAS parameters in subduction regions that experienced M7.5+ megathrust earthquakes. Longer regional as well as shorter sequence-specific selections of the global NEIC earthquake catalogue were prepared to calibrate the ETAS model. The results suggest that:

- The ETAS parameters from the longer catalogues (Cases 1 and 2) have smaller standard errors and are less variable than those of sequence-specific catalogues (Case 3), because the number of events in sequence-specific sub-catalogues of M7.5-8.5 earthquakes is relatively small given the high M_{cut} of the NEIC catalogue.
- No obvious systematic regional dependency of parameters is observed in either Case 1 or 2. The median ETAS parameters of Papua New Guinea and South America are similar from Cases 1 and 2, which seems robust given the larger sample sizes and wider magnitude bins here than in other regions.
- A test of correlation between ETAS parameters and mainshock parameters revealed no statistically significant results, except for K_0 in Case 1, but we interpret the dependency as a result of known biases due to the ETAS model formulation, namely the assumed isotropic aftershock distribution.

- The variability of parameters estimated from multiple sequences (M9.0 and M8.0 events) in the same subduction zones (Indonesia, Chile, and Japan) is small, because the M9.0 sequences dominate the input catalogues and M8.0 sequences have a smaller impact on the parameter estimation.

On the basis of the estimated parameters with known biases due to the isotropic spatial distribution and an evaluation of their quality, the median values and standard errors of the ETAS parameters for future M9.0-class events are suggested: K_0 = 0.04±0.02, α = 2.3, c = 0.03±0.01, p = 1.21±0.08, γ =1.61±0.29, d = 23.48±18.17, and q = 1.68±0.55. Synthetic catalogues we generated using the suggested ETAS parameters are consistent with those observed during the 2004 Aceh-Andaman, the 2010 Maule, and the 2011 Tohoku earthquake sequences.

The limitations of this parameter estimation are noteworthy. (1) Aftershocks are modelled isotropically in space around mainshock epicentres, while observed aftershock patterns align with anisotropic mainshock rupture planes. ETAS models with an anisotropic spatial distribution (e.g., Ogata and Zhuang, 2006) should lead to less biased parameter estimates. (2) The standard error of each parameter in this study is estimated assuming other parameters are fixed. The covariance of the parameters is not explicitly included in this study. Therefore, the parameter uncertainty could be larger than the standard errors reported here, further supporting the inference that observed parameter variations are insignificant. (3) In this study we combined a quantitative statistical analysis with qualitative judgements to investigate the variability of ETAS parameters across different subduction-zone regions. However, developing a new model to find a remedy for the biases of ETAS parameters is beyond the scope of this chapter. (4) The proposed standard errors of ETAS parameters for future M9.0 sequences are large, because the standard errors include the uncertainty of ETAS parameters from different regions.

Chapter 4 Development of State-dependent Aftershock Fragility Curves of Wood-frame Houses in British Columbia, Canada[§]

4.1 Introduction

Recent earthquake sequences, such as the 2010-2011 Darfield New Zealand earthquake and the 2011 Tohoku Japan earthquake sequences, showed the destructive effects of aftershocks on buildings (Goda *et al.*, 2013; Potter *et al.*, 2015). The cumulative damage due to aftershocks can have a significant impact on the post-earthquake risk assessment immediately after a mainshock, for example, building tagging, inspection prioritisation, and retrofitting (Bazzurro *et al.*, 2004; Yeo and Cornell, 2004, 2009b; Ebrahimian *et al.*, 2014; Iervolino *et al.*, 2014).

Similar destructive mainshock-aftershock sequences could occur in other active seismic regions. For example, based on turbidite records in the past 10,000 years, the Cascadia subduction zone (CSZ) from Vancouver Island to Northern California ruptured 19 times with M9-class earthquakes (Goldfinger *et al.*, 2012), resulting in an average recurrence period of 526 years. According to Ventura *et al.* (2005), 56% of buildings in British Columbia are wood-frame houses, 40% of which were built before 1970. Since seismic provisions of the National Building Code of Canada were adopted and enforced in British Columbia after 1973, the majority of old residential houses can be considered as 'non-engineered' from seismic design

[§] This chapter was accepted at Earthquake Engineering and Structural Dynamics:

Zhang, L., K. Goda, F. De Luca, and R. De Risi (2020) Mainshock-aftershock state-dependent fragility curves: the case of wood-frame houses in British Columbia, Canada, *Earthq. Eng. Struct. Dyn* (accepted).

viewpoints. Consequently, many wood-frame houses with low seismic resistance may suffer significant damage due to a M9.0 mainshock and aftershocks in the CSZ.

To account for cumulative damage from an earthquake sequence, a fragility model that can estimate the damage state of the structure after each event during the earthquake sequence is desirable. A set of state-dependent fragility curves was developed by Luco *et al.* (2004). Luco *et al.* (2004) used pushover analysis to define the damage states (DS) associated with the maximum roof drift ratio (MaxRDR), and a structural model was subjected to scaled mainshock records to attain pre-damage states. Following that, the aftershock records (which are identical to the mainshock record set) were applied to the mainshock-damaged building by performing incremental dynamic analysis (IDA) to attain post-damage states due to the aftershocks. This is so-called back-to-back application of mainshock records (Luco *et al.*, 2004). Finally, the median spectral acceleration was adopted as residual capacity for developing the state-dependent fragility model. Raghunandan *et al.* (2015) extended Luco *et al.*'s approach to a reinforced concrete building by modelling it as a nonlinear multi-degree-of-freedom system and used the maximum inter-storey drift ratio (MaxISDR) as the engineering demand parameter (EDP). The effects due to aftershocks are captured by the damage accumulation from the pre-structural responses (pre-EDP) to the post-structural responses (post-EDP), noting that pre-EDP can include the effects due to a mainshock and preceding aftershocks (i.e., the initial condition of a structure does not have to be intact).

The procedure by Luco *et al.* (2004) facilitates various post-earthquake decision-making, such as building-tagging and seismic loss estimation, because the aftershock fragility curves are state-dependent. However, there are three aspects that can be improved. (1) The EDP may be overestimated, when the back-to-back application of mainshock records is used for aftershock records with IDA (Goda, 2015). (2) The back-to-back application of input ground motions eliminates the link between the pre-structural response by the mainshock and

the post-structural response by the aftershock; thus, real mainshock-aftershock records are desirable. (3) The computational cost of the back-to-back approach with IDA is high (Raghunandan *et al.*, 2015a).

When the state-dependent fragility curves are developed under the performance-based earthquake engineering (PBEE) framework (Deierlein *et al.*, 2003; Porter, 2003), an appropriate set of intensity measure (IM) and EDP needs to be selected to represent the intensity of ground motions and structural responses, respectively. The spectral acceleration (Sa) at the fundamental period of a structure is widely used as the IM (Cornell *et al.*, 2002; Luco, 2002; Luco and Cornell, 2007; Kostinakis *et al.*, 2017). However, using a single-period Sa may not be the most effective, because (1) higher mode effects and period elongation of the structure are also important (e.g., Bradley, 2011), and (2) a sufficient IM would allow one to scale the records with moderate scaling factors and have more data points with good estimates (Vamvatsikos and Cornell, 2002). Therefore, other IMs, such as Arias intensity (AI), cumulative absolute velocity (CAV), spectral intensity (SI), and peak ground velocity (PGV), should be taken into consideration in defining the most suitable IM for the development of aftershock fragility curves.

This chapter focuses on the cumulative damage of wood-frame houses in Victoria, British Columbia, Canada, due to the mainshock-aftershock ground motion sequences from the CSZ. The novelties of this study are that (1) to avoid the bias in estimating EDP and reduce the computational cost from the back-to-back approach, a new method to conduct the fragility assessment considering pre-EDP, IM, and post-EDP is developed using cloud analysis. (2) Considering the M9.0 mainshock can potentially trigger both subduction-zone and crustal aftershocks (Zhang *et al.*, 2018), a large set of real mainshock-aftershock sequences with wide ranges of rupture distances (0-270km) and magnitudes (5.0-9.0) is used for the fragility assessment. To assess the structural responses of Canadian wood-frame houses subject to

multiple events, the UBC-SAWS (seismic analysis of wood-frame structure) model (White and Ventura, 2006) is implemented with real 596 mainshock-aftershock records (Goda and Taylor, 2012; Goda *et al.*, 2015). Different combinations of IMs and EDPs are evaluated in developing state-dependent seismic fragility curves. The two objectives of this study are (1) to identify an appropriate IM-EDP set for seismic fragility assessment of mainshock-aftershock sequences, and (2) to produce state-dependent fragility curves for estimating the cumulative damage of the wood-frame houses.

To illustrate the key concept of cumulative damage due to repeated earthquakes and state-dependent fragility, a schematic diagram of cumulative damage by multiple events is shown in **Figure 4-1** (Luco *et al.*, 2004; Iervolino *et al.*, 2016). The residual capacity of the house is decreased as more events affect the house. To update the damage state of the house after each event, the state-dependent fragility curves are considered. Since the EDP can be associated with the DS of the structure, the state-dependent fragility curves are related to pre-DS, IM of the event, and post-DS. With IM_1 of the first event, the post-DS after the first event can be estimated. Subsequently, with IM_i of the *i*-th shock and pre-DS before the *i*-th shock, the post-DS can be evaluated, and this procedure can be applied recursively. Therefore, the fragility curves can be used to assess the cumulative damage of the structure under an earthquake sequence.

In **Section 4.2**, the literature review of the SAWS model, mainshock-aftershock ground motion selection, EDPs, IMs, and state-dependent fragility curves is provided. **Section 4.3** discusses the evaluation of different EDPs and IMs. The information of ground motion records is described in **Section 4.3.2**. In addition, to show that the selection of the mainshock-aftershock records is appropriate, the IM-EDP plots of this study are compared with the IDA approach and cloud analysis from Goda and Salami (2014) in **Section 4.3.3**. After identifying the appropriate EDP and IM from **Sections 4.3.4** and **4.3.5**, respectively, **Section 4.4** explains

a new procedure to develop the state-dependent fragility curves and present the results of fragility curves for the wood-frame houses.

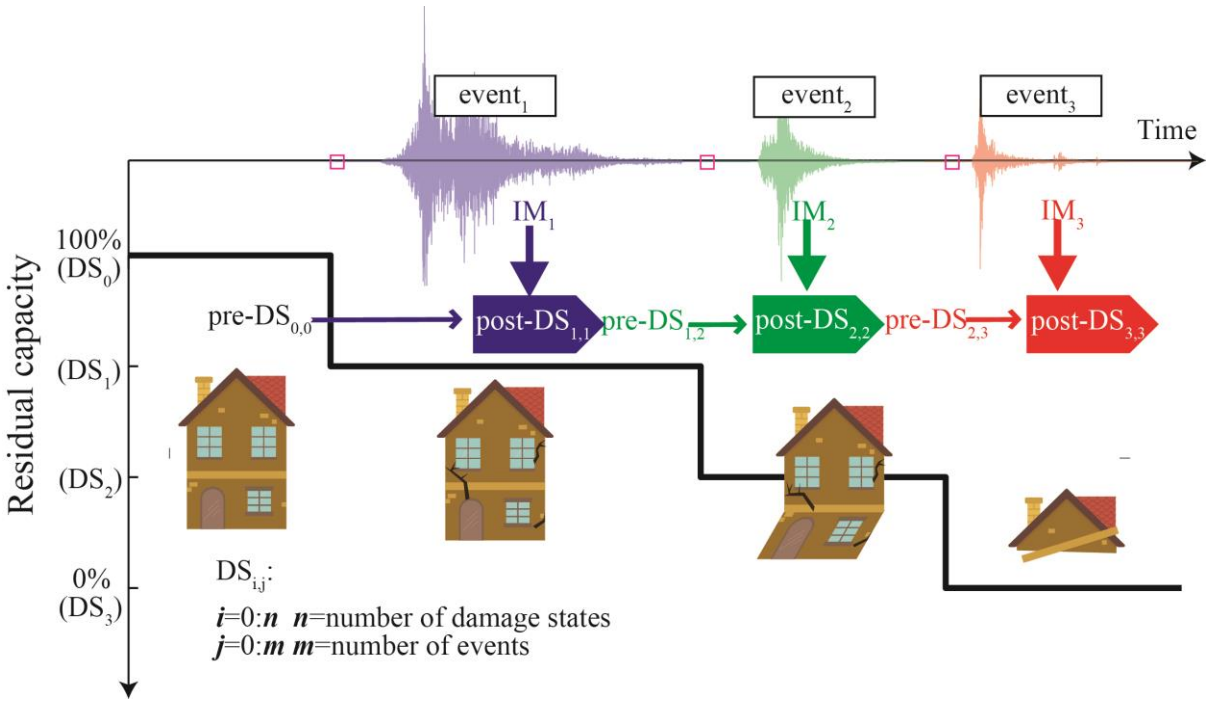

Figure 4-1. Illustration of damage accumulation due to aftershocks.

4.2 Cumulative damage due to mainshock-aftershock sequences

The PBEE framework (Deierlein *et al.*, 2003) is adopted to consider all key uncertainties from seismic hazard to risk analysis for decision-making. A general formulation for evaluating seismic risk can be expressed as:

$$\lambda_{PBEE}(DV) = \iiint G(DV|DM) \cdot dG(DM|EDP) \cdot |dG(EDP|IM)| \cdot |d\lambda(IM)| \quad (4\text{-}1)$$

where *DV* is the decision variable that is related to seismic risk mitigation, such as seismic loss. *DM* is the damage measure describing the damage state of the structure. *EDP* describes the structural response by ground motions. *IM* describes the shaking intensity of the ground motion. To develop state-dependent fragility curves (**Section 4.4**), five aspects that are related to the evaluations of *dG(DM|EDP)* and *dG(EDP|IM)* in **Equation (4-1)** are discussed:

- UBC-SAWS model
- Selection of mainshock-aftershock records
- Selection of EDPs
- Selection of IMs
- Procedure to develop aftershock fragility curves

4.2.1 UBC-SAWS model

The UBC-SAWS model is a structural model of typical wood-frame houses in British Columbia, Canada (White and Ventura, 2006). It is based on the SAWS model (Folz and Filiatrault, 2004a,b) with modifications of the model parameters for Canadian wooden house construction. The basic assumptions of the UBC-SAWS model are: (1) floor and roof diaphragms are rigid (length = 7.62m, width = 6.10m, and height = 2.74m), (2) shear walls are represented by nonlinear springs, hysteresis of which is characterised by the Cyclic Analysis of SHEar Walls (CASHEW) model (Folz and Filiatrault, 2001; see **Figure 4-2**a), and (3) bi-directional horizontal seismic excitations are considered but ignoring the vertical excitation. The parameters of the UBC-SAWS model are calibrated from the static and dynamic wall tests of wall panels with different configurations and the shake-table tests of full-scale houses that were conducted at the University of British Columbia (White and Ventura, 2006). The sheathing materials of the shear wall include horizontal board (shiplap), gypsum wallboard (GWB), plywood, oriented strand board (OSB), and stucco. The analytical results from the UBC-SAWS model show a good agreement with experimental results for MaxISDR in the range of 0.01-0.04.

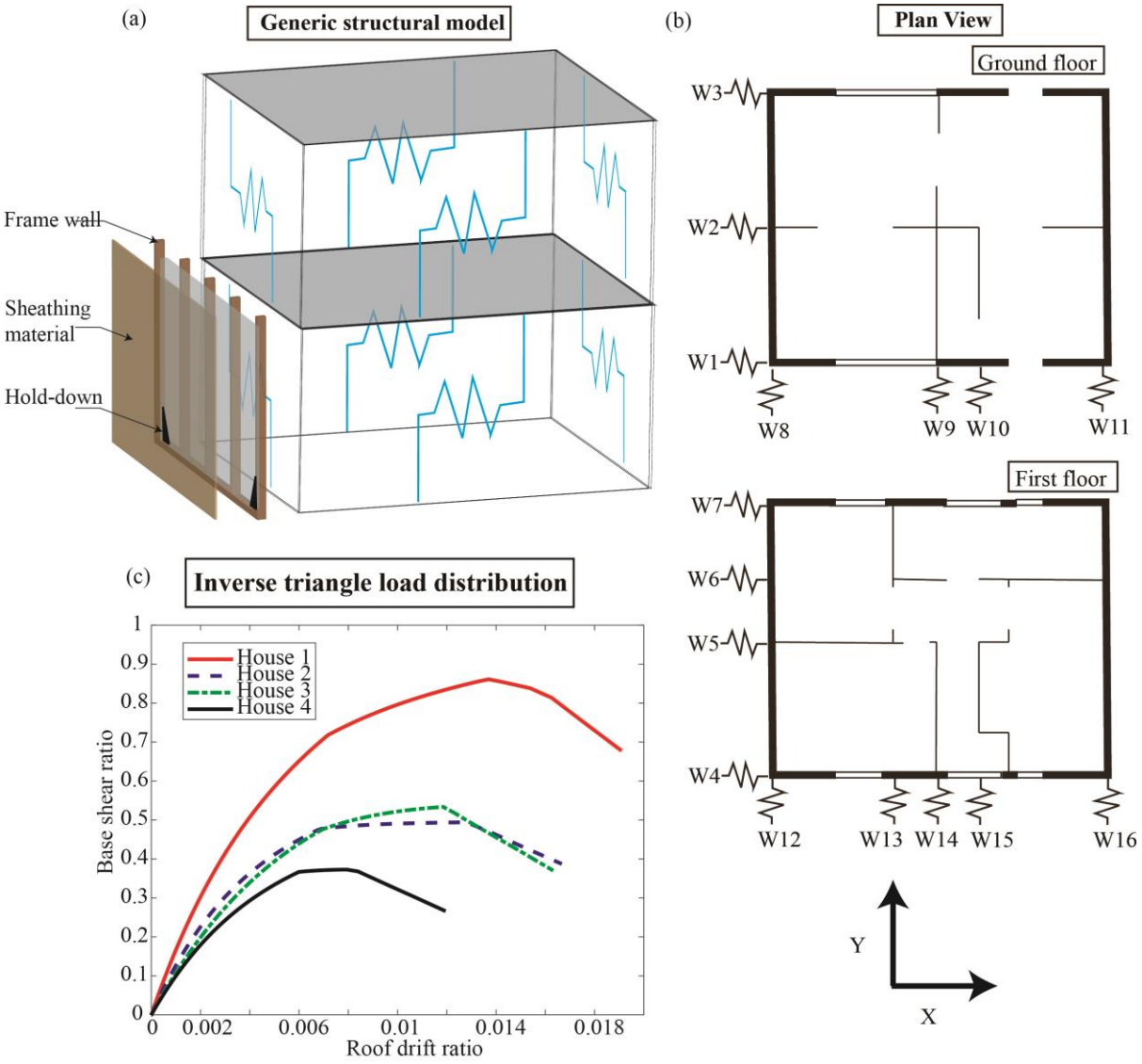

Figure 4-2. Illustration of the UBC-SAWS model: (a) generic model of wood-frame houses, (b) ground and first floor plans of wood-frame houses, and (c) pushover analysis of Houses 1-4.

Based on different shear-wall configurations, four types of two-storey wood-frame houses are defined in the UBC-SAWS model: (1) House 1 with stucco/engineered OSB/GWB, (2) House 2 with engineered OSB/GWB, (3) House 3 with non-engineered OSB/GWB, and (4) House 4 with horizontal boards (shiplap)/GWB. The term 'Engineered' for Houses 1 and 2 indicates that hold-downs and blocking of the wall panel are used to increase its seismic resistance and to meet the seismic code requirements. Due to the design layout of the house

model in **Figure 4-2**(b) (e.g., the dimensions of the house along x-axis and y-axis and the location of the windows and doors), the stiffness along the x-axis is smaller than that along the y-axis, and the expected failure mode of the house models is the soft-storey collapse of the ground floor level due to large openings. The fundamental vibration periods along the x-axis of Houses 1-4 are 0.25 s, 0.3 s, 0.35 s, and 0.4 s, respectively, whereas those along the y-axis are about 0.22 s for all houses (White and Ventura, 2006). In **Figure 4-2**(b), 16 walls, which are represented by springs, are present along the x-axis and y-axis on the ground and first floors. The pushover analysis results of Houses 1-4 by using the inverse triangle load distribution are shown in **Figure 4-2**(c). The base shear ratio on the vertical axis is the ratio of the base shear force and the total weight of the house. In terms of pushover curves, House 1 has the highest seismic capacity; Houses 2 and 3 have similar seismic resistance; and House 4 has the lowest seismic capacity. Pan *et al.* (2018) indicated House 4 with horizontal boards is not applicable in high seismic regions.

4.2.2 Mainshock-aftershock ground motion records

Using appropriate ground motion records to represent real mainshock-aftershock sequences is important for seismic demand estimation. Specifically, for a megathrust subduction mainshock triggering crustal and subduction-zone aftershocks, an extensive set of mainshock-aftershock records from subduction and crustal earthquakes is needed.

Table 4-1 summarises the information of mainshocks and mainshock-aftershock records that have been used for investigating the seismic demand estimation of structures in the literature. Luco *et al.* (2004) and Raghunandan *et al.* (2015) used 30 mainshock ground motion records from California (Vamvatsikos and Cornell, 2006) to represent mainshock and aftershock ground motions. The aftershock ground motions were generated from the scaled mainshock ground motions. However, using repeated mainshock records as aftershock records

may not be appropriate, because the records of mainshock and aftershock from an earthquake sequence can have different characteristics (Goda, 2015). For example, Ruiz-García and Negrete-Manriquez (2011) demonstrated that the predominant periods of ground motions of mainshocks and aftershocks are different and have different effects on the calculated structural responses.

Li and Ellingwood (2007) showed that repeated mainshock records as aftershock records overestimate MaxISDR of steel moment frame buildings using 30 ground motion records for Los Angeles. Uma *et al.* (2010) used 30 mainshock ground motions from the PEER Next Generation Attenuation (NGA) database with M6.5-7.2 and rupture distance 15-30km. The response spectra of the records were scaled to 0.2g at the period of T=1.1s, which corresponded to the fundamental vibration period of an inelastic SDOF system. Following that, IDA was implemented with scaling factors from 0.2g to 2.0g. Christidis *et al.* (2013) used 100 global ground motion records to investigate the relationship between the maximum roof drift ratio (MaxRDR) and the residual roof drift ratio (ResRDR). Han *et al.* (2014) generated synthetic aftershock records to conduct seismic risk analysis. The aftershock records were synthesised based on mainshocks, site conditions, and rupture mechanisms of faults using Latin Hypercube sampling. They found that for the buildings with longer fundamental periods the synthetic aftershock records have similar results in comparison with real aftershock records in the Western United States. However, other studies have shown that artificial mainshock-aftershock records may overestimate EDPs (Ruiz-García and Negrete-Manriquez, 2011; Goda and Taylor, 2012). Ruiz-García and Aguilar (2015) used 29 mainshock-aftershock records from the 1994 Northridge earthquake to carry out the aftershock seismic assessment for California in the United States. Jalayer and Ebrahimian (2017) selected 50 European mainshock records with M5.5-7.5 and rupture distance around 80km and 43 European aftershock records with M4.2-6.2 and rupture distance around 40km from the NGA-West2 database.

Table 4-1. Summary of ground motion record information in the literature

Authors	Ground motion records	References of ground motion records (Crustal/subduction records)	Regions of ground motion records	Record scaling	Structural model
Luco *et al.* (2004)	30 real mainshock records aftershock records are the scaled mainshock records	Crustal records - Vamvatsikos and Cornell (2006)	The United States	IDA	3-storey steel moment-resisting frame, represented by an equivalent SDOF model
Li and Ellingwood (2007)	30 real mainshock records aftershock records are the scaled mainshock records	Crustal records - Somerville (1997)	The United States	No	Steel moment frame buildings, represented by an equivalent SDOF model
Uma *et al.* (2010)	30 real mainshock records	Crustal records - Pacific Earthquake Engineering Research (PEER) Centre	The United States, Kobe, Japan, Turkey	IDA	SDOF model
Ruiz-García and Negrete-Manriquez (2011) and Ruiz-García and Aguilar (2015)	29 real mainshock-aftershock sequences	Crustal records - PEER	The United States	No	4-storey steel building as MDOF models
Christidis *et al.* (2013)	100 real mainshock records	Crustal records - PEER	Global records	No	Moment resisting steel frames as MDOF models
Goda and Salami (2014)	290 real mainshock-aftershock sequences	Crustal and subduction records-NGA and K/KiK/SK records	Global records	IDA and cloud analysis	UBC-SAWS models
Han *et al.* (2014)	32 real mainshock-aftershock records 32 real mainshock with synthetic aftershock records	Crustal records - PEER and Centre for Engineering strong motion data (CESMD)	Western United States	No	Non-ductile reinforced concrete frame buildings as MDOF models
Raghunandan *et al.* (2015)	30 mainshocks	Crustal records - Vamvatsikos and Cornell (2006)	The United States	IDA	Reinforced concrete framed buildings as MDOF model
Tesfamariam and Goda (2015)	100 real mainshock and 100 mainshock-aftershock sequences	Crustal and subduction records - Goda and Taylor (2012) and Goda *et al.* (2015)	Global records	IDA	Non-ductile reinforced concrete buildings as MDOF models
Jalayer and Ebrahimian (2017)	50 real mainshock and 43 real aftershock records	Crustal records - NGA-West2 Ancheta *et al.* (2014)	Europe	Cloud analysis	Reinforced concrete moment-resisting frame as MDOF model

Goda and Taylor (2012) constructed strong mainshock-aftershock ground motions from the NGA database. 75 mainshock-aftershock ground motion sequences were defined based on global crustal mainshock-aftershock sequences. Later, Goda *et al.* (2015) constructed a real mainshock-aftershock record database from the K-NET, KiK-net, and SK-net in Japan. In total, 531 mainshock-aftershock record sequences were defined based on 20 mainshock-aftershock earthquake sequences in Japan, which included records from large subduction earthquakes, such as the 2003 Tokachi-oki earthquake and the 2011 Tohoku earthquake. Goda and Salami (2014) used the NGA records (Goda and Taylor, 2012) and the database from the K-NET, KiK-net and SK-net in Japan but not including the 2011 Tohoku sequence. In total, 290 real mainshock-aftershock sequences were applied to the UBC-SAWS model with cloud analysis, whereas 50 mainshock-aftershock sequences were selected by conditional mean spectra (CMS; Baker, 2010; Goda and Atkinson, 2011) for IDA. Tesfamariam and Goda (2015) selected records from the combined database from Goda and Taylor (2012) and Goda *et al.* (2015) by considering the regional seismic hazard of Victoria, Canada and CMS. They used 100 mainshock records and 100 mainshock-aftershock sequences in IDA to assess the impact of aftershocks on reinforced concrete frame buildings.

Most of the studies listed in **Table 4-1** considered specific building types (e.g., steel moment frame and reinforced concrete buildings) in seismic regions of interest, therefore, the record selections should be region-specific, reflecting seismotectonic conditions (e.g. active continental crust versus subduction region) and magnitude-rupture distance distributions. However, for seismic risk assessments in Victoria, strong ground motion records from local sources are not available. The combined database from Goda and Taylor (2012) and Goda *et al.* (2015) is one of the largest databases that are available in the literature and consists of 606 real mainshock-aftershock sequences, including the data from the 2011 Tohoku Japan earthquake. These real sequences are valuable, because similar M9.0 Tohoku-like megathrust

subduction earthquake sequences could occur in the CSZ, affecting residential houses in Victoria, Canada.

4.2.3 EDPs

The EDP is a key parameter to link seismic hazard analysis and seismic risk analysis (**Equation (4-1)**). Different EDPs are used in literature: maximum roof drift ratio (MaxRDR), residual roof drift ratio (ResRDR), maximum inter-storey drift ratio (MaxISDR), residual inter-storey drift ratio (ResISDR), and maximum incremental inter-storey drift ratio (MaxIISDR) (Luco *et al.*, 2004; Ebrahimian *et al.*, 2014; Goda and Tesfamariam, 2015). Raghunandan *et al.* (2015) ranked MaxRDR, ResRDR, MaxISDR and ResISDR, based on the slope between normalised EDPs and the percentages of reduced collapse capacities, and with regard to observability. The higher the slope is, the more effective the EDP is. Spectral displacement at the fundamental period of the building was considered as the IM in their study. They concluded that MaxISDR is the best EDP based on the slope, closely followed by ResISDR and MaxRDR. In terms of observability, ResISDR was the best among others.

When MaxIISDR is considered to estimate cumulative damage of aftershocks in the seismic risk assessment, a pair of MaxISDR and ResISDR is needed in the simulation. Several studies considered the maximum and residual roof/inter-storey drift ratios simultaneously in the seismic risk assessment, because:

- the maximum and residual drift ratios depend on each other (Uma *et al.*, 2010; Tesfamariam and Goda, 2015b),
- the maximum drift ratio is widely used to conduct damage state and loss estimations (Christidis *et al.*, 2013; Raghunandan *et al.*, 2015a),

- the residual drift ratio can be observed more easily after earthquakes, but the uncertainty of the residual drift ratio is usually larger than that of the maximum drift ratio (Erochko *et al.*, 2010).

Joint probability distributions of MaxISDR and ResISDR were estimated by Uma *et al.* (2010) and Tesfamariam and Goda (2015). The former used a multivariate lognormal distribution to investigate the probability of MaxISDR and ResISDR, while the latter estimated the joint probability distribution of MaxISDR and ResISDR of mainshock-aftershock sequences using copulas (McNeil *et al.*, 2005). Because of the observability of the residual drift ratio, Christidis *et al.* (2013) developed a new method to estimate MaxRDR from ResRDR, and the estimated MaxRDR can be applied for the post-earthquake risk assessment (FEMA, 2009).

To assess the effect of aftershocks on the cumulative damage, different EDPs have been selected in the literature. Luco *et al.* (2004) used MaxRDR as pre-EDP to define five damage states. Median spectral accelerations at the fundamental period of the building with 5% damping were used to describe the residual capacity, when the building reached different damage states by IDA. Erochko *et al.* (2010) investigated the effect of mainshock-aftershock sequences (one mainshock and one aftershock) on pre-EDP and post-EDP. The pre-EDP was ResISDR after the mainshock, whereas the post-EDP was the ratio between MaxIISDR of aftershocks and MaxISDR of the mainshock. Erochko *et al.* (2010) concluded that as the pre-EDP became higher than 1%, the post-EDPs were increased significantly up to 1.2 for a 6-storey structure and 1.6 for a 12-storey structure. Ruiz-García and Aguilar (2017) used ResISDR as post-EDP to assess the effect of aftershocks on cumulative damage. The aftershock records were scaled from real mainshock records. They concluded that when the strong aftershock records were used (i.e. scaled mainshock records to attain seismic excitation levels at 2% probability of exceedance in 50 years), the post-ResISDR after the mainshock was

increased when the pre-ResISDR was within 0.1%-0.5%. However, when the aftershock intensity was relatively small (corresponding to the seismic hazard level at 10% probability of exceedance in 50 years), the post-ResISDR due to some of the mainshocks was decreased due to the re-centering effect given the pre-ResISDR was approximately 1.4%.

For the case of a megathrust subduction mainshock triggering crustal and subduction-zone aftershocks, more than one major aftershock can occur. The damage state after $event_i$ is dependent on not only maximum storey drift ratio by the $event_i$, but also residual storey drift ratio by $event_{i-1}$ (Iervolino *et al.*, 2016). Therefore, considering incremental drift ratio is useful for defining the damage state of buildings immediately from the $event_{i-1}$ to the $event_i$.

In this study, three EDPs, i.e. ResISDR, MaxISDR, and MaxIISDR, are discussed. The SAWS model computes the displacement time-history of each shear wall, represented by a nonlinear spring (**Figure 4-2**). For an earthquake sequence consisting of *m* events, $MaxISDR_i$ is defined as the maximum absolute displacement among the walls on the ground floor over the height of the ground floor for the *i*-th excitation, $ResISDR_i$ is the permanent displacement among the walls on the ground floor over the height of the ground floor after the *i*-th excitation, and $MaxIISDR_i$ is the maximum difference between $MaxISDR_i$ and $ResISDR_i$ for the *i*-th excitation.

Figure 4-3(a) illustrates a mainshock-aftershock sequence from the Tohoku sequence, and **Figure 4-3**(b) and (c) display the structural displacement response time-history and hysteretic response, respectively, using the UBC-SAWS model for Wall 1 on the ground floor of House 4. In the figure, the maximum, residual, and maximum incremental displacements of Wall 1 are indicated. $MaxISDR_1$ and $MaxIISDR_1$ of the first event are identical, because the residual displacement before the first event is zero.

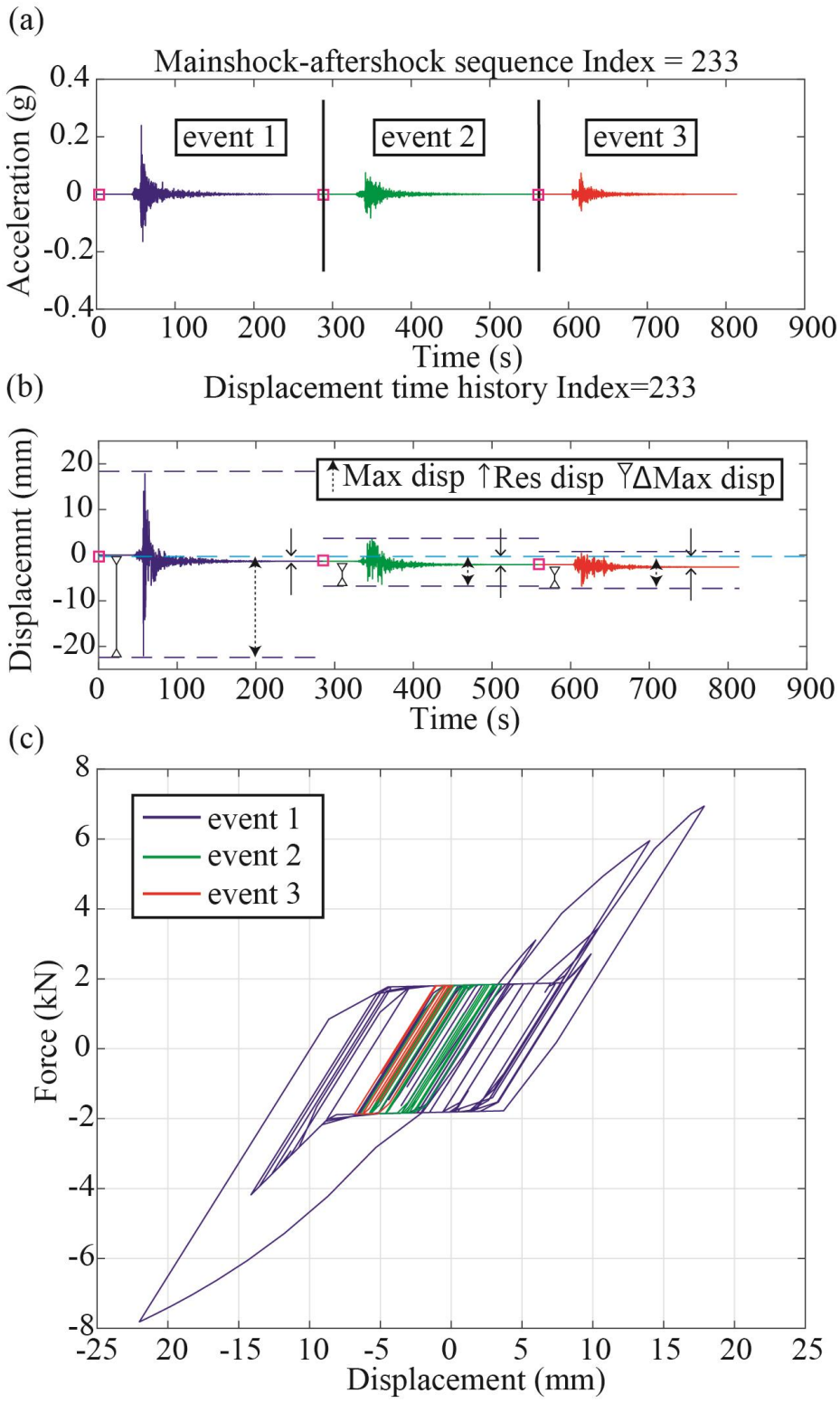

Figure 4-3. (a) An example of the 2011 Tohoku mainshock-aftershock sequence with (b) the displacement response time-history of House 4 of the maximum displacement (Max disp), the residual displacement (Res disp) and the incremental maximum displacement (Δ Max disp), and (c) hysteretic response plot.

4.2.4 IMs

The IM is an important parameter that links the seismic hazard intensity of a ground motion record with the response of the structure from the seismic demand model (**Equation (4-1)**). The IM should be evaluated based on the scope of the study and a perfect IM that works for all structure types is infeasible. An ideal IM should have small variability associated with predicted values of EDPs that represent structural responses of the UBC-SAWS models. IMs that are considered in this study are summarised in **Table 4-2**. The first three IMs (AI, CAV, and PGV) represent the specific characteristics of ground motion records, which are referred to as non-structure-specific IMs (Mollaioli *et al.*, 2013; Ebrahimian *et al.*, 2015).

Conventionally, Sa(T) has been widely used for seismic design codes and guidelines in North America and Europe (e.g., FEMA and EC8). Sa(T) is well correlated with the structural response of elastic MDOF systems (Kostinakis *et al.*, 2017). However, recent studies show that Sa(T) is not the most suitable IM for tall buildings with long vibration periods, because higher modes of tall buildings have significant effects on the structural response (Shome *et al.*, 1998; Luco and Cornell, 2007). Since Sa(T) only represents the fundamental period of the structure and the period of the structure could be changed due to its nonlinear behaviour, spectral intensity (SI) may be more suitable as it accounts for spectral velocities over a period range from 0.1 s to 2.5 s (Housner, 1952). Riddell (2007) showed that SI is the best IM among IMs in the intermediate period range.

Table 4-2. Summary of IMs in this study.

Notation	Description	Equation	Unit	Reference
AI	Arias intensity	$AI = \frac{\pi}{2g}\int_0^{t_{max}} a(t)^2 dt$	m/s	Arias (1970)
CAV	Cumulative absolute velocity	$CAV = \int_0^{t_{max}} \lvert a(t)\rvert dt$	g-s	EPRI (1988)

PGV	Peak ground velocity	$PGV = \max \lvert v(t) \rvert$	m/s	Trifunac and Brady (1975)
Sa(T)	Pseudo-spectral acceleration	$Sa = acceleration\ spectrum\ (T, \xi = 0.05)$ where ξ is the damping ratio	g	E.g., Chopra (2001)
SI	Spectral intensity	$SI = \int_{0.1}^{2.5} S_v(T, \xi = 0.05) dT$ where $S_v = S_a \times \frac{T}{2\pi}$	m	Housner (1952)

4.2.4.1 *Evaluation of IMs*

To evaluate different IMs, various studies have focused on the efficiency, sufficiency, and relative sufficiency of IM (Luco, 2002; Luco and Cornell, 2007; Jalayer *et al.*, 2012). Efficiency means that the prediction variability of EDP is small given IM, which can potentially reduce the number of structural response analyses. Consider a linear relationship between IM and EDP in logarithmic scale (base 10):

$$\log_{10}(EDP) = \log_{10}(a_{IM}) + b_{IM} \times \log_{10}(IM) \quad (4\text{-}2)$$

where a_{IM} and b_{IM} are the coefficients of the linear regression. The efficiency is calculated by (Ebrahimian *et al.*, 2015):

$$\beta_{IM} = \sqrt{\frac{\sum_{i=1}^{m}(\log_{10}(EDP_i) - \log_{10}(a_{IM} \times IM_i^{b_{IM}}))^2}{m-2}} \quad (4\text{-}3)$$

Sufficiency of IM indicates that the EDP is independent of other explanatory variables, such as rupture distance and magnitude, when IM is taken into account. Therefore, if IM is sufficient, as implied in **Equation (4-1)**, the inclusion of other variables, in addition to the main IM, does not affect the distribution of EDP. To evaluate the sufficiency of IM, the residual (Res_{IM}) between IM and EDP from **Equation (4-2)** is calculated as:

$$Res_{IM} = \log_{10}(EDP) - \log_{10}(a_{IM} \times IM^{b_{IM}}) \quad (4\text{-}4)$$

Following that, the dependency of Res_{IM} on rupture distance (R_{rup}) and magnitude (M) can be examined by:

$$Res_{IM} = c_{IM} + d_{IM} \times \log_{10}(R_{rup}) \quad (4\text{-}5)$$

$$Res_{IM} = c_{IM} + d_{IM} \times M \tag{4-6}$$

where c_{IM} and d_{IM} are the coefficients of the regression. The sufficiency of IM can be quantified by the significance level (p_{IM}-value) for d_{IM} (Luco, 2002).

Moreover, Jalayer *et al.* (2012) proposed relative sufficiency as a measure to compare the sufficiency between different IMs based on the concept of relative entropy from information theory. The relative sufficiency between two IMs is calculated by:

$$I\left(IM_j \middle| IM_k\right) = \frac{1}{m} \times \sum_{i=1}^{m} log_2 \left(\frac{\beta_{IM_k}}{\beta_{IM_j}} \frac{\phi\left(\frac{\log_{10}(EDP_i) - \log_{10}(a_{IM_{j.i}} \times IM_{j.i}^{b_{IM_{j.i}}})}{\beta_{IM_j}} \right)}{\phi\left(\frac{\log_{10}(EDP_i) - \log_{10}(a_{IM_{k.i}} \times IM_{k.i}^{b_{IM_{k.i}}})}{\beta_{IM_k}} \right)} \right) \tag{4-7}$$

where IM_j and IM_k represent different IMs, and β_{IM} is calculated from **Equation (4-3)**.

4.2.5 Methods to develop seismic fragility curves

The formulations of the cumulative lognormal distribution and multinomial distribution are described in this section for the development of fragility curves.

4.2.5.1 *Cumulative lognormal distribution*

The cumulative lognormal distribution has been widely used to fit seismic fragility curves (e.g. Baker, 2015). The advantages of using the cumulative lognormal distribution for the fragility curve fitting are that (1) it is easy to apply because it has a simple format with a median and a logarithmic standard deviation as model parameters, and (2) it usually fits the data reasonably well (Porter *et al.*, 2006). The cumulative lognormal distribution is defined as:

$$P\ (IM) = \Phi\left(\frac{\ln\left({}^{IM}/_{\theta_{IM}} \right)}{\beta_{IM}} \right) \tag{4-8}$$

where Φ is the standard normal distribution, θ_{IM} is the median value of the fragility curve, and β_{IM} is calculated from **Equation (4-3)**.

4.2.5.2 *Multinomial distribution*

The multinomial distribution has been applied to recent studies on fragility modelling (Charvet *et al.*, 2014; De Risi *et al.*, 2017). In comparison with the cumulative lognormal distribution, the advantages of the multinomial distribution are that (1) the multinomial distribution does not require binning the IM, so the pair of IM_i and post-DS_i given the same pre-DS can be used as the input directly to estimate the coefficient of the multinomial distribution, and (2) since the multinomial distribution can accommodate the hierarchical nature of damage state severity, derived fragility curves do not intersect. The multinomial probability distribution is given by:

$$P(DS_i) = \frac{1}{\prod_{j=1}^{nDS} y_{ij}!} \cdot \prod_{j=1}^{nDS} \pi_{ij}^{y_{ij}} \quad (4\text{-}9)$$

where *nDS* is the total number of DS, y_{ij} is the number of data points in the *i*th IM falling in DS*j*, and π_{ij} is the probability that the *i*th observation is in DS*j*. The systematic component of the model is:

$$f(\pi_{ij}) = \theta_{j,0} + \sum_{k=i}^{nP} \theta_{j,k} \cdot \chi_k \quad (4\text{-}10)$$

where θ is the regression parameter, *nP* is the number of explanatory variables χ. The explanatory variable can be IM, structure type, and pre-DS if a large number of data points are available.

4.2.6 Aftershock fragility curves

Recent studies have developed aftershock fragility curves to account for the cumulative damage due to aftershocks. Ebrahimian *et al.* (2014) combined a temporal epidemic type aftershock sequence (ETAS) model with aftershock fragility curves of structural collapse to conduct seismic risk forecasting for rapid decision-making. The 2009 L'Aquila earthquake sequence was considered as an example and therefore ground motions from the L'Aquila earthquake sequence alone were used. The structural model was progressively damaged until

it reached a collapse damage state by the aftershock record selected from a record pool. This is referred to as sequential cloud analysis. Subsequently, Jalayer and Ebrahimian (2017) used a larger ground motion record dataset (see **Table 4-1**) to develop a comprehensive framework to assess the time-dependent risk due to cumulative damage of mainshock-aftershock sequences. Although the real mainshock and aftershock records are used, the aftershock sequence was built from the pool of aftershocks. Therefore, the actual sequence was not considered in their studies.

To estimate the state-dependent fragility curves of aftershocks, the method proposed by Luco *et al.* (2004) can be adopted. A general procedure is as follows:

(1) Damage states are pre-defined in terms of pre-EDP.

(2) Mainshock records are scaled to reach each damage state.

(3) Aftershock IDA is used to estimate the residual capacity of mainshock-damaged buildings for each damage state.

(4) The state-dependent fragility curves are produced by the median values of the residual capacities.

The state-dependent fragility curve can be applied to building-tagging and seismic loss estimation. However, two aspects could be further investigated for the development of state-dependent aftershock fragility curves of wood-frame houses in Canada under M9.0 sequences. Firstly, the back-to-back approach of aftershock records which was implemented in Luco *et al.* (2004) may not be able to capture the realistic characteristics of aftershocks. To assess the cumulative damage from both subduction and crustal earthquakes, real mainshock-aftershock records are desirable. Secondly, the computation cost of IDA is high. For a given DS, by considering only 30 mainshock records and 11 scaling factors, 9900 runs of nonlinear dynamic analysis (30 records × 30 records ×11 scaling factors) are required for each building. In this chapter, to avoid the overestimation of the EDP from the back-to-back approach and the high

computational cost from aftershock IDA, cloud analysis with an extensive mainshock-aftershock record database (e.g., Goda *et al.* 2015) is applied to the UBC-SAWS model. The novelties of this chapter are (1) a large number of real crustal and subduction ground motion records with 596 mainshock-aftershock sequences are used **(Section 4.3.2**). (2) Different combinations of EDPs and IMs are tested to represent the pre-EDP-IM-post-EDP set (**Sections 4.3.4** and **4.3.5**) using the 596 real mainshock-aftershock sequences. (3) A new method considering the pre-EDP-IM-post-EDP is adopted to develop the state-dependent fragility curves (**Section 4.4**). Since the DSs can be linked with pre- and post-EDPs, the 3D dataset (pre-EDP-IM-post-EDP) is binned based on the pre-DS, and the post-DS aftershock fragility curves for each pre-DS are developed using the cumulative lognormal distribution and multinomial distribution.

4.3 Evaluation of EDPs and IMs using real ground motion records

To develop state-dependent aftershock fragility curves in **Section 4.4**, this section presents exploratory phases of the model development by introducing pre-EDP, describing the real mainshock-aftershock record dataset, investigating the suitability of EDPs for pre-EDP and post-EDP, and evaluating the efficiency and sufficiency of IMs. In order to link the damage states before and after each event and estimate the cumulative damage after an earthquake sequence, several measures of pre-EDP are combined with IM and post-EDP in **Section 4.3.1**. This leads to a 3D plot of pre-EDP, IM, and post-EDP. Since pre-EDP for a mainshock is zero and the majority of studies from literature focuses on mainshocks only, a relationship between IM and post-EDP due to mainshocks and a relationship of pre-EDP-IM-post-EDP due to aftershocks are presented separately. Next, the real mainshock-aftershock record dataset from Goda and Taylor (2012) and Goda *et al.* (2015) is described in **Section 4.3.2**. To link the results from other studies with this study, the mainshock damage assessment (2D post-EDP and IM

plots) is compared with the previous study of Goda and Salami (2014) in **Section 4.3.3**. Subsequently, all combinations of pre-EDPs, IMs, and post-EDPs from aftershocks are discussed in **Section 4.3.4**. Finally, the efficiency and sufficiency IMs are evaluated in **Section 4.3.5**. The geometric mean of IMs in two horizontal components is used for the evaluation of IM and the development of the fragility curves in **Sections 4.3** and **4.4**, respectively.

4.3.1 Pre-EDP

The conventional seismic fragility assessment for mainshock ground motions requires IM and post-EDP (e.g., only $event_1$ in **Figure 4-4**). In this study, to derive state-dependent aftershock fragility curves, pre-EDP needs to be specified. **Figure 4-4** shows an example of the 2011 Tohoku mainshock-aftershock sequence with the displacement response time-history of House 4. Four pairs of pre- and post-EDPs can be obtained from four events in this sequence. Pre-EDP_{i-1} links EDPs before and after the $event_i$. The pre-EDP is necessary to investigate the progressive damage due to the mainshock-aftershock records. In this study, rather than selecting aftershock records from mainshocks (Luco *et al.*, 2004), real mainshock-aftershock ground motion records are used and described in the next subsection to evaluate the structure response before and after each event.

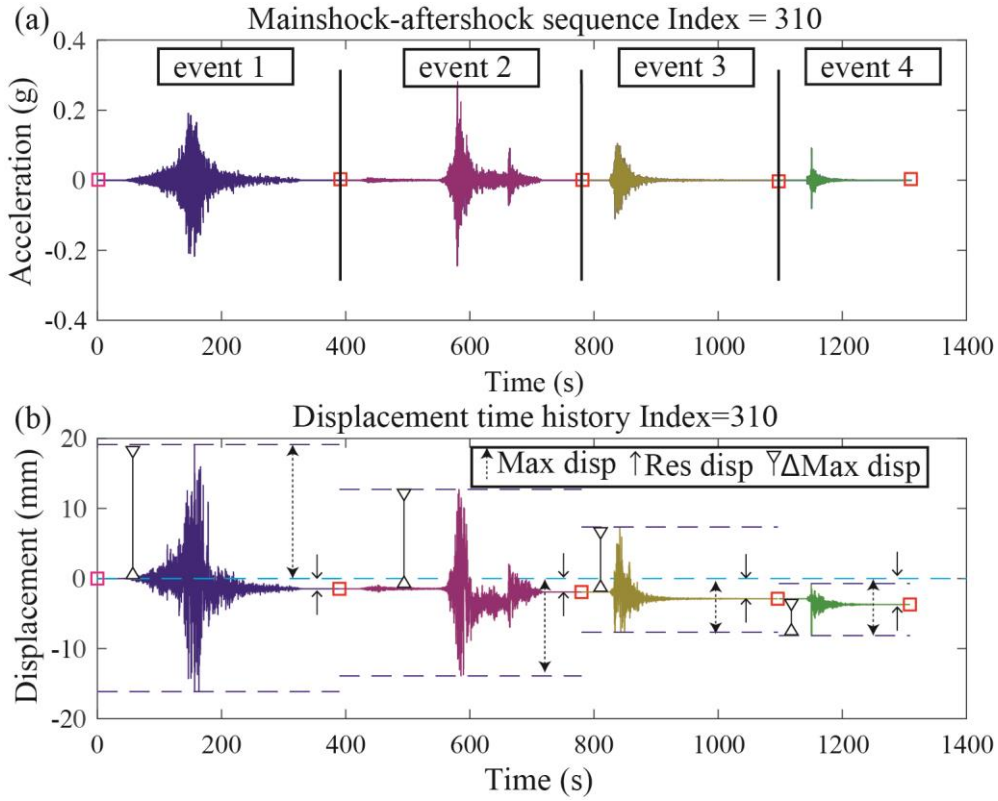

Figure 4-4. (a) An example of the 2011 Tohoku mainshock-aftershock sequence with (b) the displacement response time-history of House 4 of the maximum displacement (Max disp), the residual displacement (Res disp) and the incremental maximum displacement (Δ Max disp).

4.3.2 Ground motion records

The ground motion records from Goda and Taylor (2012) and Goda *et al.* (2015) are used in this study, which consist of 606 mainshock-aftershock sequences of real earthquakes. 10 sequences are removed, because the number of events in the sequences is more than 20. The magnitude-distance plots of the 596 mainshocks (with filled colours) and 1685 aftershocks (with unfilled colours) are shown in **Figure 4-5** by classifying crustal event records from the NGA database, and crustal, interface, and inslab event records from the K/KiK/SK-net database. Crustal earthquakes from the NGA and K/KiK/SK-net databases have lower magnitudes and shorter distances than the interface and inslab events from the K/KiK/SK-net database.

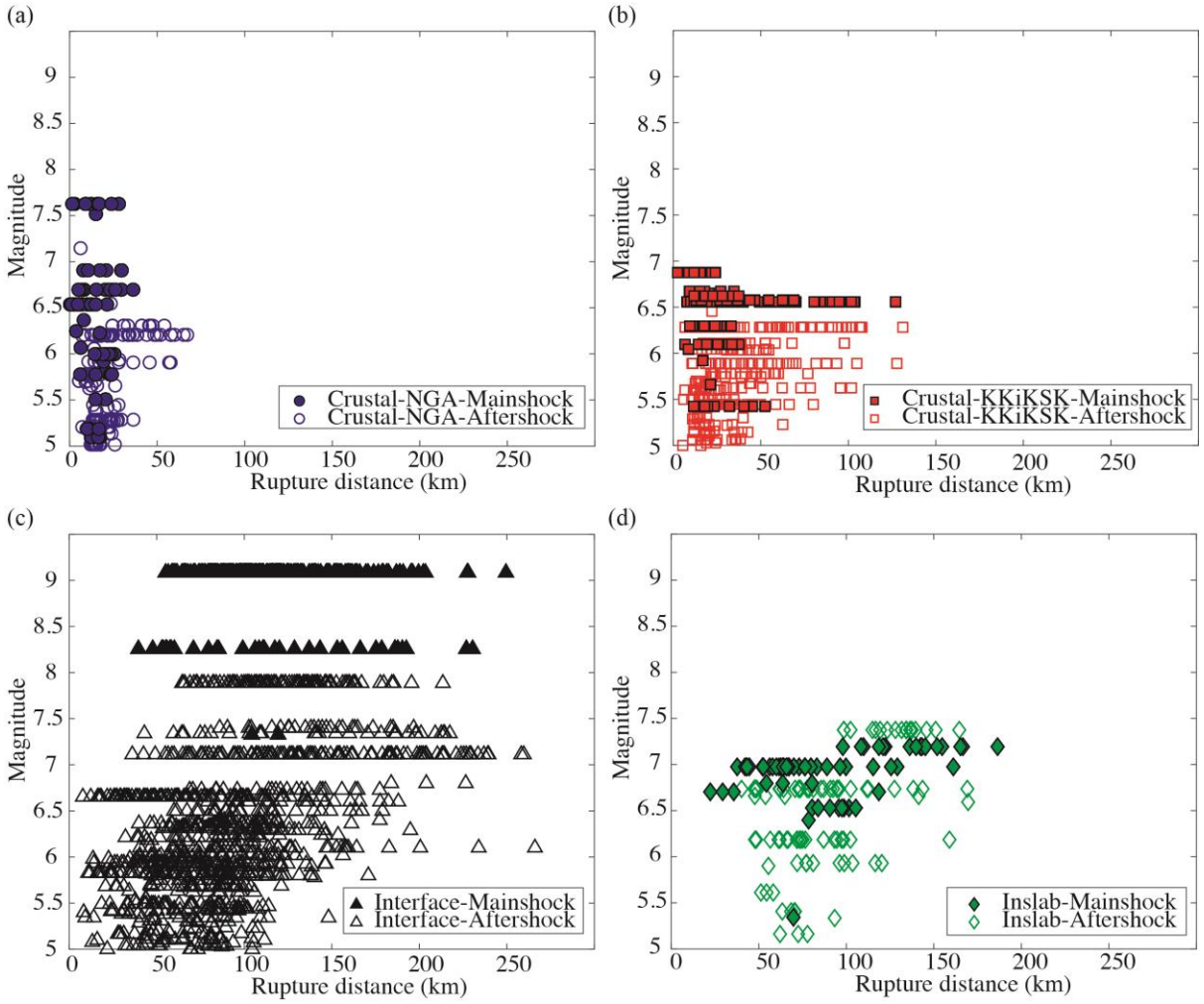

Figure 4-5. Magnitude-distance plot of the mainshocks (with filled colours) and aftershocks (with unfilled colours) including (a) crustal-NGA, (b) crustal-KKiKSK, (c) interface, and (d) inslab events. Rupture distance is the closest distance from the earthquake rupture plate to the site.

In comparison with the 290 mainshock-aftershock records from Goda and Salami (2014) with the magnitude range of 5.5-8.0 and rupture distance<200km, the 596 records from this study have some lower magnitude events less than 5.5 from all types of events, and include the 2011 M9.0 Tohoku sequences with rupture distances up to 270km. There are 2281 records (202 crustal NGA records, 374 crustal-K/KiK/SK records, 1538 interface records, and 167

inslab records) from 596 sequences × 2 horizontal components, thus 4562 pre-EDP-IM-post-EDP triplets (1192 mainshocks and 3370 aftershocks) can be obtained.

The design spectrum with site class C in Victoria (Halchuk *et al.*, 2014) and response spectra with median and 16^{th}/84^{th} percentiles of mainshocks and aftershocks are shown in **Figure 4-6**(a). Because some large subduction earthquake records (e.g., the 2011 Tohoku event with Mw 9.0) were recorded hundreds of kilometres away from the record stations, the response spectra of the mainshocks is not strong in comparison with the design spectra. The response spectra of the mainshocks are generally higher than those of the aftershocks. Such inherent characteristics of natural records should be automatically incorporated in developing state-dependent seismic fragility curves using the above defined sets of mainshock-aftershock series. **Figure 4-6**(b) shows the response spectra of median and 16^{th}/84^{th} percentiles of all earthquake types. The expected spectral shape of near crustal events from proper ground motion selection (e.g., CMS in Figure 4 from Goda and Atkinson (2011)) should have a high Sa in the short vibration period, while the response spectra of large interface events with M≥8 should dominate the long vibration period. However, considering the longer rupture distance and wider magnitude range from all 596 sequences in this study, the response spectra from crustal-KKiKSK, interface, and inslab events are similar. Only the crustal-NGA events with the mainshock rupture distance less than 50km have a higher Sa in the long vibration period.

Given the median response spectra of aftershock are small in comparison with the mainshock, scaling factors are necessary to ensure the structure reaches collapse state for the development of fragility curves. Unlike other IDA studies (Goda and Atkinson, 2011; Goda and Salami, 2014) that performed detailed record selection (e.g., CMS) and allowed high scaling factors up to 10, this study uses cloud analysis with 596 mainshock-aftershock sequences. Vamvatsikos and Cornell (2002) indicated that the sufficiency of IM is important to allow a high scaling factor for record scaling. In this study by evaluating different IMs and

EDPs from **Sections 4.3.4** and **4.3.5**, respectively, moderate scaling factors (e.g., scaling factors less than 5 for the whole mainshock-aftershock sequences) are considered to be acceptable for cloud analysis, as suggested by other studies (Lagaros and Fragiadakis, 2007; Goda and Salami, 2014).

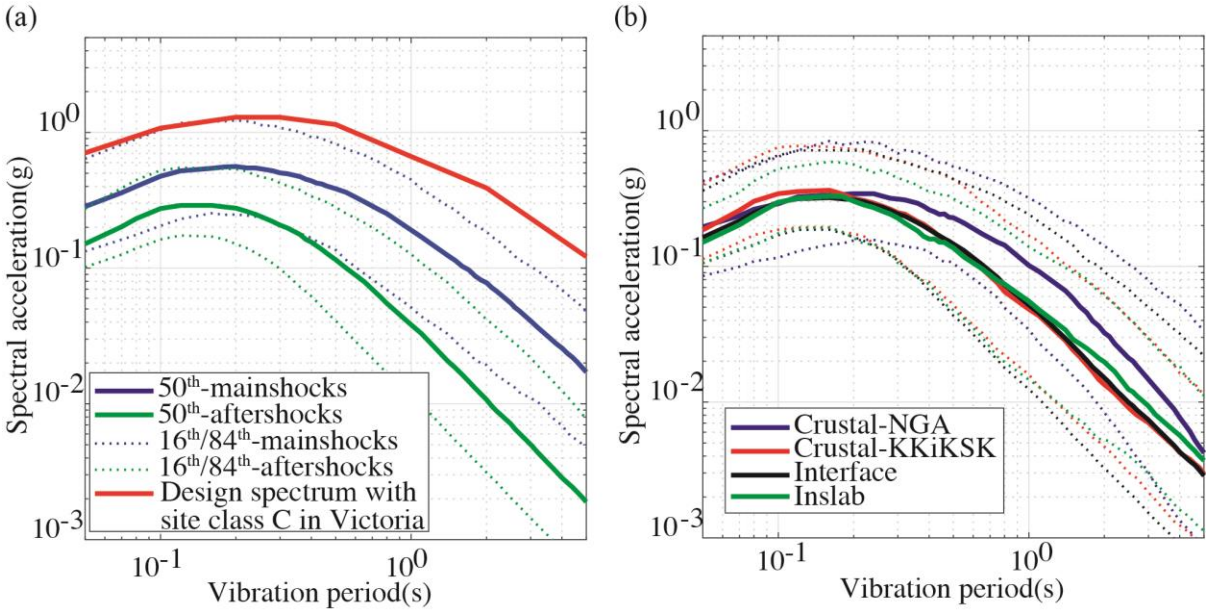

Figure 4-6. Response spectra (a) of mainshocks and aftershocks with 16th, 50th, and 84th percentiles, and design spectrum with site class C in Victoria (b) of different earthquake types from both mainshocks and aftershocks with 16th, 50th, and 84th percentiles.

4.3.3 Mainshock EDP-IM

Goda and Salami (2014) assessed the effects of aftershocks on the structural demand analysis of the UBC-SAWS model by comparing MaxISDR of mainshock with the highest MaxISDR after mainshock-aftershock sequences. They considered Sa(T=0.3s) as the IM for the fragility assessment of Houses 1-4, because this period is in the middle of the fundamental periods of Houses 1-4 (Goda and Atkinson, 2011). To contrast this study with Goda and Salami (2014) and show that the record selection is appropriate for the structural response analysis, the IM-EDP plot of House 4 of the mainshocks (the first event of the sequence) is compared with the

IM-EDP plots of IDA approach and cloud analysis from Goda and Salami (2014) in **Figure 4-7**. The scaling factors 1-5 are applied to the 596 mainshocks which are identical to the scaling factors considered by Goda and Salami (2014) in their cloud analysis.

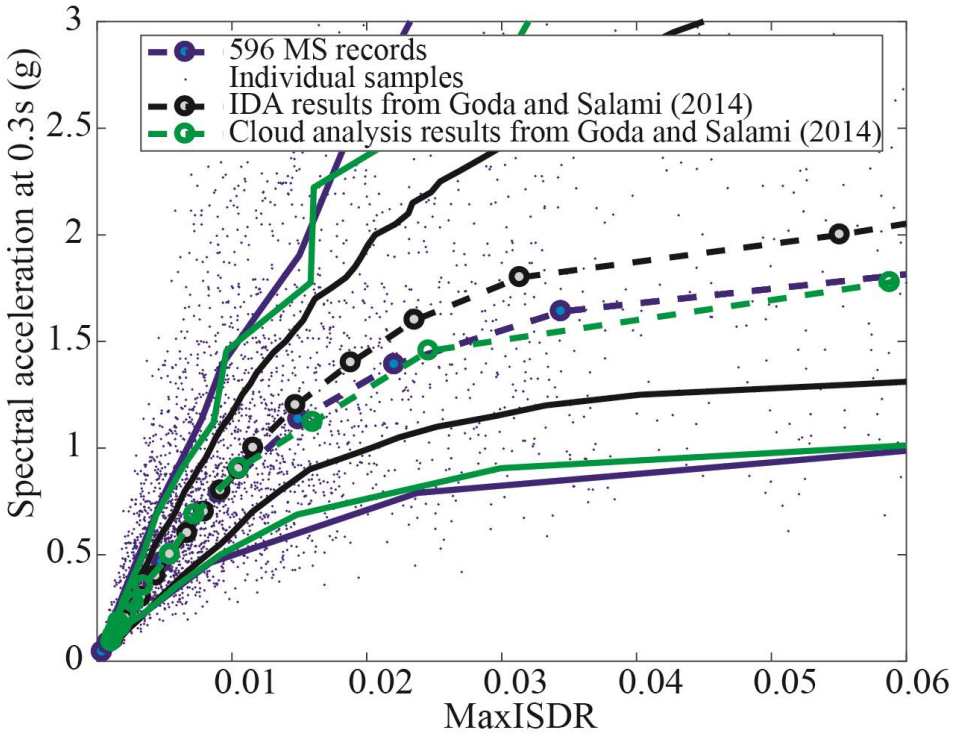

Figure 4-7. IM-EDP plots of mainshocks of this study and Goda and Salami (2014).

In **Figure 4-7**, the median values of IM-EDP plots between this study and the cloud analysis results from Goda and Salami (2014) show a good agreement. However, the median values of the MaxISDR with Sa(T=0.3s)>1g of the IDA results from Goda and Salami (2014) are lower than this study. An explanation is that given the median Sa(T=0.3s) of mainshock equals to 0.5g in **Figure 4-6** and the scaling factors 1-5 are applied in the cloud analysis, more points from the cloud analysis are in Sa(T=0.3s)<1.5 in comparison with IDA results from Goda and Salami (2014). Therefore, higher damage is observed for MaxISDR>1% in the cloud analysis. In addition, similar large scatter is observed from the cloud analysis of both studies. This is because the cloud analysis from this study and Goda and Salami (2014) added more

mainshock-aftershock records (see **Figure 4-5**) in comparison with 50 mainshock-aftershock sequences for IDA. Consequently, the consideration of a wider range of ground motion records results in wider scatter of the IDA results in terms of 16^{th} and 84^{th} percentile curves (solid lines). Applying scaling factors 1-5 to the updated 596 mainshock-aftershock sequences is considered to be appropriate, because the IM-EDP plot from this study are in the similar range of Goda and Salami (2014).

4.3.4 Evaluation of EDPs

Different combinations of EDPs for pre- and post-earthquake conditions are assessed by focusing upon three EDPs, i.e. MaxISDR, MaxIISDR, and ResISDR. In total, 9 combinations of pre-EDP and post-EDP are considered. Sa(T=0.3s) at the fundamental period of the SAWS model is considered to visualise 9 pre-EDPs and post-EDPs using unscaled records from the UBC-SAWS House 4 model in **Figure 4-8**.

Individual pre-EDP_i should represent the damage state of the structure from $event_1$ to $event_i$. In other words, since IM is the only input of the current fragility simulation framework, pre-EDP that only represents the damage state of individual $event_i$ is not suitable for the state-dependent aftershock fragility curves. For example, MaxIISDR might not be appropriate as pre-EDP, because for an earthquake sequence with the total number of *m* events, the ideal pre-EDP for $event_i$ ($i<m$) should represent the pre-condition of the structure (i.e. cumulative effect) from the first event ($event_1$) of the earthquake sequence to $event_{i-1}$. However, $MaxIISDR_i$, which estimates the structural response caused by IM_i from $event_i$, only describes the relative damage state between $event_{i-1}$ and $event_i$. Based on that, Cases 2 (pre-MaxIISDR and post-MaxISDR), 5 (pre-MaxIISDR and post- MaxIISDR), and 8 (pre-MaxIISDR and post-ResISDR) are excluded from fragility fitting.

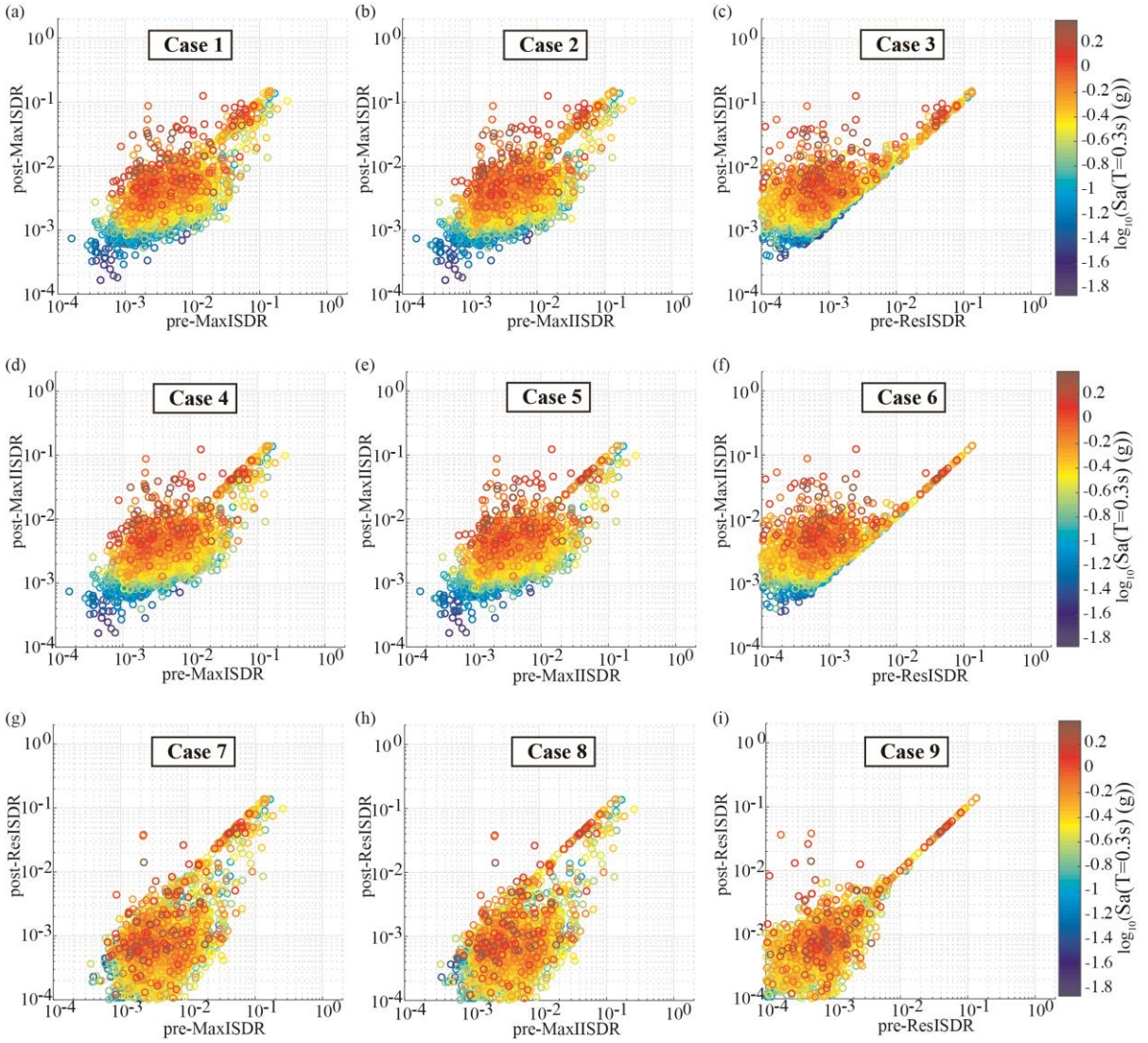

Figure 4-8. Plots of 9 Cases of post-EDPs against pre-EDPs colour-coded based on $\log_{10}(Sa(T=0.3s))$ for House 4 (a) pre-MaxISDR and post-MaxISDR, (b) pre-MaxIISDR and post-MaxISDR, (c) pre-ResISDR and post-MaxISDR, (d) pre-MaxISDR and post-MaxIISDR, (e) pre-MaxIISDR and post- MaxIISDR, (f) pre-ResISDR and post-MaxIISDR, (g) pre-MaxISDR and post-ResISDR, (h) pre-MaxIISDR and post-ResISDR, (i) pre-ResISDR and post- ResISDR.

An ideal pair of pre-EDP and post-EDP for developing state-dependent fragility curves should include as many IM-EDP points as possible to have a robust development of the fragility curve, and a higher pre-EDP should correspond to a higher post-EDP to represent the

cumulative damage due to an earthquake sequence. To include more IM-EDP points for the development of the fragility curves, the EDP pairs of Cases 3 (pre-ResISDR and post-MaxISDR), and 6 (pre-ResISDR and post-MaxIISDR) are more suitable than Cases 1, 4, 7, and 9. This is because the points in Cases 1, 4, 7, and 9 need to be divided into two parts which are pre-EDPs>post-EDPs and pre-EDPs<post-EDPs, respectively. The former would be no damage scenario and only the latter part can be used for the aftershock fragility development. On the other hand, when Cases 3 and 6 are considered in **Figure 4-8**(c) and (f), since the absolute maximum displacement is always larger than the absolute residual displacement, all points can be used for the development of the fragility curves, resulting in more robust curve fitting.

Cases 3 and 6 seem the most suitable options for the development of aftershock fragility curves. However, an issue in applying Case 6 is that the post-DS definitions of the MaxIISDR may need to change with the pre-ResISDR. In other words, the damage state associated with MaxIISDR is not constant given different pre-DSs, because the $MaxIISDR_i$ only represents the response of $event_i$. Considering the MaxIISDR has not been widely used in comparison with the MaxISDR, therefore in this study only Case 3 (pre-ResISDR and post-MaxISDR) is considered to represent pre- and post-EDPs in the following.

4.3.5 Evaluation of IMs

To evaluate different IMs, metrics for efficiency, sufficiency, and relative sufficiency are calculated for Sa(T=0.05s-5s), AI, CAV, PGV, and SI. The non-collapse EDP values (Christovasilis *et al.*, 2009a) are used for the evaluation of IMs from the unscaled records of mainshock-aftershock sequences. The efficiency is checked based on **Equation (4-3)** from **Section 4.2.4**. A small β_{IM} indicates less variability of the IM-EDP relationship (i.e., higher predictability). The values of β_{IM} in a range of 0.2 to 0.3 and 0.3 to 0.4 are considered as a good

and acceptable IM in terms of efficiency, respectively (Mollaioli *et al.*, 2013). According to **Figure 4-9**(a), Sa(T=0.3s-0.5s), PGV, and SI are more efficient than others.

Next, the sufficiency of IMs is checked against source parameters (rupture distance and magnitude). p_{IM} captures the statistical independence between the source parameters and IM given $p_{IM}>0.05$. The sufficiency of IMs in terms of rupture distance and magnitude is shown in **Figure 4-9** (b) and (c), respectively. Sa with periods 0.2-2s, PGV, and SI are good candidates of IM. On the other hand, Sa with periods 0.05-0.2s and 2-5s, AI, and CAV show a high dependence on the source parameters, which indicates that these IMs are not appropriate for use as sole IM for the fragility curve fitting for the wood-frame houses.

The relative sufficiency is plotted in **Figure 4-9** (d) to rank different IMs. The fundamental period of the wood-frame house (T=0.3s) is considered as a reference IM, therefore, the relative sufficiency of Sa (T=0.3s) is 0. Sa values with periods T=0.32-1s, PGV and SI have superior performance than Sa(T=0.3s). Especially, Sa(T=0.4-0.5s) and PGV have the highest relative entropy. This suggests the period elongation of the damaged structure in comparison with the fundamental period of 0.3s.

The efficiency, sufficiency, and relative sufficiency of Houses 1-3 are provided in **Appendix F.** For Houses 1-3, PGV does not improve the relative sufficiency for the UBC-SAWS House 1-3 models, whereas p_{IM} is lower than 0.05 given rupture distance for all IMs. This suggests that the prediction of EDP may be improved by including information on rupture distance but not on magnitude for Houses 1-3 with higher seismic resistance. This might be because some large subduction earthquake records (e.g., the 2011 Tohoku event with M9.0) were recorded hundreds of kilometres away from the record stations, and the IM is not sensitive to magnitude due to the long rupture distance.

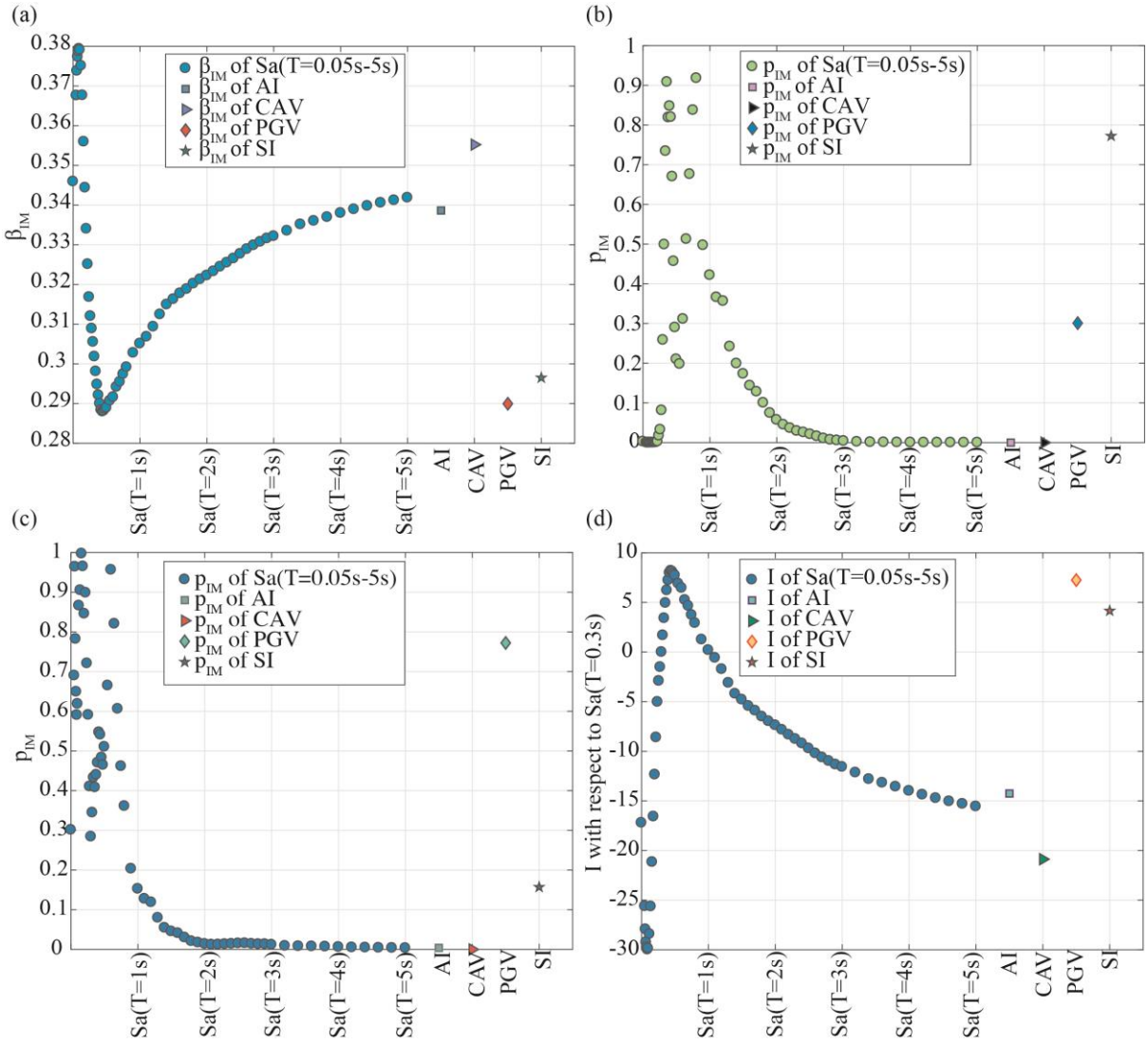

Figure 4-9. Plot of (a) efficiency (β_{IM}), sufficiency (p_{IM}) for (b) rupture distance and (c) magnitude, and (d) relative sufficiency of each IM given the non-collapse EDP with unscaled records for House 4.

The most suitable IMs based on the relative sufficiency are Sa (T=0.3s, 0.36s, 0.4s, and 0.44s) for Houses 1-4, respectively. Since these preferred IMs are in the range of 0.3s-0.5s and PGV shows a good performance of House 4, in this study Sa (T=0.3s and 0.5s) and PGV are used to derive the state-dependent fragility curves in **Section 4.4**. In addition, the selection of the IM should also take into account the availability of the GMPEs, because a seismic risk assessment is carried out in **Chapter 5**. Sa(T) has been widely used as outputs from crustal and

subduction-zone earthquakes (e.g., Atkinson and Boore, 2003; Zhao *et al.*, 2006; Abrahamson *et al.*, 2014). Although PGV is not widely used for the subduction GMPEs based on the global dataset (Abrahamson *et al.*, 2016), other GMPEs for CSZ have considered PGV as the output (Ghofrani and Atkinson, 2014). In addition, SI seems to be an appropriate IM based on the results of sufficiency and efficiency. However, SI is calculated by taking the integral of spectral accelerations over a period range from 0.1 s to 2.5 s, which requires a high computational cost with the spatial correlation. In addition, the correlations between periods are also necessary; therefore, in this study SI is not considered in the development of aftershock fragility curves.

4.4 State-dependent fragility modelling

In this section, two DS definitions of the wood-frame houses, which are Case 1 (four DSs of immediate occupancy, life safety, collapse prevention, and collapse) and Case 2 (three DSs of building tagging consisting of Green, Yellow, and Red tags), are defined in **Section 4.4.1**. Subsequently, three approaches are described to develop the state-dependent fragility curves in **Section 4.4.2**. The first two approaches consider different methods of IM bin counts with the cumulative lognormal distribution, and the third approach uses the multinomial distribution for the aftershock fragility curve development. Using House 4, results of fragility curves are discussed by focusing upon IMs, DS definitions (Cases 1 and 2), and fitting approaches 1-3 as shown in **Sections 4.4.3**, **4.4.4**, and **4.4.5**, respectively. After defining the most suitable IM, DS definition, and fitting approach, the aftershock fragility curves of Houses 1-4 are provided in **Section 4.4.6**.

4.4.1 Pre- and post-DS definitions

This subsection defines DSs in terms of pre-ResISDR and post-MaxISDR of Houses 1-4. Various studies investigated the relationship between ResISDR and MaxISDR for different

types of structures, e.g., moment resisting steel frames and non-ductile reinforced concrete buildings (Christidis *et al.*, 2013; Tesfamariam and Goda, 2015b). For wood-frame houses, FEMA 356 (2000) defined DSs of wood stud walls based on MaxISDR. MaxISDR thresholds with DS_1-1%, DS_2-2%, and DS_3-3% are considered as immediate occupancy, life safety, and collapse prevention, respectively. Nazari *et al.* (2013) modified the DS definition of the wood-frame house from Christovasilis *et al.* (2009b). They considered MaxISDR thresholds with 1%, 2%, 4.5%, and 7% as DS_{1-4}. In terms of the collapse state (DS_4) associated with the MaxISDR, Christovasilis *et al.* (2009a) defined the collapse state of the SAWS model as MaxISDR>7%. Based on different shear wall types of wood-frame houses and record durations, Pan *et al.* (2018) defined the collapse state of the wood-frame houses (same hysteretic model as this study but with modified hysteretic parameters) based on the short and long durations of the records. Regarding the damage states associated with ResISDR, FEMA 356 (2000) considered DS_{1-3} of wood stud walls based on the ResISDR thresholds with 0.25%, 1%, and 3%, while FEMA P-58 (2014) suggested ResISDR of 0.2%, 0.5%, 1%, and 2% for DS_{1-4}. FEMA P-58 (2014) also suggested that MaxISDR should be larger than ResISDR until the collapse state, and eventually MaxISDR and ResISDR would converge at the collapse state.

On the other hand, in terms of building tagging for the post-earthquake evaluation, 3 tagging levels are usually considered, which are Green tag (unrestricted access), Yellow tag (restricted access), and Red tag (no access) (Bazzurro *et al.*, 2004). In this study, two cases of DS definitions are considered. (1) Case 1: the four DSs are defined first which correspond to the immediate occupancy, life safety, collapse prevention, and collapse in FEMA P-58 (2014). (2) Case 2: the three DSs associated with building tagging including Green tag, Yellow tag, and Red tag are defined (Bazzurro *et al.*, 2004; Yeo and Cornell, 2004).

Given the push-over analysis results of Houses 1-4 are significantly different in **Figure 4-2**, the DS thresholds of each house model should be defined individually based on the

literature and the IM-EDP results from this study. The following procedures are carried out to define the DSs for Cases 1 and 2 with MaxISDR and ResISDR of the Houses 1-4. The collapse states of ResISDR and MaxISDR are determined first:

- The collapse state associated with MaxISDR for Houses 1-4 is defined by taking the average collapse state limits of short and long record durations from Pan *et al.* (2018), which is 7%, 6%, 6%, and 5.5% for Houses 1-4 (**Table 4-3**). This is because the ground motion records used in that study include both short- and long-duration records, and the application of the fragility curves would focus on both crustal and subduction-zone earthquakes.
- The collapse state associated with ResISDR for Houses 1-4 is determined by the IM-EDP results from this study. The 3D dataset including pre-ResISDR, Sa(T=0.3s), and post-MaxISDR is binned by pre-ResISDR (0%-0.3%, 0.3%-0.5%, 0.5%-1%, 1%-2%, 2%-3%, 3%-4%, 4%-5%, 5%-6%, 6%-7%, and 7%-8%). The slope of log(Sa(T=0.3s)) and log(non-collapsed post-MaxISDR) given each binned pre-ResISDR is used to detect the change of post-MaxISDR as pre-ResISDR is close to the collapse state. The slope < 0.1 is considered as a stable trend of MaxISDR against IM, which leads to the collapse state associated with ResISDR 4%, 4%, 3%, and 3% for Houses 1-4.

By having the collapse state limits of ResISDR and MaxISDR, other DSs are defined by:

- Case 1: To calculate the $DS_{1\text{-}3}$ from DS_4 for both MaxISDR and ResISDR, the ratios between $DS_{1\text{-}3}$ and DS_4 are estimated based on the literature (Nazari *et al.*, 2013; FEMA P-58, 2014) and summarised in **Table 4-4**.
- Case 2: The ratios between 3 tagging levels and collapse state are also provided in **Table 4-4** based on the damage state descriptions from FEMA 356 (2000)

and Bazzurro *et al.* (2004). Green tag can be regarded to be equivalent as immediate occupancy (Bazzurro *et al.*, 2004). Yellow tag is the intermediate damage state between life safety and collapse prevention, because Yellow tag is defined for only acceptable entry for workers doing maintenance which is beyond the life safety (Yeo and Cornell, 2004). Red tag is the intermediate damage state between collapse prevention and collapse because Red tag forbids assess to a damage building and the building is assumed to be non-collapsed.

Table 4-3. Collapse state limits of Houses 1-4.

	House 1	House 2	House 3	House 4
ResISDR	4%	4%	3%	3%
MaxISDR	7%	6%	6%	5.5%

Two cases of DS definitions are summarised in terms of pre-ResISDR and post-MaxISDR in **Table 4-4**. The description of each damage state is also summarised in **Table 4-4** based on FEMA 356 (2000), the Static and Dynamic Testing of Shear Wall Panels Project for the UBC-SAWS model (Rudolf *et al.*, 1998), and the Earthquake 99 Wood-frame House Project EQ 99 Project (White and Ventura, 2006). Wall components that are described in **Table 4-4**, including wall frame, sheathing material, and hold down, are shown in **Figure 4-2**(a).

Table 4-4. Summary of DSs for Cases 1 and 2 associated with the lower limits of ResISDR and MaxISDR (CS=collapse state).

Case 1	DS_0	DS_1	DS_2	DS_3	DS_4
ResISDR	0.01%	0.10×CS	0.25×CS	0.50×CS	CS
MaxISDR	0.01%	0.10×CS	0.25×CS	0.50×CS	CS
Case 2	No damage	Green tag	Yellow tag	Red tag	
ResISDR	0.01%	0.10×CS	0.30×CS	0.70×CS	
MaxISDR	0.01%	0.10×CS	0.30×CS	0.70×CS	
DS	No damage	Immediate occupancy	Life safety	Collapse prevention	Collapse

Description of damage state	No damage is observed.	Minor cracks are observed in sheathing materials. Hairline cracks are observed in external walls.	Studs are attached to the sheathing at end but are easy to bend in the middle. Nails partially loose and are attached to the stud for OSB of Houses 1-3. Sheathing is detached in the middle. Glass is partially damaged.	Studs are not attached to sheathing for some shear walls. Nails are pulled out on the sheathing. Some sheathing failure. Some fasteners on GWB are pushed. Glass is significantly damaged. Hold downs are loose for Houses 1-2.	Ground floor of the house is collapsed.

A scatter plot of the evaluated EDPs (post-MaxISDR versus pre-ResISDR) with the unscaled records for House 4, which is colour-coded based on Sa(T=0.3s), is shown in **Figure 4-10**. Although, all 596 mainshock-aftershock sequences are included in the structural analysis, small sample sizes with the number of points less than 100 are observed with pre-$DS_{2\text{-}3}$ from Case 1. This indicates that the scaling factors are necessary to apply.

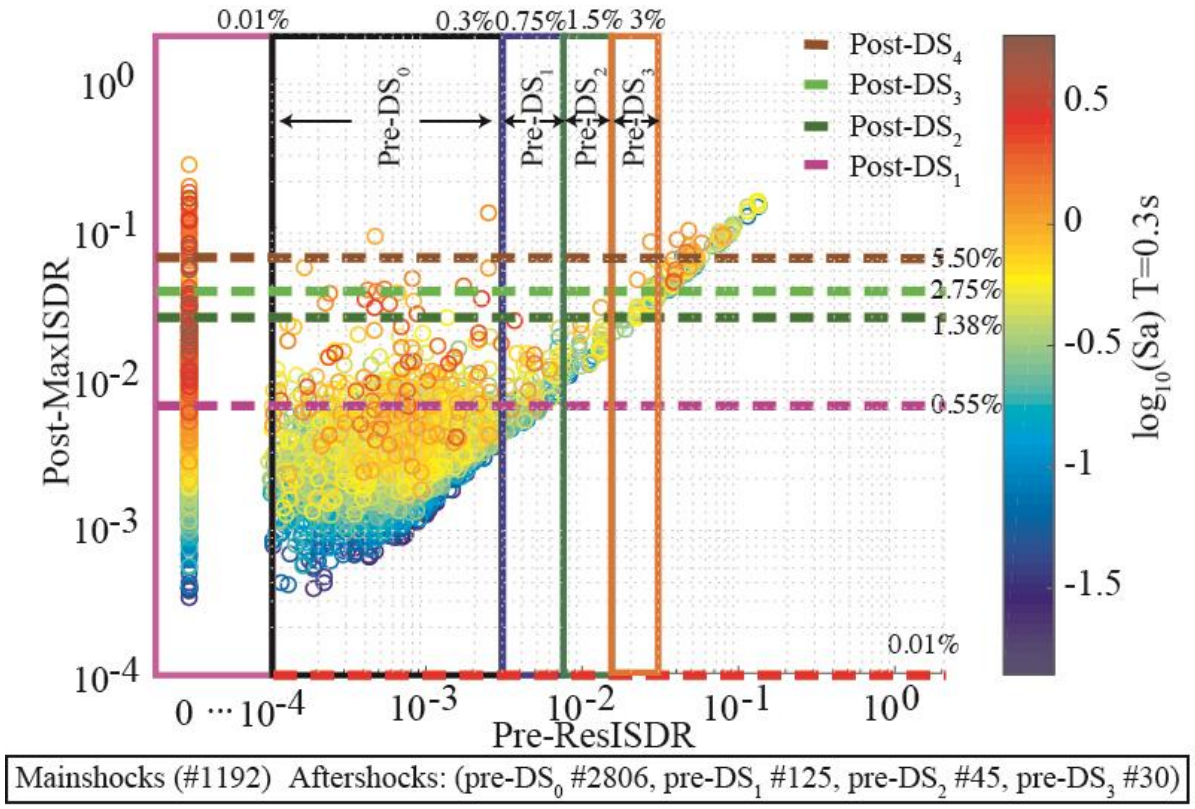

Figure 4-10. Plot of post-MaxISDR against pre-ResISDR with Sa(T=0.3s) for House 4 using unscaled records.

4.4.2 Procedures to develop the aftershock fragility curves

Due to a small number of data points of pre-$DS_{1\text{-}3}$ in **Figure 4-10**, the pre-EDPs, IMs, and post-EDPs with the scaling factors 1-5 are used; this leads to 4,562×5=22,810 points in total, including 5,960 and 16,850 data points for mainshocks and aftershocks, respectively. Since the frequency content of mainshocks are much different from those of the aftershocks (**Figure 4-6**), the mainshock fragility curves and the state-dependent aftershock fragility curves are produced separately. The DS definition based on Case 1 in **Table 4-4** is used as an example to show how the pre-EDP, IM, and post-EDP are processed to develop the fragility curves using the cumulative lognormal distribution and multinomial distribution from **Section 4.2.5**. A plot of post-MaxISDR against Sa(T=0.3s) for mainshocks only given pre-ResISDR=0% with post-$DS_{1\text{-}4}$ is shown in **Figure 4-11**(a).

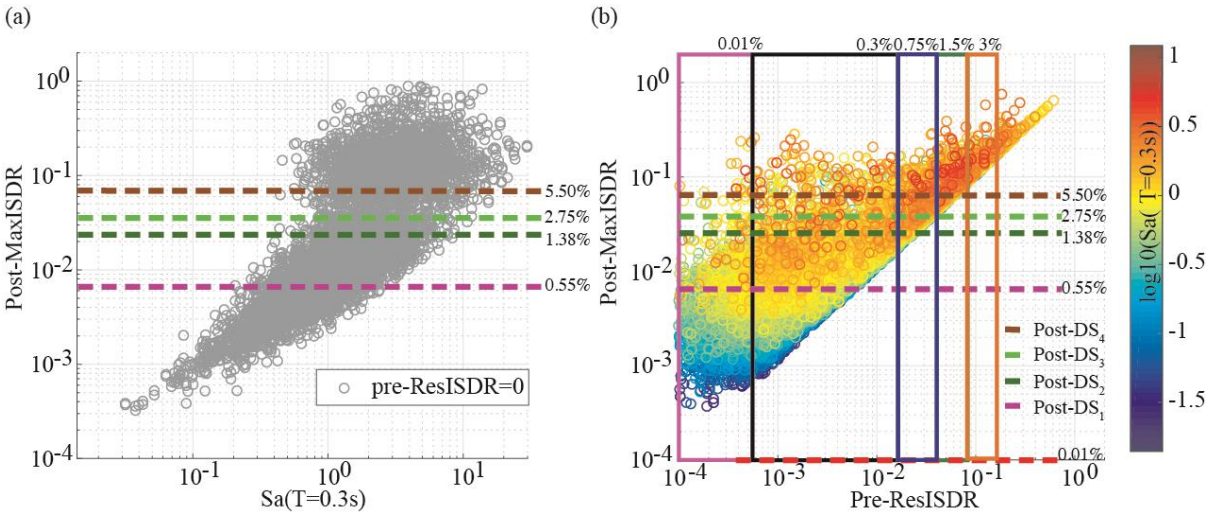

Figure 4-11. (a) Plot of post-MaxISDR against Sa(T=0.3s) of House 4 for mainshocks only (596 records × 2 horizontal components × 5 scaling factors=5960 points). (b) Plot of post-MaxISDR against pre-ResISDR for aftershocks (1685 records × 2 horizontal components × 5 scaling factors=16850 points).

Taking Case 1 for illustration, a procedure to develop the state-dependent fragility curves of aftershocks is as follows:

1. The 16,850 data points in **Figure 4-11**(b) are classified into pre-$DS_{0\sim3}$ based on the pre-ResISDR in **Table 4-4**. The subplots of Max-ISDR against Sa(T=0.3s) for pre-$DS_{0\sim3}$ are shown in **Figure 4-12**(a)-(d).
2. For each pre-DS_i (i=0, 1, 2, and 3), the number of post-MaxISDR>post-DS_i (i=1, 2, 3, and 4) (i.e. exceeding the damage threshold of the MaxISDR in **Table 4-4**) is counted.
3. To produce a fragility curve in a robust manner, three approaches are used to develop the fragility curves, the first two approaches consider two IM bin counting methods with the cumulative lognormal distribution:
    a. Approach 1: By looking at the histogram count of IM given pre-DS_i, fixed IM bins are defined for all pre-DSs in **Figure 4-12** to allow to fit consistently for all pre-DS_i given the same post-DS_i.
    b. Approach 2: the IM bins in **Figure 4-12** are defined such that the same number of data points of each bin is available. The number of data points in each bin is 5% of the total points given the same pre-DS but is constrained in the range of 50 - 200 in **Figure 4-12**.
    c. The fraction of post-EDP>post-DS_i (i=1, 2, 3, and 4) from Approaches 1 and 2 is used to develop the fragility curves associated with IM for each pre-DS (Baker, 2015).
4. Approach 3: Multinomial fitting is used to develop the post-DS curves with IM given the same pre-DS (Charvet *et al.*, 2014; De Risi *et al.*, 2017).

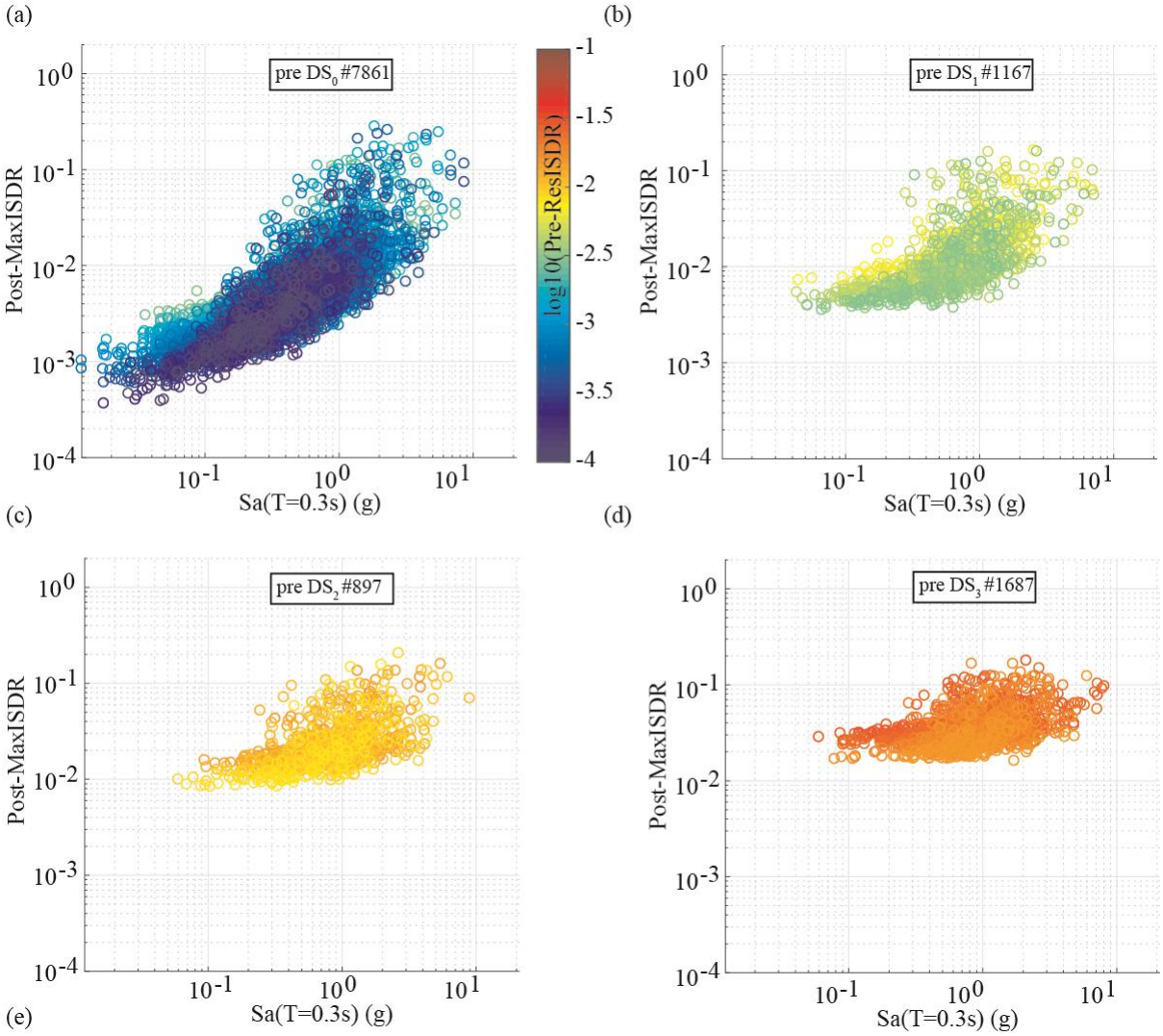

Figure 4-12. Plot of post-MaxISDRs against IM(T=0.3s) for House 4 with scaling factors 1-5 given pre-ResISDR (a) 0.01%-0.3%, (b) 0.3%-0.75%, (c) 0.75%-1.5%, and (d) 1.5%-3% from **Table 4-4**.

4.4.3 Comparison of aftershock fragility curves with Sa(T=0.3s), Sa(T=0.5s), and PGV

To make a fair comparison, the state-dependent fragility curves of House 4 with Sa(T=0.3s), Sa(T=0.5s), and PGV using the DS definition based on Case 1 and Approach 1 are shown in **Figure 4-13**, **Figure 4-14**, and **Figure 4-15**, respectively. Different cases and approaches are presented in the next two subsections (**Sections 4.4.4 and 4.4.5**). The limit of x-axis is constrained by the maximum IM from the observed records. Since the state-dependent fragility

curves are developed based on post-DSs given the same pre-DS, post-DSs from the same pre-DS should not intersect. Therefore, the same post-DS_i from pre-DS_0 to pre-DS_{i-1} are presented in all fragility curve plots. The estimated median values (θ_{IM}) and standard deviations (β_{IM}) from **Figure 4-13**, **Figure 4-14**, and **Figure 4-15** are summarised in **Table 4-5**.

Although Sa(T=0.3s) has been used as IM for the mainshock fragility curves (Goda and Atkinson, 2011), aftershock fragility curves with Sa(T=0.3s) in **Figure 4-13** are not well fitted by the cumulative lognormal distribution with the standard deviation larger than 1 for the collapse state in **Table 4-5**. On the other hand, in **Figure 4-14** and **Figure 4-15**, PGV and Sa(T=0.5s) show better performances of aftershock fragility curves for representing the cumulative damage effects than Sa(T=0.3s). PGV and Sa(T=0.5s) have larger variabilities to cover higher exceeding probability of post-DS_4 from pre-DS_{0-3} than Sa(T=0.3s) in **Figure 4-14**(e) and **Figure 4-15**(e), respectively.

All logarithmic standard deviations for different IMs in **Table 4-5** are increased from pre-DS_0 to pre-DS_3, the standard deviations of aftershock fragility curves of Sa(T=0.3s) and Sa(T=0.5s) are higher than 0.8. This might suggest that stronger records of aftershocks are needed to include more points in the fragility curve development for Sa(T=0.3s) and Sa(T=0.5s) in the range from 2g to 3g. Large standard deviations (e.g., 0.79) of state-dependent fragility curves were also observed from the back-to-back approach with IDA (Raghunandan, 2013). On the other hand, PGV shows a better performance for the development of aftershock fragility curves with standard deviations lower than 0.6. The median values of Sa(T=0.5s) and PGV decrease from pre-DS_0 to pre-DS_3 in **Table 4-5**, which shows that the damaged house requires a low IM to reach the same post-DS. Overall, PGV is the most suitable IM for the cumulative damage aftershock fragility curves of wood-frame houses.

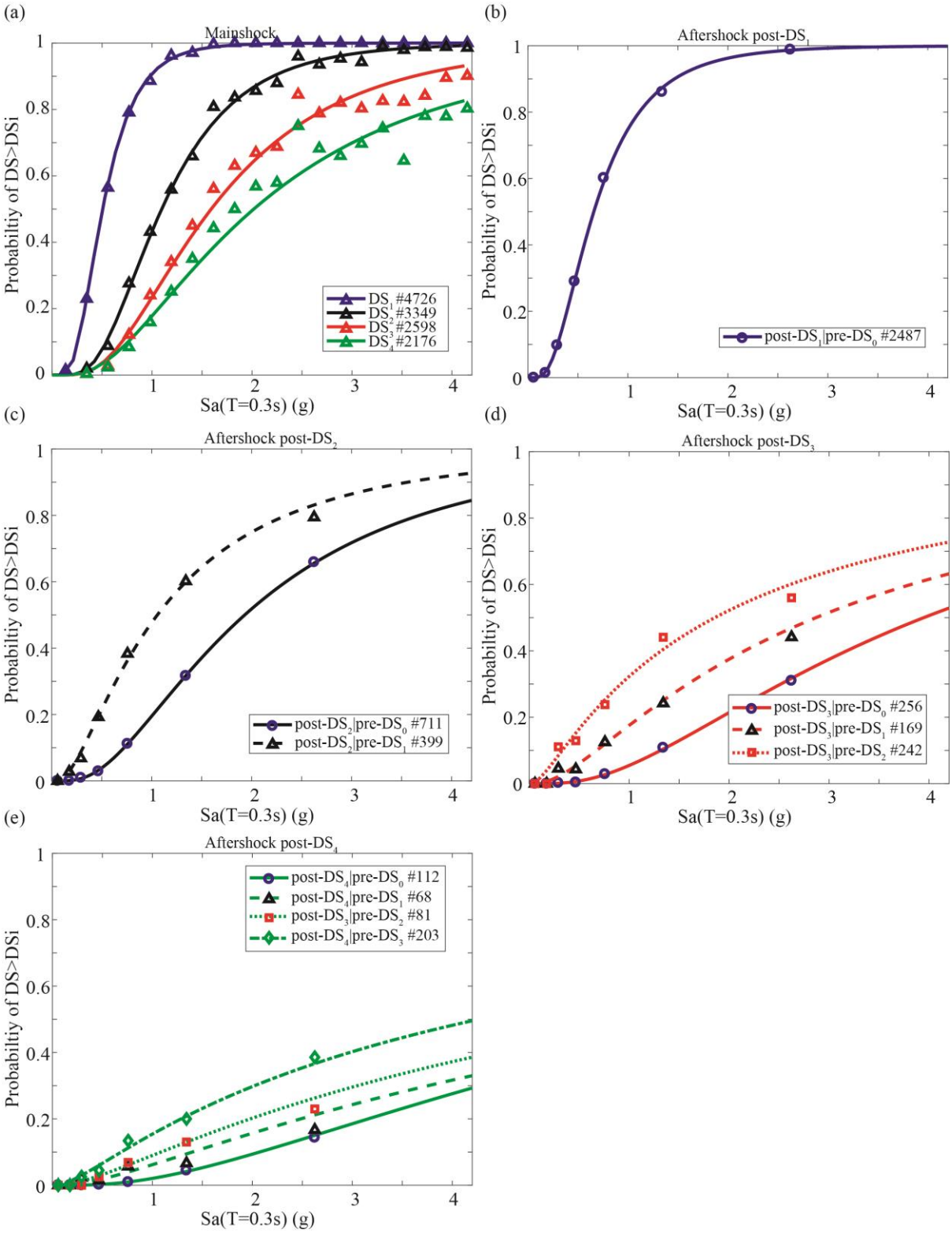

Figure 4-13. Plots of (a) the mainshock fragility curves, and the plots of aftershock fragility curves for (b) post-DS_1, (c) post-DS_2, (d) post-DS_3, (e) post-DS_4 based on pre-ResISDR, post-

MaxISDR, and Sa(T=0.3s) for House 4 considering the DS definition based on Case 1 and fitting Approach 1.

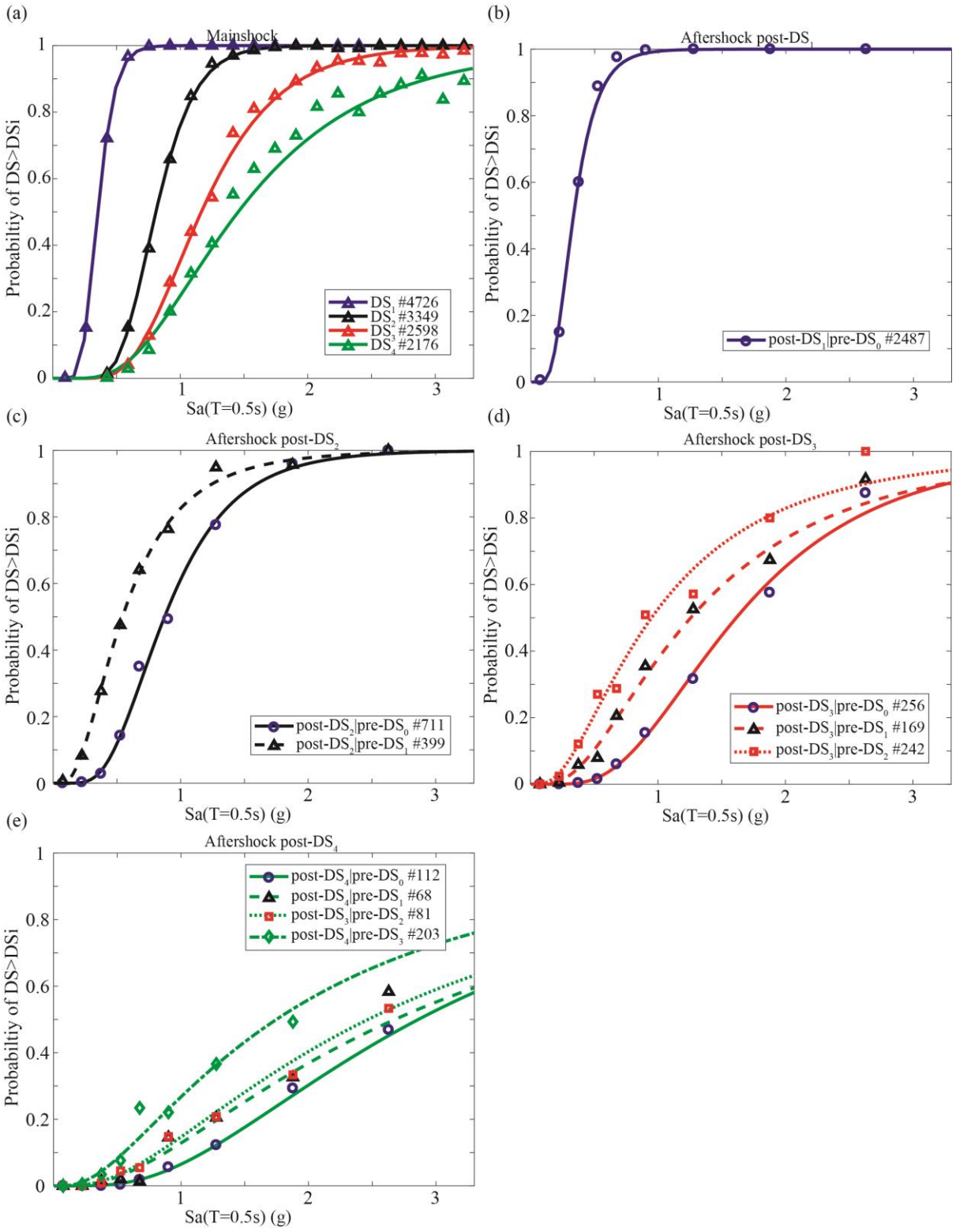

Figure 4-14. Plots of (a) the mainshock fragility curves, and the plots of aftershock fragility curves for (b) post-DS_1, (c) post-DS_2, (d) post-DS_3, (e) post-DS_4 based on pre-ResISDR, post-

MaxISDR, and Sa(T=0.5s) for House 4 considering the DS definition based on Case 1 and fitting Approach 1.

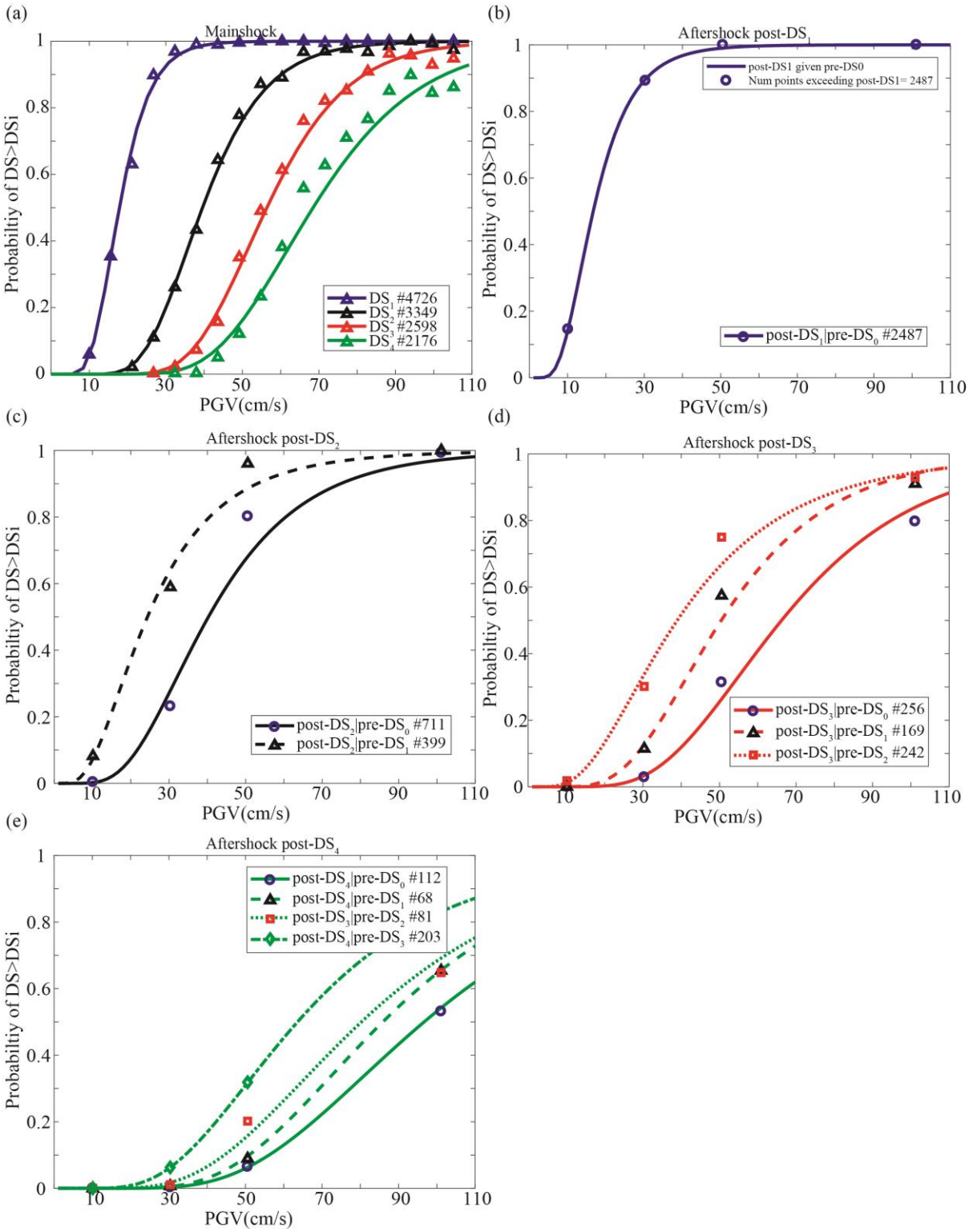

Figure 4-15. Plots of (a) the mainshock fragility curves, and the plots of aftershock fragility curves for (b) post-DS_1, (c) post-DS_2, (d) post-DS_3, (e) post-DS_4 based on pre-ResISDR, post-

MaxISDR, and PGV for House 4 considering the DS definition based on Case 1 and fitting Approach 1.

Table 4-5. Median values (θ_{IM}) of mainshock-aftershock fragility curves (standard deviations (β_{IM}) are shown in the parentheses) from the cumulative lognormal distribution with damage state definition Case 1 and fitting Approach 1.

House 4 (Sa(T=0.3s))	post-DS_1	post-DS_2	post-DS_3	post-DS_4
pre-DS_0 (MS)	0.5054 (0.5132)	1.0965 (0.5467)	1.5919 (0.6407)	2.0179 (0.7601)
pre-DS_0	0.6588 (0.6239)	1.9314 (0.7655)	3.9468 (0.8578)	7.0806 (0.9586)
pre-DS_1		1.0572 (0.9486)	2.8686 (1.1294)	7.4551 (1.3052)
pre-DS_2			1.8569 (1.3465)	6.2399 (1.3640)
pre-DS_3				4.2678 (1.4237)
House 4 (Sa(T=0.5s))				
pre-DS_0 (MS)	0.3522 (0.2963)	0.8086 (0.2989)	1.1645 (0.4044)	1.4537 (0.5502)
pre-DS_0	0.3340 (0.4393)	0.8741 (0.4722)	1.6141 (0.5432)	2.8616 (0.6941)
pre-DS_1		0.5434 (0.6501)	1.2572 (0.7291)	2.6772 (0.8690)
pre-DS_2			0.9496 (0.7850)	2.4671 (0.8600)
pre-DS_3				1.7483 (0.8999)
House 4 (PGV)				
pre-DS_0 (MS)	17.8444 (0.3579)	39.5652 (0.3258)	56.3923 (0.2912)	68.4639 (0.3180)
pre-DS_0	16.6729 (0.4736)	40.2802 (0.4830)	66.2261 (0.4268)	96.6949 (0.4239)
pre-DS_1		24.3442 (0.6066)	50.4636 (0.4452)	85.9017 (0.4081)
pre-DS_2			38.9646 (0.5998)	80.3086 (0.4609)
pre-DS_3				63.6121 (0.4836)

4.4.4 Comparison of aftershock fragility curves with DS definitions based on Cases 1 and 2

The state-dependent fragility curves of House 4 with Sa(T=0.3s), Sa(T=0.5s), and PGV using the DS definition based on Case 2 and Approach 1 are shown in **Figure 4-16**, **Figure 4-17**, and **Figure 4-18**, respectively. The estimated median values (θ_{IM}) and standard deviations (β_{IM}) from **Figure 4-16**, **Figure 4-17**, and **Figure 4-18** are summarised in **Table 4-6**. In comparison with Case 1, Case 2 with three DSs has more than 100 points in every binned post-DS given pre-DS_i in **Figure 4-16**(e) and shows a slightly better performance of the aftershock fragility curve development for Sa(T=0.3s), Sa(T=0.5s), and PGV with smaller standard deviations than Case 1. In addition, since the number of points of post-DS_4 given pre-$DS_{2\text{-}3}$ for House 4 is less

than 100 in **Figure 4-15**(f) and the seismic performance of Houses 1-3 is better than House 4, less points will be observed given the DS definition based on Case 1 for Houses 1-3. Following that, Case 2 allows a more robust fitting for Houses 1-3. In terms of IMs, PGV is the most suitable IM for the aftershock fragility curves of wood-frame houses and has a better fit with cumulative lognormal distribution than Sa(T=0.3s) and Sa(T=0.5s) in both Cases 1 and 2.

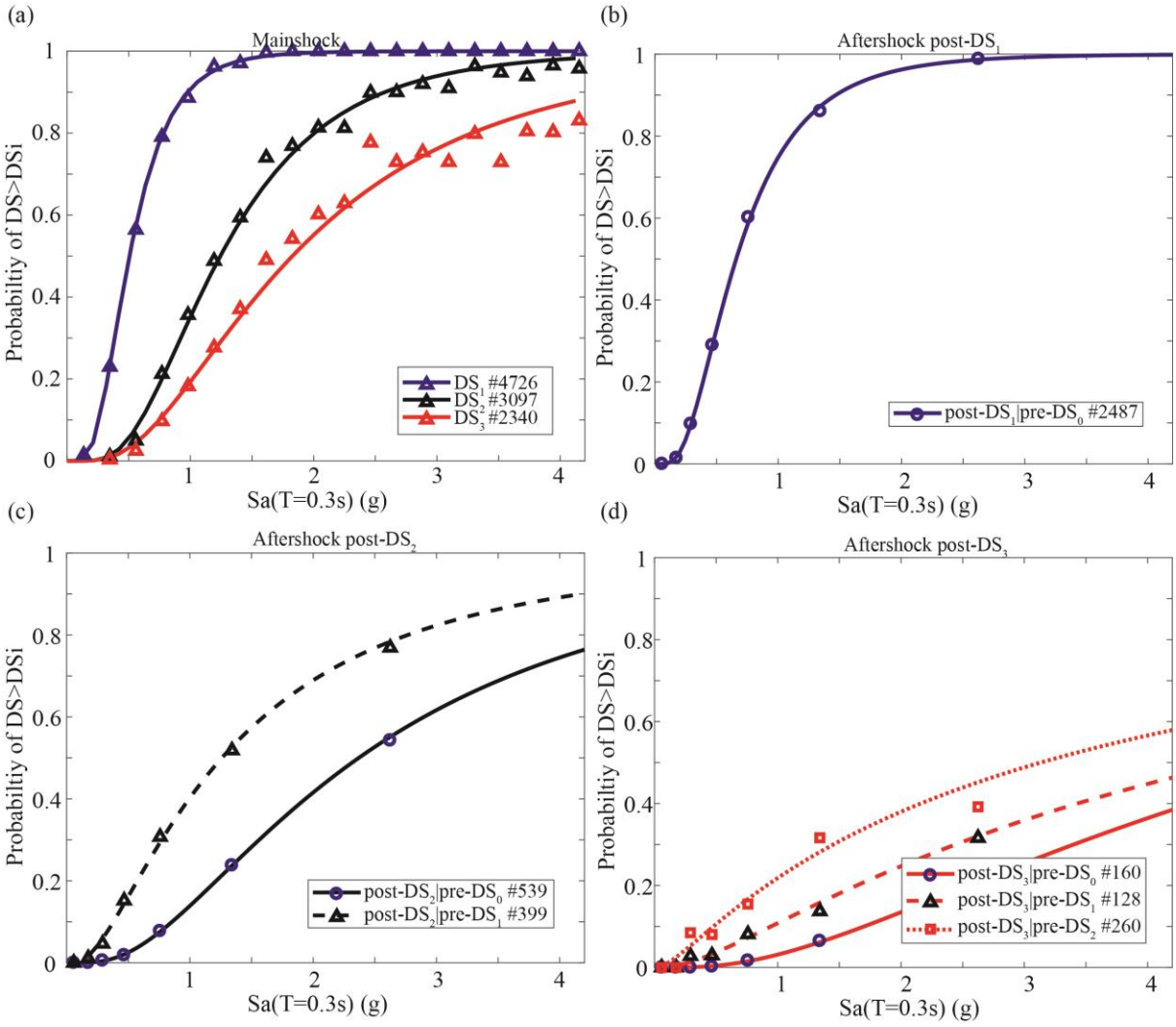

Figure 4-16. Plots of (a) the mainshock fragility curves, and the plots of aftershock fragility curves for (b) post-DS_1, (c) post-DS_2, (d) post-DS_3 based on pre-ResISDR, post-MaxISDR, and Sa(T=0.3s) for House 4 considering the DS definition based on Case 2 and fitting Approach 1.

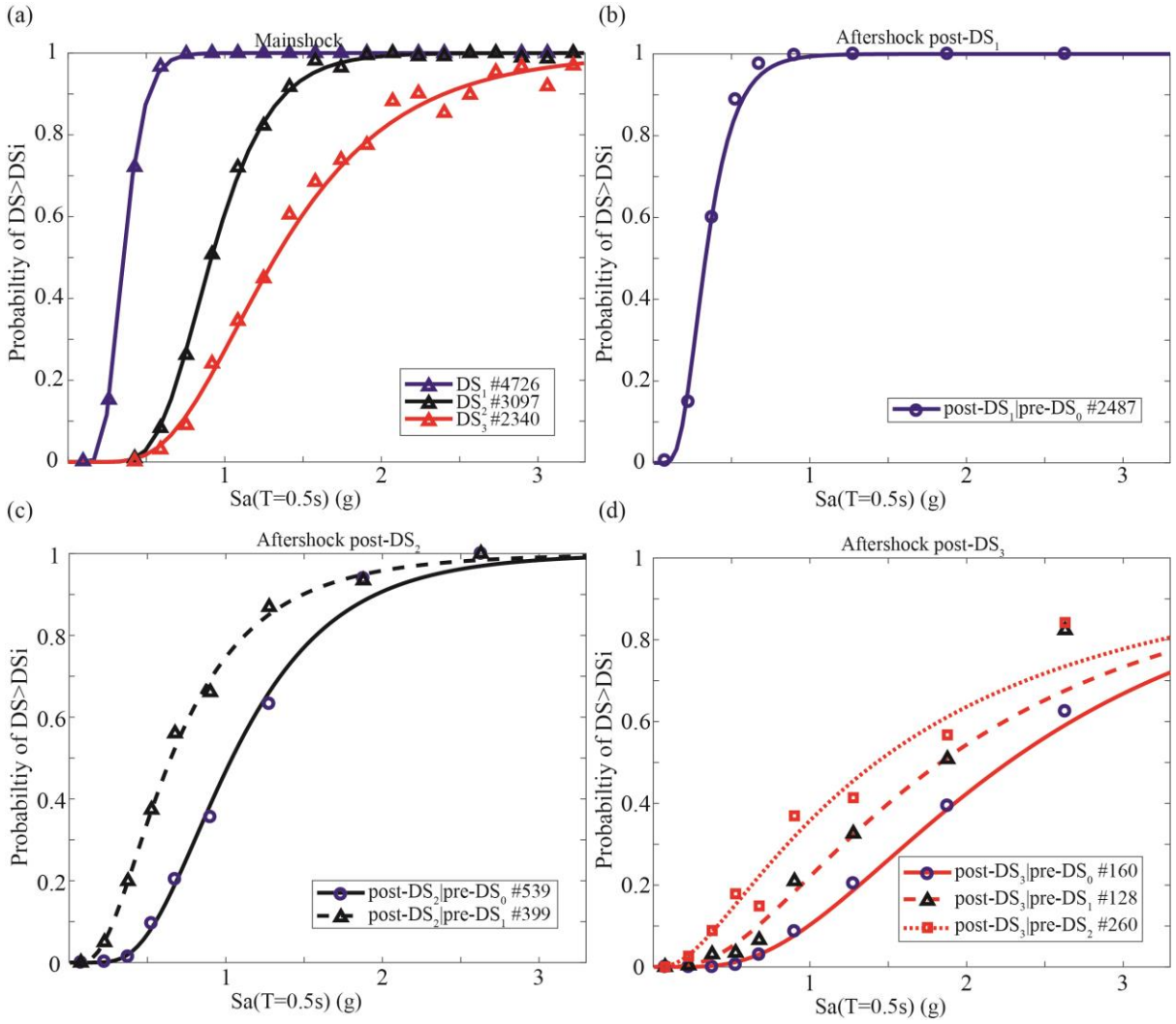

Figure 4-17. Plots of (a) the mainshock fragility curves, and the plots of aftershock fragility curves for (b) post-DS_1, (c) post-DS_2, (d) post-DS_3 based on pre-ResISDR, post-MaxISDR, and Sa(T=0.5s) for House 4 considering the DS definition based on Case 2 and fitting Approach 1.

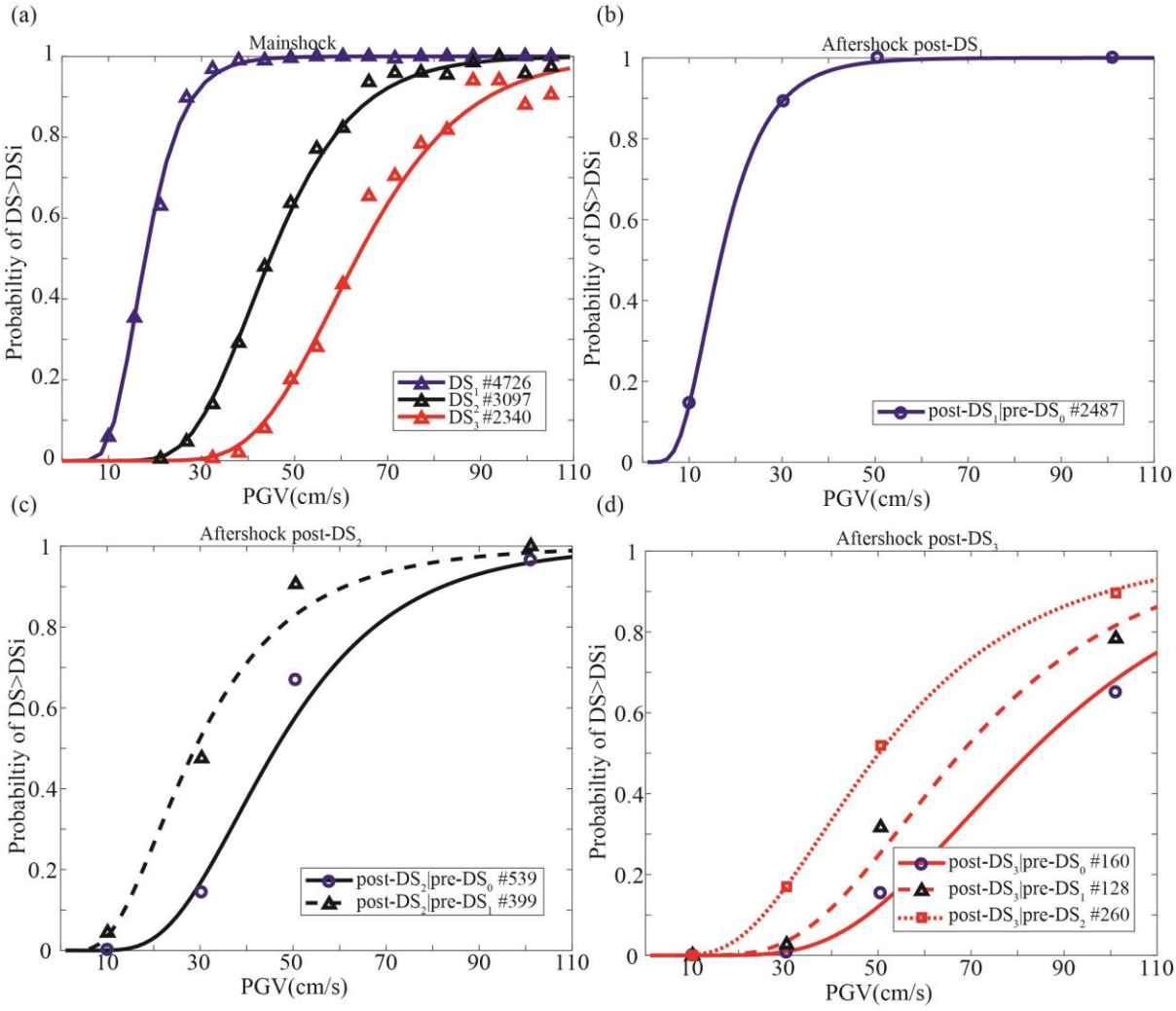

Figure 4-18. Plots of (a) the mainshock fragility curves, and the plots of aftershock fragility curves for (b) post-DS_1, (c) post-DS_2, (d) post-DS_3 based on pre-ResISDR, post-MaxISDR, and PGV for House 4 considering the DS definition based on Case 2 and fitting Approach 1.

Table 4-6. Median values (θ_{IM}) of mainshock-aftershock fragility curves (standard deviations (β_{IM}) are shown in the parentheses) from the cumulative lognormal distribution with damage state definition Case 2 and fitting Approach 1.

House 4 (Sa(T=0.3s))	post-DS_1	post-DS_2	post-DS_3
pre-DS_0 (MS)	0.5054 (0.5132)	1.2426 (0.5691)	1.8275 (0.6964)
pre-DS_0	0.6588 (0.6239)	2.3693 (0.7952)	5.4944 (0.9156)
pre-DS_1		1.2592 (0.9354)	4.7140 (1.2545)
pre-DS_2			3.1317 (1.4680)
House 4 (Sa(T=0.5s))			
pre-DS_0 (MS)	0.3522 (0.2963)	0.9156 (0.3235)	1.3239 (0.4641)
pre-DS_0	0.3340 (0.4393)	1.0399 (0.4939)	2.2649 (0.6458)
pre-DS_1		0.6497 (0.6490)	1.8344 (0.7893)
pre-DS_2			1.4257 (0.9737)
House 4 (PGV)			
pre-DS_0 (MS)	17.8444 (0.3579)	44.7305 (0.3161)	63.3467 (0.2881)
pre-DS_0	16.6729 (0.4736)	46.2898 (0.4472)	82.5473 (0.4268)
pre-DS_1		28.9280 (0.5830)	67.8020 (0.4441)
pre-DS_2			50.2048 (0.5332)

4.4.5 Comparison of aftershock fragility curves using approaches 1-3

In this subsection, three approaches are used to develop the fragility curves of House 4 with PGV and the DS definition based on Case 1. The aftershock fragility curves based on Approaches 1-3 are shown in **Figure 4-15**, **Figure 4-19**, and **Figure 4-20**, respectively. The estimated median values (θ_{IM}) and standard deviations (β_{IM}) from **Figure 4-19**, and **Figure 4-20** are summarised in **Table 4-7**. Similar performances can be observed from Approaches 1 and 3 by the fixed IM bin counts of the cumulative lognormal distribution and multinomial distribution, respectively. Approach 2 with the same number of data points in each bin does not show a good fit, as the fragility curves for post-DS_4 given pre-$DS_{0\text{-}2}$ intersect in **Figure 4-19**. This suggests Approach 2 might need more data points to have a robust fitting. On the other hand, Approach 2 has smaller standard deviations than Approach 1, because the same number of points are counted in each bin.

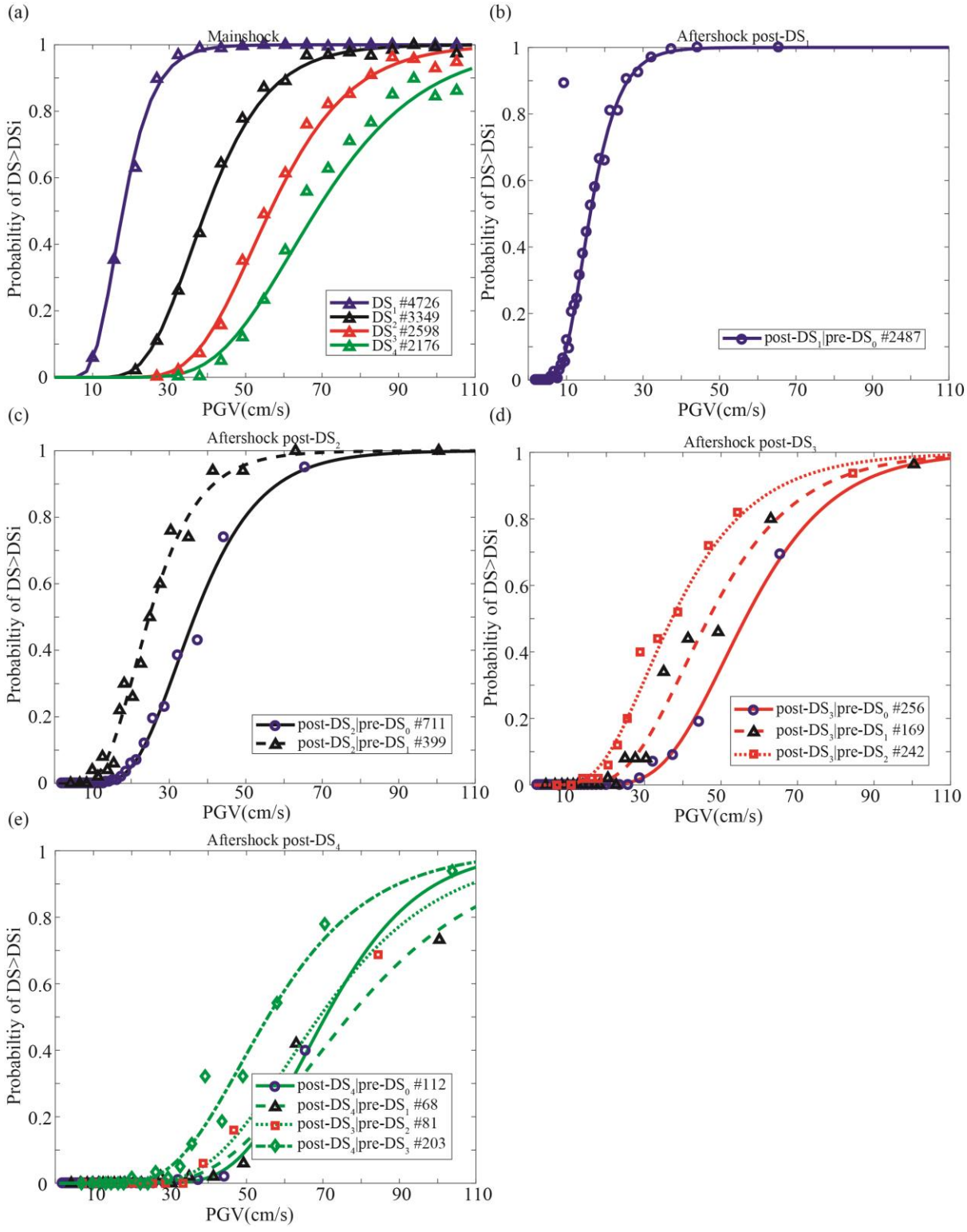

Figure 4-19. Plots of (a) the mainshock fragility curves, and the plots of aftershock fragility curves for (b) post-DS_1, (c) post-DS_2, (d) post-DS_3, (e) post-DS_4 based on pre-ResISDR, post-MaxISDR, and Sa(T=0.3s) for House 4 considering the DS definition based on Case 1 and fitting Approach 2.

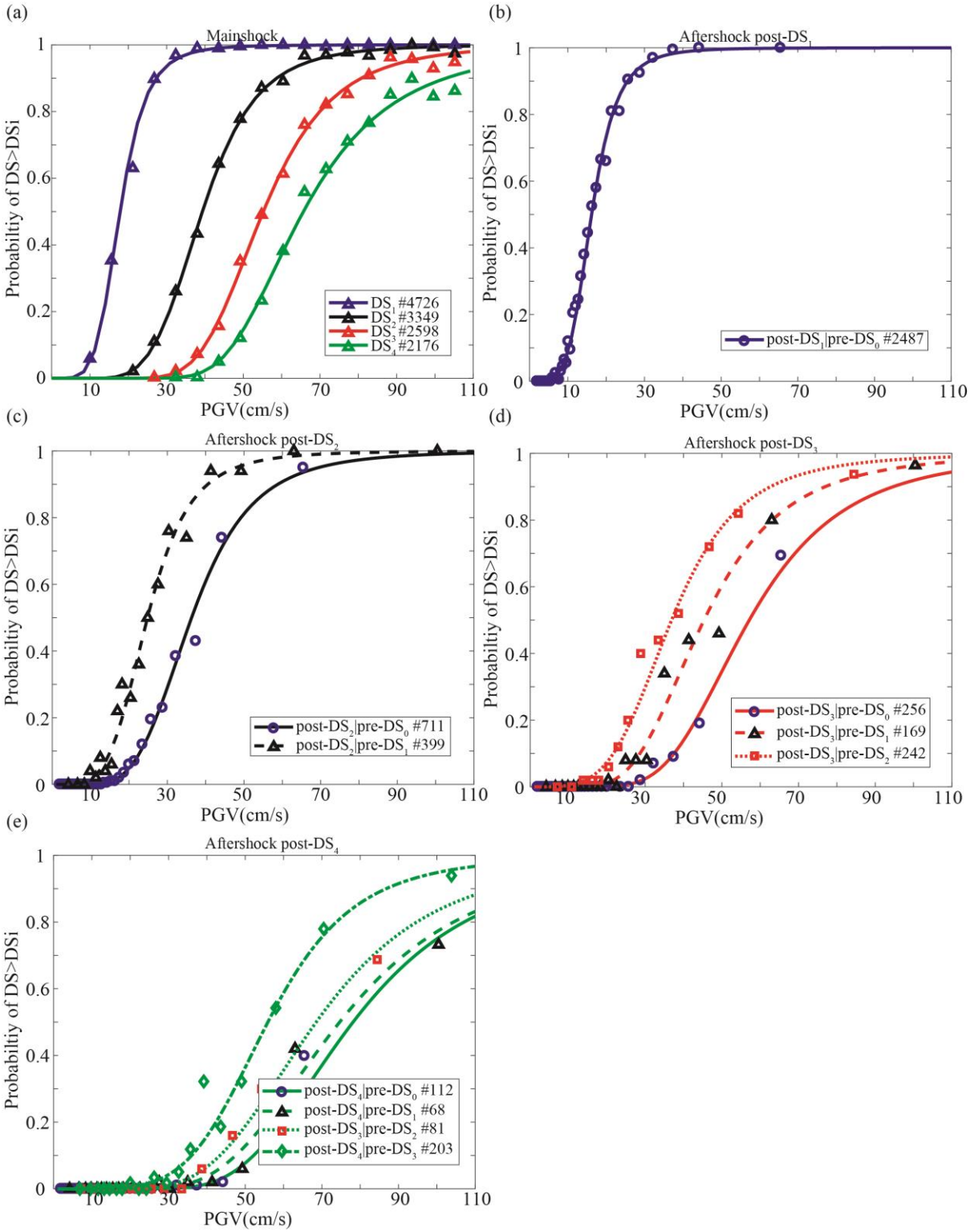

Figure 4-20. Plots of (a) the mainshock fragility curves, and the plots of aftershock fragility curves for (b) post-DS_1, (c) post-DS_2, (d) post-DS_3, (e) post-DS_4 based on pre-ResISDR, post-MaxISDR, and Sa(T=0.3s) for House 4 considering the DS definition based on Case 1 and fitting Approach 3.

Although both Approaches 1 and 3 perform well in the development of the fragility curves, Approach 3 with multinomial fitting is a better option. This is because the fixed IM bin counts from Approach 1 require a careful assessment of the histogram count of IMs given pre-DSs, and less than 10 IM bin counts are included to have a robust fitting. On the other hand, the multinomial distribution only requires IM and post-DSs given each pre-DS_i to fit the curves progressively. Based on that, fitting Approach 3 and the DS definition based on Case 2 are used to develop the aftershock fragility curves for Houses 1-4 in the next subsection.

Table 4-7. Estimated parameters of mainshock-aftershock fragility curves of House 4 from Approach 2 (cumulative lognormal distribution) and Approach 3 (multinomial distributions).

House 4 (PGV) - Approach 2	post-DS_1	post-DS_2	post-DS_3	post-DS_4
pre-DS_0 (MS)	17.8444 (0.3579)	39.5652 (0.3258)	56.3923 (0.2912)	68.4639 (0.3180)
pre-DS_0	16.1864 (0.3707)	36.5879 (0.3648)	56.3267 (0.3189)	70.6424 (0.2691)
pre-DS_1		24.7093 (0.4065)	46.7092 (0.3850)	76.7832 (0.3739)
pre-DS_2			37.1480 (0.4478)	69.0519 (0.3543)
pre-DS_3				55.6106 (0.3736)
House 4 (PGV)-Approach 3				
pre-DS_0 (MS)	14.9360, -5.1841	20.0088, -5.4581	21.7765, -5.5068	15.8504, -3.9668
pre-DS_0	13.4086, -4.8162	16.1923, -4.5184	16.3994, -4.1164	16.7045, -3.9504
pre-DS_1		14.3954, -4.4819	15.2061, -4.0220	16.5257, -3.8905
pre-DS_2			14.9610, -4.1469	17.2828, -4.1248
pre-DS_3				20.1258, -5.0017

4.4.6 Aftershock fragility curves of Houses 1-4 with PGV

The plots of state-dependent fragility curves for Houses 1-4 are provided in **Figure 4-21**-**Figure 4-24**. The estimated median values (θ_{IM}) and standard deviations (β_{IM}) are summarised in **Table 4-8**. By considering PGV as IM with the DS definition based on Case 2 and multinomial distribution, the fragility curves of Houses 1-4 show a good agreement with the description of seismic resistance in **Section 4.2.1**. For example, by looking at the PGV values with 50% exceedance probability of collapse damage state given intact conditions in **Figure 4-21**(d)-**Figure 4-24**(d). House 1 has the highest PGV value (110cm/s), whereas the median

value of PGV for House 4 is 65cm/s. This indicates the better performance of the engineered OSB sheathing than horizontal board sheathing (Pan *et al.*, 2018). In addition, since only three DSs are used based on Case 2, the developed fragility curves are well separated showing good estimates of cumulative damage effects due to aftershocks.

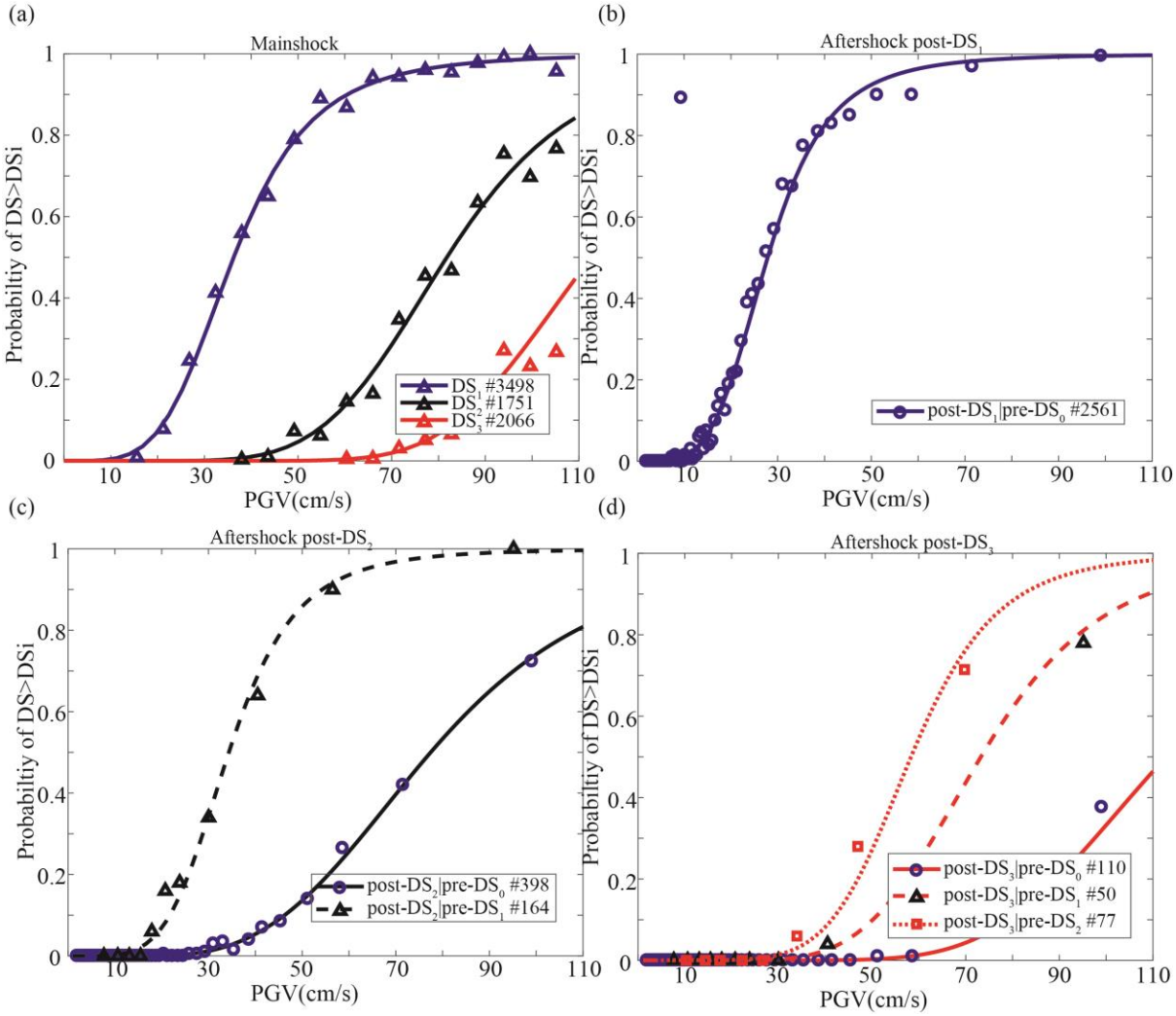

Figure 4-21. Plots of (a) the mainshock fragility curves, and the plots of aftershock fragility curves for (b) post-DS_1, (c) post-DS_2, (d) post-DS_3 based on pre-ResISDR, post-MaxISDR, and PGV for House 1 considering the DS definition based on Case 2 and fitting Approach 3.

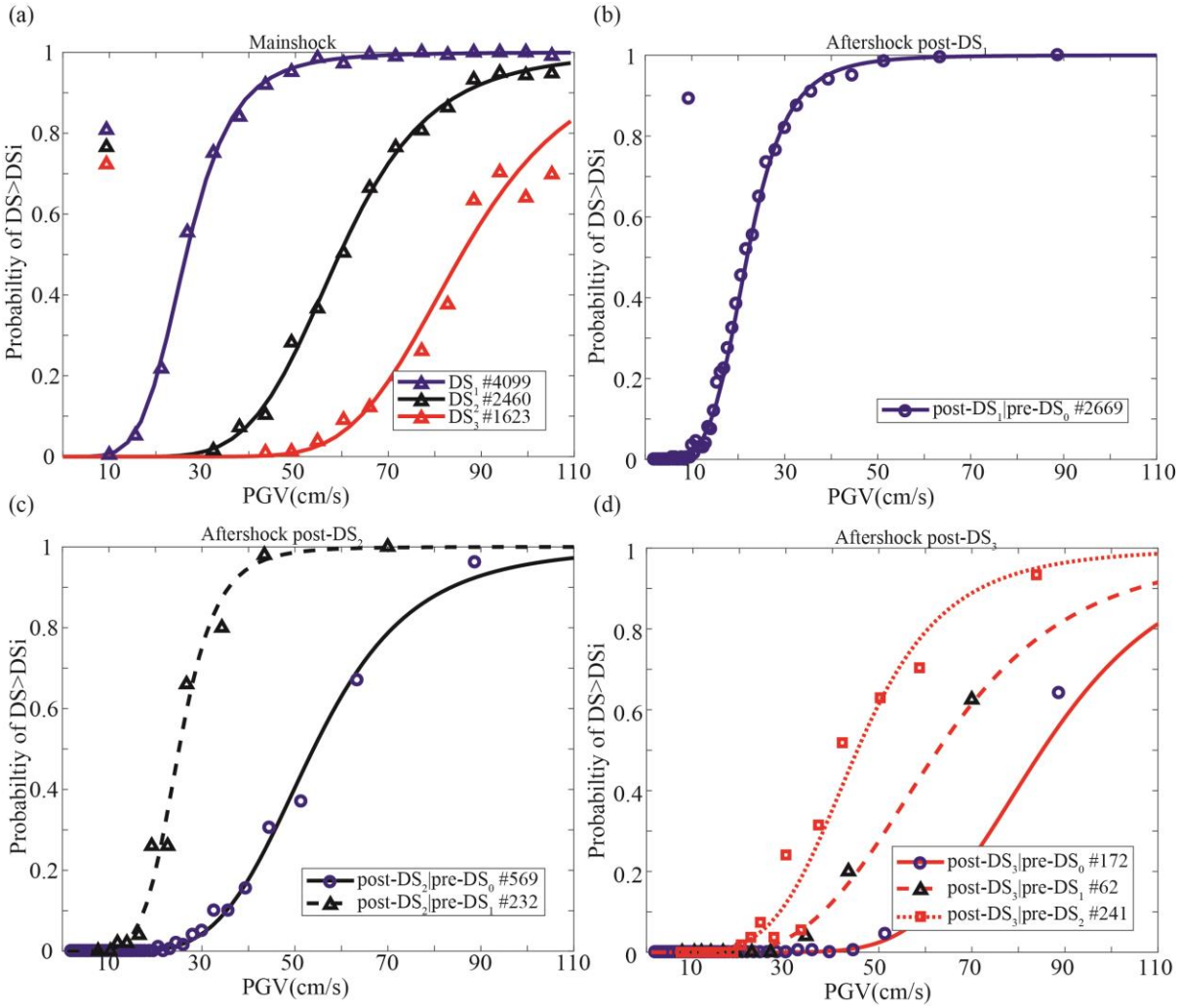

Figure 4-22. Plots of (a) the mainshock fragility curves, and the plots of aftershock fragility curves for (b) post-DS_1, (c) post-DS_2, (d) post-DS_3 based on pre-ResISDR, post-MaxISDR, and PGV for House 2 considering the DS definition based on Case 2 and fitting Approach 3.

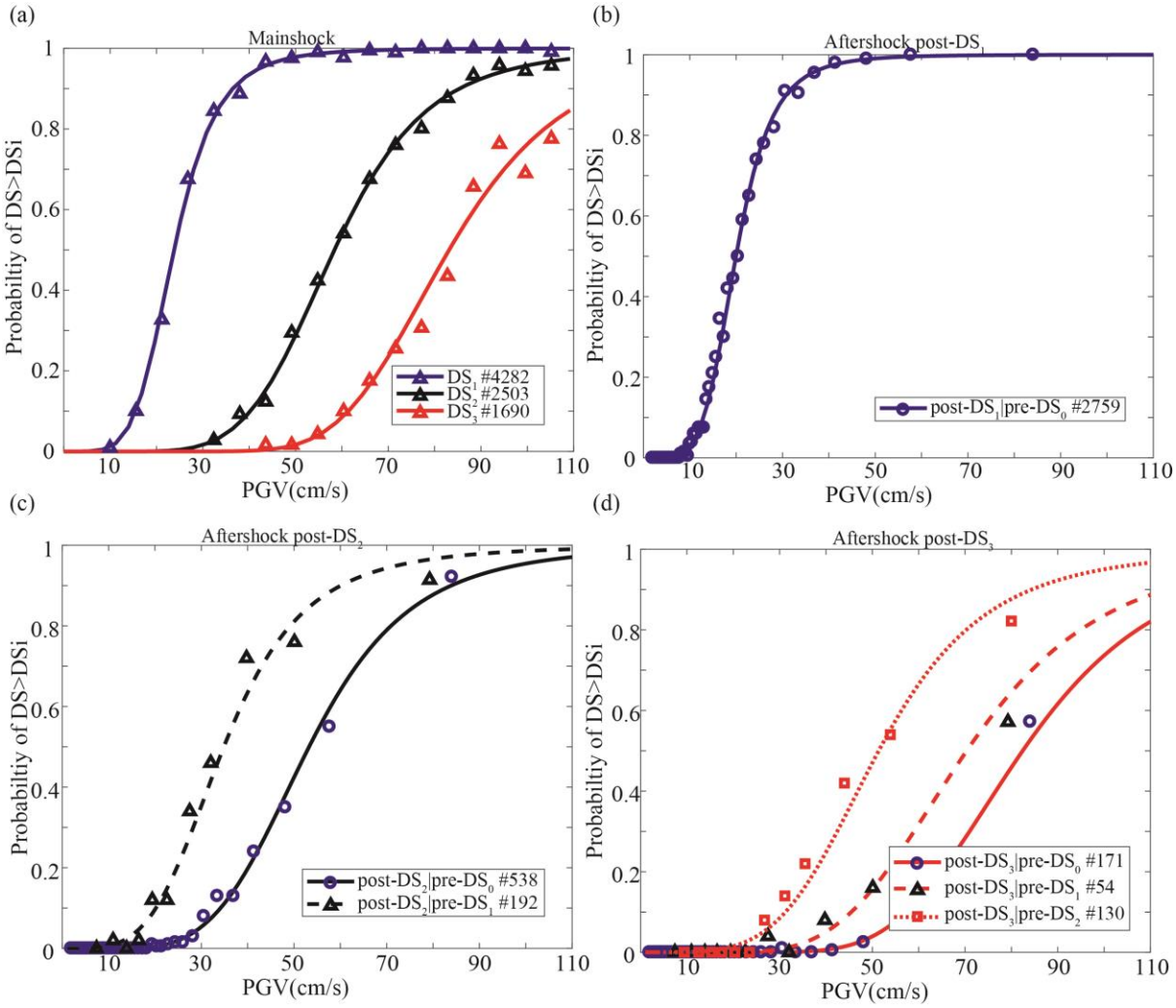

Figure 4-23. Plots of (a) the mainshock fragility curves, and the plots of aftershock fragility curves for (b) post-DS_1, (c) post-DS_2, (d) post-DS_3 based on pre-ResISDR, post-MaxISDR, and PGV for House 3 considering the DS definition based on Case 2 and fitting Approach 3.

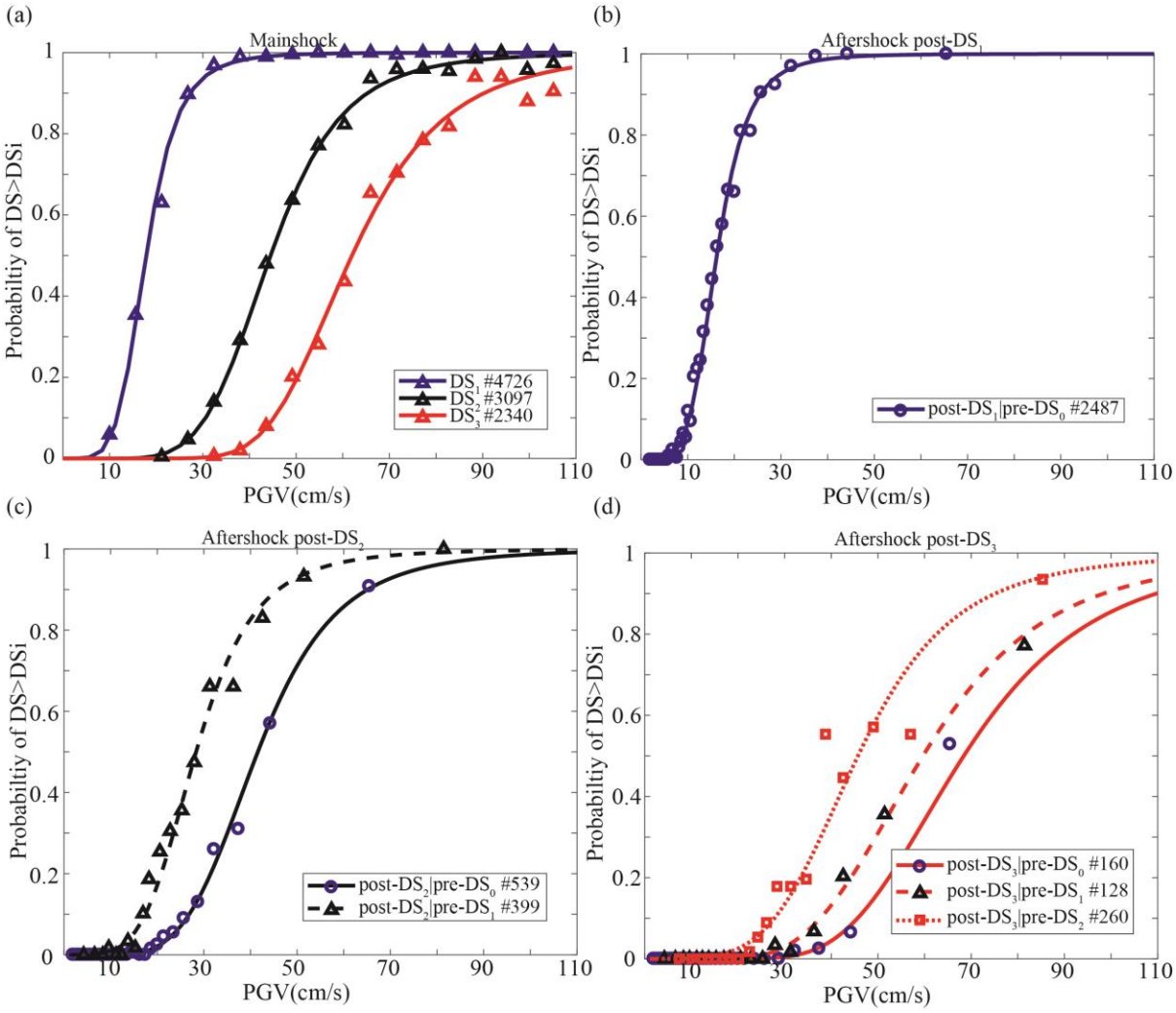

Figure 4-24. Plots of (a) the mainshock fragility curves, and the plots of aftershock fragility curves for (b) post-DS_1, (c) post-DS_2, (d) post-DS_3 based on pre-ResISDR, post-MaxISDR, and PGV for House 4 considering the DS definition based on Case 2 and fitting Approach 3.

The developed aftershock fragility curves of Houses 1-4 can be further applied for estimating the DSs with spatiotemporal risk assessment for a M9.0 mainshock triggering both crustal and subduction-zone aftershocks (e.g., Zhang *et al.*, 2018) in British Columbia, Canada. The evaluated PGV and real mainshock-aftershock sequences could allow a good estimate of cumulative damage of wood-frame houses. The output of the risk assessment could provide not only the likelihood of the DSs on the day of the inspection for building tagging (Luco *et al.*, 2011) but also daily forecasts of the DSs in a short-time period after the inspection day.

This could be part of inspection combining with the conventional building tagging (e.g., residual displacement check of the structure components) and providing additional information for the decision-maker (e.g., structural engineers).

Table 4-8. Parameters θ_1 and θ_2 from the multinomial distribution using the DS definition based on Case 2 and fitting approach 3 for Houses 1-4.

House 1 (PGV)	post-DS_1	post-DS_2	post-DS_3
pre-DS_0 (MS)	15.3990, -4.2888	25.4000, -5.7811	28.8500, -6.1736
pre-DS_0	14.2479, -4.2833	17.6972, -4.0744	24.6379, -5.3050
pre-DS_1		16.9857, -4.8035	23.5667, -5.5006
pre-DS_2			26.0654, -6.4104
House 2 (PGV)			
pre-DS_0 (MS)	16.9164, -5.1627	24.2333, -5.9384	27.9523, -6.3295
pre-DS_0	15.7371, -5.0999	19.9384, -5.0038	24.4394, -5.5447
pre-DS_1		19.9190, -6.1824	17.4554, -4.2196
pre-DS_2			18.2991, -4.7967
House 3 (PGV)			
pre-DS_0 (MS)	16.3270, -5.1518	23.4798, -5.7778	26.1668, -5.9783
pre-DS_0	15.2144, -5.0817	19.1436, -4.8195	22.0045, -5.0425
pre-DS_1		14.3320, -4.0356	19.1927, -4.5398
pre-DS_2			17.4424, -4.4280
House 4 (PGV)			
pre-DS_0 (MS)	14.9360, -5.1841	21.7635, -5.7376	22.5530, -5.5382
pre-DS_0	13.4086, -4.8162	18.1529, -4.8758	18.7181, -4.4713
pre-DS_1		15.1806, -4.5396	17.6272, -4.3279
pre-DS_2			16.9071, -4.4229

4.5 Conclusions

This chapter applied a new method using 596 real mainshock-aftershock records with cloud analysis to develop the state-dependent fragility curves of aftershocks for wood-frame houses in Canada. To capture the real characteristics of aftershocks in the cumulative damage assessments of mainshock and aftershock sequences, a IM and post-EDP dataset was used to develop the mainshock fragility curves, and pre-EDP combining with IM and post-EDP was introduced for developing the state-dependent aftershock fragility curves. The selection of IMs (from Sa, AI, CAV, PGV, and SI) and EDPs (from ResISDR, MaxISDR, and MaxIISDR) was

discussed in this study. To account for the cumulative damage after $event_n$, the pre-ResISDR and post-MaxISDR are considered to be the most suitable EDPs to represent the pre-EDP and post-EDP, respectively. To evaluate different IMs, the efficiency, sufficiency, and relative sufficiency were calculated for each IM. Sa(T=0.3s-0.5s) and PGV show better performances than other IMs.

The mainshock-aftershock fragility curves were produced with pre-ResISDR and post-MaxISDR by considering IMs (Sa(T=0.3s), Sa(T=0.5s) and PGV). PGV showed a better performance to capture the cumulative damage effects of aftershocks for the wood-frame structure using real mainshock aftershock sequences than other IMs. Different fitting approaches (cumulative lognormal distribution and multinomial distribution) and the DS definitions (Case 1: immediate occupancy, life safety, collapse prevention, and collapse and Case 2: Green, Yellow, and Red tags) were also compared. The multinomial distribution performs better to fit the fragility curves than the lognormal distribution, because the former does not require careful bin counts to avoid the intersections of aftershock fragility curves for post-DS conditioned on different pre-DSs. Case 2 with three DSs shows a better performance than Case 1, because more points are included in each post-DS given pre-DS_i. Combining the DS definition based on Case 2 with the multinormal distribution would allow us to produce more robust aftershock fragility curves than other approaches.

The limitations of the aftershock fragility curves are that (1) the state-dependent fragility curves are not appropriate when one or more foreshocks are included in the sequence. (2) More destructive aftershock records should be included to have a better fitting of fragility models with a smaller logarithmic standard deviation for Sa(T=0.3s) and Sa(T=0.5s). This would also allow to produce robust aftershock fragility curves with four DSs (Case 1). (3) In addition, if more destructive aftershock records are included, ground motion records could be further classified by earthquake types, so aftershock fragility curves can be developed by

crustal and subduction-zone records which represent the differences of spectra shape between the crustal and subduction-zone earthquakes (Raghunandan *et al.*, 2015b).

By having the spatiotemporal hazard assessment of M9.0 sequences (e.g., Zhang *et al.*, 2018), the aftershock fragility curves from this study can provide the time-dependent probability of DSs as secondary information for the conventional post-risk assessment (Bazzurro *et al.*, 2004) when the building tagging is conducted after the mainshock occurs.

Chapter 5 Spatiotemporal Risk Assessment of Wood-frame Houses under M9.0 Earthquake Sequences in Victoria, British Columbia, Canada[**]

5.1 Introduction

Recent M9.0 earthquake sequences, such as the 2004 Aceh-Andaman earthquake, the 2010 Maule earthquake, and 2011 Tohoku earthquake, triggered large aftershock events (e.g., M≥7.0) on the subduction interface and in the overriding crust, demonstrating the destructive effects of aftershocks on buildings (Hirose *et al.*, 2011; Fukushima *et al.*, 2013; Goda *et al.*, 2013). Because the time to repair damaged buildings between a mainshock and aftershocks is often short, the cumulative damage effect of buildings due to aftershocks can have a significant impact on post-earthquake risk assessment (Nazari *et al.*, 2013; Ebrahimian *et al.*, 2014; Iervolino *et al.*, 2014). A spatiotemporal seismic risk assessment that considers the cumulative damage effect due to M9.0 earthquake sequences is necessary to quantify the impact of aftershocks on post-event risk management decision-making, including resource allocation,

[**] This chapter was submitted and is under review at Earthquake Engineering and Structural Dynamics:

Zhang, L., K. Goda, M.J. Werner, and S. Tesfamariam (2020) Spatiotemporal seismic hazard and risk assessment of M9.0 megathrust earthquake sequences of wood-frame houses in Victoria, British Columbia, Canada, *Earthq. Eng. Struct. Dyn*. (under review).

and part of this chapter is based on the conference paper:

Zhang, L. and K. Goda (2019) Spatiotemporal Seismic Risk Assessment of Wood-frame Houses in Victoria, Canada under M9 Megathrust Subduction Sequences, In: *13th International Conference on Applications of Statistics and Probability in Civil Engineering(ICASP13)*, Seoul, South Korea, May 26-30, 2019.

evacuation planning, building-tagging, and rapid seismic loss estimation (Jordan and Jones, 2010; Field *et al.*, 2016).

Devastating M9.0 events are not limited to the most active seismic regions mentioned above and could occur in other subduction zones. For example, according to turbidite records of the past 10,000 years, the Cascadia subduction zone (CSZ) ruptured 19 times (Goldfinger *et al*., 2012). The current best estimate of the mean recurrence period for M9.0 events in the CSZ is 526 years, and the last event occurred in 1700 (Satake *et al.*, 1996). Meanwhile, Ventura *et al.* (2005) estimated that 56% of buildings in British Columbia, Canada, are wood-frame houses, 40% of which were built before 1970. Since seismic provisions of the National Building Code of Canada were adopted and enforced in British Columbia after 1973, the seismic resistance of old residential houses is likely to be below the current seismic standard of the building stock in British Columbia. Consequently, in the urban areas (e.g., Victoria and Vancouver) of British Columbia, a large number of wood-frame houses (Onur *et al.*, 2005) may be particularly at risk from M9.0 subduction earthquake sequences.

To conduct a spatiotemporal seismic risk assessment, a model that can describe the time-dependent seismicity rate in space and time is necessary. An epidemic type aftershock sequence (ETAS) model (Ogata, 1998; Lombardi and Marzocchi, 2010; Field *et al.*, 2017a) is such a spatiotemporal seismicity model. The model has been employed to conduct operational earthquake loss forecasting in California and Italy (Iervolino *et al.*, 2015; Field *et al.*, 2017b). All above-mentioned studies, however, focussed on shallow crustal seismicity; a regional spatiotemporal seismic risk assessment in subduction zones is rarely carried out. In **Chapter 2**, the ETAS model was applied to subduction-zone regions, and a new simulation framework was developed to assess spatiotemporal seismic hazard and risk due to aftershocks triggered by M9.0 events. A case study of Tohoku-like events in **Chapter 2** showed that synthetic catalogues from the new simulation framework are in good agreement with the observed M9.0

Tohoku sequence. In **Chapter 3**, the variability of ETAS parameters across different subduction-zone regions was investigated using global earthquake catalogues and preferred ETAS parameters were suggested for future M9.0 earthquake sequences. The outputs of **Chapter 2** and **Chapter 3** allow forecasting spatiotemporal seismic hazard due to M9.0 sequences in subduction zones using catalogues in global subduction zones.

For seismic risk assessment, recent studies have investigated the seismic performance of individual buildings in western Canada when exposed to hypothetical M9 events in the CSZ (Koduru and Haukaas, 2010; Goda and Atkinson, 2011; Tesfamariam and Goda, 2015a). For instance, Koduru and Haukaas (2010) highlighted the significant contribution (up to 75%) of megathrust subduction events to the total monetary loss for the case of a single 15-story high rise building in Vancouver. In terms of the impact of aftershocks occurring in the CSZ on individual buildings, Salami and Goda (2014) showed that mainshock-aftershock sequences can cause an additional 5%-20% damage in comparison with mainshocks alone. On the other hand, megathrust earthquakes affect many buildings simultaneously. Therefore, city-wide seismic risk assessments have been conducted to make decisions more efficiently for Vancouver and Victoria (Onur *et al.*, 2005; Goda and Hong, 2008; Goda *et al.*, 2011). However, seismic risk assessments of multiple buildings within a city/municipality subjected to M9.0 earthquake sequences in the CSZ have not been investigated in the literature. In addition, most spatiotemporal seismic risk studies ignore the cumulative damage effect due to aftershocks (Iervolino *et al.*, 2015). This is because (1) a seismicity model to describe the mainshock-aftershock sequences in space and time is not available in the CSZ, and (2) state-dependent aftershock fragility curves are not available for various types of building typologies, and only mainshock fragility curves that do not account for the cumulative damage effect of aftershocks were used. In **Chapter 4**, state-dependent fragility curves of wood-frame houses in British Columbia were developed to estimate the damage state (DS) of wood-frame houses

after each event during an earthquake sequence. The new state-dependent fragility curves can be combined with the quasi-real-time aftershock forecasting hazard assessment from **Chapter 2** to build a simulation framework of city-wide spatiotemporal seismic hazard and risk assessments of megathrust subduction earthquake sequences in the CSZ.

This chapter conducts a spatiotemporal seismic risk assessment of M9.0 sequences using a realistic building portfolio of wood-frame houses in Victoria, British Columbia, Canada. The impact of aftershocks triggered by M9.0 events in the CSZ on spatially distributed wood-frame houses is investigated. The developed simulation framework of spatiotemporal seismic hazard and risk assessment of M9.0 sequences from **Chapter 2** is applied to Victoria. In comparison with the Tohoku case study in **Chapter 2**, two key components of the simulation framework are updated. The first component is the ETAS seismicity model for the CSZ. Unlike the Tohoku case, where many observed events are available to calibrate the ETAS parameters, the CSZ lacks direct observations; thus, its ETAS parameters for M9.0 scenarios need to be selected carefully by reflecting the regional seismicity. More specifically, the applicability of the global ETAS parameters of M9.0 earthquakes from **Chapter 3** is examined by comparing with the 2012 M7.8 Haida Gwaii sequence (Event 28 in **Chapter 3**), the largest recent megathrust earthquake near the northern CSZ (Lay *et al.*, 2013), as well as the local seismicity in the CSZ. Secondly, state-dependent aftershock fragility curves of wood-frame houses are used, developed in **Chapter 4**, to better estimate the cumulative damage effect of mainshock-aftershock sequences and to build a real-time risk forecasting framework for decision-making. In addition, a realistic building dataset of wood-frame houses in Victoria is employed aimed at estimating the total seismic loss for the building portfolio to assess the impact of aftershocks.

The objectives of this chapter are: 1) to show how the simulation framework of spatiotemporal seismic hazard and risk assessment, developed for active subduction regions, can be applied to the CSZ, 2) to quantify the impact of aftershocks on the short-term seismic

risk assessment in terms of damage state (DS) and seismic loss estimation, and 3) to demonstrate how the outputs of the framework can be used for decision-making (e.g., real-time DS forecasting of individual houses). In the following, **Section 5.2** describes the framework of the spatiotemporal seismic hazard and risk assessment for Victoria. **Section 5.3** discusses the impact of mainshocks and aftershocks on the municipality-wide seismic risk assessment in Victoria.

5.2 Spatiotemporal seismic hazard and risk assessment in Victoria

An overview of the framework of spatiotemporal seismic hazard and risk assessment with key updates is given in this section. The framework consists of a seismicity model (ETAS model), a ground motion model (GMPEs), and a seismic fragility model (aftershock fragility curves) as shown in **Figure 5-1**. Synthetic catalogues are generated from ETAS simulations as described in **Chapter 2** and **Chapter 3**. The synthetic catalogues contain the times, magnitudes, and locations of mainshock-aftershock sequence events. Subsequently, the synthetic catalogues and local soil conditions (V_{s30}) are used as inputs to GMPEs to estimate the ground motion intensity measures of mainshock-aftershock sequences at different sites. Next, the intensity measures at multiple sites are applied to the aftershock fragility curves from **Chapter 4** to estimate the DSs and losses of multiple wood-frame houses at different times after a mainshock.

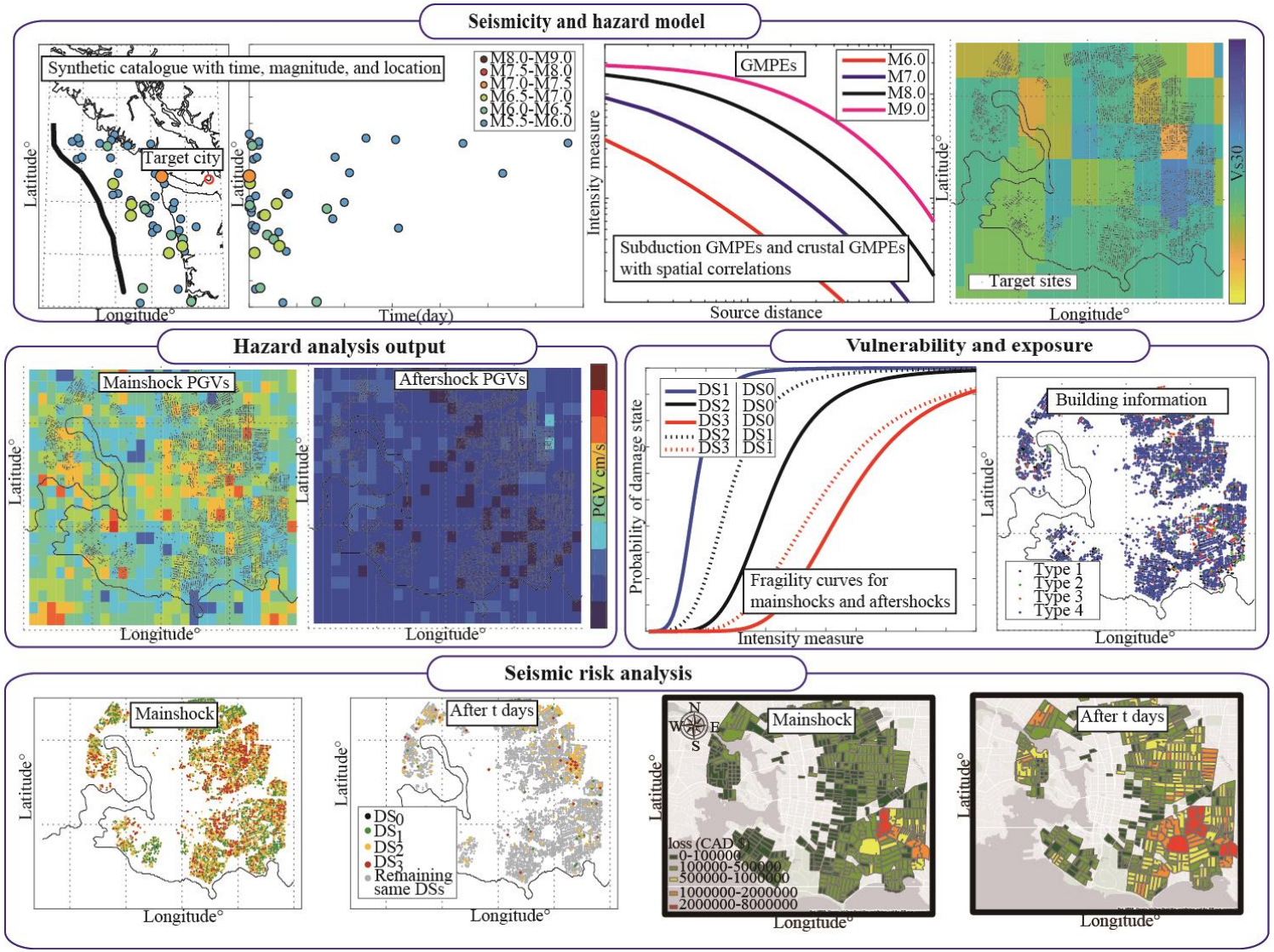

Figure 5-1. Simulation framework of spatiotemporal seismic hazard and risk assessments (the same figure as **Figure 1-1**).

5.2.1 Seismicity model

This subsection analyses regional seismicity in the CSZ and discusses preferred ETAS parameters for the CSZ. In **Section 5.2.1.1**, the Advanced National Seismic System (ANSS) (https://www.ncedc.org/anss/catalog-search.html) and the Seismic Hazard Earthquake Epicentre File (SHEEF) catalogues (Halchuk *et al.*, 2015) are analysed to investigate the main characteristics of the regional seismicity. Due to the limited number of observed events in the CSZ, ETAS parameters cannot be estimated robustly. In **Section 5.2.1.2**, the M7.8 Haida Gwaii event (Event 28 from Case 1 in **Chapter 3**, referred as Haida Gwaii case in this chapter) is considered as a relevant case, which is the largest thrust event recorded in the digital age near Queen Charlotte Island (to the north of Vancouver Island). We compare the proposed global ETAS parameters from **Chapter 3** with those based on the long-time period sub-catalogue (from 1981-2017) spatially filtered by the rupture plane of 2012 M7.8 Haida Gwaii event. ETAS simulations for the CSZ are presented in **Section 5.2.1.3**.

5.2.1.1 *Analysis of ANSS and SHEEF catalogues in the CSZ*

Although the few observed events do not allow calibrating the ETAS parameters, *b*-value estimation is easier and important because the generic ETAS simulation framework assumes *b* = 1. The local ANSS and SHEEF databases are used to estimate the M_c and *b*-value because they include more events than the global NEIC catalogue that was analysed in **Chapter 3**. In addition, the SHEFF catalogue consists of a uniform magnitude type and revised earthquake hypocenters (Halchuk *et al.*, 2015). A shortcoming of the SHEFF catalogue is that only the seismicity in the vicinity of Canada until 2010 is available (e.g., seismicity data in Oregon are missing). We therefore search the ANSS catalogue for more events in a larger spatiotemporal window.

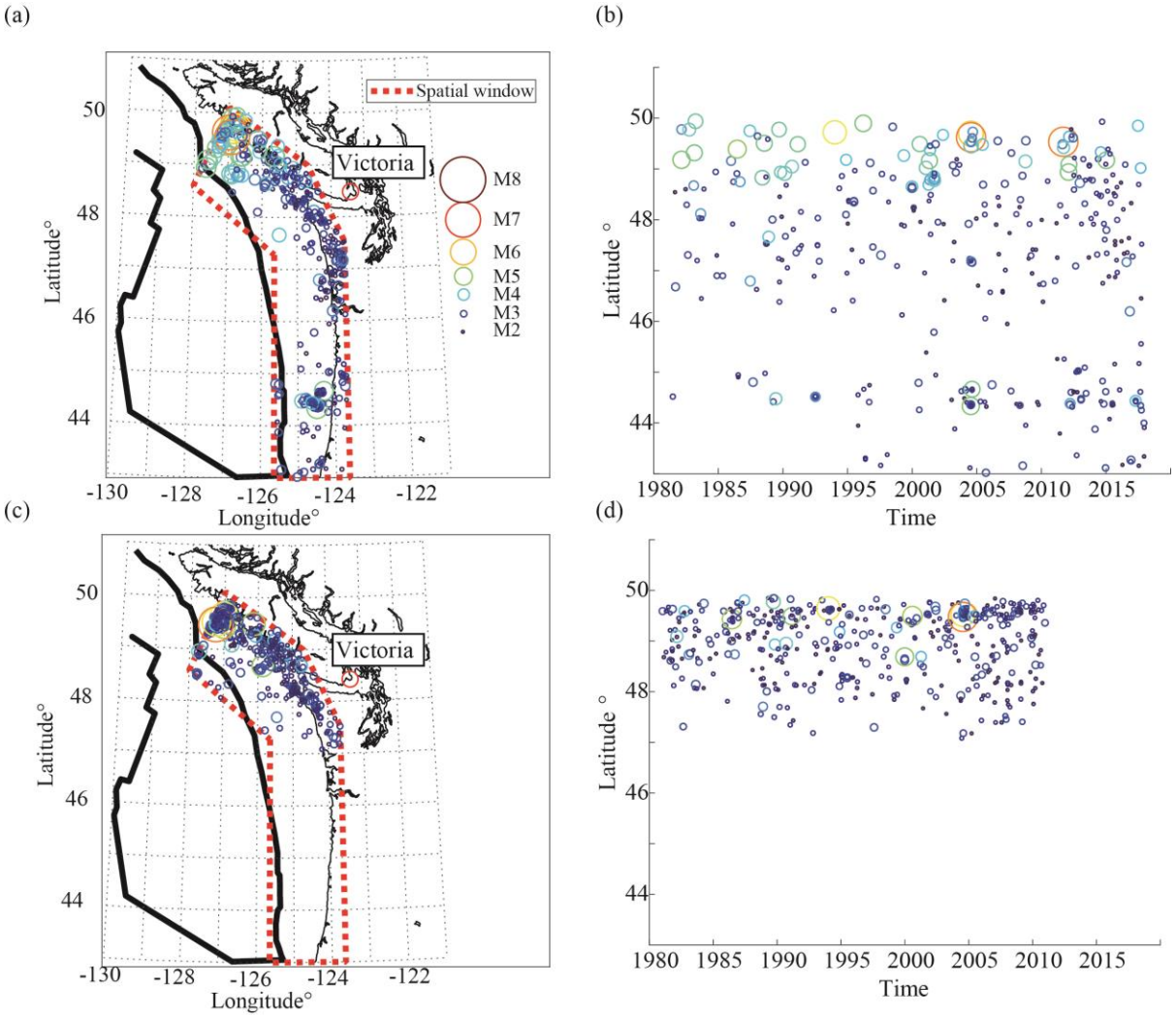

Figure 5-2. Seismicity of the Cascadia Subduction Zone in target window (dashed red polygon) listed in the ANSS catalogue (top) and the SHEEF catalogue (bottom) during 1981-2017: (a, c) epicentral locations and (b, d) latitudinal distribution.

Events are selected from the ANSS and SHEFF catalogues between 1 January 1981 and 31 December 2017 with depth < 100km. Following the 2014 USGS national seismic hazard model (Petersen *et al.*, 2014), we select a spatial window in **Figure 5-2**(a) that encloses the M9.0 mainshock rupture model down-dip to estimated rupture limits of the CSZ (Flück *et al.*, 1997; Wang *et al.*, 2003; Hyndman, 2013); its eastern boundary extends to the western coastline of Vancouver Island. The southern edge of the target window is not extended into northern California (e.g., lower than 43°N), because some M7.0 events took place in the

Mendocino Triple Junction rather than within the CSZ (e.g., the 2010 M6.5 Gorda Plate event and the 2014 M6.8 Ferndale event) (Storesund *et al.*, 2010). **Figure 5-2** shows spatiotemporal plots of observed events with M⩾2.0 from the ANSS and SHEFF catalogues. The ANSS catalogue (**Figure 5-2**(b)) covers a larger area in the western coast of Washington and Oregon States and includes more events after 2010 than the SHEEF catalogue. The SHEEF catalogue contains more smaller events near 50° latitude before 1990 as shown in **Figure 5-2**(d). In the following, two sub-catalogues from the ANSS and SHEFF are used to estimate the *b*-values.

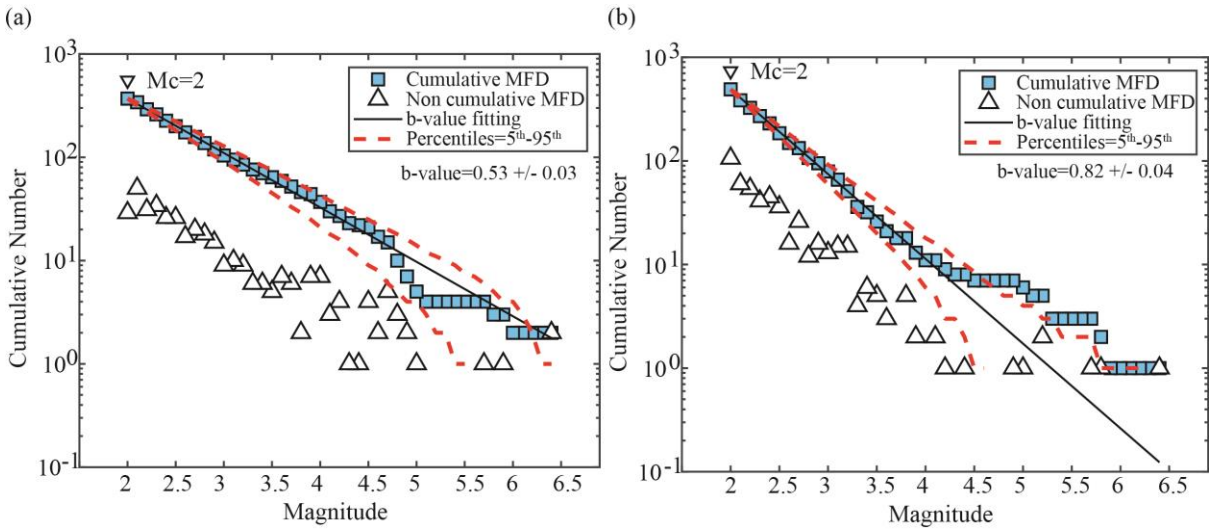

Figure 5-3. Observed magnitude–frequency distributions (MFD) and fitted Gutenberg–Richter laws with the maximum-likelihood estimates of the *b*-values and 5th–95th percentiles from (a) the ANSS and (b) the SHEFF catalogues.

In **Figure 5-3**, the *b*-values of the CSZ based on the ANSS and SHEFF catalogues are estimated as 0.53±0.03 and 0.82±0.04, respectively. The *b*-value = 0.82 from the SHEFF catalogue suggests that the northern CSZ has a magnitude-frequency distribution similar to other regions with *b*-value ≈ 1. The low *b*-value from the ANSS catalogue is due to missing events before 2000. Because of the few events in the CSZ (less than 100 with M_{cut} = 4), reliable

ETAS parameters cannot be estimated solely based on local catalogues. ETAS estimation (a prerequisite for modelling) requires well-recorded sequences, as discussed in **Chapter 2** and **Chapter 3**.

5.2.1.2 *ETAS parameters in global subduction zones and Queen Charlotte Island*

In selecting a suitable ETAS parameters for the CSZ, the 2012 M7.8 Haida Gwaii event near Queen Charlotte Island is relevant: it is the largest and closest thrust event near the CSZ (Hyndman, 2015; Kao *et al.*, 2015). The same sub-catalogue as shown in **Chapter 3** based on the 2012 M7.8 Haida Gwaii event (Event 28) is presented here. Specifically, the spatial window is based on the rupture dimension of the 2012 M7.8 Haida Gwaii event, and the events from the NEIC catalogue are selected between 1 January 1981 and 31 December 2017 with depth < 100 km. **Figure 5-4**(a) and (b) show a spatiotemporal plot of the observed events in the spatial window with M$\geqslant$3.0. Most of the aftershocks triggered by the 2012 M7.8 Haida Gwaii event were clustered spatially within 1 degree of longitude and latitude of the mainshock epicentre. In **Figure 5-5**, we show the magnitude distribution and the *b*-value estimate of 0.76±0.04. Because of the 2012 M7.8 Haida Gwaii event, more events near Queen Charlotte Island were triggered to allow calibrating the ETAS model.

The proposed ETAS parameters based on the global subduction zones from **Chapter 3** and the ETAS parameters based on the Haida Gwaii case are summarised in **Table 5-1**. As discussed in **Chapter 3,** due to the bias of the isotropic spatial disruption, the α-value is fixed to 2.3. The K_0-values between the proposed global ETAS parameters and Haida Gwaii case are similar, which suggests that the number of triggered aftershocks by M9.0 events near the CSZ may be similar to recently observed M9.0-class sequences in Indonesia, Chile, and Japan. The temporal parameters (*p* and *c*) from the global subduction zones are in the ranges of the temporal ETAS parameters from the Haida Gwaii case considering their uncertainties.

However, the median values of temporal parameters from the Haida Gwaii case are slightly larger than the proposed global ETAS spatial parameters. This is consistent with the conclusion in **Chapter 3** that the temporal parameters could be biased upwards due to a small number of events (e.g., less than 200). The spatial parameters are not estimated robustly, because as concluded in **Chapter 3** unusually large q and d values (e.g., $q \geq 4$ and $d \geq 500$) indicate insufficient data with distance to fit the spatial power law robustly (see **Figure 5-4**). Based on the observation from **Table 2-3**, the proposed global ETAS parameters are used to generate synthetic catalogues in the CSZ (K_0 = 0.04±0.02, α = 2.3, c = 0.03±0.01, p = 1.21±0.08, γ =1.61±0.29, d = 23.48±18.17, and q = 1.68±0.55).

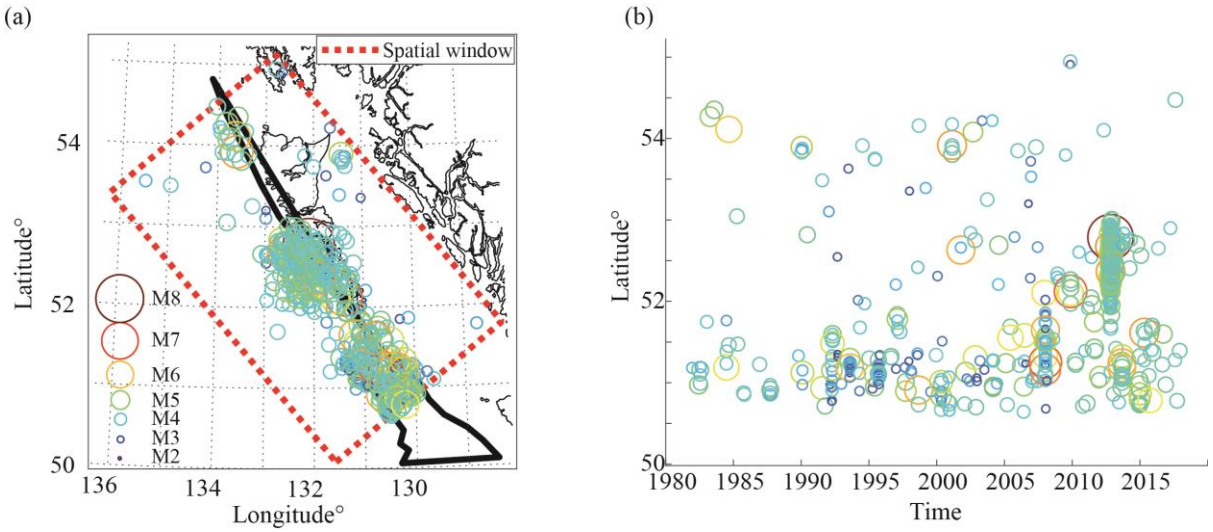

Figure 5-4. (a) Epicentres, and (b) latitudinal distribution of earthquakes during 1981-2017 near Queen Charlotte Island. The spatial window is based on the rupture plane of the 2012 M7.8 Haida Gwaii event.

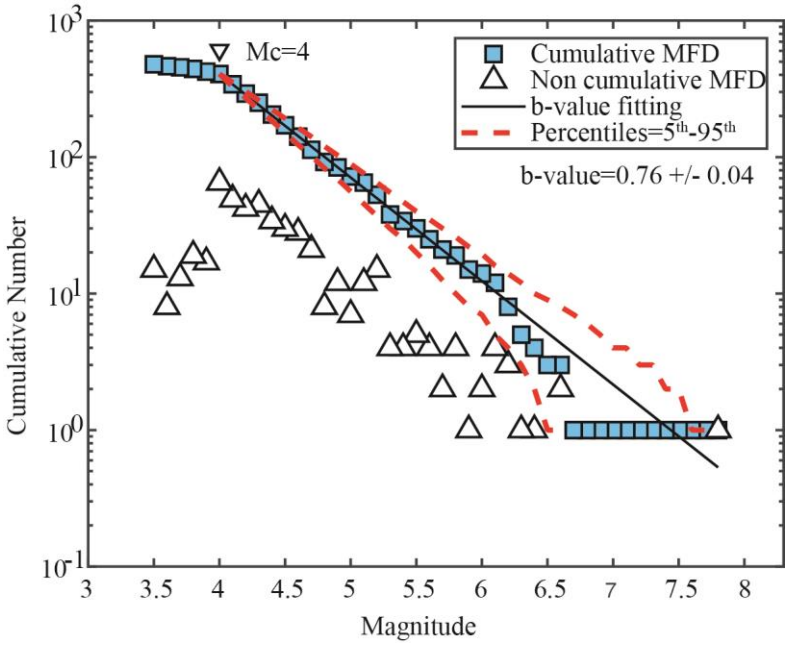

Figure 5-5. Observed magnitude–frequency distribution and fitted Gutenberg–Richter law with a maximum-likelihood *b*-value and 5th–95th percentiles of the seismicity in **Figure 5-4**.

Table 5-1. ETAS parameter estimates from global subduction zones and the Haida Gwaii event (standard errors are shown in parentheses).

	K_0 (event/day)	α (magnitude^{-1})	c (day)	p	d (km^2)	γ (magnitude^{-1})	q
Global catalogues from **Chapter 3**	0.04 (0.020)	2.3 (0)	0.03 (0.01)	1.21 (0.08)	23.48 (18.17)	1.61 (0.29)	1.68 (0.55)
Haida Gwaii case	0.04 (0.003)	2.3 (0)	0.05 (0.03)	1.35 (0.09)	333.69 (522.36)	1.09 (0.22)	4.26 (3.77)

5.2.1.3 *ETAS simulation*

The ETAS simulation framework with the anisotropic power-law kernel from **Chapter 2** is employed to generate synthetic catalogues of aftershocks given a M9.0 earthquake. The developed anisotropic power-law kernel combines the simulated 2D rupture area with a power-law beyond the rupture area, which can distribute the first generation of aftershocks anisotropically in space. However, in comparison with the rectangular rupture area of the Tohoku mainshock, several studies suggested a longer and narrower shape of the mainshock

rupture area for the CSZ (e.g., Petersen *et al.*, 2014; Wang and Tréhu, 2016). The M9.0 rupture dimensions of the CSZ are more similar to the 2004 M9.1 Aceh-Andaman earthquake, which has a greater rupture length-to-width ratio than the Tohoku mainshock (Mai and Thingbaijam, 2014). The shape of the rupture area is modelled and constrained by the down-dip edge models (Flück *et al.*, 1997; Wang *et al.*, 2003; Hyndman, 2013), and the rupture dimensions are simulated from the empirical scaling law (Thingbaijam *et al.*, 2017). The down-dip edge model of CSZ is critical for the hazard calculation, as it primarily controls the rupture distances from the mainshock to the coastal city (e.g., Victoria). Different down-dip edge models have been developed based on different assumptions of geothermal conditions, episodic tremor and slip zones, etc (Hyndman, 2013). In this study, rupture widths are simulated to capture the locations of different down-dip edge models from the 2014 USGS national seismic hazard model. In terms of the aftershock decay outside the CSZ rupture area, the same procedures are applied to build a power-law decay as in the Tohoku case study using 1D and 2D power laws. **Figure 5-6** shows the probability density distribution of the aftershock spatial distribution of the M9.0 event with a rupture length of 1100 km and width of 130 km.

Additional features including the depth, earthquake type, and focal mechanism, are assigned to each event in synthetic catalogues as in **Chapter 2**. These additional features allow simulating the rupture plane of large crustal and subduction-zone aftershocks ($M \geq 6.5$) and evaluating seismic intensity measures (IMs) using GMPEs.

Depths for earthquakes with $M<8$ are sampled from empirical cumulative distribution functions (ECDFs) of depths obtained from past observations in the CSZ (as in **Chapter 2).** The slab model (Hayes *et al.*, 2012) of the CSZ (see **Figure 5-6**) is divided into sub-regions with 10 km width from the trench line to the continental crust to estimate the ECDFs of depth in each sub-region. We use past earthquakes $M \geq 2$ from the ANSS catalogue within the slab model. Events with depths less than 5 km are eliminated because the majority of these events

are remote events, and their depths are poorly estimated with depths of 0 km (Power *et al.*, 1994). The histogram of depths from the past events with M≥2 is shown in **Figure 5-7**.

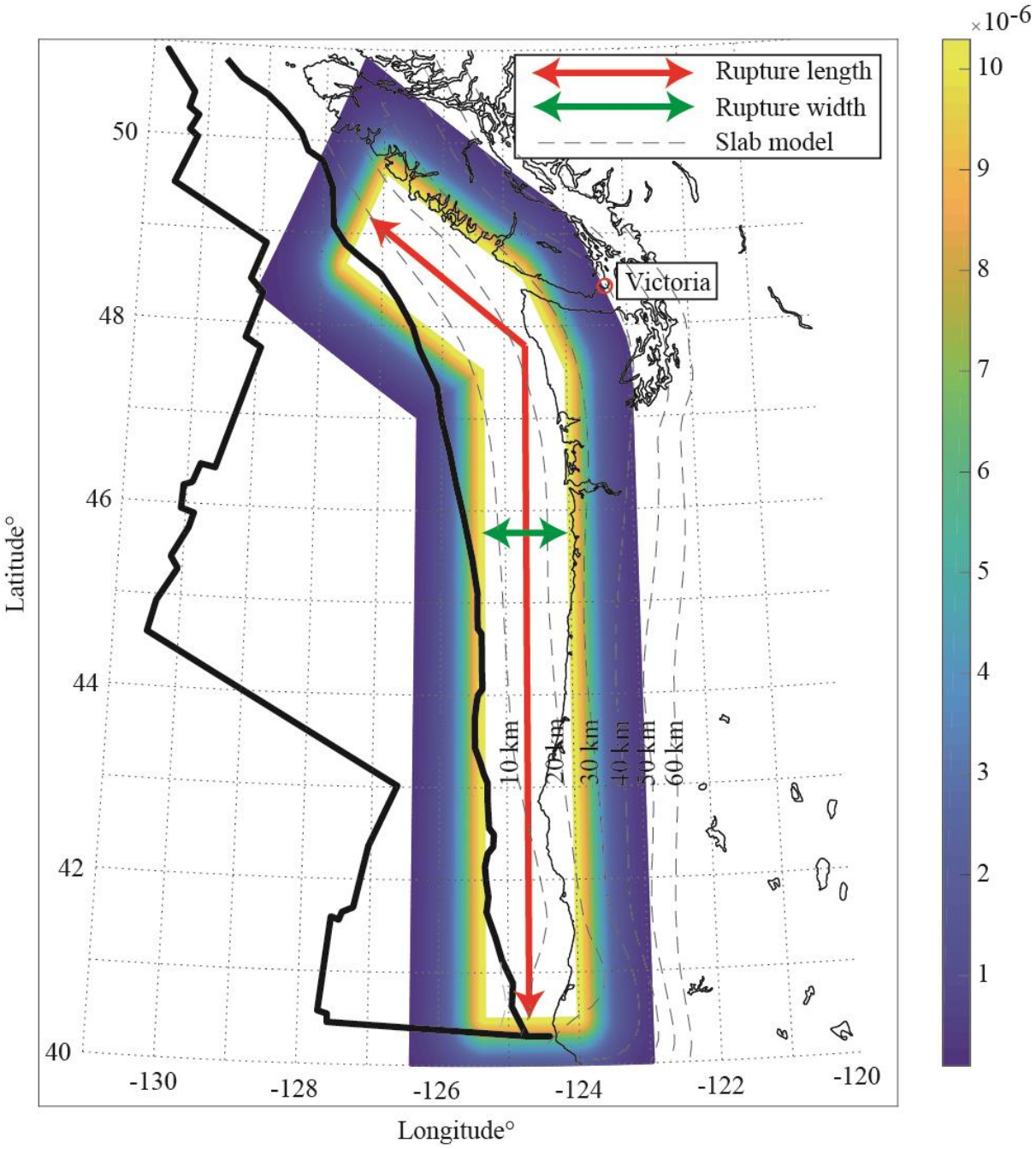

Figure 5-6. An example of the spatial probability density function of the first generation of aftershocks outside a simulated rupture area (rupture length × rupture width = 1100 km × 130 km).

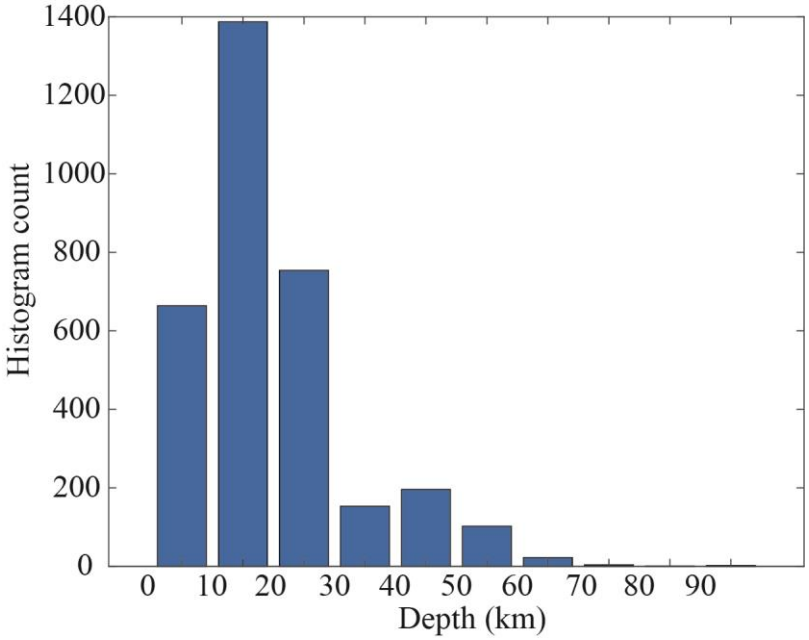

Figure 5-7. Histogram of depths from past events with M≥2.

All simulated earthquakes with M≥8 are treated as subduction-interface earthquakes, and the depths are assigned directly from the slab model (Hayes *et al.*, 2012) (see the slab model in **Figure 5-6**). Earthquake types (continental-crust, subduction plate-boundary, or subduction intra-plate) are defined by the sampled depths and the slab model: earthquakes more than 20 km above the plate interface are defined as crustal earthquakes, the layer within ±20km of the plate interface is classified as subduction-interface earthquakes (allowing for depth uncertainty), and remaining deep earthquakes are treated as intra-slab earthquakes.

As discussed in **Chapter 2,** due to the plate motion of the subduction zone, the crustal and subduction-zone earthquakes may have similar strike directions as the subduction plane. Following that, the strike and dip angles of the subduction and crustal aftershock are assumed to be similar to the strike and dip angles of the subduction plane. The ECDFs of strike and dip angles for crustal and subduction earthquakes are evaluated from the global Centroid Moment Tensor (gCMT) catalogue, and the sampled angles are assigned to the large aftershocks with M≥6.5. Specifically, given the target city is Victoria, British Columbia, Canada, the strike angle

of nodal planes 1 and 2 that is closer to the strike angles (320°-350°) of the subduction plane of the northern and central CSZ is selected (Hayes *et al.*, 2012).

In total, 10,000 synthetic mainshock-aftershock catalogues are generated over a one-year period. The magnitude frequency distribution and the daily number of events in a square root scale are shown in **Figure 5-8**. The aftershock seismicity rate with M≥5.5 is high immediately after the mainshock and gradually decays after day 5.

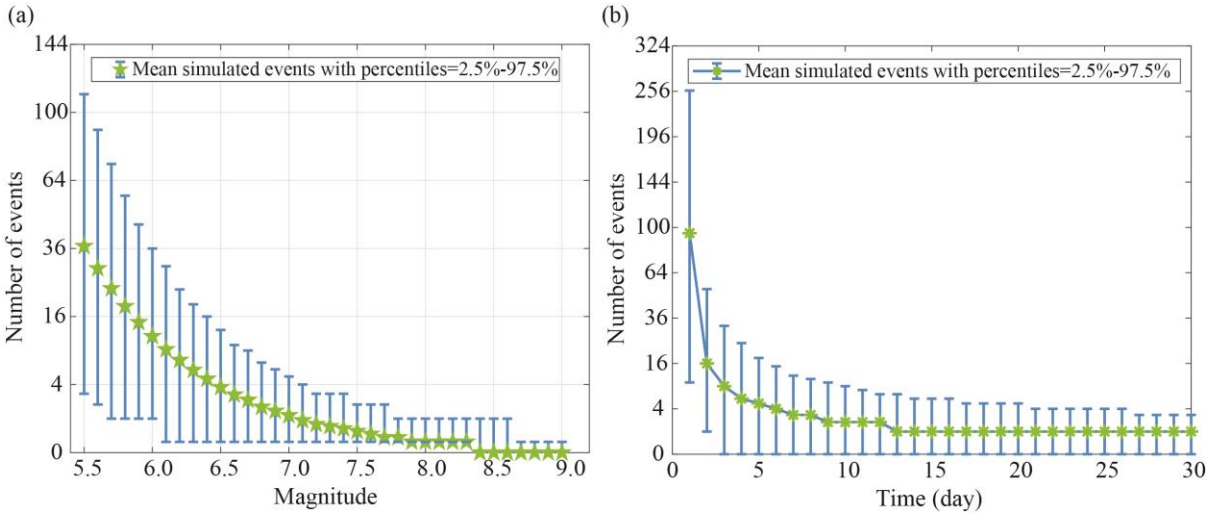

Figure 5-8. (a) Simulated magnitude frequency distributions of aftershocks. (b) The daily number of simulated events over a month after the mainshock.

5.2.2 Ground motion model

To compute scenario-based shake maps of M9.0 earthquake sequences for the City of Victoria, the following GMPEs and V_{s30} information are used. PGV is adopted as IM in the risk analysis because PGV shows a better performance in capturing the cumulative damage effects of wood-frame houses (**Section 4.4, Chapter 3**). Accordingly, the GMPEs by Ghofrani and Atkinson (2014) and Boore *et al.* (2014) are selected to compute the PGV for subduction-zone and crustal earthquakes, respectively.

Ground motion models to be used for the CSZ should reflect seismological findings from recent major subduction and crustal events. Although other global subduction-zone

GMPEs are available (e.g., Atkinson and Boore, 2003; Zhao *et al.*, 2006), they do not include the ground motion from the 2011 Tohoku sequences, and thus the equations need to be extrapolated beyond the range of the underlying ground motion data. On the other hand, PGV is not always included as the output variable of the newest subduction-zone GMPEs (Abrahamson *et al.*, 2016; Zhao *et al.*, 2016). Therefore, we use the GMPEs from Ghofrani and Atkinson (2014), which includes the ground motion records from the 2011 Tohoku event together with adjustment factors for the CSZ to account for its deeper soil profile compared with Japan. In comparison with other crustal GMPEs from the NGA-West2, the GMPE by Boore *et al.* (2014) requires less input information (e.g., unknown options for fault type and hanging wall effect). This is more suitable for southwestern British Columbia, since a complete inventory of active faults and their geometry is not available, except for a few fault systems, such as the Leech River fault (Morell *et al.*, 2017).

The synthetic catalogues with times, magnitudes, locations, and earthquake types are applied to the GMPEs to calculate the median value of PGV. Source models for M≥6.5 crustal and subduction-zone aftershocks are generated from empirical scaling laws (Thingbaijam *et al.*, 2017) and the ECDFs of strike and dip angles. This allows calculating the shortest rupture distances from the simulated rupture dimension to target sites.

Examples of median values of PGVs for subduction and crustal earthquake from Ghofrani and Atkinson (2014) and Boore *et al.* (2014) with V_{s30} = 300 m/s are shown in **Figure 5-9**, noting that V_{s30} = 300 m/s corresponds to an average stiff soil condition in the City of Victoria. Considering the rupture distance of the M9.0 mainshock to Victoria is about 70-80 km, the corresponding median PGV value is 30 cm/s (**Figure 5-9**(a)). On the other hand, the median PGV of a crustal event, for example, a M6.0 event with rupture distance < 5 km in the Leech River fault (Morell *et al.*, 2017), is 35 cm/s as shown in **Figure 5-9**(b).

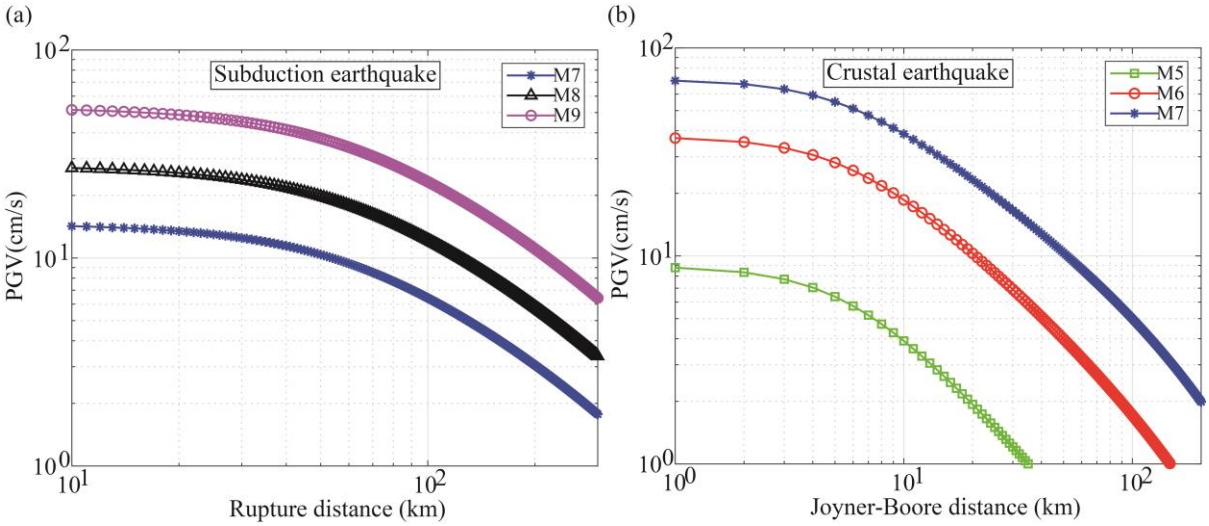

Figure 5-9. (a) Median values of peak ground velocity (PGV) with V_{S30} = 300 m/s for subduction earthquakes from M 7.0–9.0, using the ground-motion prediction equation (GMPE) by Ghofrani and Atkinson (2014) (b) Median values of PGV with V_{S30} = 300 m/s for crustal earthquakes from M 5.0–7.0, using the GMPE by Boore *et al.* (2014).

Figure 5-10 shows the V_{s30} map of the City of Victoria from Wald and Allen (2007). The V_{s30} map is consistent with the observations from Monahan and Levson (2001). The soil conditions in Victoria generally correspond to the National Earthquake Hazard Reduction Program (NEHRP) site classes C to E (e.g., V_{s30} < 760 m/s). We use a grid size of 500 m × 500 m for the City of Victoria to produce the mainshock and aftershock shaking maps. We consider the spatial correlation models from Goda and Hong (2008) and Goda and Atkinson (2010) for subduction-zone and crustal events, respectively. The error terms are sampled from the inter-event sigma and the intra-event sigma with the spatial correlation models.

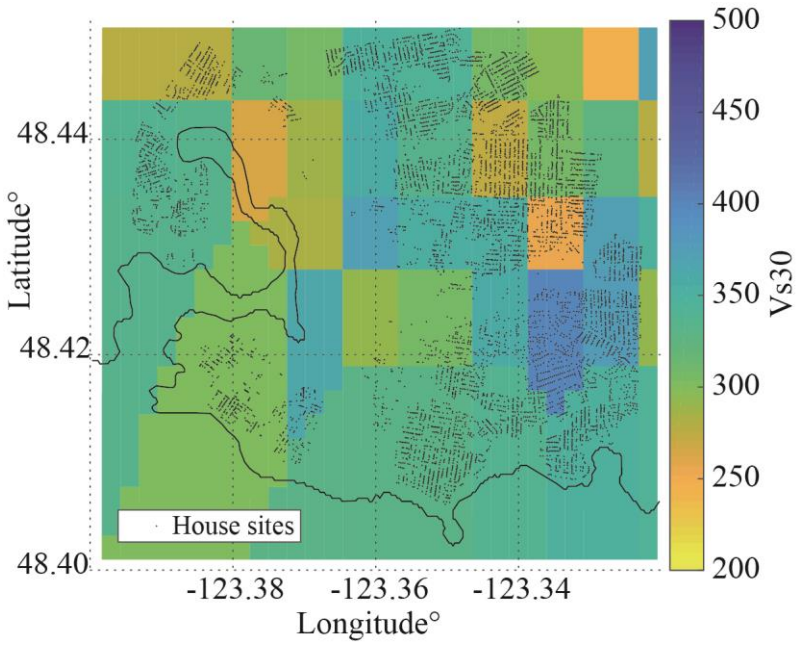

Figure 5-10. V_{s30} map of the City of Victoria from Wald and Allen (2007).

5.2.3 Seismic risk model

The state-dependent fragility curves of wood-frame houses from **Chapter 4** are used to assess the performance of the wood-frame houses under a M9.0 megathrust subduction earthquake sequence. Due to variable shear-wall configurations of different wood-frame houses, in **Chapter 4** four types of two-storey wood-frame houses are defined: (1) House 1 with stucco/engineered oriented strand board (OSB)/gypsum wallboard (GWB), (2) House 2 with engineered OSB/GWB, (3) House 3 with non-engineered OSB/GWB, and (4) House 4 with horizontal boards (shiplap)/GWB. The term 'engineered' for Houses 1 and 2 indicates that hold-downs and blocking of the wall panel are used to increase its seismic resistance and to meet the seismic code requirements (White and Ventura, 2006).

The state-dependent fragility curves of House 4 are shown in **Figure 5-11**. The parameters of the fragility curves with the multinomial distribution for Houses 1-4 are provided in **Table 4-8** (**Chapter 4**). Three performance thresholds corresponding to the Green, Yellow, and Red tags (hereafter referred to as DS_1, DS_2, and DS_3) are defined in **Chapter 4**. Green tag

(DS_1) represents a case where the house is inspected by a structural engineer and can be immediately occupied, Yellow tag (DS_2) indicates that access is limited except for professional maintenance, and Red tag (DS_3) means the house is unsafe to occupy and requires retrofitting or rebuilding (Bazzurro *et al.*, 2004).

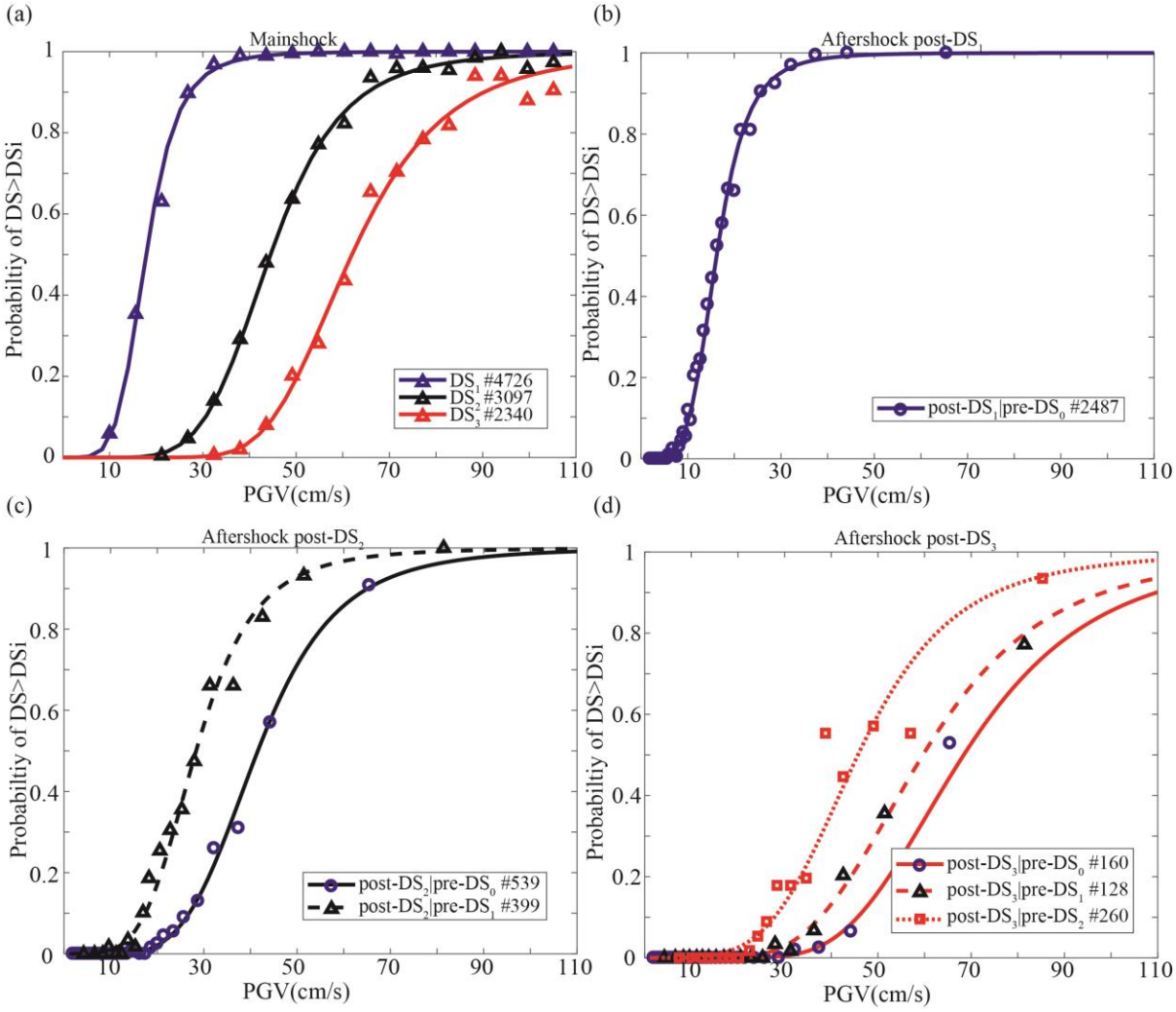

Figure 5-11. (a) mainshock fragility curves, and aftershock fragility curves for (b) post-DS_1, (c) post-DS_2, and (d) post-DS_3 for House 4.

According to **Figure 5-11**(a), the median value of DS_1 is 22 cm/s. Considering the median PGV of M9.0 in Victoria is approximately 30 cm/s (**Figure 5-9**), the probability that House 4 changes from DS_0 (no damage) to DS_1 by a mainshock is high. Subsequently, if a crustal event is triggered near Victoria (with median PGV value 35 cm/s as suggested in **Figure**

5-9), House 4 with DS_1 will change to DS_2 with 50% probability given that the median value of DS_2 is 30 cm/s in **Figure 5-11**(c).

In total, 6,711 houses are considered for the seismic risk assessment in the City of Victoria[††]. To link the fragility curves of Houses 1-4 with individual houses in the building data, the wood-frame houses are classified into Houses 1-4 according to construction years, which reflects seismic performances of the houses. Four different house types are considered: (1) House 1 - after 1991, (2) House 2 - from 1981 to 1990, (3) House 3 - from 1971-1980, and (4) House 4 - before 1970. The numbers of Houses 1-4 are 387, 197, 257, and 5870, respectively. This is consistent with the descriptions from White and Ventura (2006) that the majority of the wood-frame houses were built before 1973 and thus may be deficient in seismic capacity compared with the current seismic design standard in British Columbia. **Figure 5-12** shows a plot of spatially distributed Houses 1-4 in Victoria.

To evaluate the seismic damage to each house, we interpolate the simulated PGVs of mainshock-aftershock shaking maps with 500 m × 500 m grid size linearly to each house location and apply the fragility curves. The total asset of the 6,711 houses is approximately $930 million Canadian dollars. The seismic loss of the wood-frame houses is calculated based on the approach from Onur *et al.* (2005). Mean damage ratios of 5%, 40%, and 80% (slight, heavy, and major) are considered for Green (DS_1), Yellow (DS_2), and Red (DS_3) tags, respectively.

[††] The building dataset for Victoria, Canada is obtained by the personal communication with Dr. Solomon Tesfamariam, University of British Columbia.

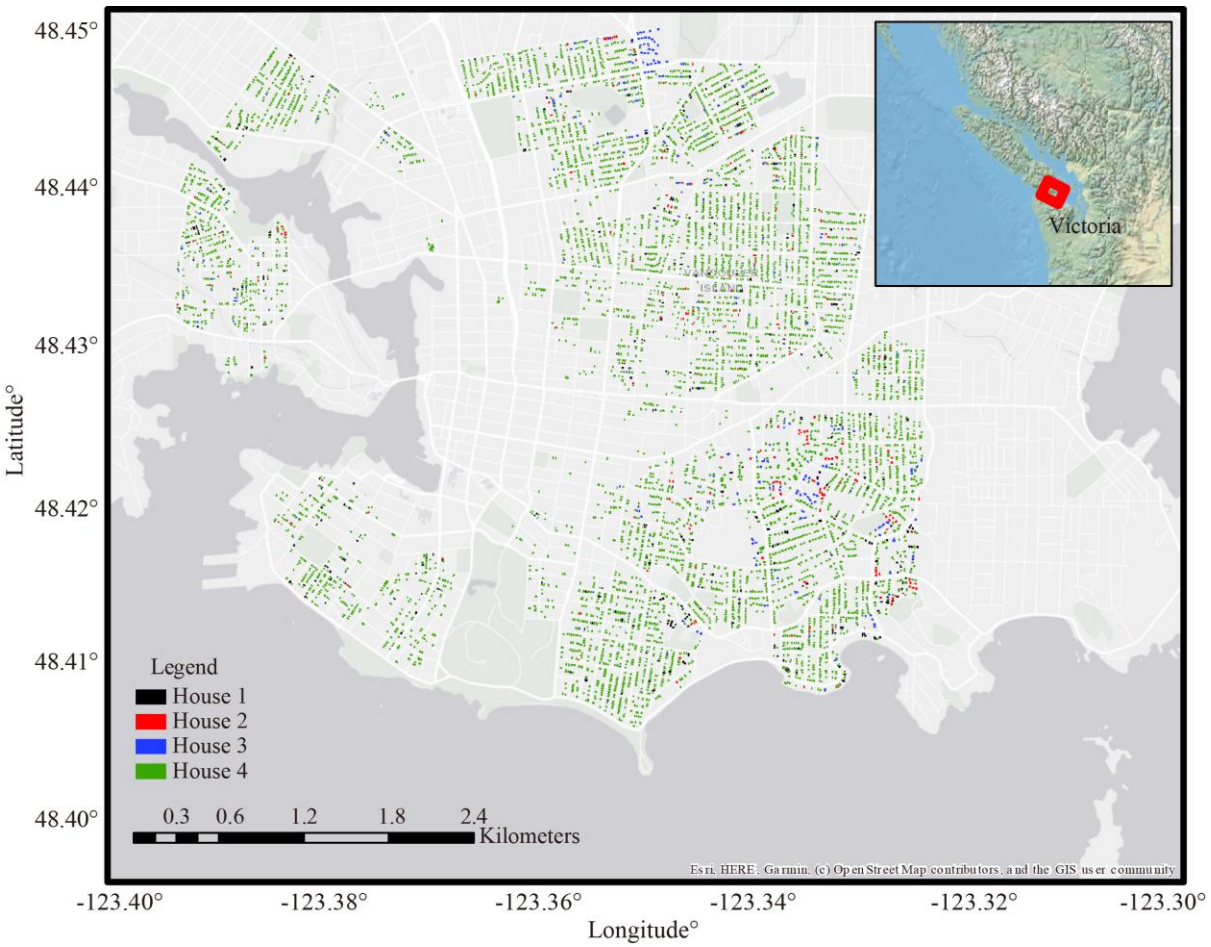

Figure 5-12. Spatial distribution of wood-frame houses in Victoria (6,711 in total with House 1 #387, House 2 #197, House 3 #257, and House 4 #5,869).

5.3 Results and discussion

This section discusses the impact of mainshocks and aftershocks on the municipality-wide seismic risk assessment in Victoria. **Section 5.3.1** investigates the effects of mainshocks on DS distributions and seismic loss estimates of the wood-frame houses. Moreover, three single mainshock simulations corresponding to 10^{th}, 50^{th}, and 90^{th} loss scenarios in terms of total seismic loss due to mainshocks are displayed. **Section 5.3.2** quantifies the effects of aftershock sequences on DS distributions and seismic loss estimations of the wood-frame houses in Victoria for different durations (1 day, 1 week, 1 month, and 1 year). To visualise the impact of different aftershocks (e.g., distant and close M7.0-class subduction aftershocks) on the

seismic risk assessment, **Section 5.3.2** also presents individual simulation results of synthetic catalogues, mainshock-aftershock hazard maps, and spatial distributions of DSs and loss maps corresponding to 10^{th}, 50^{th}, and 90^{th} percentiles of total losses within 7 days after the mainshock. To display the impact of potential destructive crustal aftershocks near Victoria, **Section 5.3.3** presents individual simulation results corresponding to the 90^{th} percentile of total losses from 10,000 simulations within 30 days after the mainshock.

5.3.1 Impact of mainshocks on DS and loss estimations

Figure 5-13 shows the damage probability of Houses 1-4 due to mainshocks only for the building portfolio of wood-frame houses (6,711 houses in total) in Victoria. House 4 makes up almost 90% of the wood-frame houses and is susceptible to significant damage. As concluded in **Section 5.2.3**, the probability that House 4 can change from DS_0 to DS_1 due to the mainshocks is approximately 50%. A similar observation can be drawn in **Figure 5-13**(a), which shows that the probabilities of DS_1, DS_2, and DS_3 right after the mainshocks are 51.3%, 9.2%, and 4.5%, respectively. Considering the total number of Houses 4 is 5,870, on average, 265 Houses 4 could change from DS_0 to DS_3 after the mainshocks. In **Figure 5-13**(b), the 10^{th}, 50^{th}, and 90^{th} percentiles of total aggregated losses by the mainshocks are 14, 66, and 194 million Canadian dollars, respectively. High estimated seismic losses (e.g., 500 million Canadian dollars with 0.001 exceedance probability) in the right tail in **Figure 5-13**(b) represent the effects of extreme IMs from the mainshocks. The large variability of PGV values of the mainshocks is due to two sources. The first source is the uncertainty of PGV from the GMPE by Ghofrani and Atkinson (2014). The second source is the shortest distance from the mainshock rupture plane to Victoria, which depends on the down-dip edge models of the CSZ.

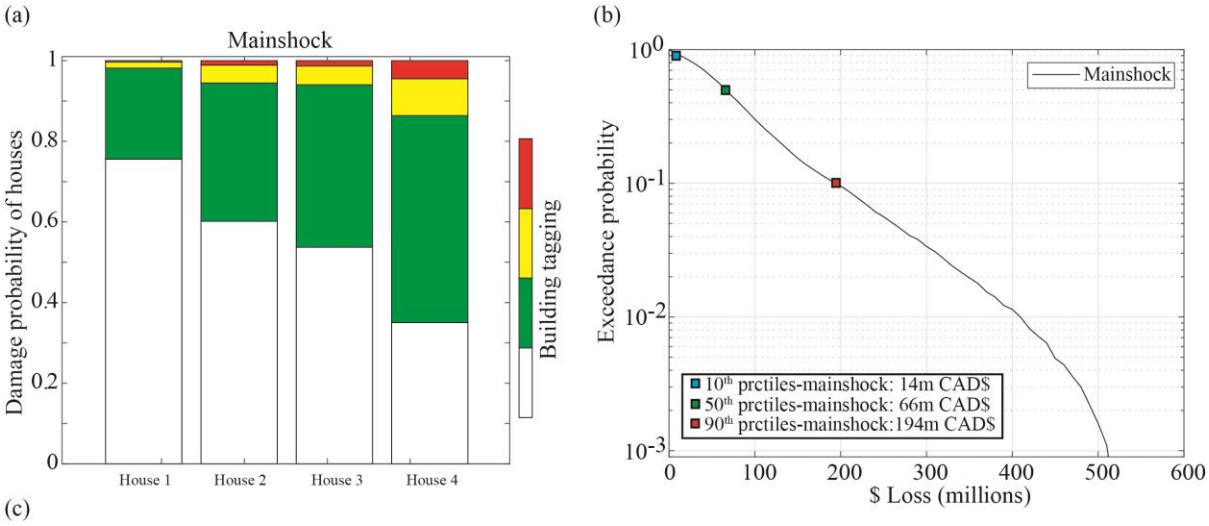

Figure 5-13. (a) Damage probability of Houses 1-4 after mainshocks based on 6,711 houses in Victoria. (b) Loss exceedance curves of mainshocks. 10th, 50th, and 90th percentiles of aggregated losses by mainshocks are 14, 66, and 194million Canadian dollars (m CAD$), respectively.

To visualise the uncertainty of the mainshocks on hazard analysis and quantify the impact of the mainshocks on risk assessment, single simulations of mainshock shaking maps, and DS and loss distributions corresponding to the 10th, 50th, and 90th percentiles of total losses are examined closely. **Figure 5-14** shows the mainshock shaking maps corresponding to the 10th, 50th, and 90th percentiles of total losses. The maximum and average PGV values of each shaking map are also summarised in **Figure 5-14**. The average PGV values of 10th, 50th, and 90th percentile scenarios are 14, 25, and 44 cm/s, respectively, whereas the maximum PGV values of **Figure 5-14**(a)-(c) are 30, 52, and 90 cm/s., respectively.

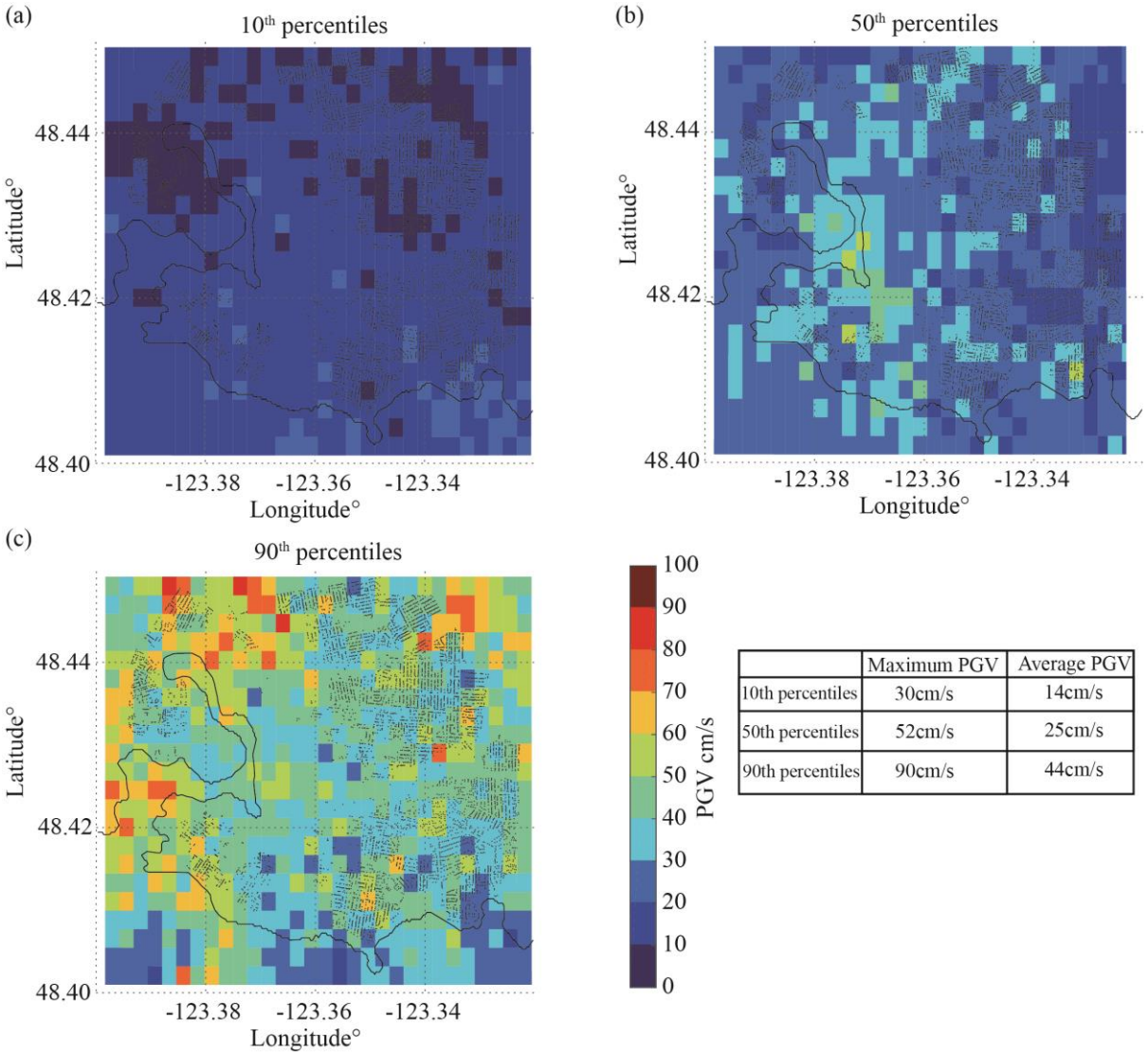

	Maximum PGV	Average PGV
10th percentiles	30cm/s	14cm/s
50th percentiles	52cm/s	25cm/s
90th percentiles	90cm/s	44cm/s

Figure 5-14. Plots of single simulations of mainshock shaking maps corresponding to (a) 10th, (b) 50th, and (c) 90th percentiles of total losses.

The hazard results from **Figure 5-14** can be further applied to seismic risk analysis (the state-dependent fragility curves of wood-frame houses and the real building dataset) to estimate the DS of each house and the total seismic loss. **Figure 5-15**(a) shows the number of houses with DS_0, DS_1, DS_2, and DS_3 for different scenarios. The 10th percentile scenario only has 992 and 4 houses with DS_1 and DS_2, respectively, which suggest most of the houses can be immediately occupied if no major aftershocks are triggered in a short-time period. The number of houses with DS_0, DS_1, DS_2 and DS_3 for the 50th percentile scenario is 2106, 4394, 207, and

4, respectively in **Figure 5-15**(c). The 90th percentile scenario has a greater number of houses with DS_2 and DS_3, which are 2183 and 726, respectively, as indicated in **Figure 5-15**(e). The significantly increased number of houses with DS_3 is a result of the large PGV values with 44 cm/s on average in the 90th percentile scenario. The large PGV values in **Figure 5-14**(c) are spatially correlated in the northern and eastern parts of the City of Victoria, where many houses are located. On the other hand, **Figure 5-15**(b), (d), and (f) show the block maps of loss distributions corresponding to the different scenarios, which are 14, 66, and 194 million Canadian dollars.

In the post-earthquake risk management of an M9.0 event in the CSZ, if a mainshock source model is available right after the mainshock, quasi-real-time aftershock hazard and risk assessments can be performed using the developed framework. For instance, if the 90th percentile scenario is applicable (see **Figure 5-14**), the aftershock forecasting can be useful to evaluate the seismic risk of critical infrastructures on day 1 (e.g., transportation system, electricity and water supply), and ensure that the service would be available given any future destructive aftershocks. In addition, for the purpose of accurate building tagging, the uncertainty of the mainshock PGV can be constrained by the observed value, which is usually available right after the mainshock (e.g., USGS's ShakeMap system). This would allow reducing the uncertainty of the IM from GMPEs, and more accurate DSs of wood-frame houses can be estimated.

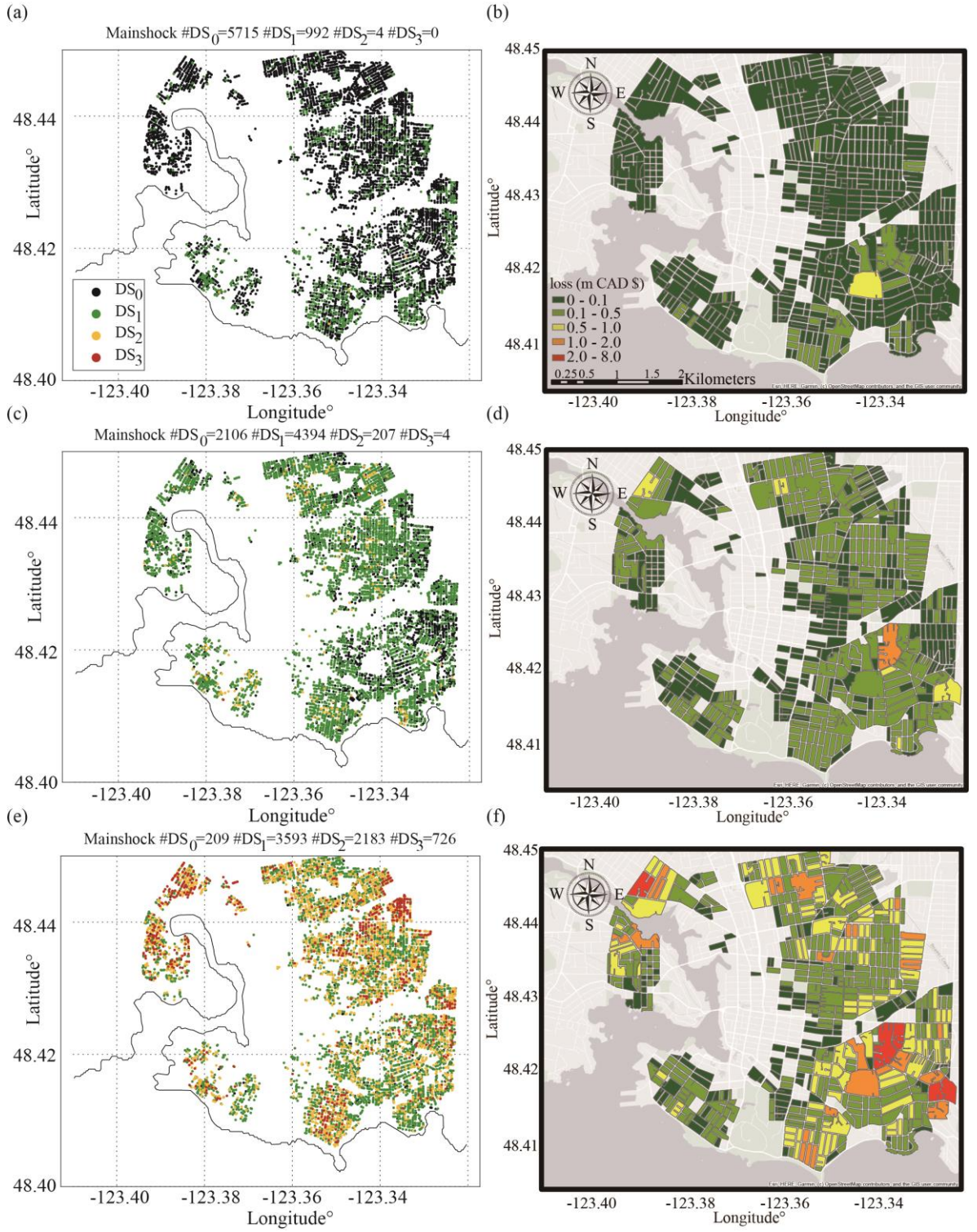

Figure 5-15. Plots of a single simulation of DS distributions of wood-frame houses for (a) 10th, (c) 50th, and (e) 90th percentiles of total losses (m $CAD) by mainshocks. The block map of seismic loss distribution of wood-frame houses in the City of Victoria for (b) 10th, (d) 50th, and (f) 90th percentile scenarios.

5.3.2 Impact of aftershocks on DS and loss estimations

This subsection explores the impact of aftershocks on damage probability and loss estimation of the wood-frame houses. To demonstrate the impact of aftershocks on seismic hazard and risk assessment, three single simulations within 7 days after the mainshocks corresponding to 10^{th}, 50^{th}, and 90^{th} percentiles of total losses are presented. These three cases represent three different scenarios of large aftershocks for the City of Victoria: (1) distant large aftershock (10^{th} percentile), (2) moderate-distance large aftershock (50^{th} percentile), and (3) close large aftershock (90^{th} percentile). Due to the large variability of mainshock PGVs from GMPEs, the mainshock PGVs of 10^{th}, 50^{th}, and 90^{th} percentiles of Day 7 are selected with the similar PGVs as in **Figure 5-14**. This is to ensure the impact of aftershocks on risk analysis is not overestimated or underestimated due to the variability of mainshock PGVs.

Figure 5-16(a) shows the average damage probability of Houses 1-4 in Victoria (i.e., 6,711 buildings in total) for mainshocks only, and durations of 1 day, 1 week, 1 month, and 1 year after the mainshock. The impact of aftershocks on the DS of Houses 1-4 is different, noting that House 4 has a higher probability of resulting in DS_1 by the mainshocks than Houses 1-3. In comparison with the damage probability of Houses 1-4 by the mainshocks, the probabilities that damage conditions of Houses 1-4 are changed from DS_0 to DS_1 by aftershocks are 4.0%, 2.5%, 3.6%, and 2.0%, respectively. A plausible explanation could be that Houses 1-3 have higher probabilities of sustaining no damage after the mainshocks than House 4, which leads to higher probabilities for Houses 1-3 changing from DS_0 to DS_1 due to aftershocks. Compared with the damage probability of the mainshock, an additional 1.7%, 3.1%, 2.6%, and 3.8% of Houses 1-4 could change to DS_2 due to aftershocks, whereas the probabilities that aftershocks cause further damage to DS_3 are 0.3%, 0.9%, 0.7%, and 1.4%, respectively. This indicates that House 4 damaged by the mainshocks tends to have further damage to change to DS_2 and DS_3. The higher damage probability of DS_3 for House 4 suggests that the retrofitting of House 4 to

meet the seismic provisions of the National Building Code of Canada (Houses 1 or 2) might be necessary to reduce the probability of demolition and reconstruction of House 4 after M9.0 sequences.

The loss exceedance curves of mainshock-aftershock sequences for mainshocks only, and durations of 1 day, 1 week, 1 month, and 1 year are shown in **Figure 5-16**(b). The 10th, 50th, and 90th percentiles of total aggregated losses by Day 7 are 20, 71, and 224 million Canadian dollars, respectively. On average, aftershocks could cause additional 10% and 20% losses after 1 week and 1 year of the mainshock, respectively, in comparison with the loss exceedance curves of the mainshocks. The effects of aftershocks on seismic loss estimation are consistent with other studies (e.g., Salami and Goda, 2014).

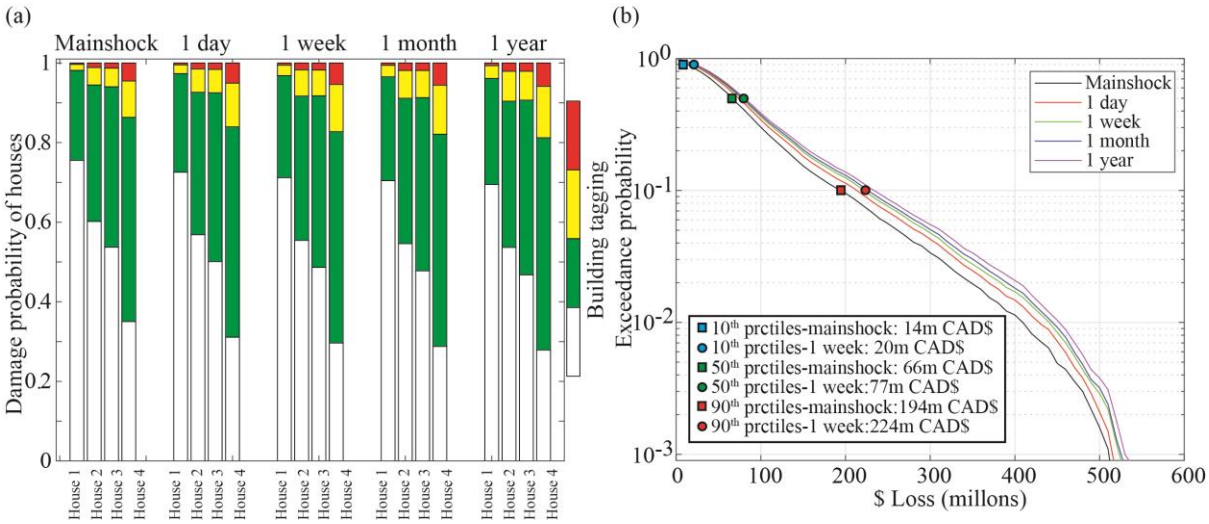

Figure 5-16. (a) Damage probability of Houses 1-4 and (b) loss exceedance curves of mainshock-aftershock sequences at durations of 1 day, 1 week, 1 month, and 1 year based on 6,711 houses in Victoria. 10th, 50th, and 90th percentiles of aggregated losses by mainshock-aftershocks within 1 week are 20, 77, and 224 million Canadian dollars (m CAD$), respectively.

To illustrate different scenarios for risk management decisions, the seismic hazard and risk results within 7 days after the mainshocks corresponding to 10th, 50th, and 90th percentiles

of total losses are presented in the following. **Figure 5-17** shows plots of three single simulations of aftershock epicentres and latitudinal distribution of aftershocks up to day 7 after the mainshock from 10,000 simulations. These three scenarios represent (1) a distant large aftershock (10^{th} percentile in **Figure 5-17**(a) and (b)), (2) a moderate-distance large aftershock (50^{th} percentile in **Figure 5-17**(c) and (d)), and (3) a closer large aftershock (90^{th} percentile in **Figure 5-17**(e) and (f)) of M7.0-class aftershocks. In comparison with the distant M7.0-class aftershocks from 10^{th} and 50^{th} percentiles scenarios, the M7.2 subduction aftershock (48.49°N, 124.69°W) in the 90^{th} percentile scenario in **Figure 5-17**(e) is much closer to Victoria and may cause higher seismic losses.

Figure 5-18 shows three single simulations of mainshock PGV maps, and the maximum aftershock PGV maps corresponding to the seismicity plots in **Figure 5-17**. Similar ranges of the maximum and average mainshock PGVs are selected in **Figure 5-18**(a), (c), and (e) as in **Figure 5-14**. Although two M7-class events from the 10^{th} percentile scenario are triggered in the offshore region as shown in **Figure 5-17**(a), the impact of the two M7.0-class events on the ground motion hazard is limited due to the long rupture distances. No large aftershocks are triggered near Victoria (e.g., within 50 km); therefore, only a few patches in the maximum aftershock PGV map by day 7 have PGV values larger than 10 cm/s in **Figure 5-18**(b). Although the epicentre of the M7.8 aftershock (47.74°N, 125,27°W) from the 50^{th} percentile scenario is 200 km away from Victoria, the rupture distance is 110 km when a large finite fault plane is accounted based on the scaling law of fault dimensions (Thingbaijam *et al.*, 2017) and some sites in the east of Victoria have PGV values larger than 10cm/s in **Figure 5-18**(d). The impact of the M7.2 event from the 90^{th} percentile scenario on the hazard map in **Figure 5-18**(f) is significant. The majority of the maximum aftershock PGV values exceeds 10 cm/s almost everywhere across the City of Victoria.

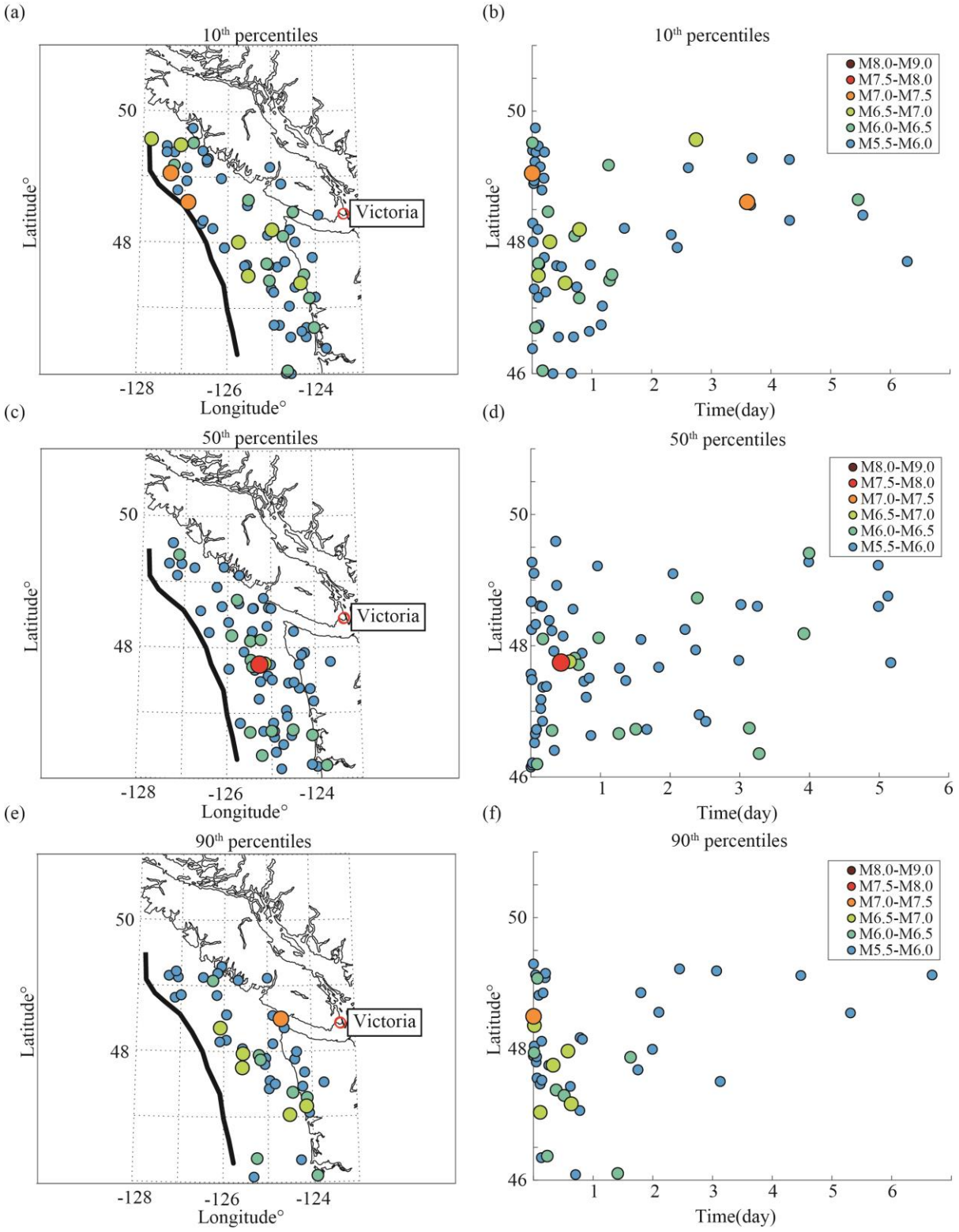

Figure 5-17. Plots of three single simulations of aftershock epicentres and latitudinal distribution of aftershocks with time on day 7 after the mainshock in the western Canada corresponding to (a, b) 10th percentiles, (c, d) 50th percentiles, and (e, f) 90th percentiles of total losses.

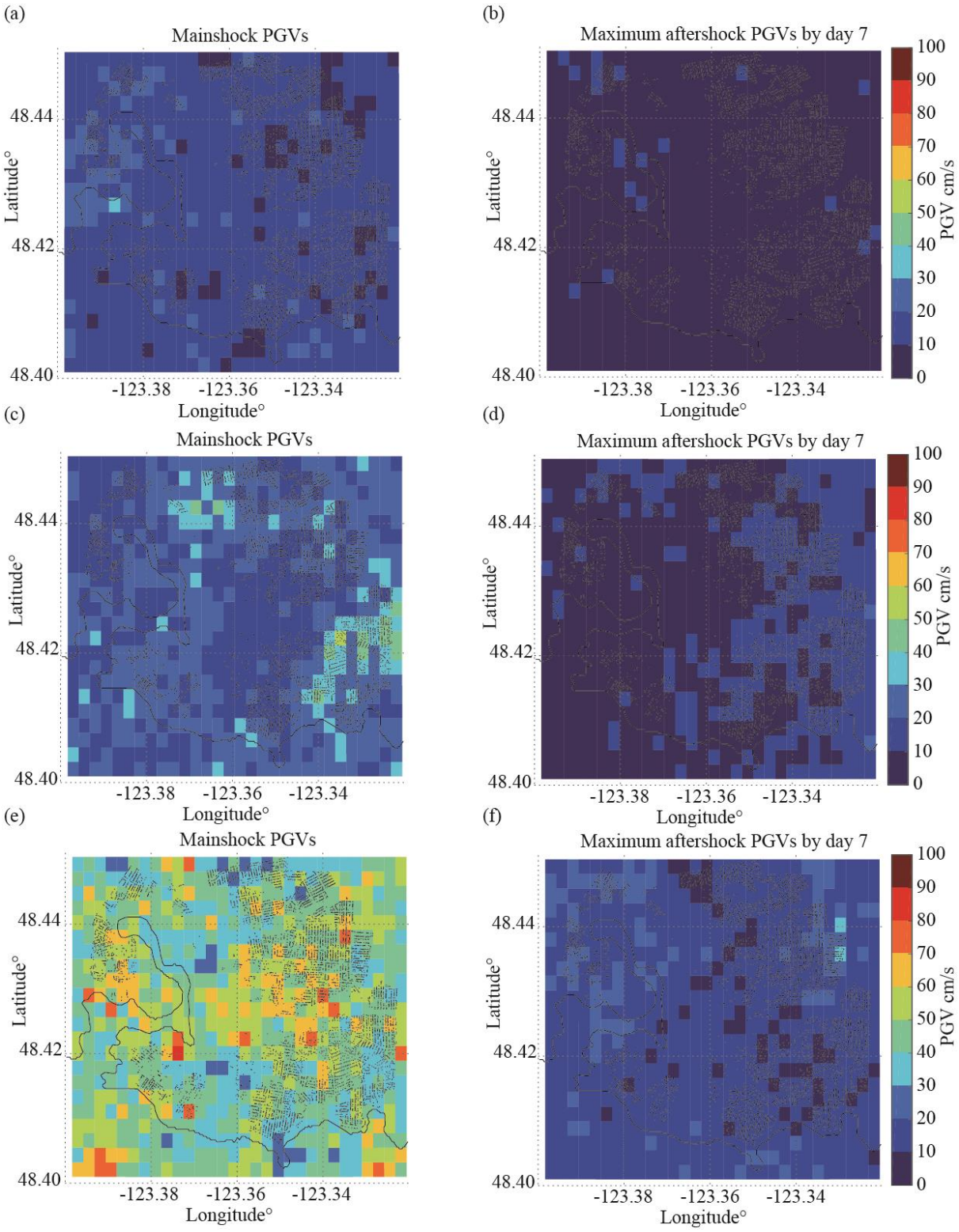

Figure 5-18. Plots of three single simulations of mainshock PGV map, and maximum aftershock PGV hazard map by day 7 for the city of Victoria, Canada corresponding to (a, b) 10th percentiles, (c, d) 50th percentiles, and (e, f) 90th percentiles of total losses.

The DS distributions of wood-frame houses by mainshock and mainshock-aftershock sequences on day 7 are shown in **Figure 5-19**. For the 10th percentile scenario, the number of houses with DS_1 and DS_2 is increased by 103 and 4, due to aftershocks within 7 days after the mainshock. The aftershocks from the 10th percentile scenario contribute a few patches on the aftershock hazard map with PGV > 10 cm/s in **Figure 5-18**(b), which could not cause significant damage to houses. Most of the houses would remain intact or experience minor damage (DS_1). In terms of the 50th percentile scenario, the M7.5-class event causes some moderate damage to the houses in Victoria. From **Figure 5-19**(c) and (d), the number of houses with DS_1, DS_2, and DS_3 due to the mainshock is 4164, 267, and 19, respectively. After one week, the numbers of houses with DS_1, DS_2, DS_3 increase to 4372, 343, and 22, respectively. More houses are changed to DS_2 in eastern Victoria, which is consistent with the aftershock hazard map in **Figure 5-18**(d). The impact of the M7.0-class event from the 90th percentile scenario on the seismic risk assessment is substantial. The number of houses with DS_1, DS_2, and DS_3 by the mainshock is 3264, 2345, and 900, respectively. After one week of the mainshock, due to the M7.2 aftershock, the number of houses with DS_1, DS_2, and DS_3 is 3081, 2537, and 931, respectively.

Figure 5-20 shows the block map of seismic loss distributions of wood-frame houses in the City of Victoria by mainshock and the mainshock-aftershock sequence on day 7. In total, the aggregate seismic loss of the 10th percentile case shown in **Figure 5-19**(a) and (b) is increased from 18 million Canadian dollars to 20 million Canadian dollars. The aggregate losses of the 50th percentile case from **Figure 5-19**(c) and (d) are increased from 71 million Canadian dollars to 77 million Canadian dollars. For the 90th percentile case, the aggregate loss is increased by 9 million Canadian dollars in **Figure 5-19**(f) in comparison with the 215 million Canadian dollars by the mainshock.

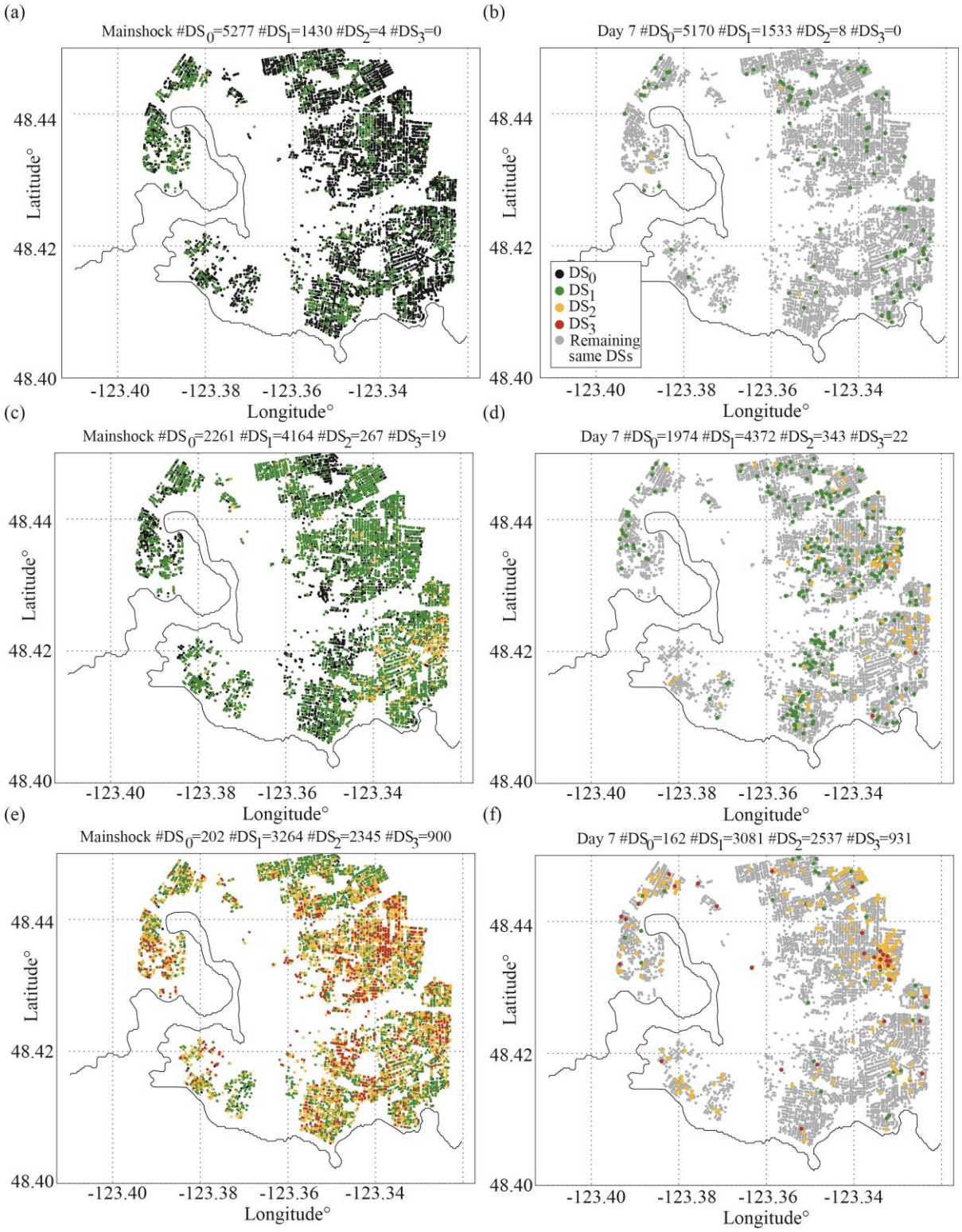

Figure 5-19. Three single simulations of DS distributions of wood-frame houses due to the mainshock (left panels) and additional damage to the aftershock sequence within 1 week (right panels) corresponding to (a, b) 10th percentiles, (c, d) 50th percentiles, and (e, f) 90th percentiles of total losses.

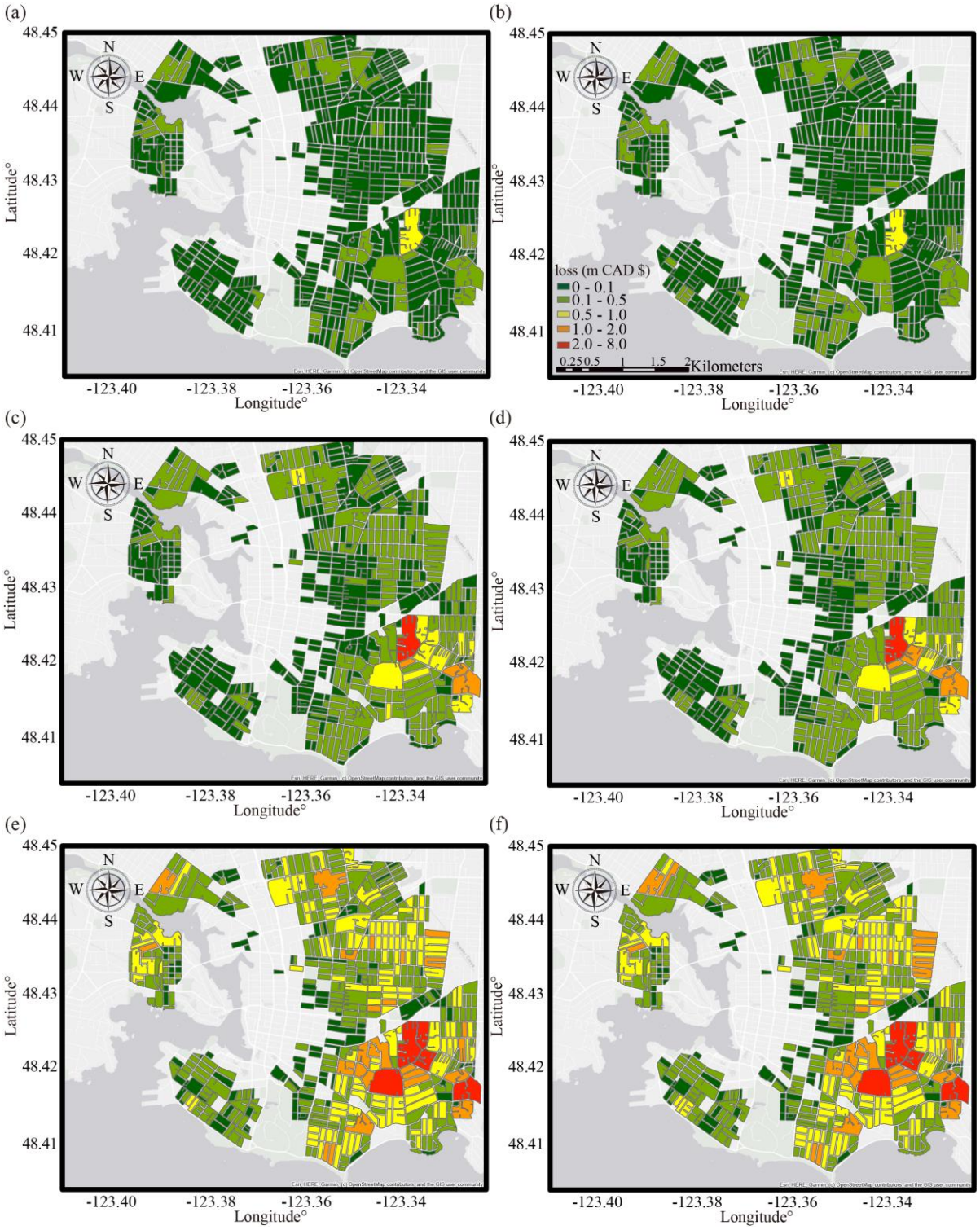

Figure 5-20. Three single simulations of seismic loss distribution (m $CAD) of wood-frame houses due to the mainshock (left panels) and additional damage to the aftershock sequence within 1 week (right panels) corresponding to (a, b) 10th percentiles, (c, d) 50th percentiles, and (e, f) 90th percentiles of total losses.

For the post-earthquake risk management of M9.0 events, after 1 week of the mainshock, the quasi-real-time aftershock hazard and risk assessment in **Figure 5-18**, **Figure 5-19**, and **Figure 5-20** can be helpful for the building tagging and inspection of wood-frame houses. For example, the output of the framework can provide the probability distribution of the DSs on the day of the inspection for building tagging and daily forecasts of the DSs in a short-time period after the inspection day. This can be part of building inspection along with conventional building tagging (Bazzurro *et al.*, 2004) to provide additional information for the structural inspector.

5.3.3 Extreme case with a triggered crustal aftershock near Victoria

A more destructive crustal aftershock case is presented in this subsection. The single simulation example of the 90th percentiles of total losses within one month after the mainshock is shown in **Figure 5-21**. To show the potential impact of destructive aftershocks on hazard and risk assessment for the City of Victoria, a single simulation with a lower maximum mainshock PGV is considered (81 cm/s) in **Figure 5-21**(c), compared with 90 cm/s in the 90th percentile of the mainshocks simulations in **Figure 5-14**. A M6.5 aftershock is triggered near Victoria, which is a shallow crustal aftershock (48.39°N, 123,24°W) with a rupture distance less than 10 km to Victoria. The maximum aftershock PGV values in **Figure 5-21**(d) are contributed by the triggered shallow crustal event. This type of shallow crustal event has been previously identified in potential damaging scenarios near Victoria in past studies, for example, the Leech River fault-M6.0 event and Devils Mountain fault-M7.5 event (Personius *et al.*, 2014; Morell *et al.*, 2017).

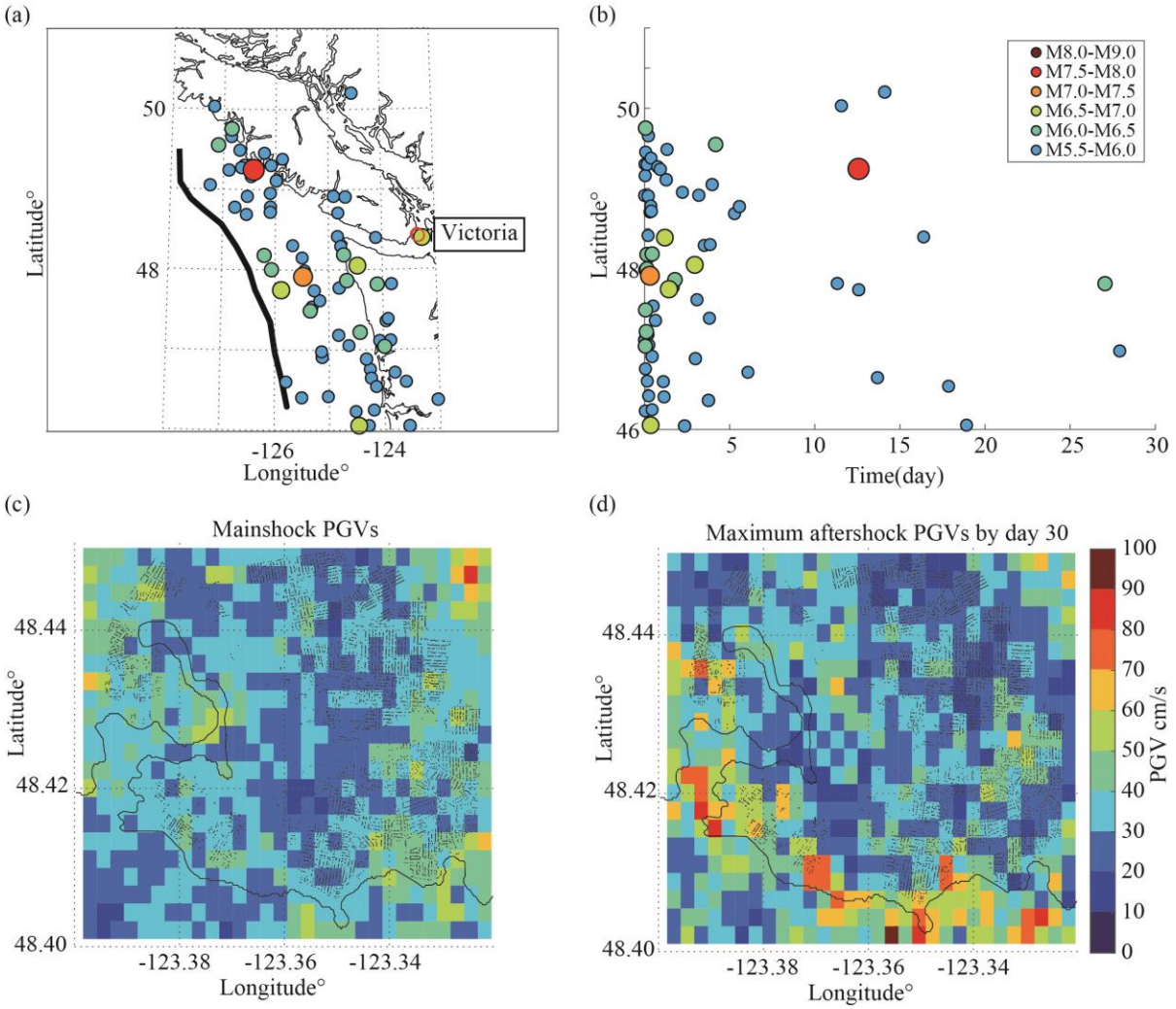

Figure 5-21. Single simulation corresponding to the 90th percentile of total losses: (a) aftershock epicentres, (b) latitudinal distribution of aftershocks with time to day 30 after the mainshock, (c) mainshock hazard map, and (d) the maximum aftershock hazard map within 30 days after the mainshock for the City of Victoria, Canada.

In **Figure 5-22**, due to the triggered crustal event, the number of houses with DS_2 and DS_3 are increased by 2213 and 440, respectively. Less than 10% of houses remain in DS_0. The aggregate loss estimations are increased by 108 million Canadian dollars in comparison with the 121 million Canadian dollars due to the mainshock. The losses due to the aftershocks are almost the same amount as those due to the mainshock.

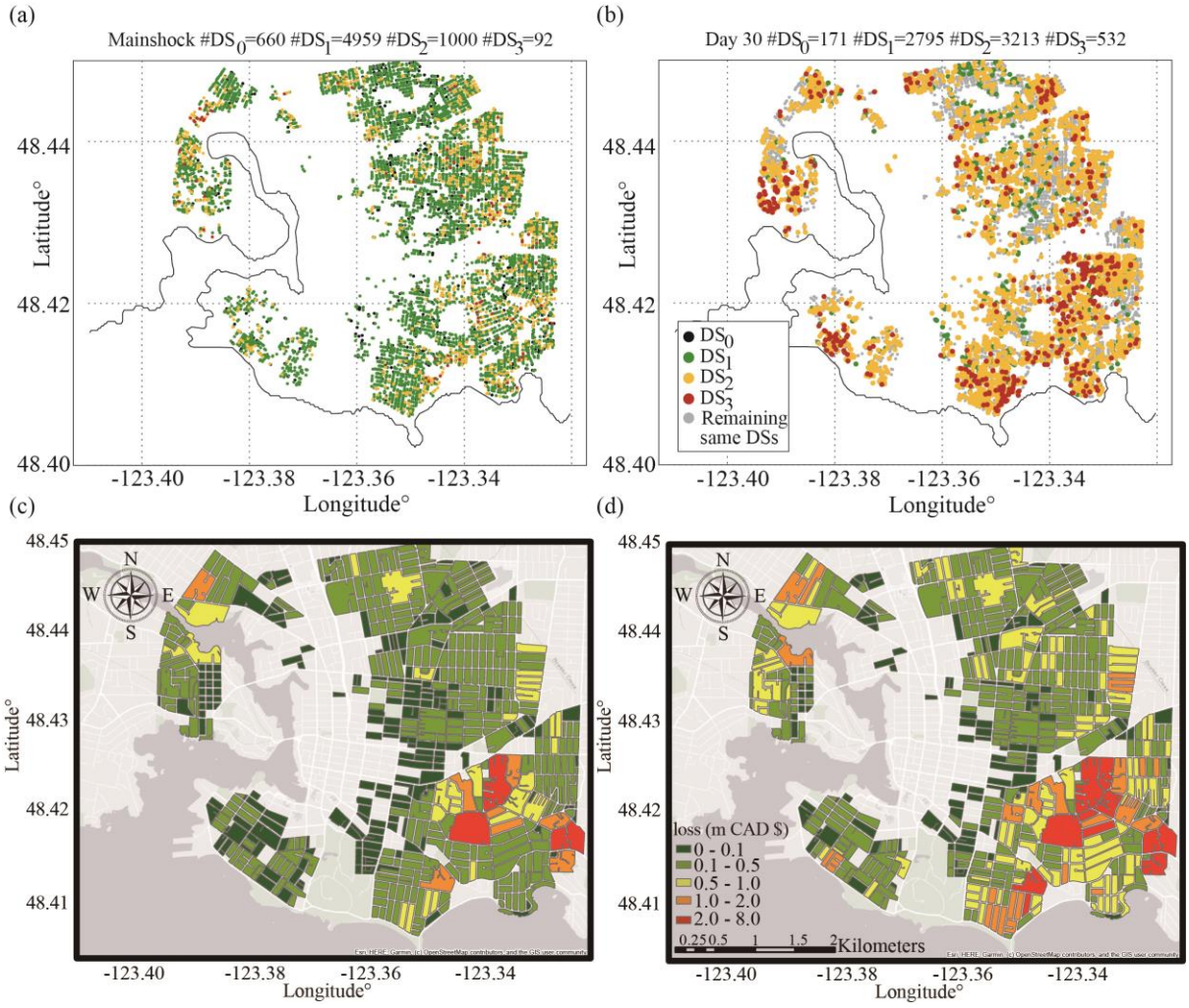

Figure 5-22. Plots of a single simulation of DS distribution of wood-frame houses for 90th percentiles of total losses by (a) mainshock and (b) mainshock-aftershock sequences on day 30. The block map of seismic loss distribution (m CAD$) of wood-frame houses in the City of Victoria by (c) mainshock and (d) mainshock-aftershock sequence on day 30.

For the post-earthquake risk assessment, after one month of the mainshock, depending on the building tagging, re-occupancy or demolition can be carried out for the wood-frame houses. A simple approach to quantify and guide the decision-making is the benefit-cost ratio ($R_{bc} = P_{bc} \times L_{bc}/C_{bc}$) (Cauzzi *et al.*, 2016), where L_{bc} is the loss with a probability P_{bc} to occur that can be prevented by taking remedial actions with the cost C_{bc}. For the example of a damaged wood-frame house, P_{bc} is the probability that the house could reach higher building

tags and create additional loss (L_{bc}) due to future aftershocks. The demolition and reconstruction costs are C_{bc}. If the benefit-cost ratio is larger than 1, the demolition and reconstruction of the house could take place.

The 90th percentile scenarios for different durations (1 week and 1 month) suggest that the impact of destructive aftershocks on seismic risk assessment could be moderate events (e.g., a M6.0-class crustal event) with short rupture distances in the shallow crust or large events (e.g., a M7.5-class subduction-zone event) with greater rupture distances on the subduction-zone interface. The examples of the large M7.2 subduction-zone aftershock in **Section 5.3.2** and the shallow crustal event with the shortest rupture distance of less than 10 km to Victoria in this section demonstrate the potential impact of destructive aftershocks on a municipality-wide risk assessment.

5.4 Conclusions

This chapter implemented the simulation framework for a spatiotemporal seismic hazard and risk assessment of M9.0 sequences for the CSZ. The simulation framework developed in **Chapter 2** with the suggested ETAS parameters from **Chapter 3** was applied to generate stochastic M9.0 earthquake sequences for the CSZ. Applicable GMPEs were selected for the CSZ to calculate the time-dependent hazard results at multiple sites accounting for spatial correlations. The hazard results were further applied to state-dependent fragility models to assess the spatiotemporal risk to multiple wood-frame houses in the City of Victoria, Canada.

The results showed that:

- The impact of the variability of mainshock PGVs on total losses is significant. The 10th, 50th, and 90th percentiles of total mainshock losses (corresponding to the average mainshock PGV values with 14 cm/s, 25 cm/s, and 44 cm/s) are 14, 66, and 194 million Canadian dollars, respectively.

- On average, aftershocks could cause additional 10% and 20% losses after 1 week and 1 year of the mainshock, respectively. Single simulations of mainshock-aftershock results show that the developed simulation framework can capture the subduction and crustal aftershock rates in space and time and further estimate the DS and loss distributions for risk management decisions.
- Destructive aftershocks could be triggered by M9.0 events. Occurrence of a M6.0-class crustal event or a M7.5-class subduction-zone event could lead to 90^{th} percentiles of total losses.
- If the mainshock source model is available right after the mainshock, this framework can conduct quasi-real-time aftershock hazard and risk assessments. This can be beneficial for: (1) the building tagging of wood-frame houses to provide not only the probability of the building tagging of each house but also a building tagging forecast in a short time period on the inspection day, and (2) the decision-making of demolition and reconstruction of houses based on cost-benefit ratios.

The limitations of this study are that (1) due to the lack of the observed M9.0 mainshock-aftershock sequences in the CSZ, further investigation of the spatial distributions of depths and focal mechanisms from observed megathrust sequences (e.g., the 2010 Maule and the 2011 Tohoku sequences) is necessary, (2) for more accurate hazard estimates, a high-resolution V_{s30} map is necessary, (3) more GMPEs for subduction-zone events that use PGV as the output and include M9.0 observed records need to be considered, (4) We do not have an aftershock fragility model that distinguishes crustal and subduction-zone events. The aftershock fragility model considering different earthquake types might be necessary to represent the differences of spectra shape between the crustal and subduction-zone earthquakes. (5) and the aim of the loss estimation is to show the impact of aftershocks on the short-term seismic risk assessment. Accurate loss estimations (considering different EDPs for

structural and non-structural components) would require more state-dependent fragility curves for various structure types, which are beyond the scope of this chapter.

Chapter 6 Conclusions and Outlook

6.1 Conclusions

This thesis developed a new simulation framework of spatiotemporal seismic hazard and risk assessment of global M9.0 earthquake sequences. The developed spatiotemporal simulation framework is innovative, and its major novelty is attributed to the integration of two compatible components: (1) the ETAS seismicity model with a new spatially anisotropic aftershock kernel for the global M9.0 sequences (**Chapter 2**) that is calibrated on the basis of global subduction-zone earthquake catalogues (**Chapter 3**), and (2) a new approach to develop the state-dependent fragility model of Canadian wood-frame houses with real mainshock-aftershock records (**Chapter 4**). By having the compatible components in the developed simulation framework, a case study of spatiotemporal seismic hazard and risk assessments of future M9.0 megathrust sequences in the city of Victoria, Canada was conducted (**Chapter 5**).

This thesis was divided into four main chapters, and the main conclusions of each chapter are discussed in the following.

1) **Chapter 2** investigated the importance of subduction and crustal aftershocks triggered by a M9.0 megathrust subduction event in spatiotemporal seismic hazard and risk assessments. The developed framework includes a seismicity model, hazard analysis, and risk analysis. Specifically, the ETAS model was convolved with a GMPE and fragility model to conduct the hazard and risk analyses. To model the M9.0 megathrust subduction sequences in space, a new spatial distribution of the first-generation aftershocks was proposed by combining the latest scaling law of rupture area with a power-law decay beyond the main rupture area. By using this new spatial distribution, good agreement is achieved between the observed 2011 Tohoku sequence and the

simulated daily seismicity rates with M≥5.5 and PGV rates ≥ 1 cm/s. The results showed that:

- The aftershock hazard rate contributes about 23% of the PGV rate on Day 1 in Sendai. Fukushima II NPP shows a similar proportion on Day 1, but the mainshock and aftershock rates are higher than Sendai by a factor of 1.5. This is because Fukushima II NPP is closer to the mainshock rupture plane than Sendai.
- Triggered subduction earthquakes are more numerous than crustal counterparts above M5.5, but the crustal aftershocks contribute greater hazard above PGV = 60 cm/s (MMI VIII) and V_{s30} = 300 m/s than the subduction aftershocks. Therefore, the subduction aftershocks have a significant impact on MMI VII, whereas the crustal earthquakes contribute more to MMI IX and beyond.
- Assuming V_{s30} = 300 m/s, the simulated mainshock and aftershocks contribute approximately 80% and 20% to the total DS_1 rate at Sendai and Fukushima II NPP on Day 1, and the mean damage state rate gradually decreases from Day 2 to 5. Crustal aftershocks have a higher probability to damage the wood-frame houses than the subduction earthquakes in Sendai and Fukushima II NPP.

2) **Chapter 3** investigated the global variability of the ETAS parameters in subduction regions that experienced M7.5+ megathrust earthquakes. Longer regional as well as shorter sequence-specific selections of the global NEIC earthquake catalogues were prepared to calibrate the ETAS model. The results suggest that:

- The ETAS parameters from the longer catalogues have smaller standard errors and are less variable than those of sequence-specific catalogues, because the number of events in sequence-specific sub-catalogues of M7.5-8.5 earthquakes is relatively small given the high M_{cut} of the NEIC catalogue.

- The variability of parameters estimated from multiple sequences (M9.0 and M8.0 events) in the same subduction zones (Indonesia, Chile, and Japan) is small because the M9.0 sequences dominate the input catalogues and M8.0 sequences have a smaller impact on the parameter estimation.
- On the basis of the estimated parameters with known biases due to the isotropic spatial distribution and an evaluation of their quality, ETAS parameters for future M9.0-class events are suggested: K_0 = 0.04±0.02, α = 2.3, c = 0.03±0.01, p = 1.21±0.08, γ =1.61±0.29, d = 23.48±18.17, and q = 1.68±0.55. Synthetic catalogues that were generated using the suggested ETAS parameters are consistent with those observed during the 2004 Aceh-Andaman, the 2010 Maule, and the 2011 Tohoku earthquake sequences.

3) **Chapter 4** applied a new method using 596 real mainshock-aftershock records with cloud analysis to develop the state-dependent fragility curves of aftershocks for the wood-frame houses in Canada. To capture the real characteristics of aftershocks in the cumulative damage assessments of mainshock and aftershock sequences, the pre-EDP combining with IM and post-EDP in 3D was introduced for developing the state-dependent aftershock fragility curves. The selection of IMs (from Sa, AI, CAV, PGV, and SI) and EDPs (from ResISDR, MaxISDR, and MaxIISDR) for wood-frame houses was discussed in this study. To account for the cumulative damage of mainshock-aftershock sequences, the pre-ResISDR and post-MaxISDR are considered to be the most suitable EDPs to represent the pre-EDP and post-EDP, respectively. To evaluate different IMs, the efficiency, sufficiency, and relative sufficiency were calculated for each IM. Sa(T=0.3s-0.5s) and PGV show better performances than other IMs. The results showed that:

- The mainshock-aftershock fragility curves were developed with pre-ResISDR and post-MaxISDR by considering IMs (Sa(T=0.3s), Sa(T=0.5s) and PGV). PGV showed better performance to capture the cumulative damage effects of aftershocks for the wood-frame structure using real mainshock-aftershock sequences.
- Different fragility functions (the lognormal and multinomial distributions) were also compared. The multinomial distribution was considered as more suitable to fit the fragility curves than the lognormal distribution, because the former does not require careful bin counts to avoid the intersections of aftershock fragility curves for post-DS conditioned on different pre-DSs. Combining the building-tagging-based DS definitions together with the multinomial distribution lead to the development of robust aftershock fragility curves.
- The developed aftershock fragility curves of Houses 1-4 can be employed to estimate the DSs implementing a spatiotemporal risk assessment for a M 9.0 mainshock triggering both crustal and subduction-zone aftershocks (e.g., **Chapter 5**) in British Columbia, Canada. The evaluated PGV and real mainshock-aftershock sequences facilitate the estimation of cumulative damage of wood-frame houses. The outputs of the risk assessment provide not only the likelihood of the DSs on the day of the inspection for building tagging but also daily forecasts of the DSs in a short-time period after the inspection day.

4) **Chapter 5** implemented the simulation framework of spatiotemporal seismic hazard and risk assessment of M9.0 sequences for the CSZ. The developed simulation framework in **Chapter 2** with the suggested ETAS parameters from **Chapter 3** was applied to generate stochastic M9.0 earthquake sequences for the CSZ. Applicable GMPEs were selected for the CSZ to calculate the time-dependent hazard results at multiple sites considering spatial correlations. The hazard results were further applied

to the state-dependent fragility models to conduct the spatiotemporal risk assessment of multiple wood-frame houses in the City of Victoria, Canada. The results showed that:

- The impact of the variability of mainshock PGVs on total losses is significant. The 10^{th}, 50^{th}, and 90^{th} percentiles of total mainshock losses (corresponding to the average mainshock PGV values with 14 cm/s, 25 cm/s, and 44 cm/s) are 14, 66, and 194 million Canadian dollars, respectively.
- On average, aftershocks could cause additional 10% and 20% losses after 1 week and 1 year of the mainshock, respectively. Single simulations of mainshock-aftershock results show that the developed simulation framework can capture the subduction and crustal aftershock rates in space and time and further estimate the DS and loss distributions for risk management decisions.
- Destructive aftershocks could be triggered by M9.0 events. The occurrence of a M6.0-class crustal event or a M7.5-class subduction-zone event could lead to 90^{th} percentiles of total losses.
- If the mainshock source model is available right after the mainshock, this framework can conduct quasi-real-time aftershock hazard and risk assessments. This can be beneficial for: (1) The building tagging of wood-frame houses to provide not only the probability of the building tagging of each house but also a building tagging forecast in a short time period on the inspection day. (2) The decision-making of demolition and reconstruction of houses based on cost-benefit ratios.

6.2 Future research

The developed spatiotemporal simulation framework can be further improved and extended; some possible future researches are:

- Further applications of the output from the current simulation framework of the short-term post-earthquake risk assessment can be discussed. For example, the decision-making of the appropriate time to demolish and rebuild the wood-frame houses for the whole city of Victoria.
- The proposed approach of the development of state-dependent fragility curves can be applied to different structural models. Different EDPs and IMs could be included to develop the state-dependent fragility curves. As more structural models are included, a more comprehensive risk assessment and a more accurate seismic loss estimation can be achieved.
- If more destructive aftershock records are available, ground motion records could be further classified by earthquake types, so aftershock fragility curves can be developed by crustal and subduction-zone records which represent the differences of spectra shape between the crustal and subduction-zone earthquakes.
- Rather than the sequence-based spatiotemporal seismic hazard and risk assessment in the current study, a long-term spatiotemporal framework can be built. This requires more efforts to model long-term hazard rates. To simulate the long-term synthetic catalogues, one approach is to model the long-term seismicity rate with a Poisson process using the declustered catalogue from the PSHA, and the stochastic synthetic catalogue of mainshocks can be generated. Subsequently, the developed ETAS simulation can be used to simulate the aftershocks. In addition, a Brownian passage time model also can be implemented to model the long-term time-dependent seismicity rate of large earthquakes (e.g., Fitzenz, 2018).
- In comparison with the sequence-based spatiotemporal risk assessment that may focus on the post-earthquake risk assessment, applications of the long-term spatiotemporal

framework would be more helpful for different stakeholders (e.g., insurance and reinsurance purpose for the capital market, building code and zoning for authority).

- Considering this typical M9.0 event could trigger secondary hazards (e.g., tsunami, liquefaction, and landside), conducting multi-hazard and risk assessment, including mainshock-aftershock sequences and its secondary hazards for the urban regions is necessary. This would require more efforts to assess damage accumulations from both earthquake and its secondary hazards.

Appendix A

A.1 2D Gaussian distribution

Following Ogata (1998) and Ogata and Zhuang (2006), we assess the fit of a 2D Gaussian distribution to the spatial distribution of aftershocks. The anisotropic Gaussian distribution is defined by:

$$f_{A1}(x,y) = A\exp\left(-\left(\frac{(x-x_0)^2}{2\sigma_x^2}\right) + \left(\frac{(y-y_0)^2}{2\sigma_y^2}\right)\right) \quad \text{(A-1)}$$

where A is a constant, x and y are the spatial coordinates, σ_x and σ_y are the standard deviations, and x_0 and y_0 are the centroid coordinates of the aftershocks. In the simulation framework, x_0 and y_0 are assumed to equal the mainshock epicentre of a bilateral rupture area. The sampled rupture length and width from the empirical scaling law (Thingbaijam *et al.*, 2017) can be applied to the 2D Gaussian distribution by manipulating the standard deviations. An example of the probability density function (PDF) with rupture length and width of 500km×300km, respectively, is shown in **Figure A-1**. While the anisotropic 2D Gaussian aftershock distribution offers several advantages, we do not employ it here. First, the 2D Gaussian distribution decays more rapidly than the power law near and beyond the boundaries of the rupture area, which does not represent the spatial aftershock distribution well (Felzer and Brodsky, 2006). Second, the 2D Gaussian distribution with a high concentration in the centre point does not agree with the observed aftershock distribution along the rupture plane. For example, **Figure A-2** shows a simulated 2D Gaussian aftershock histogram with M≥5.5 during the 100 days after the mainshock. In comparison with the observed 2D aftershock histogram of the 2011 Tohoku sequence in **Figure 2-3**(d), more events are clustered near the epicentre of the mainshock and the spatial distribution of aftershocks in **Figure A-2** underestimates the seismicity rate in the far field.

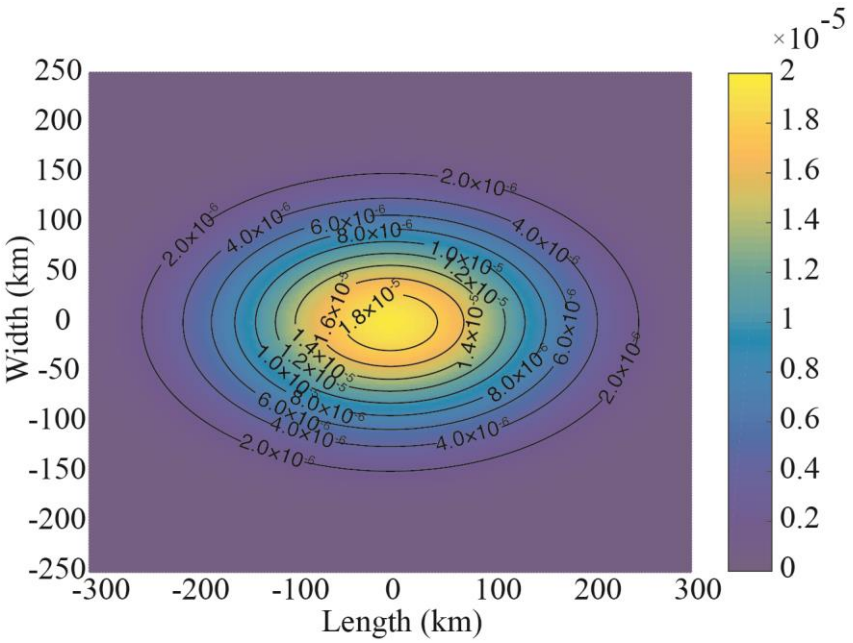

Figure A-1. An example of the spatial PDF of the first generation of aftershocks with a simulated rupture area (500 km×300 km).

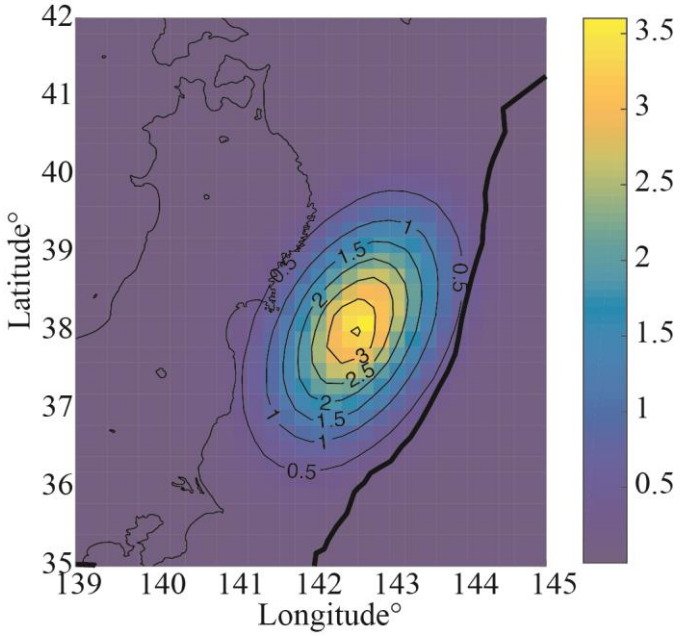

Figure A-2. Simulated 2D aftershock histogram with M≥5.5 during the 100 days after the mainshock.

A.2 Anisotropic power law distribution

We also consider an anisotropic power law kernel to simulate the spatial distribution of aftershocks (Kagan and Jackson, 1994; Wang *et al.*, 2011; Ramanna and Dodagoudar, 2012).

$$f_{A2}(x,y) = \frac{1}{\pi h^2}\frac{1+\delta cos^2\phi}{1+\delta/2}\left(1+\frac{x^2+y^2}{h^2}\right)^{-2} \quad \text{(A-2)}$$

where h is the kernel bandwidth and is identical to the bandwidth from **Equations (2-7)** and **(2-8)**, ϕ is related to the strike angle of the fault plane, and δ determines the length-width ratio of the mainshock rupture area. An example of the plot of PDF with rupture length and width of 500km×300km, respectively, is shown in **Figure A-3**. The irregular shape in **Figure A-3** is not supported by the observed aftershock distribution, and the spatial aftershock rates along the mainshock rupture length could be underestimated. Therefore, we decide not to use this anisotropic power law kernel for spatial aftershock distributions.

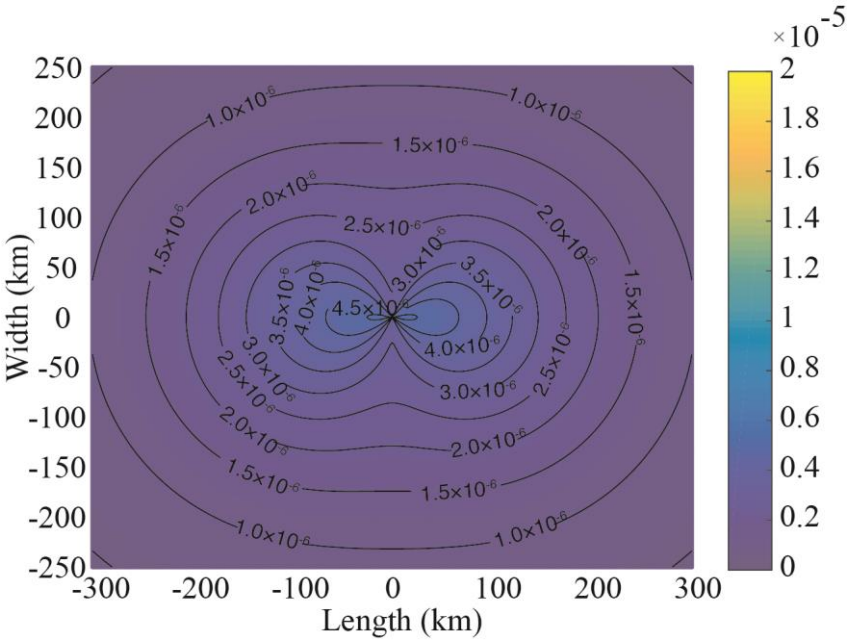

Figure A-3. An example of the spatial PDF of the first generation of aftershocks with a simulated rupture area (500 km×300 km).

Appendix B

B.1 Daily hazard rate from JSHIS

The 2% long-term hazard map in 50 years from JSHIS is estimated by a Poisson distribution:

$$P_A = 1 - e^{-\lambda_A t_A} \quad \text{(B-1)}$$

where P_A is the probability that a given intensity measure could be exceeded in t_A years with an annual occurrence rate of λ_A. In **Figure 2-13** and **Figure 2-14**, the daily hazard rate (λ_{JSHIS}) based on the long-term hazard map from JSHIS is calculated by:

$$\lambda_{JSHIS} = \ln\left(\frac{1}{1-P_A}\right) \times \frac{1}{t_A} \times \frac{1}{N_{days}} \quad \text{(B-2)}$$

where N_{days} is the number of days in one year. λ_{JSHIS} is shown in **Figure 2-13** and **Figure 2-14** with dash-dotted lines.

B.2 Daily mainshock-aftershock hazard rate from the ETAS model

The daily mainshock-aftershock hazard rate $\lambda_{MsAs}(t)$ on day t in **Figure 2-13** (both 2010 and 2017 versions) is estimated from the aftershock hazard rate given the mainshock occurs from the ETAS model multiplying by the daily rate of the mainshock, and is calculated by:

$$\lambda_{MsAs}(\mathrm{t}) = \lambda_{Ms} \times \lambda_1(PGV_{MsAs}(\mathrm{t}) \geq PGV_{JSHIS}|\mathrm{Ms}) \times \frac{1}{N_{days}} \quad \text{(B-3)}$$

where λ_{Ms} is the annual rate of the Tohoku-like mainshock considering different return periods; λ_1 is the conditional daily exceedance hazard rate of mainshock-aftershock sequences given that the mainshock occurs; $PGV_{MsAs}(t)$ is the rate that the simulated PGVs $\geq PGV_{JSHIS}$ on day t from the hazard analysis. PGV_{JSHIS} shows that the probability the PGVs in 50 years is exceed PGV_{JSHIS} is 2%. For example, PGV_{JSHIS} from the 2017 JSHIS hazard map in Sendai is 71 cm/s.

B.3 Daily conditional and unconditional aftershock hazard rates

In **Figure 2-14** daily conditional ($\lambda_{con}(t)$) aftershock hazard rates is the daily aftershock rate right after the mainshock occurs, and daily unconditional ($\lambda_{uncon}(t)$) aftershock hazard rates is the daily aftershock rate given the mainshock occurs multiplying by the daily rate of the mainshock. Daily conditional ($\lambda_{con}(t)$) and unconditional ($\lambda_{uncon}(t)$) aftershock hazard rates in are calculated by:

$$\lambda_{con}(\mathrm{t}) = \lambda_{JSHIS} + \lambda_2\left(PGV_{As}(\mathrm{t}) \geq PGV_{JSHIS} \middle| \mathrm{Ms}\right) \tag{B-4}$$

$$\lambda_{uncon}(\mathrm{t}) = \lambda_{JSHIS} + \lambda_{Ms} \times \lambda_2\left(PGV_{As}(\mathrm{t}) \geq PGV_{JSHIS} \middle| \mathrm{Ms}\right) \times \frac{1}{N_{days}} \tag{B-5}$$

where λ_{JSHIS} is considered as the background rate from **Equation (B-2)**. λ_{Ms} is the annual rate of the Tohoku-like mainshock considering different return periods. λ_2 is the conditional daily exceeding hazard rate of aftershocks given the mainshock occurs. $PGV_{As}(t)$ is the rate that the simulated PGVs of aftershocks $\geq PGV_{JSHIS}$ on day t from the hazard analysis. $\lambda_{con}(t)$ and $\lambda_{uncon}(t)$ are shown as upward-pointing triangle and circle, respectively, in **Figure 2-14**.

Appendix C

C.1 Comparison of the mainshock rupture model and the scaling law

The purpose of **Appendix C** is to compare the scaling law of Thingbaijam *et al.* (2017) with the estimated rupture lengths and widths of the global megathrust events in **Table 3-2**, as we will apply the scaling law in the ETAS simulation framework to simulate the anisotropic mainshock rupture dimensions (and their variability). Most M≥8 earthquakes agree well with the scaling laws, but there are small discrepancies. For example, 10 of 13 M≥8 events are in the range of one standard deviation of the rupture area scaling law in **Figure C-1**(c). However, 14 out of 23 events with M7.5-7.9 fall outside the mean plus/minus one standard deviation range, showing a larger fluctuation than M8.0-M9.0 events. This suggests the standard deviation of the scaling law is smaller than the observed variability of M7.5-7.9 events. In addition, the rupture areas of Events 23, 26, and 28 (orange circles in **Figure C-1**(c)) are smaller than expected. This may be because the fault type of these events has a strike-slip component (oblique reverse) and the scaling law for strike-slip events predicts smaller areas than for subduction-interface events (Thingbaijam *et al.*, 2017). Because the bulk of the M8.0-M9.0 earthquakes agree with the scaling laws, however, we conclude that the laws are appropriated for the purpose of simulating anisotropic mainshock ruptures.

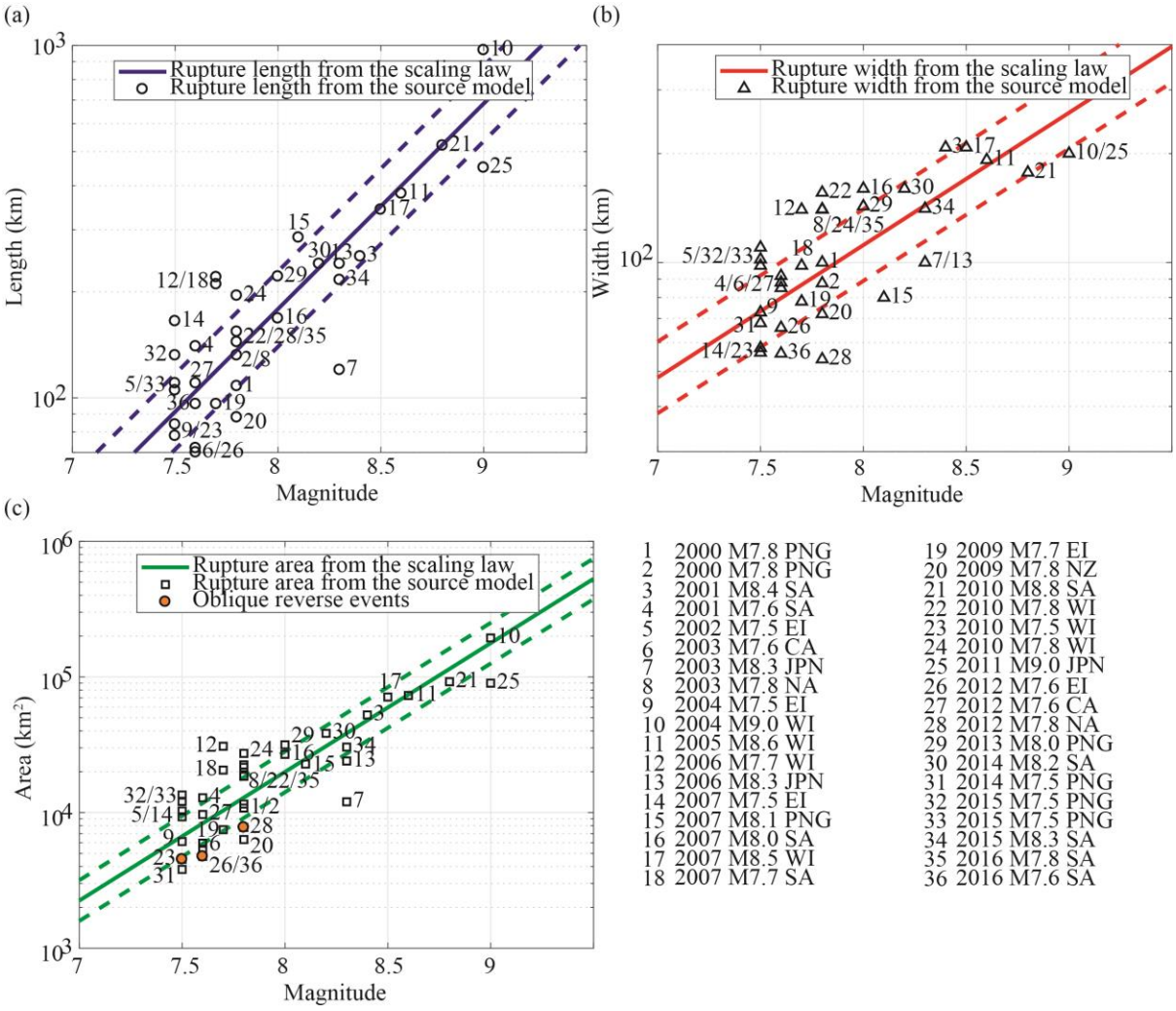

Figure C-1. Comparisons between empirical scaling laws (Thingbaijam *et al.*, 2017)and effective rupture models of megathrust M≥7.5 earthquakes: (a) rupture length, (b) rupture width, and (c) rupture area.

Appendix D

To assess the goodness-of-fit of the calibrated models to the catalogues in **Chapter 3**, **Appendix D** includes residual analyses of Cases 1 and 2 (**Figure D-1** - **Figure D-18**), and log-likelihood values and Akaike Information Criterion values for Cases 1 and 2 (**Table D-1**).

D.1 ETAS residual results of Cases 1 and 2

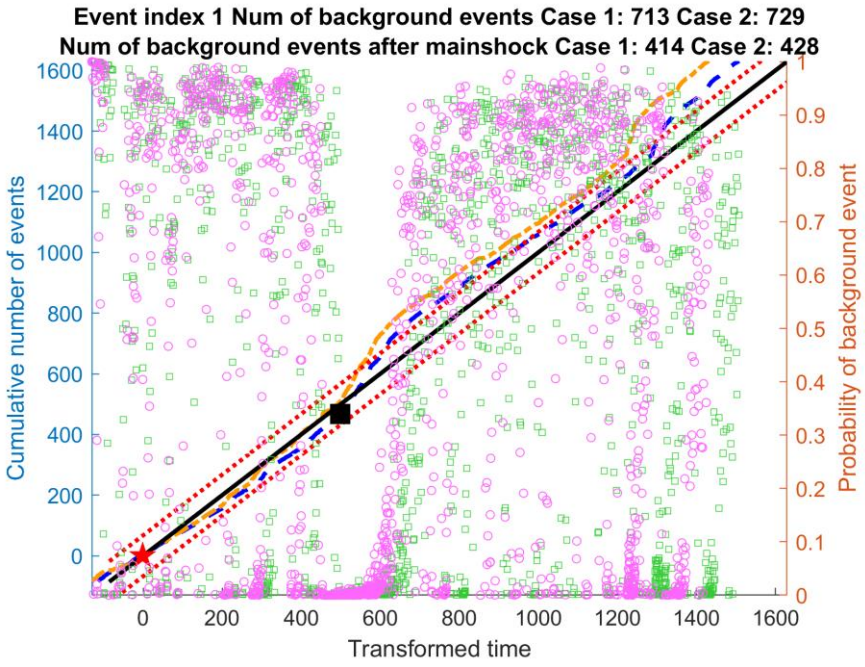

Figure D-1. Residual analysis of Cases 1 (dashed line) and 2 (dash-dotted line) for Event 1 with Poisson unit rate (solid line) and 99% error bonds (dotted line) on left y axis (filled square is the start time of the mainshock and filled pentagon is the start time of the target window). Background probability of Case 1 (unfilled-square) and Case 2 (unfilled-circle) on right y axis.

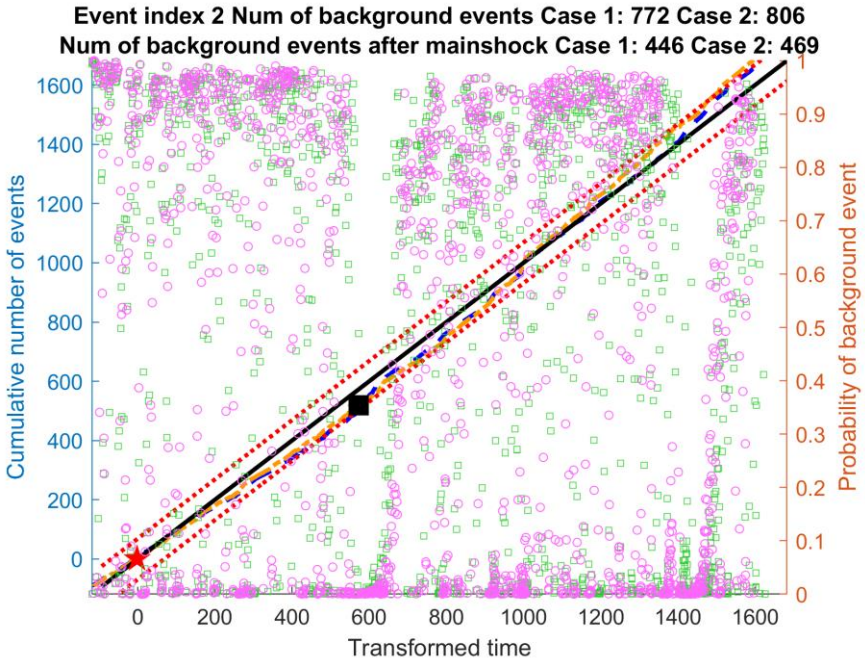

Figure D-2. Residual analysis of Cases 1 (dashed line) and 2 (dash-dotted line) for Event 2.

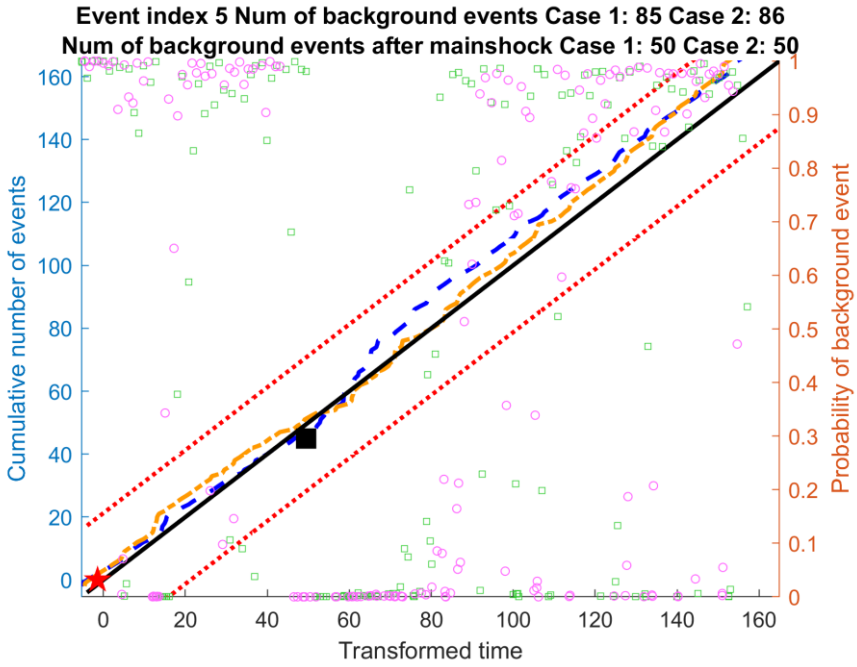

Figure D-3. Residual analysis of Cases 1 (dashed line) and 2 (dash-dotted line) for Event 5.

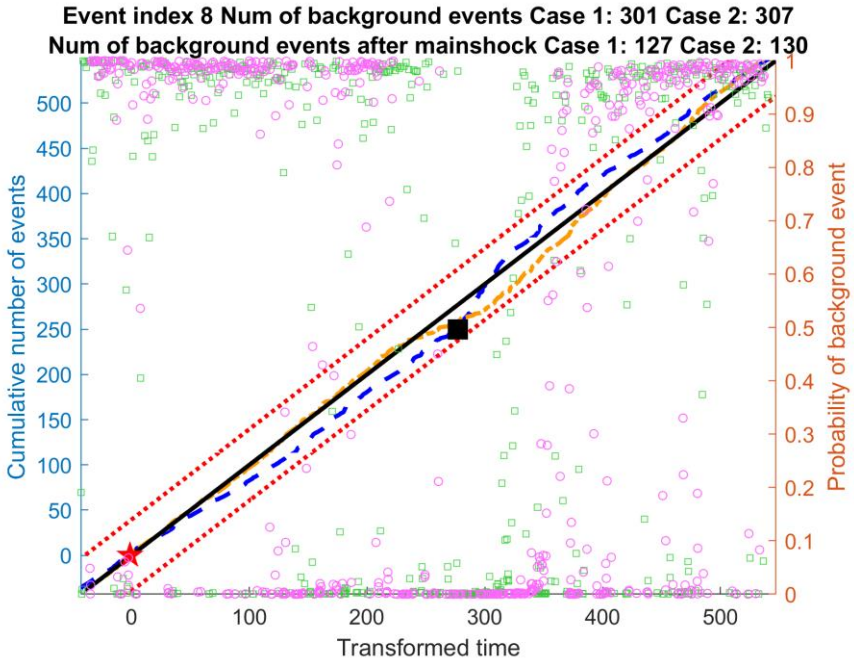

Figure D-4. Residual analysis of Cases 1 (dashed line) and 2 (dash-dotted line) for Event 8.

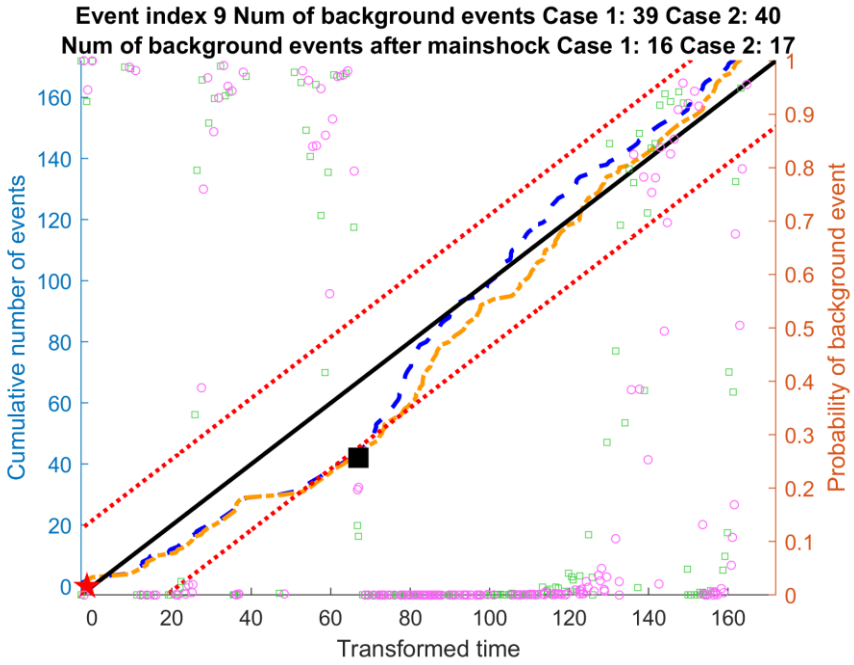

Figure D-5. Residual analysis of Cases 1 (dashed line) and 2 (dash-dotted line) for Event 9.

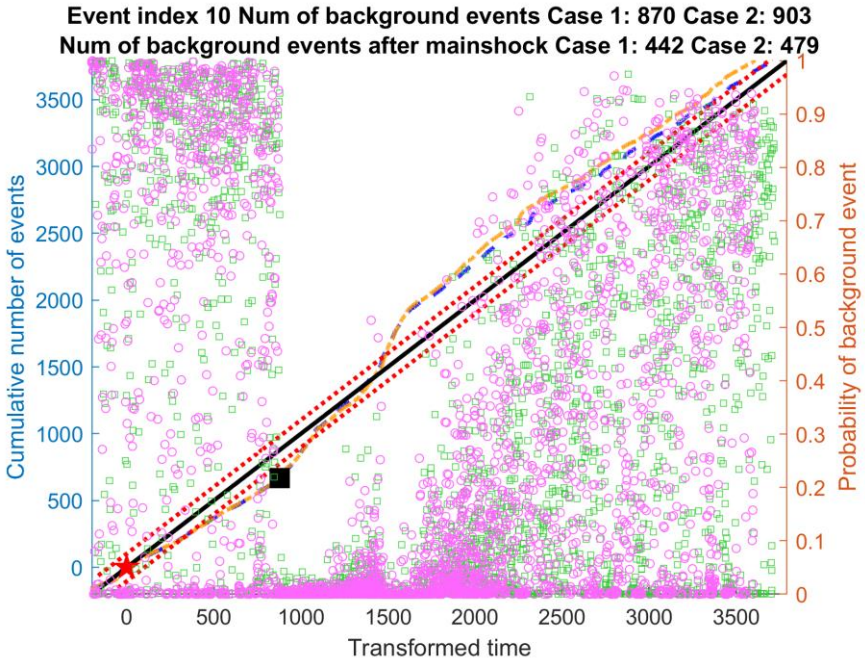

Figure D-6. Residual analysis of Cases 1 (dashed line) and 2 (dash-dotted line) for Event 10.

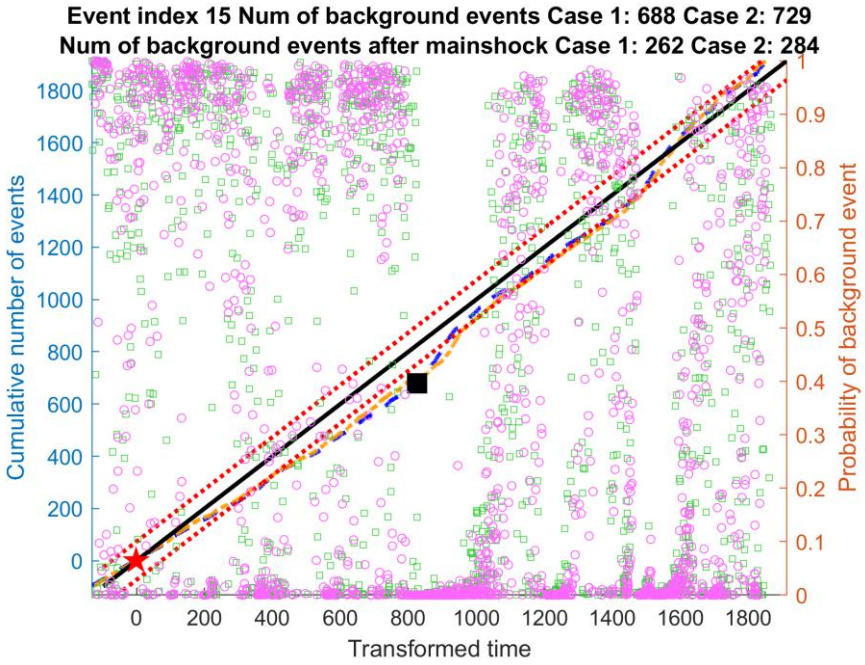

Figure D-7. Residual analysis of Cases 1 (dashed line) and 2 (dash-dotted line) for Event 15.

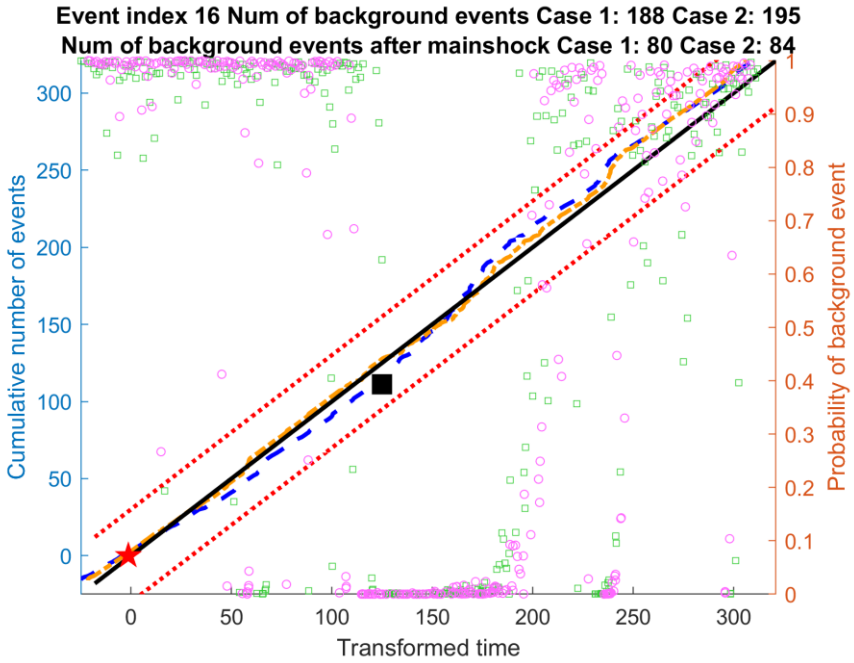

Figure D-8. Residual analysis of Cases 1 (dashed line) and 2 (dash-dotted line) for Event 16.

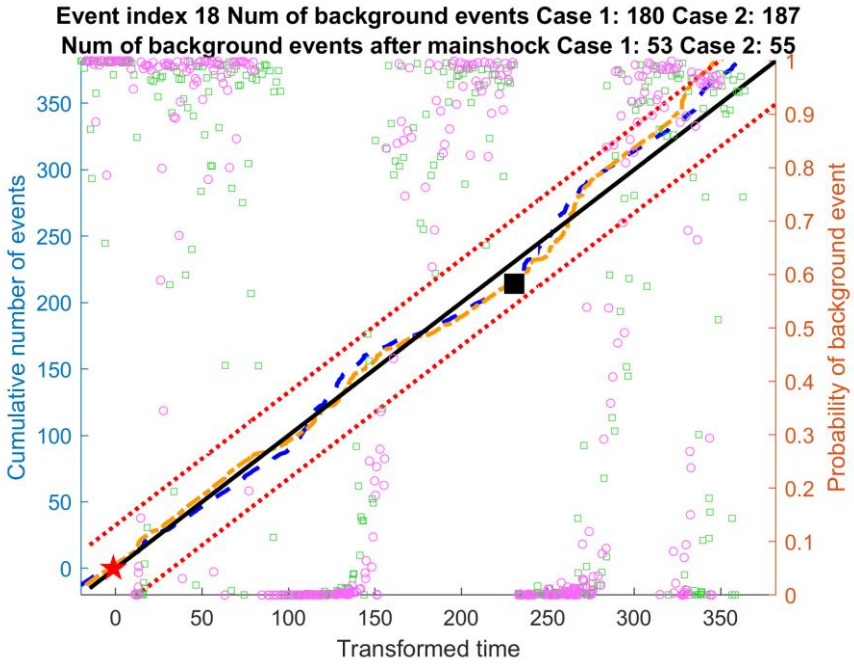

Figure D-9. Residual analysis of Cases 1 (dashed line) and 2 (dash-dotted line) for Event 118.

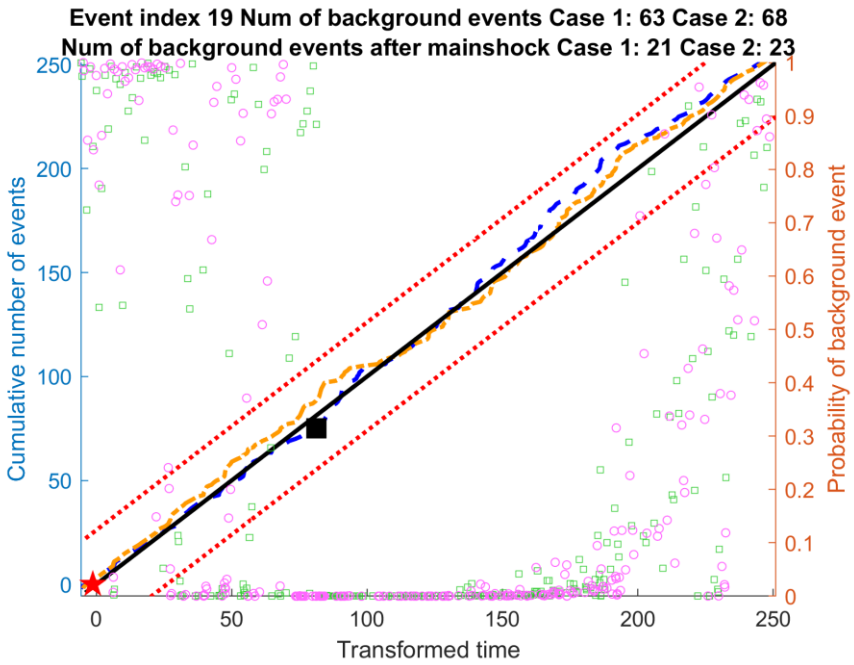

Figure D-10. Residual analysis of Cases 1 (dashed line) and 2 (dash-dotted line) for Event 19.

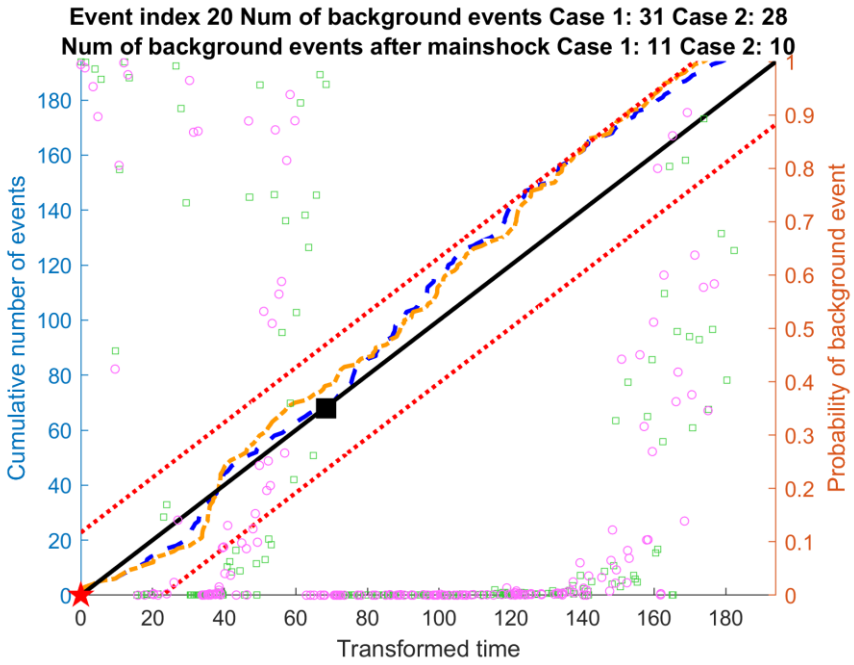

Figure D-11. Residual analysis of Cases 1 (dashed line) and 2 (dash-dotted line) for Event 20.

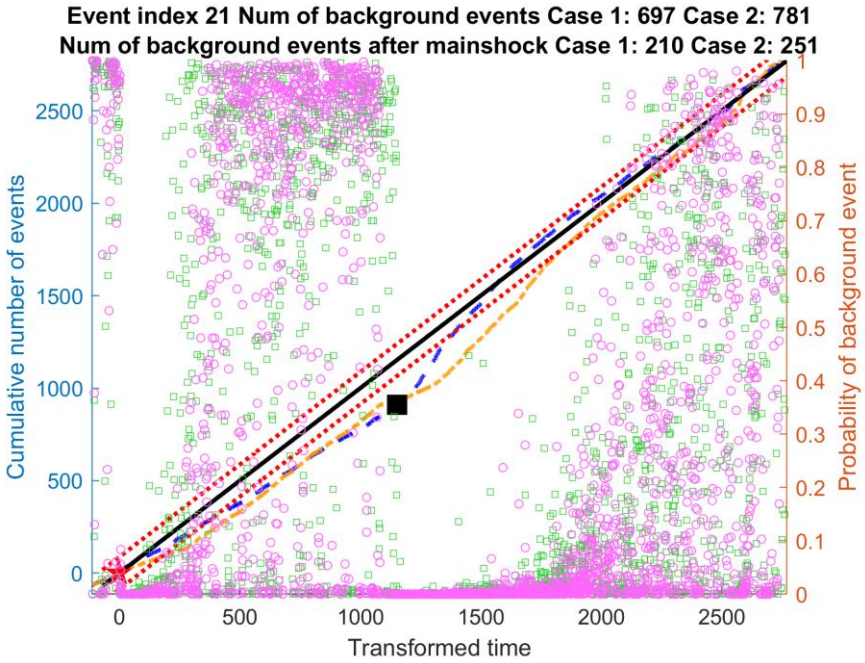

Figure D-12. Residual analysis of Cases 1 (dashed line) and 2 (dash-dotted line) for Event 21.

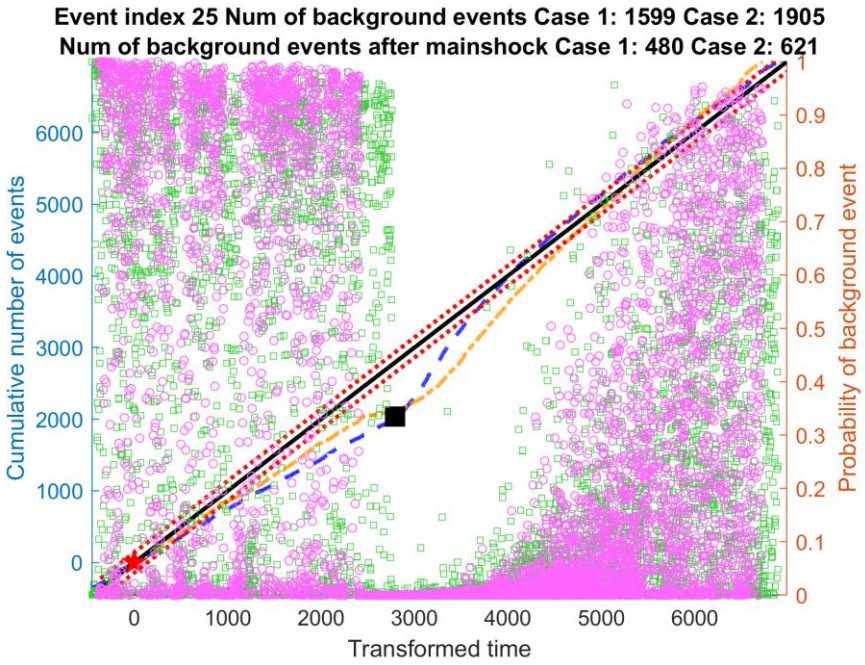

Figure D-13. Residual analysis of Cases 1 (dashed line) and 2 (dash-dotted line) for Event 25.

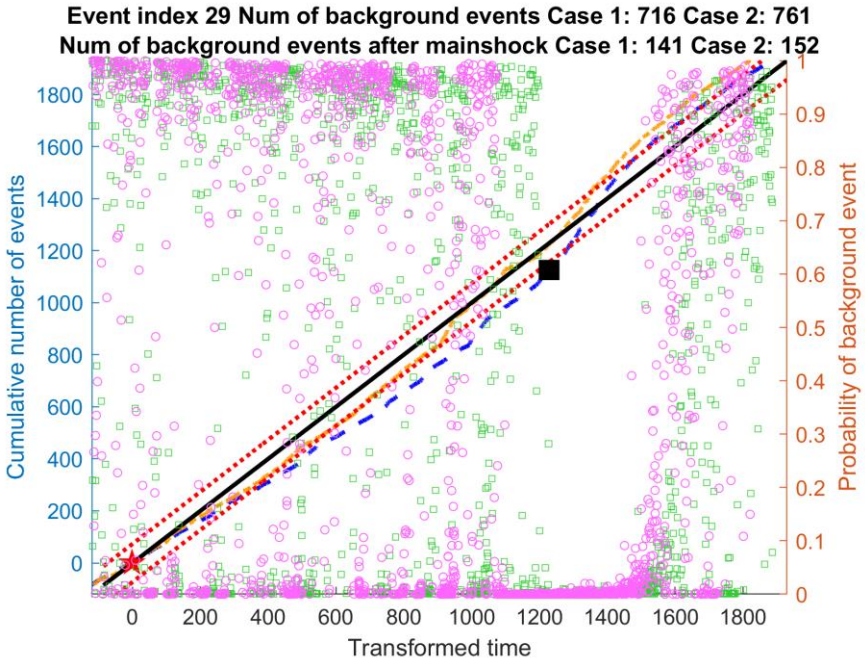

Figure D-14. Residual analysis of Cases 1 (dashed line) and 2 (dash-dotted line) for Event 29.

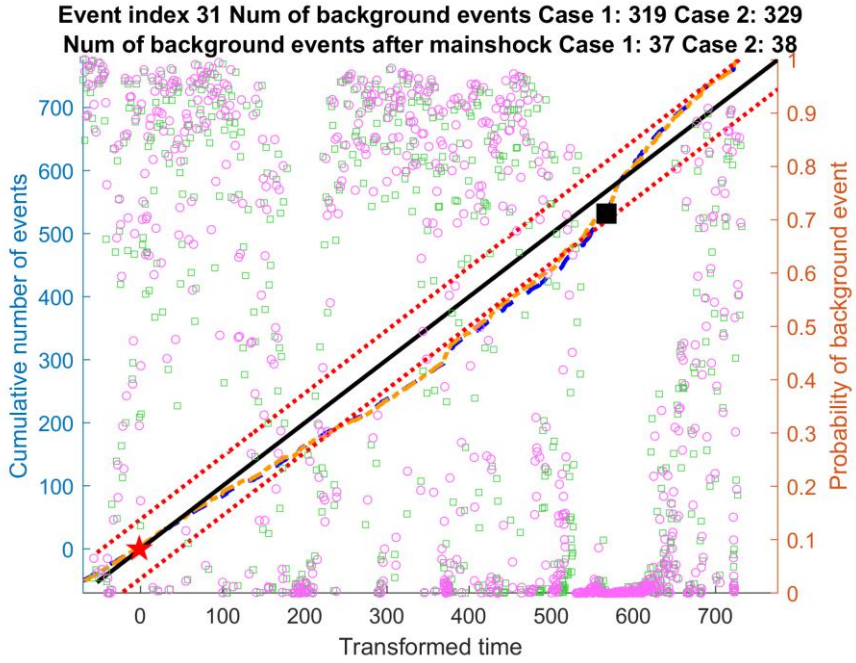

Figure D-15. Residual analysis of Cases 1 (dashed line) and 2 (dash-dotted line) for Event 31.

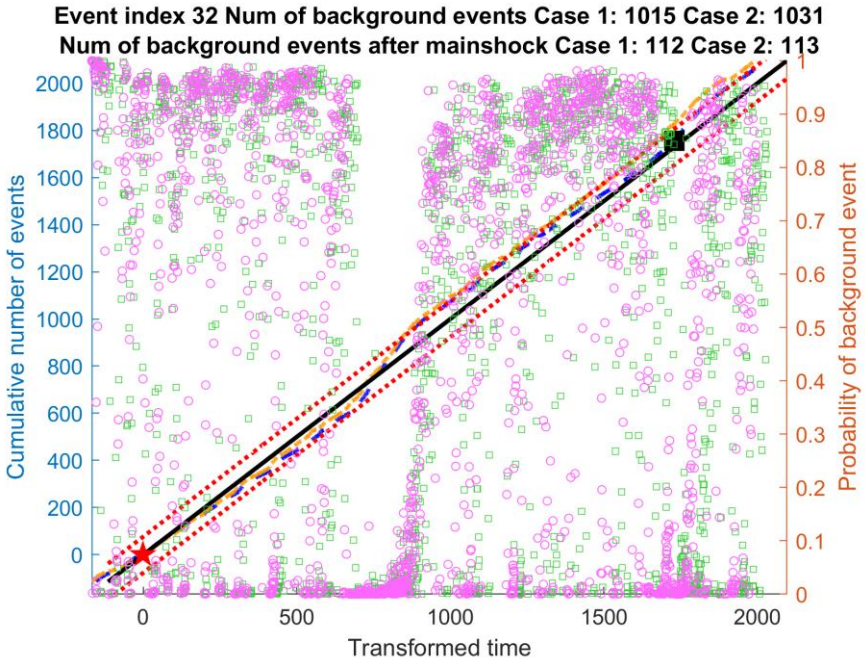

Figure D-16. Residual analysis of Cases 1 (dashed line) and 2 (dash-dotted line) for Event 32.

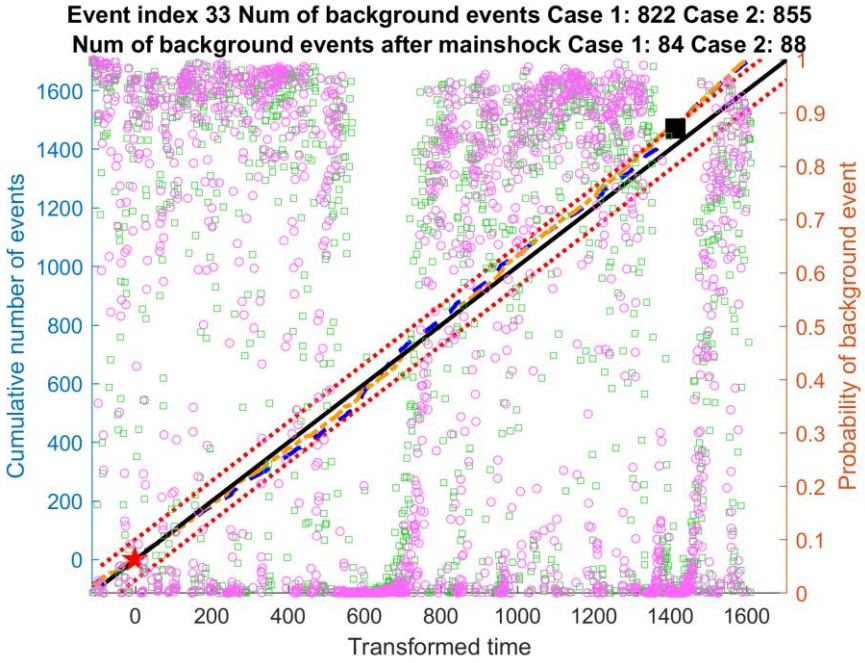

Figure D-17. Residual analysis of Cases 1 (dashed line) and 2 (dash-dotted line) for Event 33.

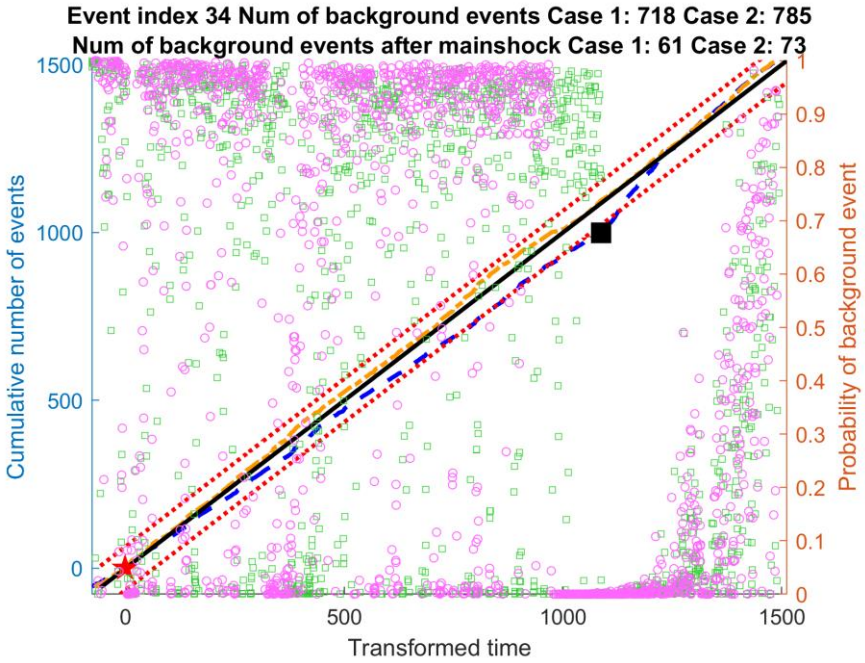

Figure D-18. Residual analysis of Cases 1 (dashed line) and 2 (dash-dotted line) for Event 34.

D.2 Log-likelihood values and Akaike information criterion values

Table D-1. Log-likelihood values and Akaike information criterion (AIC) values for Cases 1 and 2.

Event index	Case 1		Case 2	
	Log-likelihood values	AIC values	Log-likelihood values	AIC values
1	-18912.00	37839.94	-18982.10	37978.13
2	-19650.00	39315.98	-19759.00	39531.96
5	-2228.01	4472.02	-2244.17	4502.34
8	-6869.38	13754.76	-6949.10	13912.21
9	-1871.85	3759.70	-1879.31	3772.62
10	-59787.90	119591.70	-60971.70	121957.50
15	-20913.30	41842.57	-21063.30	42140.51
16	-4259.93	8535.87	-4277.92	8569.83
18	-5047.01	10110.02	-5106.53	10227.06
19	-2660.31	5336.62	-2668.97	5351.94
20	-2165.53	4347.06	-2186.92	4387.84
21	-32175.90	64367.89	-32685.20	65384.42
25	-78454.90	156925.80	-79391.50	158797.00
29	-20799.30	41614.57	-20924.00	41861.94
31	-8418.86	16853.71	-8428.47	16870.94
32	-24010.60	48037.21	-24092.50	48199.00
33	-19954.30	39924.53	-20030.00	40074.09
34	-18278.60	36573.18	-18420.30	36854.51

Appendix E

To quantify the change of the ETAS parameters across regions, boxplots of the ETAS parameters in each region (**Figure E-1** and **Figure E-4**) and the detailed calculation of the total standard error of each parameter for the boxplots are provided in **Appendix E**. ETAS parameter results, which are classified by magnitudes for Case 1 and regions for Case 2, are shown in **Figure E-2** and **Figure E-3**, respectively.

E.1 Standard errors of ETAS parameters for each geographical region from boxplots

The total stand error (SE_{total}) of ETAS parameters for each geographical region is calculated by:

$$\mathrm{SE_{total}} = \sqrt[2]{(\mathrm{SE_{mean}})^2 + (\mathrm{SE_{individual}})^2} \quad \text{(E-1)}$$

where SE_{mean} is the standard deviation of the estimated ETAS parameters in each geographical region and $SE_{individual}$ is the square root of the mean of all variances in each region.

Boxplots of the ETAS parameters for Case 1

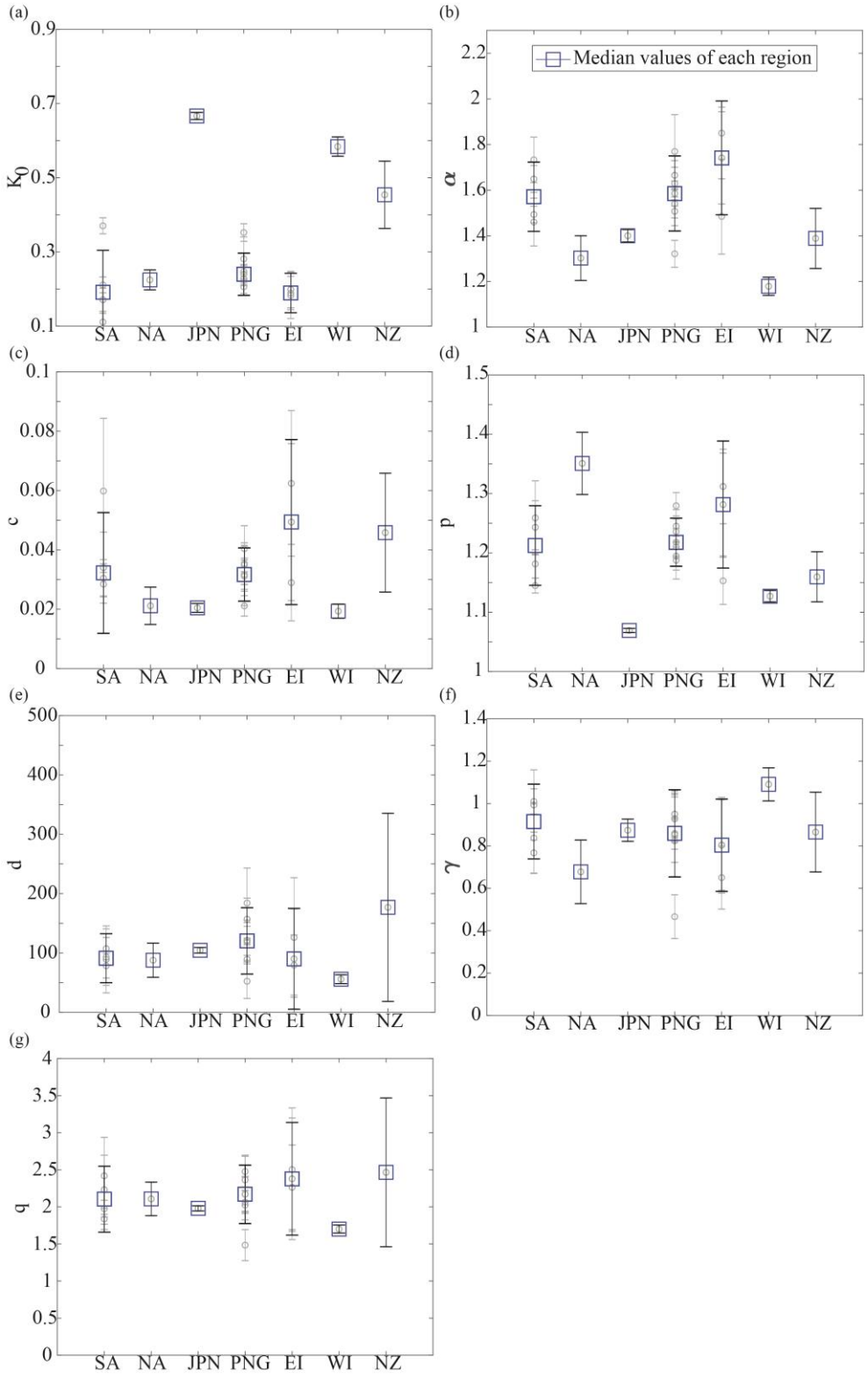

Figure E-1. Boxplots of the ETAS parameter estimates classified by region in South America (SA), North America (NA), Japan (JPN), Papua New Guinea (PNG), Eastern Indonesia (EI), Western Indonesia (WI), and New Zealand (NZ) for Case 1.

ETAS parameters classified by the largest magnitude in each sub-catalogue for Case 1

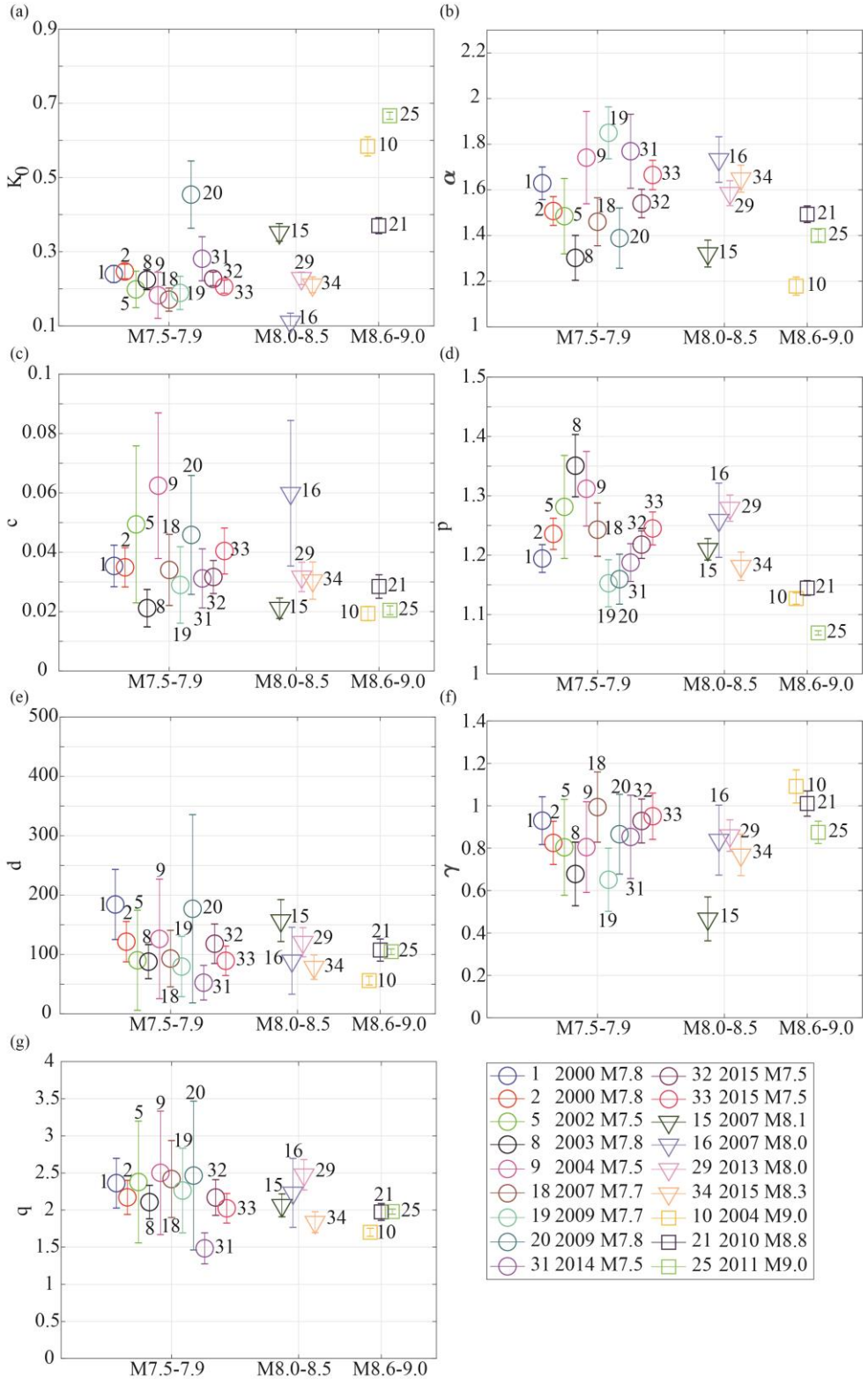

Figure E-2. ETAS parameter results classified by the largest magnitude for Case 1 based on long time period catalogues with all ETAS parameters free.

ETAS parameters classified by region for Case 2

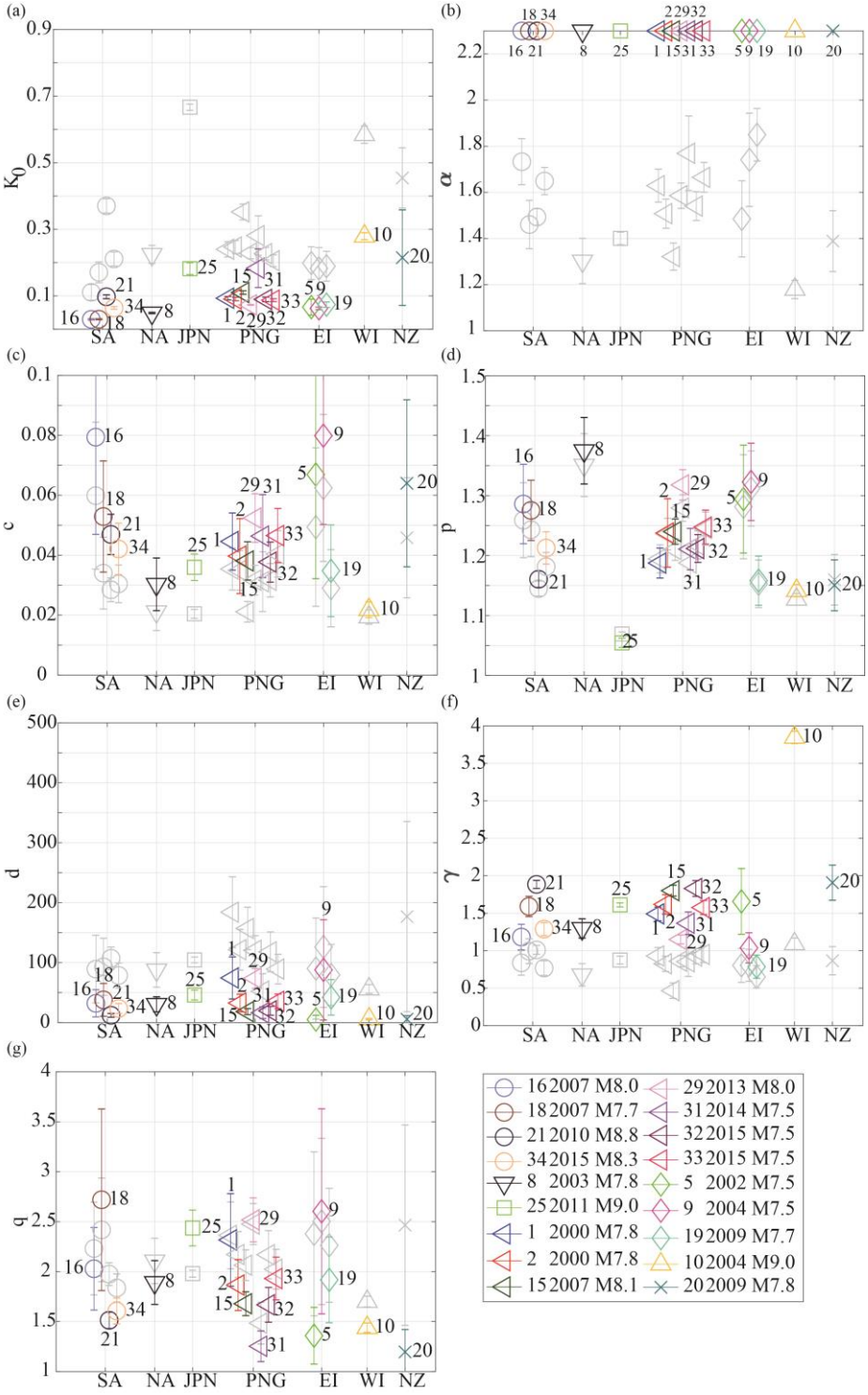

Figure E-3. ETAS parameter results classified by region in South America (SA), North America (NA), Japan (JPN), Papua New Guinea (PNG), Eastern Indonesia (EI), western Indonesia (WI), and New Zealand (NZ) for Case 2 based on long time period catalogues with fixed α.

Boxplots of the ETAS parameters for Case 2

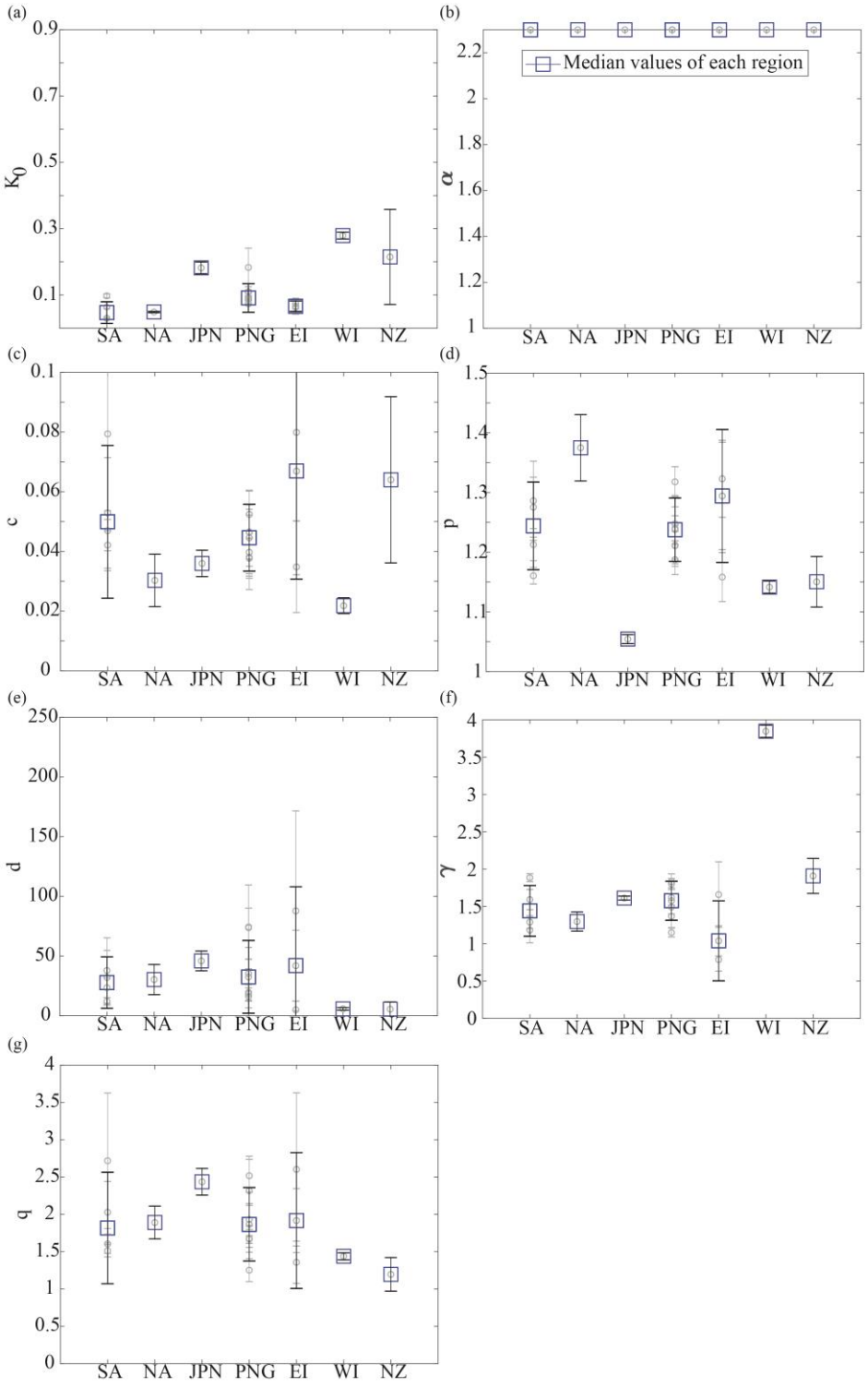

Figure E-4. Boxplots of the ETAS parameter estimates classified by region in South America (SA), North America (NA), Japan (JPN), Papua New Guinea (PNG), Eastern Indonesia (EI),

western Indonesia (WI), and New Zealand (NZ) for Case 2 based on long time period catalogs with fixed α. Individual samples are plotted in circles with error bars.

Table E-1. Summary of the p_{lm} values of ETAS parameters for Case 3 (Boldface indicates significant co-dependence).

	K_0	α	c	p	d	γ	q
Magnitude	1.0000	0.8345	1.0000	1.0000	1.0000	1.0000	0.2750
Rupture length	1.0000	0.8494	1.0000	1.0000	1.0000	1.0000	1.0000
Rupture width	1.0000	0.1558	1.0000	1.0000	1.0000	1.0000	1.0000
Rupture area	1.0000	0.4532	1.0000	1.0000	1.0000	1.0000	1.0000

Appendix F

To evaluate different IMs, metrics for efficiency, sufficiency, and relative sufficiency of Houses 1-3 are calculated for Sa(T=0.05s-5s), AI, CAV, PGV, and SI in **Appendix F**.

F.1 Sufficiency and efficiency of IMs for Houses 1-3.

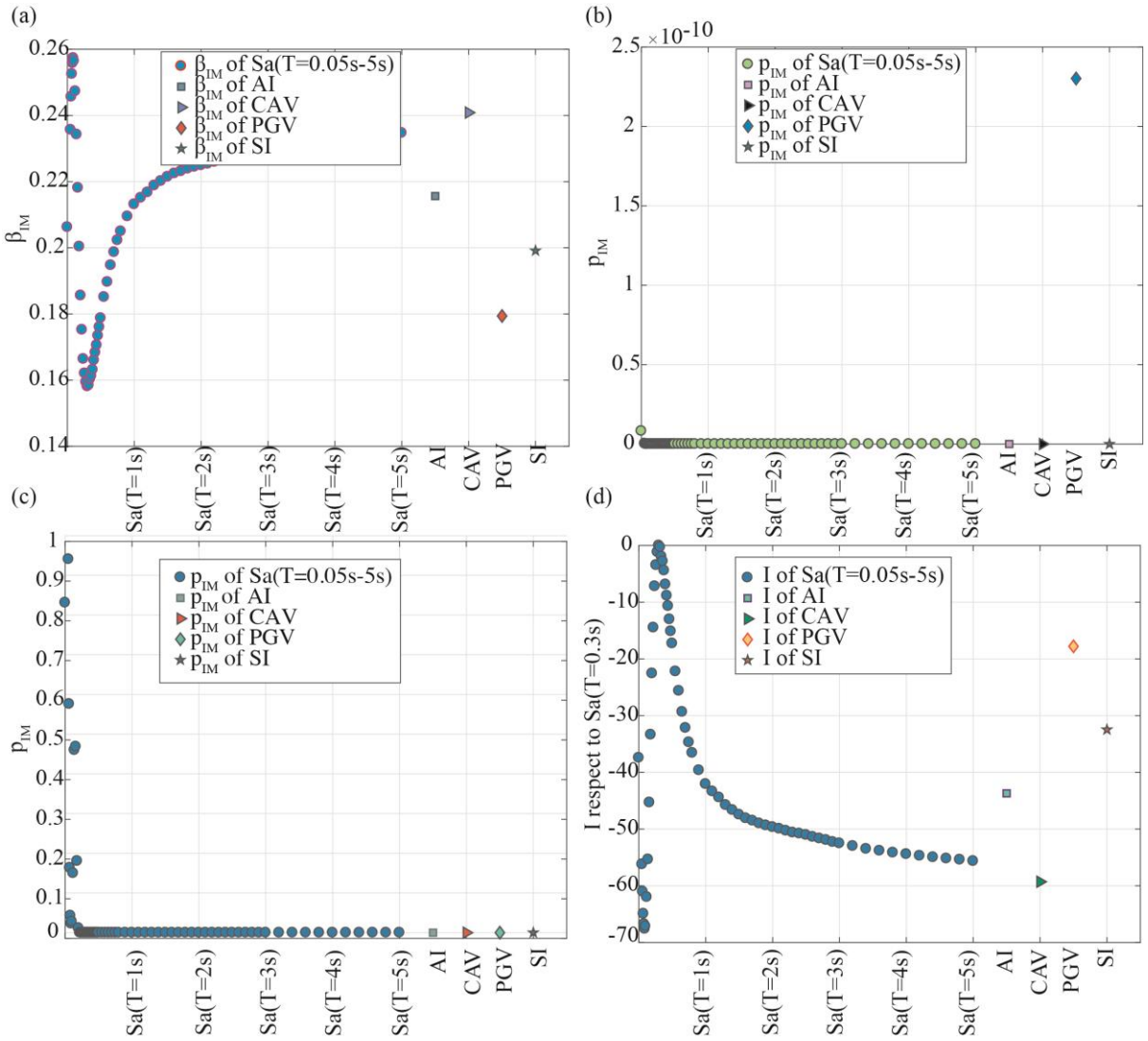

Figure F-1. Plot of (a) efficiency (β_{IM}), sufficiency (p_{IM}) for (b) rupture distance and (c) magnitude, and (d) relative sufficiency of each IM given the non-collapse EDP with unscaled records for House 1.

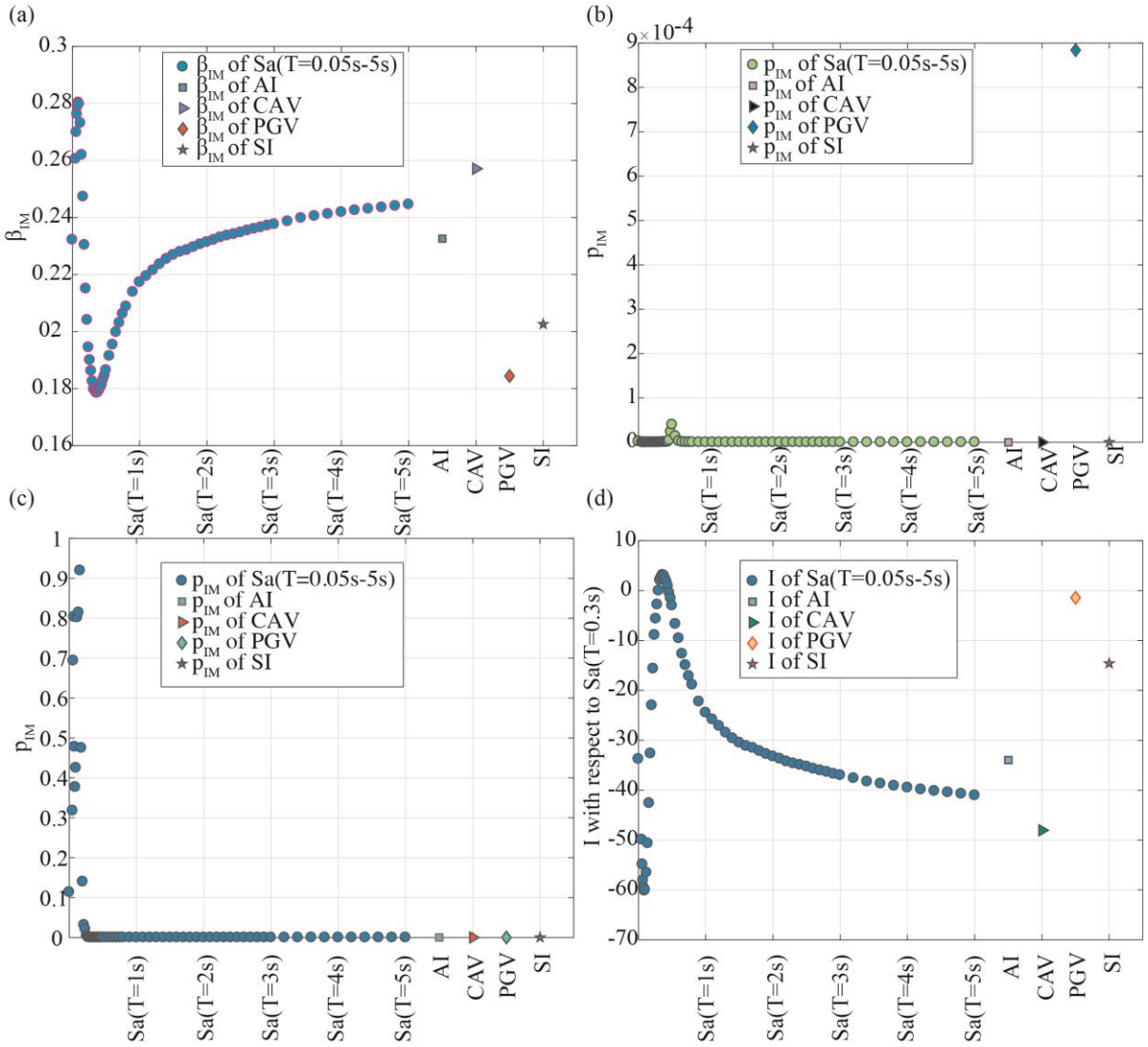

Figure F-2. Plot of (a) efficiency (β_{IM}), sufficiency (p_{IM}) for (b) rupture distance and (c) magnitude, and (d) relative sufficiency of each IM given the non-collapse EDP with unscaled records for House 2.

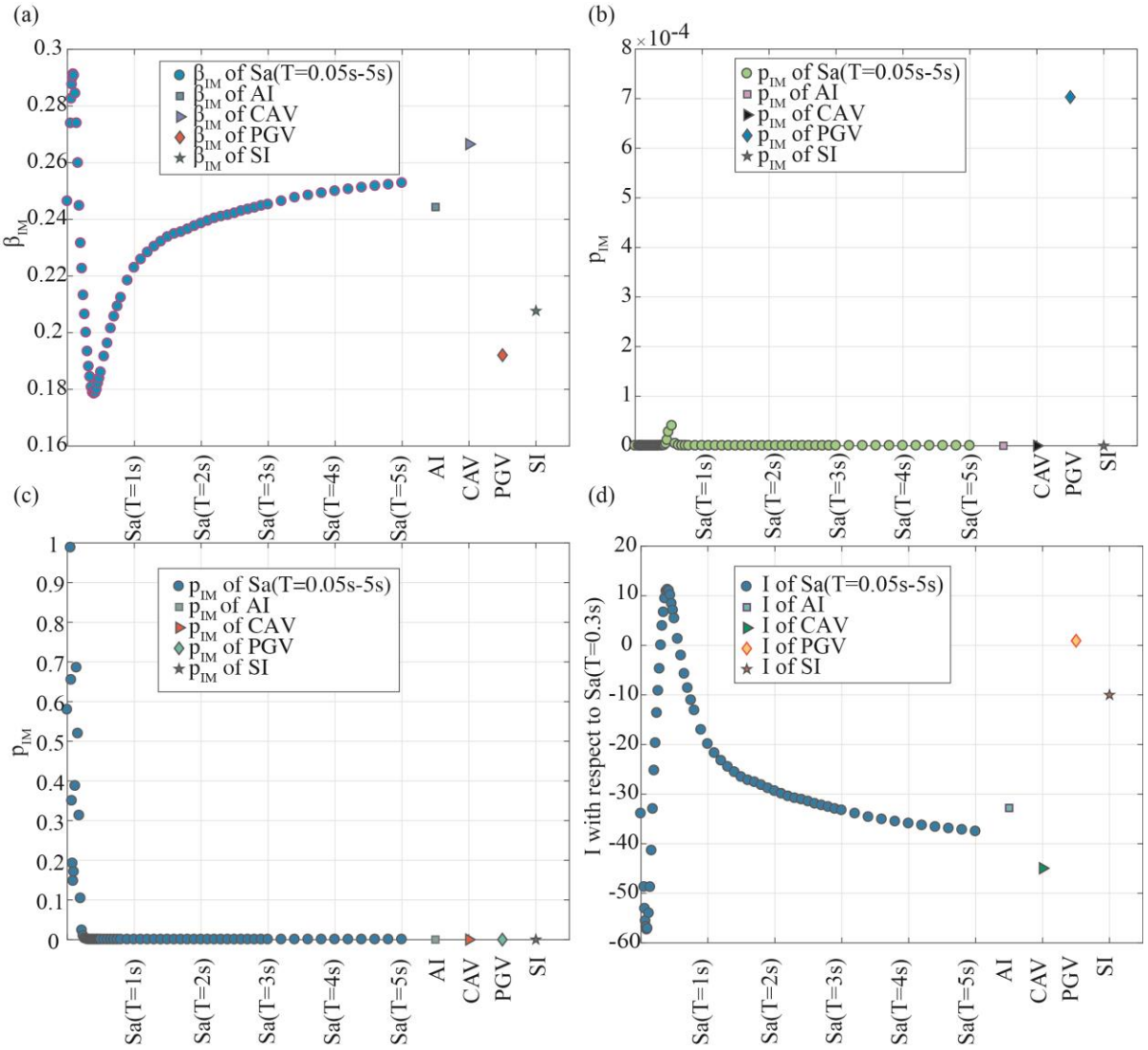

Figure F-3. Plot of (a) efficiency (β_{IM}), sufficiency (p_{IM}) for (b) rupture distance and (c) magnitude, and (d) relative sufficiency of each IM given the non-collapse EDP with unscaled records for House 3.

References

Abrahamson, N., N. Gregor, and K. Addo (2016) BC Hydro ground motion prediction equations for subduction earthquakes, *Earthq. Spectra* **32**, 23–44.

Abrahamson, N., W. Silva, and R. Kamai (2014) Summary of the ASK14 ground motion relation for active crustal regions, *Earthq. Spectra* **30**, 1025–1055.

Aki, K. (1965) Maximum likelihood estimate of b in the formula log N= a-bM and its confidence limits, *Bull. Earthq. Res. Inst., Tokyo Univ.* **43**, 237–239.

Amorèse, D. (2007) Applying a change-point detection method on frequency-magnitude distributions, *Bull. Seismol. Soc. Am.* **97**, 1742–1749.

Ancheta, T.D., R.B. Darragh, J.P. Stewart, E. Seyhan, W.J. Silva, B.S.-J. Chiou, K.E. Wooddell, R.W. Graves, A.R. Kottke, D.M. Boore, and others (2014) NGA-West2 database, *Earthq. Spectra* **30**, 989–1005.

Arias, A (1970). A measure of earthquake intensity, in *Seismic Design for Nuclear Power Plants*, R. J. Hansen (Editor), MIT Press, Cambridge, Massachusetts, 438–483.

Asano, K. and T. Iwata (2011) Characterization of stress drops on asperities estimated from the heterogeneous kinematic slip model for strong motion prediction for inland crustal earthquakes in Japan, *Pure Appl. Geophys.* **168**, 105–116.

Asano, Y., T. Saito, Y. Ito, K. Shiomi, H. Hirose, T. Matsumoto, S. Aoi, S. Hori, and S. Sekiguchi (2011) Spatial distribution and focal mechanisms of aftershocks of the 2011 off the Pacific coast of Tohoku Earthquake, *Earth, Planets Sp.* **63**, 669–673.

Atkinson, G.M. and D.M. Boore (2003) Empirical ground-motion relations for subduction-zone earthquakes and their application to Cascadia and other regions, *Bull. Seismol. Soc. Am.* **93**, 1703–1729.

Baker, J.W. (2010) Conditional mean spectrum: Tool for ground-motion selection, *J. Struct. Eng.* **137**, 322–331.

Baker, J.W. (2015) Efficient analytical fragility function fitting using dynamic structural analysis, *Earthq. Spectra* **31**, 579–599.

Bansal, A.R. and Y. Ogata (2013) A non-stationary epidemic type aftershock sequence model for seismicity prior to the December 26, 2004 M 9.1 Sumatra-Andaman Islands mega-earthquake, *J. Geophys. Res. Solid Earth* **118**, 616–629.

Bazzurro, P., C. A. Cornell, C. Menun, and M. Motahari (2004) Guidelines for seismic assessment of damaged buildings, in *Proc. of the 13th World Conf. on Earthquake Engineering*, Vancouver, British Columbia, Canada, 1–5 August 2004, paper no. 1708.

Béjar-Pizarro, M., D. Carrizo, A. Socquet, R. Armijo, S. Barrientos, F. Bondoux, S. Bonvalot, J. Campos, D. Comte, J.B. De Chabalier, and others (2010) Asperities and barriers on the seismogenic zone in North Chile: state-of-the-art after the 2007 M w 7.7 Tocopilla earthquake inferred by GPS and InSAR data, *Geophys. J. Int.* **183**, 390–406.

Bird, A.L. and M. Lamontagne (2015) Impacts of the October 2012 magnitude 7.8 earthquake near Haida Gwaii, Canada, *Bull. Seismol. Soc. Am.* **105**, 1178–1192.

Boore, D.M., J.P. Stewart, E. Seyhan, and G.M. Atkinson (2014) NGA-West2 equations for predicting PGA, PGV, and 5% damped PSA for shallow crustal earthquakes, *Earthq. Spectra* **30**, 1057–1085.

Boyd, O.S. (2012) Including foreshocks and aftershocks in time-independent probabilistic seismic-hazard analyses, *Bull. Seismol. Soc. Am.* **102**, 909–917.

Bradley, B.A. (2011) Empirical equations for the prediction of displacement spectrum intensity and its correlation with other intensity measures, *Soil Dyn. Earthq. Eng.* **31**, 1182–1191.

Cauzzi, C., Y. Behr, T. Le Guenan, J. Douglas, S. Auclair, J. Woessner, J. Clinton, and S. Wiemer (2016) Earthquake early warning and operational earthquake forecasting as real-time hazard information to mitigate seismic risk at nuclear facilities, *Bull. Earthq. Eng.* **14**, 2495–2512.

Charvet, I., I. Ioannou, T. Rossetto, A. Suppasri, and F. Imamura (2014) Empirical fragility assessment of buildings affected by the 2011 Great East Japan tsunami using improved statistical models, *Nat. Hazards* **73**, 951–973.

Christidis, A.A., E.G. Dimitroudi, G.D. Hatzigeorgiou, and D.E. Beskos (2013) Maximum seismic displacements evaluation of steel frames from their post-earthquake residual deformation, *Bull. Earthq. Eng.* **11**, 2233–2248.

Christovasilis, I.P., A. Filiatrault, M.C. Constantinou, and A. Wanitkorkul (2009a) Incremental dynamic analysis of woodframe buildings, *Earthq. Eng. Struct. Dyn.* **38**, 477–496.

Christovasilis, I.P., A. Filiatrault, and A. Wanitkorkul (2009b) Seismic testing of a full-scale two-story light-frame wood building: NEESWood benchmark test, MCEER Technical Report 09-0005, Multidisciplinary Center for Earthquake Engineering, Buffalo, New York, 14260.

Chu, A., F.P. Schoenberg, P. Bird, D.D. Jackson, and Y.Y. Kagan (2011) Comparison of ETAS parameter estimates across different global tectonic zones, *Bull. Seismol. Soc. Am.* **101**, 2323–2339.

Console, R., M. Murru, and A.M. Lombardi (2003) Refining earthquake clustering models, *J. Geophys. Res. Solid Earth* **108**, doi: 10.1029/2002JB002130.

Cornell, C.A. (1968) Engineering seismic risk analysis, *Bull. Seismol. Soc. Am.* **58**, 1583–1606.

Cornell, C.A., M. Asce, F. Jalayer, R.O. Hamburger, and D. a Foutch (2002) Probabilistic basis for 2000 SAC Federal Emergency Management Agency steel moment frame guidelines, **128**, 526–533.

Daniell, J.E., B. Khazai, F. Wenzel, and A. Vervaeck (2011) The CATDAT damaging earthquakes database, *Nat. Hazards Earth Syst. Sci.* **11**, 2235–2251.

Das, S. and C. Henry (2003) Spatial relation between main earthquake slip and its aftershock distribution, *Rev. Geophys.* **41**, doi: 10.1029/2002RG000119.

De Risi, R., K. Goda, T. Yasuda, and N. Mori (2017) Is flow velocity important in tsunami empirical fragility modeling?, *Earth-science Rev.* **166**, 64–82.

Deirlein, G., H. Krawinkler, and C. Cornell (2003). A framework for performance-based earthquake engineering, in *Proc. of the 2003 Pacific Conference on Earthquake Engineering*, Christchurch, New Zealand, paper no. 140.

Ebrahimian, H., F. Jalayer, D. Asprone, A.M. Lombardi, W. Marzocchi, A. Prota, and G. Manfredi (2014) A performance-based framework for adaptive seismic aftershock risk assessment, *Earthq. Eng. Struct. Dyn.* **43**, 2179–2197.

Ebrahimian, H., F. Jalayer, A. Lucchini, F. Mollaioli, and G. Manfredi (2015) Preliminary ranking of alternative scalar and vector intensity measures of ground shaking, *Bull. Earthq. Eng.* **13**, 2805–2840.

Electrical Power Research Institute (EPRI). (1988) A criterion for determining exceedance of the operating basis earthquake, EPRI NP-5930, Electrical Power Research Inst., Palo Alto, California.

Erochko, J., C. Christopoulos, R. Tremblay, and H. Choi (2010) Residual drift response of SMRFs and BRB frames in steel buildings designed according to ASCE 7-05, *J. Struct. Eng.* **137**, 589–599.

Farías, M., D. Comte, S. Roecker, D. Carrizo, and M. Pardo (2011) Crustal extensional faulting triggered by the 2010 Chilean earthquake: the Pichilemu seismic sequence, *Tectonics* **30**, doi: 10.1029/2011TC002888.

Federal Emergency Management Agency (FEMA) (2014) FEMA P-58 Seismic performance assessment of buildings, Report No. FEMA P-58, Washington, DC.

Federal Emergency Management Agency (FEMA) (2009) NEHRP recommended seismic provisions for new buildings and other structures, Report No. FEMA P-750, Washington, DC.

Federal Emergency Management Agency (FEMA) (2000) Prestandard and commentary for the seismic rehabilitation of buildings, Report No. FEMA-356, Washington, DC.

Felzer, K.R., R.E. Abercrombie, and G. Ekström (2004) A common origin for aftershocks, foreshocks, and multiplets, *Bull. Seismol. Soc. Am.* **94**, 88–98.

Felzer, K.R. and E.E. Brodsky (2006) Decay of aftershock density with distance indicates triggering by dynamic stress, *Nature* **441**, 735–738.

Field, E., K. Milner, J. Hardebeck, M. Page, N. van der Elst, T.H. Jordan, A.J. Michael, B.E. Shaw, and M.J. Werner (2017a) A spatiotemporal clustering model for the Third Uniform California Earthquake Rupture Forecast (UCERF3-ETAS): toward an operational earthquake forecast, *Bull. Seismol. Soc. Am.* **107**, 1049–1081.

Field, E., K. Porter, and K. Milner (2017b) A prototype operational earthquake loss model for California based on UCERF3-ETAS--a first look at valuation, *Earthq. Spectra* **33**, 1279–1299.

Field, E.H., T.H. Jordan, L.M. Jones, A.J. Michael, M.L. Blanpied, and others (2016) The potential uses of operational earthquake forecasting, *Seismol. Res. Lett.* **87**, 313–322.

Fitzenz, D.D. (2018) Conditional probability of what? example of the Nankai interface in Japan, *Bull. Seismol. Soc. Am.* **108**, 3169–3179.

Flück, P., R.D. Hyndman, and K. Wang (1997) Three-dimensional dislocation model for great earthquakes of the Cascadia subduction zone, *J. Geophys. Res. Solid Earth* **102**, 20539–20550.

Folz, B. and A. Filiatrault (2001) Cyclic analysis of wood shear walls, *J. Struct. Eng.* **127**, 433–441.

Folz, B. and A. Filiatrault (2004a) Seismic analysis of woodframe structures. I: Model formulation, *J. Struct. Eng.* **130**, 1353–1360.

Folz, B. and A. Filiatrault (2004b) Seismic analysis of woodframe structures. II: Model

implementation and verification, *J. Struct. Eng.* **130**, 1361–1370.

Fukushima, Y., Y. Takada, and M. Hashimoto (2013) Complex ruptures of the 11 April 2011 Mw 6.6 Iwaki earthquake triggered by the 11 March 2011 Mw 9.0 Tohoku earthquake, Japan, *Bull. Seismol. Soc. Am.* **103**, 1572–1583.

Gerstenberger, M., G. McVerry, D. Rhoades, and M. Stirling (2014) Seismic hazard modeling for the recovery of Christchurch, *Earthq. Spectra* **30**, 17–29.

Ghofrani, H. and G.M. Atkinson (2014) Ground-motion prediction equations for interface earthquakes of M7 to M9 based on empirical data from Japan, *Bull. Earthq. Eng.* **12**, 549–571.

Goda, K. (2015) Record selection for aftershock incremental dynamic analysis, *Earthq. Eng. Struct. Dyn.* **44**, 1157–1162.

Goda, K. and G.M. Atkinson (2010) Intraevent spatial correlation of ground-motion parameters using SK-net data, *Bull. Seismol. Soc. Am.* **100**, 3055–3067.

Goda, K. and G.M. Atkinson (2011) Seismic performance of wood-frame houses in south-western British Columbia, *Earthq. Eng. Struct. Dyn.* **40**, 903–924.

Goda, K., G.M. Atkinson, and H.P. Hong (2011) Seismic loss estimation of wood-frame houses in south-western British Columbia, *Struct. Saf.* **33**, 123–135.

Goda, K. and H.P. Hong (2008) Estimation of seismic loss for spatially distributed buildings, *Earthq. Spectra* **24**, 889–910.

Goda, K., A. Pomonis, S.C. Chian, M. Offord, K. Saito, P. Sammonds, S. Fraser, A. Raby, and J. Macabuag (2013) Ground motion characteristics and shaking damage of the 11th March 2011 M w 9.0 Great East Japan earthquake, *Bull. Earthq. Eng.* **11**, 141–170.

Goda, K. and M.R. Salami (2014) Inelastic seismic demand estimation of wood-frame houses subjected to mainshock-aftershock sequences, *Bull. Earthq. Eng.* **12**, 855–874.

Goda, K. and C.A. Taylor (2012) Effects of aftershocks on peak ductility demand due to strong

ground motion records from shallow crustal earthquakes, *Earthq. Eng. Struct. Dyn.* **41**, 2311–2330.

Goda, K. and S. Tesfamariam (2015) Multi-variate seismic demand modelling using copulas: Application to non-ductile reinforced concrete frame in Victoria, Canada, *Struct. Saf.* **56**, 39–51.

Goda, K., F. Wenzel, and R. De Risi (2015) Empirical assessment of non-linear seismic demand of mainshock-aftershock ground-motion sequences for Japanese earthquakes, *Front. Built Environ.* **1**, 6, doi: 10.3389/fbuil.2015.00006.

Goda, K., T. Yasuda, N. Mori, and T. Maruyama (2016) New scaling relationships of earthquake source parameters for stochastic tsunami simulation, *Coast. Eng. J.* **58**, doi: 10.1142/S0578563416500108.

Goldfinger, C., C.H. Nelson, a. E. Morey, J. Joel E, J. Patton, E. Karabanov, J. Gutierrez-Pastor, A. Eriksson, E. Gracia, G. Dunhill, R. Enkin, A. Dallimore, and T. Valiier (2012) Turbidite event history — methods and implications for holocene paleoseismicity of the Cascadia Subduction Zone, *U.S. Geol. Surv. Prof. Pap. 1661-F* 170 p.

Gutenberg, B. and C.F. Richter (1944) Frequency of earthquakes in California, *Bull. Seismol. Soc. Am.* **34**, 185–188.

Hainzl, S. (2016) Apparent triggering function of aftershocks resulting from rate-dependent incompleteness of earthquake catalogs, *J. Geophys. Res. Solid Earth* **121**, 6499–6509.

Hainzl, S., A. Christophersen, and B. Enescu (2008) Impact of earthquake rupture extensions on parameter estimations of point-process models, *Bull. Seismol. Soc. Am.* **98**, 2066–2072.

Hainzl, S., J. Moradpour, and J. Davidsen (2014) Static stress triggering explains the empirical aftershock distance decay, *Geophys. Res. Lett.* **41**, 8818–8824.

Hainzl, S., O. Zakharova, and D. Marsan (2013) Impact of aseismic transients on the estimation of aftershock productivity parameters, *Bull. Seismol. Soc. Am.* **103**, 1723–1732.

Halchuk, S., T.I. Allen, J. Adams, and G.C. Rogers (2014) Fifth generation seismic hazard model input files as proposed to produce values for the 2015 National Building Code of Canada, *Geol. Surv. Canada, Open File* **7576**.

Halchuk, S., T.I. Allen, G.C. Rogers, and J. Adams (2015) Seismic hazard earthquake epicentre file (SHEEF2010) used in the fifth generation seismic hazard maps of Canada, *Geol. Surv. Canada Open File* **7724**, doi: 10.4095/296908.

Han, R., Y. Li, and J. van de Lindt (2014) Assessment of seismic performance of buildings with incorporation of aftershocks, *J. Perform. Constr. Facil.* **29**, doi: 10.1061/(ASCE)CF.

Harte, D.S. (2012) Bias in fitting the ETAS model: A case study based on New Zealand seismicity, *Geophys. J. Int.* **192**, 390–412.

Harte, D.S. (2015) Model parameter estimation bias induced by earthquake magnitude cut-off, *Geophys. J. Int.* **204**, 1266–1287.

Hayes, G.P., E.K. Meyers, J.W. Dewey, R.W. Briggs, P.S. Earle, H.M. Benz, G.M. Smoczyk, H.E. Flamme, W.D. Barnhart, R.D. Gold, and others (2017) Tectonic summaries of magnitude 7 and greater earthquakes from 2000 to 2015 (No. 2016–1192). Reston: US Geological Survey.

Hayes, G.P., D.J. Wald, and R.L. Johnson (2012) Slab1.0: a three-dimensional model of global subduction zone geometries, *J. Geophys. Res. Solid Earth* **117**, doi: 10.1029/2011JB008524.

Helmstetter, A., Y.Y. Kagan, and D.D. Jackson (2006) Comparison of short-term and time-independent earthquake forecast models for southern California, *Bull. Seismol. Soc. Am.* **96**, 90–106.

Helmstetter, A., Y.Y. Kagan, and D.D. Jackson (2005) Importance of small earthquakes for stress transfers and earthquake triggering, *J. Geophys. Res. Solid Earth* **110**, doi: 10.1029/2004JB003286.

Helmstetter, A. and D. Sornette (2002) Subcritical and supercritical regimes in epidemic models of earthquake aftershocks, *J. Geophys. Res. Solid Earth* **107**, doi: 10.1029/2001JB001580.

Hirose, F., K. Miyaoka, N. Hayashimoto, T. Yamazaki, and M. Nakamura (2011) Outline of the 2011 off the Pacific coast of Tohoku earthquake (Mw 9.0)—seismicity: foreshocks, mainshock, aftershocks, and induced activity—, *Earth, planets Sp.* **63**, 513–518.

Housner, G. W. (1952) Spectrum intensity of strong-motion earthquakes, in *Proc. of Symp. Earthquake and Blast Effects on Structures*, Earthquake Engineering Research Institute, Los Angeles, California, 26–28 June 1952, 20–36.

Hyndman, R.D. (2013) Downdip landward limit of Cascadia great earthquake rupture, *J. Geophys. Res. Solid Earth* **118**, 5530–5549.

Hyndman, R.D. (2015) Tectonics and structure of the Queen Charlotte fault zone, Haida Gwaii, and large thrust earthquakes, *Bull. Seismol. Soc. Am.* **105**, 1058–1075.

Iervolino, I., E. Chioccarelli, M. Giorgio, W. Marzocchi, G. Zuccaro, M. Dolce, and G. Manfredi (2015) Operational (short-term) earthquake loss forecasting in Italy, *Bull. Seismol. Soc. Am.* **105**, 2286–2298.

Iervolino, I., M. Giorgio, and E. Chioccarelli (2014) Closed-form aftershock reliability of damage-cumulating elastic-perfectly-plastic systems, *Earthq. Eng. Struct. Dyn.* **43**, 613–625.

Iervolino, I., M. Giorgio, and E. Chioccarelli (2016) Markovian modeling of seismic damage accumulation, *Earthq. Eng. Struct. Dyn.* **45**, 441–461.

Imanishi, K., R. Ando, and Y. Kuwahara (2012) Unusual shallow normal-faulting earthquake sequence in compressional northeast Japan activated after the 2011 off the Pacific coast of Tohoku earthquake, *Geophys. Res. Lett.* **39**, doi: 10.1029/2012GL051491.

Ishibe, T., K. Shimazaki, K. Satake, and H. Tsuruoka (2011) Change in seismicity beneath the

Tokyo metropolitan area due to the 2011 off the Pacific coast of Tohoku earthquake, *Earth, planets Sp.* **63**, 731–735.

Jalayer, F., J.L. Beck, and F. Zareian (2012) Analyzing the sufficiency of alternative scalar and vector intensity measures of ground shaking based on information theory, *J. Eng. Mech.* **138**, 307–316.

Jalayer, F. and H. Ebrahimian (2017) Seismic risk assessment considering cumulative damage due to aftershocks, *Earthq. Eng. Struct. Dyn.* **46**, 369–389.

Jordan, T.H., Y.T. Chen, P. Gasparini, R. Madariaga, I. Main, W. Marzocchi, G. Papadopoulos, G. Sobolev, K. Yamaoka, and J. Zschau (2011) Operational earthquake forecasting: state of knowledge and guidelines for utilization, *Ann. Geophys.* **54**, 319–391.

Jordan, T.H. and L.M. Jones (2010) Operational earthquake forecasting: some thoughts on why and how, *Seismol. Res. Lett.* **81**, 571–574.

Kagan, Y.Y. (2002) Aftershock zone scaling, *Bull. Seismol. Soc. Am.* **92**, 641–655.

Kagan, Y.Y. (2004) Short-term properties of earthquake catalogs and models of earthquake source, *Bull. Seismol. Soc. Am.* **94**, 1207–1228.

Kagan, Y.Y. and D.D. Jackson (1994) Long-term probabilistic forecasting of earthquakes, *J. Geophys. Res. Solid Earth* **99**, 13685–13700.

Kagan, Y.Y. and D.D. Jackson (2013) Tohoku earthquake: a surprise?, *Bull. Seismol. Soc. Am.* **103**, 1181–1194.

Kagan, Y.Y. and L. Knopoff (1987) Statistical short-term earthquake prediction, *Science.* **236**, 1563–1567.

Kanaori, Y., S. Kawakami, and K. Yairi (1991) Space-time distribution patterns of destructive earthquakes in the inner belt of central Japan: activity intervals and locations of earthquakes, *Eng. Geol.* **31**, 209–230.

Kao, H., S.-J. Shan, and A.M. Farahbod (2015) Source characteristics of the 2012 Haida Gwaii

earthquake sequence, *Bull. Seismol. Soc. Am.* **105**, 1206–1218.

Kato, A., J. Fukuda, and K. Obara (2013) Response of seismicity to static and dynamic stress changes induced by the 2011 M9. 0 Tohoku-Oki earthquake, *Geophys. Res. Lett.* **40**, 3572–3578.

Koduru, S.D. and T. Haukaas (2010) Probabilistic seismic loss assessment of a Vancouver high-rise building, *J. Struct. Eng.* **136**, 235–245.

Koketsu, K., K. Hikima, S. Miyazaki, and S. Ide (2004) Joint inversion of strong motion and geodetic data for the source process of the 2003 Tokachi-oki, Hokkaido, earthquake, *Earth, planets Sp.* **56**, 329–334.

Koketsu, K., Y. Yokota, N. Nishimura, Y. Yagi, S. Miyazaki, K. Satake, Y. Fujii, H. Miyake, S. Sakai, Y. Yamanaka, and T. Okada (2011) A unified source model for the 2011 Tohoku earthquake, *Earth Planet. Sci. Lett.* **310**, 480–487.

Kostinakis, K., I.-K. Fontara, and A.M. Athanatopoulou (2017) Scalar structure-specific ground motion intensity measures for assessing the seismic performance of structures: a review, *J. Earthq. Eng.* **22**, 630–665.

Kumazawa, T., Y. Ogata, and others (2014) Nonstationary ETAS models for nonstandard earthquakes, *Ann. Appl. Stat.* **8**, 1825–1852.

Kurahashi, S. and K. Irikura (2013) Short-period source model of the 2011 Mw 9.0 off the Pacific coast of Tohoku earthquake, *Bull. Seismol. Soc. Am.* **103**, 1373–1393.

Lagaros, N.D. and M. Fragiadakis (2007) Fragility assessment of steel frames using neural networks, *Earthq. Spectra* **23**, 735–752.

Lay, T., H. Kanamori, C.J. Ammon, A.R. Hutko, K. Furlong, and L. Rivera (2009) The 2006--2007 Kuril Islands great earthquake sequence, *J. Geophys. Res. Solid Earth* **114**, doi: 10.1029/2008JB006280.

Lay, T., L. Ye, H. Kanamori, Y. Yamazaki, K.F. Cheung, K. Kwong, and K.D. Koper (2013)

The October 28, 2012 Mw 7.8 Haida Gwaii underthrusting earthquake and tsunami: Slip partitioning along the Queen Charlotte fault transpressional plate boundary, *Earth Planet. Sci. Lett.* **375**, 57–70.

Li, Q. and B.R. Ellingwood (2007) Performance evaluation and damage assessment of steel frame buildings under main shock--aftershock earthquake sequences, *Earthq. Eng. Struct. Dyn.* **36**, 405–427.

Lombardi, A.M. (2017a) SEDA: a software package for the statistical earthquake data analysis, *Sci. Rep.* **7**, doi: 10.1038/srep44171.

Lombardi, A.M. (2017b) The epistemic and aleatory uncertainties of the ETAS-type models: an application to the Central Italy seismicity, *Sci. Rep.* **7**, doi: 10.1038/s41598-017-11925-3.

Lombardi, A.M. and W. Marzocchi (2010) The ETAS model for daily forecasting of Italian seismicity in the CSEP experiment, *Ann. Geophys.* **53**, 155–164.

Luco, N. (2002) Probabilistic seismic demand analysis, SMRF connection fractures, and near-source effects, *Ph.D. thesis*, Stanford University, Standford, California.

Luco, N., P. Bazzurro, and C. A. Cornell (2004) Dynamic versus static computation of the residual capacity of a mainshock-damaged building to withstand an aftershock, in *Proc. of the 13th World Conf. on Earthquake Engineering*, Vancouver, 1–6 August 2004, paper no. 2405.

Luco, N. and C.A. Cornell (2007) Structure-specific scalar intensity measures for near-source and ordinary earthquake ground motions, *Earthq. Spectra* **23**, 357–392.

Luco, N., M.C. Gerstenberger, S.R. Uma, H. Ryu, A.B. Liel, and M. Raghunandan (2011) A methodology for post-mainshock probabilistic assessment of building collapse risk, In: *Ninth Pacific Conference on Earthquake Engineering*, Auckland, New Zealand, 14–16 April 2011.

Luttrell, K.M., X. Tong, D.T. Sandwell, B.A. Brooks, and M.G. Bevis (2011) Estimates of stress drop and crustal tectonic stress from the 27 February 2010 Maule, Chile, earthquake: Implications for fault strength, *J. Geophys. Res. Solid Earth* **116**, doi: 10.1029/2011JB008509.

Mai, P.M. and K.K.S. Thingbaijam (2014) SRCMOD: An online database of finite-fault rupture models, *Seismol. Res. Lett.* **85**, 1348–1357.

Marzocchi, W., A.M. Lombardi, and E. Casarotti (2014) The establishment of an operational earthquake forecasting system in Italy, *Seismol. Res. Lett.* **85**, 961–969.

Marzocchi, W. and L. Sandri (2003) A review and new insights on the estimation of the b-valueand its uncertainty, *Ann. Geophys.* **46**, 1271–1282.

Marzocchi, W. and M. Taroni (2014) Some thoughts on declustering in probabilistic seismic-hazard analysis, *Bull. Seismol. Soc. Am.* **104**, 1838–1845.

McGuire, R.K. (2004) *Seismic hazard and risk analysis,* EERI Monograph MNO-10, Earthquake Engineeering Research Institute, Oakland, California.

McNeil, A. J., R. Frey, and P. Embrechts (2005) *Quantitative Risk Management: Concepts, Techniques and Tools*, Princeton Univ. Press, Princeton, New Jersey.

Midorikawa, S., Y. Ito, and H. Miura (2011) Vulnerability functions of buildings based on damage survey data of earthquakes after the 1995 Kobe earthquake, *J. Japan Assoc. Earthq. Eng.* **11**, 34–47.

Miura, S., Y. Suwa, T. Sato, K. Tachibana, and A. Hasegawa (2004) Slip distribution of the 2003 northern Miyagi earthquake (M6.4) deduced from geodetic inversion, *Earth, planets Sp.* **56**, 95–101.

Mollaioli, F., A. Lucchini, Y. Cheng, and G. Monti (2013) Intensity measures for the seismic response prediction of base-isolated buildings, *Bull. Earthq. Eng.* **11**, 1841–1866.

Monahan, P.A. and V.M. Levson (2001) Development of a shear-wave velocity model of the

near-surface deposits of southwestern British Columbia, Canada, in *Proceedings 4th International Conference on Recent Advances in Geotechnical Earthquake Engineering and Soil Dynamics*, San Diego, California, March 26–31, 2001, paper no 11.16.

Morell, K.D., C. Regalla, L.J. Leonard, C. Amos, and V. Levson (2017) Quaternary rupture of a crustal fault beneath Victoria, British Columbia, Canada, *GSA Today* **27**, doi: 10.1130/GSATG291A.1.

Morikawa, N. and H. Fujiwara (2013) A new ground motion prediction equation for Japan applicable up to M9 mega-earthquake, *J. Disaster Res.* **8**, 878–888.

Nakahara, H., T. Nishimura, H. Sato, M. Ohtake, S. Kinoshita, and H. Hamaguchi (2002) Broadband source process of the 1998 Iwate prefecture, Japan, earthquake as revealed from inversion analyses of seismic waveforms and envelopes, *Bull. Seismol. Soc. Am.* **92**, 1708–1720.

Nanjo, K.Z., B. Enescu, R. Shcherbakov, D.L. Turcotte, T. Iwata, and Y. Ogata (2007) Decay of aftershock activity for Japanese earthquakes, *J. Geophys. Res. Solid Earth* **112**, doi: 10.1029/2006JB004754.

Nanjo, K.Z., T. Ishibe, H. Tsuruoka, D. Schorlemmer, Y. Ishigaki, and N. Hirata (2010) Analysis of the completeness magnitude and seismic network coverage of Japan, *Bull. Seismol. Soc. Am.* **100**, 3261–3268.

Nanjo, K.Z., S. Sakai, A. Kato, H. Tsuruoka, and N. Hirata (2013) Time-dependent earthquake probability calculations for southern Kanto after the 2011 M9.0 Tohoku earthquake, *Geophys. J. Int.* **193**, 914–919.

Narteau, C., S. Byrdina, P. Shebalin, and D. Schorlemmer (2009) Common dependence on stress for the two fundamental laws of statistical seismology, *Nature* **462**, 642–645.

Natawidjaja, D.H., K. Sieh, M. Chlieh, J. Galetzka, B.W. Suwargadi, H. Cheng, R.L. Edwards, J.-P. Avouac, and S.N. Ward (2006) Source parameters of the great Sumatran megathrust

earthquakes of 1797 and 1833 inferred from coral microatolls, *J. Geophys. Res. Solid Earth* **111**, doi: 10.1029/2005JB004025.

Nazari, N., J.W. Van De Lindt, and Y. Li (2013) Effect of mainshock-aftershock sequences on woodframe building damage fragilities, *J. Perform. Constr. Facil.* **29**, doi: 10.1061/(ASCE)CF.1943- 5509.0000512.

Nicolis, O., M. Chiodi, and G. Adelfio (2015) Windowed ETAS models with application to the Chilean seismic catalogs, *Spat. Stat.* **14**, 151–165.

Ogata, Y. (1998) Space-time point-process models for earthquake occurrences, *Ann. Inst. Stat. Math.* **50**, 379–402.

Ogata, Y. (1988) Statistical models for earthquake occurrences and residual analysis for point processes, *J. Am. Stat. Assoc.* **83**, 9–27.

Ogata, Y. and J. Zhuang (2006) Space-time ETAS models and an improved extension, *Tectonophysics* **413**, 13–23.

Onur, T., C.E. Ventura, and W.D.L. Finn (2005) Regional seismic risk in British Columbia—damage and loss distribution in Victoria and Vancouver, *Can. J. Civ. Eng.* **32**, 361–371.

Page, M.T., N. Van Der Elst, J. Hardebeck, K. Felzer, and A.J. Michael (2016) Three ingredients for improved global aftershock forecasts: tectonic region, time-dependent catalog incompleteness, and intersequence variability, *Bull. Seismol. Soc. Am.* **106**, 2290–2301.

Pan, Y., C.E. Ventura, and W.D.L. Finn (2018) Effects of ground motion duration on the seismic performance and collapse rate of light-frame wood houses, *J. Struct. Eng.* **144**, doi: 10.1061/(ASCE)ST.1943- 541X.0002104.

Personius, S.F., R.W. Briggs, A.R. Nelson, E.R. Schermer, J.Z. Maharrey, B.L. Sherrod, S.A. Spaulding, and L.-A. Bradley (2014) Holocene earthquakes and right-lateral slip on the left-lateral Darrington--Devils Mountain fault zone, northern Puget Sound, Washington,

Geosphere **10**, 1482–1500.

Petersen, M.D., M.P. Moschetti, P.M. Powers, C.S. Mueller, K.M. Haller, A.D. Frankel, Y. Zeng, S. Rezaeian, S.C. Harmsen, O.S. Boyd, N. Field, R. Chen, K.S. Rukstales, N. Luco, R.L. Wheeler, R.A. Williams, and A.H. Olsen (2014) Documentation for the 2014 update of the United States national seismic hazard maps, *U.S. Geol. Surv. Open-File Rep.* 243 p., doi: 10.3133/ofr20141091.

Porter, K. (2015) A beginner's guide to fragility, vulnerability, and risk. In M. Beer, I. A. Kougioumtzoglou, E. Patelli, and I. S.-K. Au (Editor), *Encyclopedia of Earthquake Engineering*, Springer Berlin Heidelberg, pp. 1–29.

Porter, K. (2003) An overview of PEER's performance-based earthquake engineering methodology, in *9th International Conference on Applications of Statistics and Probability in Civil Engineering (ICASP9)*, San Francisco, CA.

Porter, K., C.R. Scawthorn, and J.L. Beck (2006) Cost-effectiveness of stronger woodframe buildings, *Earthq. Spectra* **22**, 239–266.

Potter, S.H., J.S. Becker, D.M. Johnston, and K.P. Rossiter (2015) An overview of the impacts of the 2010-2011 Canterbury earthquakes, *Int. J. Disaster Risk Reduct.* **14**, 6–14.

Power, J.A., J.C. Lahr, R.A. Page, B.A. Chouet, C.D. Stephens, D.H. Harlow, T.L. Murray, and J.N. Davies (1994) Seismic evolution of the 1989--1990 eruption sequence of Redoubt Volcano, Alaska, *J. Volcanol. Geotherm. Res.* **62**, 69–94.

Raghunandan, M. (2013) Influence of long duration ground shaking on collapse of reinforced concrete structures, *Ph.D. thesis*, Department of Civil, Environmental, and Architectural Engineering, University of Colorado, Boulder.

Raghunandan, M., A.B. Liel, and N. Luco (2015a) Aftershock collapse vulnerability assessment of reinforced concrete frame structures, *Earthq. Eng. Struct. Dyn.* **44**, 419–439.

Raghunandan, M., A.B. Liel, and N. Luco (2015b) Collapse risk of buildings in the Pacific Northwest region due to subduction earthquakes, *Earthq. Spectra* **31**, 2087–2115.

Ramanna, C.K. and G.R. Dodagoudar (2012) Seismic hazard analysis using the adaptive Kernel density estimation technique for Chennai City, *Pure Appl. Geophys.* **169**, 55–69.

Rhie, J., D. Dreger, R. Bürgmann, and B. Romanowicz (2007) Slip of the 2004 Sumatra--Andaman earthquake from joint inversion of long-period global seismic waveforms and GPS static offsets, *Bull. Seismol. Soc. Am.* **97**, S115--S127.

Riddell, R. (2007) On ground motion intensity indices, *Earthq. Spectra* **23**, 147–173.

Rietbrock, A., I. Ryder, G. Hayes, C. Haberland, D. Comte, S. Roecker, and H. Lyon-Caen (2012) Aftershock seismicity of the 2010 Maule Mw=8.8, Chile, earthquake: correlation between co-seismic slip models and aftershock distribution?, *Geophys. Res. Lett.* **39**, doi: 10.1029/2012GL051308.

Rudolf, J., C.E. Ventura, and H. Prion (1998) Static and dynamic testing of shear wall panels for typical wood frame residential construction in British Columbia, Internal EERL Report No. 9804, University of British Columbia, Vancouver, Canada.

Ruiz-Garcia, J. (2012) Mainshock-aftershock ground motion features and their influence in building's seismic response, *J. Earthq. Eng.* **16**, 719–737.

Ruiz-García, J. and J.D. Aguilar (2015) Aftershock seismic assessment taking into account postmainshock residual drifts, *Earthq. Eng. Struct. Dyn.* **44**, 1391–1407.

Ruiz-García, J. and J.D. Aguilar (2017) Influence of modeling assumptions and aftershock hazard level in the seismic response of post-mainshock steel framed buildings, *Eng. Struct.* **140**, 437–446.

Ruiz-García, J. and J.C. Negrete-Manriquez (2011) Evaluation of drift demands in existing steel frames under as-recorded far-field and near-fault mainshock--aftershock seismic sequences, *Eng. Struct.* **33**, 621–634.

Ryder, I., A. Rietbrock, K. Kelson, R. Bürgmann, M. Floyd, A. Socquet, C. Vigny, and D. Carrizo (2012) Large extensional aftershocks in the continental forearc triggered by the 2010 Maule earthquake, Chile, *Geophys. J. Int.* **188**, 879–890.

Salami, M.R. and K. Goda (2014) Seismic loss estimation of residential wood-frame buildings in southwestern British Columbia considering mainshock-aftershock sequences, *J. Perform. Constr. Facil.* **28**, doi: 10.1061/(ASCE)CF.1943-5509.0000514.

Satake, K., K. Shimazaki, Y. Tsuji, and K. Ueda (1996) Time and size of a giant earthquake in Cascadia inferred from Japanese tsunami records of January 1700, *Nature* **379**, 246–249.

Schoenberg, F.P., A. Chu, and A. Veen (2010) On the relationship between lower magnitude thresholds and bias in epidemic-type aftershock sequence parameter estimates, *J. Geophys. Res. Solid Earth* **115**, doi: 10.1029/2009JB006387.

Scordilis, E. M. (2005). Globally valid relations converting M_s, m_b and M_{JMA} to M_w, *Meeting on Earthquake Monitoring and Seismic Hazard Mitigation in Balkan Countries, NATO ARW*, Borovetz, Bulgaria, 11–17 September, 158–161.

Seif, S., A. Mignan, J.D. Zechar, M.J. Werner, and S. Wiemer (2017) Estimating ETAS: the effects of truncation, missing data, and model assumptions, *J. Geophys. Res. Solid Earth* **122**, 449–469.

Shao, G., X. Li, C. Ji, and T. Maeda (2011) Focal mechanism and slip history of the 2011 Mw 9.1 off the Pacific coast of Tohoku earthquake, constrained with teleseismic body and surface waves, *Earth, Planets Sp.* **63**, 559–564.

Shcherbakov, R., K. Goda, A. Ivanian, and G.M. Atkinson (2013) Aftershock statistics of major subduction earthquakes, *Bull. Seismol. Soc. Am.* **103**, 3222–3234.

Shcherbakov, R., D.L. Turcotte, and J.B. Rundle (2004) A generalized Omori's law for earthquake aftershock decay, *Geophys. Res. Lett.* **31**, doi: 10.1029/2004GL019808.

Shi, Y. and B.A. Bolt (1982) The standard error of the magnitude-frequency b value, *Bull.*

Seismol. Soc. Am. **72**, 1677–1687.

Shome, N., C.A. Cornell, P. Bazzurro, and J.E. Carballo (1998) Earthquakes, records, and nonlinear responses, *Earthq. Spectra* **14**, 469–500.

Sieh, K., D.H. Natawidjaja, A.J. Meltzner, C.-C. Shen, H. Cheng, K.-S. Li, B.W. Suwargadi, J. Galetzka, B. Philibosian, and R.L. Edwards (2008) Earthquake supercycles inferred from sea-level changes recorded in the corals of west Sumatra, *Science.* **322**, 1674–1678.

Simons, M., S.E. Minson, A. Sladen, F. Ortega, J. Jiang, S.E. Owen, L. Meng, J.-P. Ampuero, S. Wei, R. Chu, and others (2011) The 2011 magnitude 9.0 Tohoku-Oki earthquake: mosaicking the megathrust from seconds to centuries, *Science.* **332**, 1421–1425.

Somerville, P. G., N. Smith, S. Punyamurthula, and J. Sun (1997). Development of ground motion time histories for phase 2 of the FEMA/SAC steel project, Report SAC/BD-97/04, SAC Joint Venture, Sacramento, California.

Sornette, D. and M.J. Werner (2005a) Apparent clustering and apparent background earthquakes biased by undetected seismicity, *J. Geophys. Res. Solid Earth* **110**, doi: 10.1029/2005JB003621.

Sornette, D. and M.J. Werner (2005b) Constraints on the size of the smallest triggering earthquake from the epidemic-type aftershock sequence model, Båth's law, and observed aftershock sequences, *J. Geophys. Res. Solid Earth* **110**, doi: 10.1029/2004JB003535.

Stein, R.S., S. Toda, T. Parsons, and E. Grunewald (2006) A new probabilistic seismic hazard assessment for greater Tokyo, *Philos. Trans. R. Soc. London A Math. Phys. Eng. Sci.* **364**, 1965–1988.

Storchak, D.A., J. Schweitzer, and P. Bormann (2003) The IASPEI standard seismic phase list, *Seismol. Res. Lett.* **74**, 761–772.

Storesund, R., L. Dengler, S. Mahin, B. D. Collins, M. Hanshaw, F. Turner, and K. Welsh (2010). M 6.5 earthquake offshore Northern California January 9, 2010, GEER Field Reconnaissance Summary.

Suárez, G., V. García-Acosta, and R. Gaulon (1994) Active crustal deformation in the Jalisco block, Mexico: evidence for a great historical earthquake in the 16th century, *Tectonophysics* **234**, 117–127.

Suzuki, W., S. Aoi, H. Sekiguchi, and T. Kunugi (2011) Rupture process of the 2011 Tohoku-Oki mega-thrust earthquake (M9. 0) inverted from strong-motion data, *Geophys. Res. Lett.* **38**, doi: 10.1029/2011GL049136.

Tesfamariam, S. and K. Goda (2015a) Loss estimation for non-ductile reinforced concrete building in Victoria, British Columbia, Canada: effects of mega-thrust Mw9-class subduction earthquakes and aftershocks, *Earthq. Eng. Struct. Dyn.* **44**, 2303–2320.

Tesfamariam, S. and K. Goda (2015b) Seismic performance evaluation framework considering maximum and residual inter-story drift ratios: application to non-code conforming reinforced concrete buildings in Victoria, BC, Canada, *Front. Built Environ.* **1**, doi: 10.3389/fbuil.2015.00018.

Thingbaijam, K.K.S. and P. Martin Mai (2016) Evidence for truncated exponential probability distribution of earthquake slip, *Bull. Seismol. Soc. Am.* **106**, 1802–1816.

Thingbaijam, K.K.S., P. Martin Mai, and K. Goda (2017) New empirical earthquake-source scaling laws, *Bull. Seismol. Soc. Am.* **107**, 2225–2246.

Toda, S., R.S. Stein, and J. Lin (2011) Widespread seismicity excitation throughout central Japan following the 2011 M=9.0 Tohoku earthquake and its interpretation by coulomb stress transfer, *Geophys. Res. Lett.* **38**, doi: 10.1029/2011GL047834.

Toda, S. and H. Tsutsumi (2013) Simultaneous reactivation of two, subparallel, inland normal faults during the Mw 6.6 11 April 2011 Iwaki earthquake triggered by the Mw 9.0

Tohoku-oki, Japan, earthquake, *Bull. Seismol. Soc. Am.* **103**, 1584–1602.

Toro, G. R., and W. J. Silva (2001). Scenario earthquakes for Saint Louis, MO, and Memphis, TN, and seismic hazard maps for the central United States region including the effect of site conditions, Final technical report to the USGS, 10 January 2001, Risk Engineering, Inc., Boulder, Colorado.

Trifunac, M.D. and A.G. Brady (1975) On the correlation of seismic intensity scales with the peaks of recorded strong ground motion, *Bull. Seismol. Soc. Am.* **65**, 139–162.

Uma, S.R., S. Pampanin, and C. Christopoulos (2010) Development of probabilistic framework for performance-based seismic assessment of structures considering residual deformations, *J. Earthq. Eng.* **14**, 1092–1111.

Utsu, T., Y. Ogata, and S.R. Matsu'ura (1995) The centenary of the Omori formula for a decay law of aftershock activity., *J. Phys. Earth* **43**, 1–33.

Vamvatsikos, D. and C. Allin Cornell (2006) Direct estimation of the seismic demand and capacity of oscillators with multi-linear static pushovers through IDA, *Earthq. Eng. Struct. Dyn.* **35**, 1097–1117.

Vamvatsikos, D. and C.A. Cornell (2002) Incremental dynamic analysis, *Earthq. Eng. Struct. Dyn.* **31**, 491–514.

Ventura, C.E., W.D.L. Finn, T. Onur, A. Blanquera, and M. Rezai (2005) Regional seismic risk in British Columbia : classification of buildings and development of damage probability functions, *Can. J. Civ. Eng.* **32**, 372–387.

Vere-Jones, D. (1992) Statistical methods for the description and display of earthquake catalogs, in *Statistics in the environmental and Earth sciences*, A. T. Walden and P Guttorp (Editors), Arnold Publishers, London, 220–246.

Wald, D.J. and T.I. Allen (2007) Topographic slope as a proxy for seismic site conditions and amplification, *Bull. Seismol. Soc. Am.* **97**, 1379–1395.

Wang, K. and A.M. Tréhu (2016) Invited review paper: some outstanding issues in the study of great megathrust earthquakes—The Cascadia example, *J. Geodyn.* **98**, 1–18.

Wang, K., R. Wells, S. Mazzotti, R.D. Hyndman, and T. Sagiya (2003) A revised dislocation model of interseismic deformation of the Cascadia subduction zone, *J. Geophys. Res. Solid Earth* **108**, doi: 10.1029/2001JB001227.

Wang, Q., D.D. Jackson, and Y.Y. Kagan (2011) California earthquake forecasts based on smoothed seismicity: Model choices, *Bull. Seismol. Soc. Am.* **101**, 1422–1430.

Wang, Q., D.D. Jackson, and J. Zhuang (2010) Missing links in earthquake clustering models, *Geophys. Res. Lett.* **37**, doi: 10.1029/2010GL044858.

Wei, S., R. Graves, D. Helmberger, J.-P. Avouac, and J. Jiang (2012) Sources of shaking and flooding during the Tohoku-Oki earthquake: a mixture of rupture styles, *Earth Planet. Sci. Lett.* **333**, 91–100.

Wells, D.L. and K.J. Coppersmith (1994) New empirical relationships among magnitude, rupture length, rupture width, rupture area, and surface displacement, *Bull. Seismol. Soc. Am.* **84**, 974–1002.

Werner, M.J. (2007) On the fluctuations of seismicity and uncertainties in earthquake catalogs: implications and methods for hypothesis testing, *Ph.D. thesis*, University of California, Los Angeles, California.

Werner, M.J., A. Helmstetter, D.D. Jackson, and Y.Y. Kagan (2011) High-resolution long-term and short-term earthquake forecasts for California, *Bull. Seismol. Soc. Am.* **101**, 1630–1648.

Wetzler, N., E.E. Brodsky, and T. Lay (2016) Regional and stress drop effects on aftershock productivity of large megathrust earthquakes, *Geophys. Res. Lett.* **43**, doi: https://doi.org/10.1002/2016GL071104.

White, T.W. and C.E. Ventura (2006) Seismic performance of wood-frame residential

construction in British Columbia, *Earthquake Eng. Research Facility Report No. 06-03,* University of British Columbia, Vancouver, Canada.

Woessner, J. and S. Wiemer (2005) Assessing the quality of earthquake catalogues: estimating the magnitude of completeness and its uncertainty, *Bull. Seismol. Soc. Am.* **95**, 684–698.

Woo, G. (1996) Kernel estimation methods for seismic hazard area source modeling, *Bull. Seismol. Soc. Am.* **86**, 353–362.

Wu, H., K. Masaki, K. Irikura, and S. Kurahashi (2016) Empirical fragility curves of buildings in northern Miyagi Prefecture during the 2011 off the Pacific coast of Tohoku earthquake, *J. Disaster Res.* **11**, 1253–1270.

Yaghmaei-Sabegh, S., P. Shoaeifar, and N. Shoaeifar (2017) Probabilistic seismic-hazard analysis including earthquake clusters, *Bull. Seismol. Soc. Am.* **107**, 2367–2379.

Yagi, Y. and Y. Fukahata (2011a) Introduction of uncertainty of Green's function into waveform inversion for seismic source processes, *Geophys. J. Int.* **186**, 711–720.

Yagi, Y. and Y. Fukahata (2011b) Rupture process of the 2011 Tohoku-Oki earthquake and absolute elastic strain release, *Geophys. Res. Lett.* **38**, doi: 10.1029/2011GL048701.

Yagi, Y., T. Mikumo, J. Pacheco, and G. Reyes (2004) Source rupture process of the Tecomán, Colima, Mexico earthquake of 22 January 2003, determined by joint inversion of teleseismic body-wave and near-source data, *Bull. Seismol. Soc. Am.* **94**, 1795–1807.

Yamaguchi, N. and F. Yamazaki (2001) Estimation of strong motion distribution in the 1995 Kobe earthquake based on building damage data, *Earthq. Eng. Struct. Dyn.* **30**, 787–801.

Ye, L., T. Lay, and H. Kanamori (2012) Intraplate and interplate faulting interactions during the August 31, 2012, Philippine Trench earthquake (Mw 7.6) sequence, *Geophys. Res. Lett.* **39**, doi: 10.1029/2012GL054164.

Yeo, G.L. and C.A. Cornell (2009a) A probabilistic framework for quantification of aftershock ground-motion hazard in California: methodology and parametric study, *Earthq. Eng.*

Struct. Dyn. **38**, 45–60.

Yeo, G.L. and C.A. Cornell (2004) Building tagging criteria based on aftershock PSHA, In: *13th World Conference on Earthquake Engineering*, Vancouver, Canada, paper no 3283.

Yeo, G.L. and C.A. Cornell (2009b) Post-quake decision analysis using dynamic programming, *Earthq. Eng. Struct. Dyn.* **38**, 79–93.

Youngs, R.R., N. Abrahamson, F.I. Makdisi, and K. Sadigh (1995) Magnitude-dependent variance of peak ground acceleration, *Bull. Seismol. Soc. Am.* **85**, 1161–1176.

Zakharova, O., S. Hainzl, D. Lange, and B. Enescu (2017) Spatial variations of aftershock parameters and their relation to geodetic slip models for the 2010 Mw8. 8 Maule and the 2011 Mw9. 0 Tohoku-oki earthquakes, *Pure Appl. Geophys.* **174**, 77–102.

Zaliapin, I. and Y. Ben-Zion (2016) A global classification and characterization of earthquake clusters, *Geophys. J. Int.* **207**, 608–634.

Zhang, L., M.J. Werner, and K. Goda (2018) Spatiotemporal seismic hazard and risk assessment of aftershocks of M 9 megathrust earthquakes, *Bull. Seismol. Soc. Am.* **108**, 3313–3335.

Zhao, J.X., X. Liang, F. Jiang, H. Xing, M. Zhu, R. Hou, Y. Zhang, X. Lan, D.A. Rhoades, K. Irikura, and others (2016) Ground-motion prediction equations for subduction interface earthquakes in Japan using site class and simple geometric attenuation functions, *Bull. Seismol. Soc. Am.* **106**, 1518–1534.

Zhao, J.X., J. Zhang, A. Asano, Y. Ohno, T. Oouchi, T. Takahashi, H. Ogawa, K. Irikura, H.K. Thio, P.G. Somerville, Y. Fukushima, and Y. Fukushima (2006) Attenuation relations of strong ground motion in Japan using site classification based on predominant period, *Bull. Seismol. Soc. Am.* **96**, 898–913.

Zhuang, J. (2011) Next-day earthquake forecasts for the Japan region generated by the ETAS model, *Earth Planets Sp.* **63**, 207–216.

Zhuang, J., Y. Ogata, and D. Vere-Jones (2004) Analyzing earthquake clustering features by using stochastic reconstruction, *J. Geophys. Res. Solid Earth* **109**, doi: 10.1029/2003JB002879.

Zhuang, J., Y. Ogata, and D. Vere-Jones (2002) Stochastic declustering of space-time earthquake occurrences, *J. Am. Stat. Assoc.* **97**, 369–380.